The geological record of the lowermost tectonic units of the Cretan nappe pile

The deformation history during burial and exhumation

LINA SEYBOLD

Dissertation zur Erlangung des Doktorgrades
an der Fakultät für Geowissenschaften
der Ludwig-Maximilians-Universität München

München, 21.08.2019

Erstgutacherin: Prof. Dr. Claudia A. Trepmann
Zweitgutachter: Prof. Dr. Jörn H. Kruhl
Tag der mündlichen Prüfung: 11.12.2019

Abstract

High-pressure low-temperature (HP-LT) metasediments can provide unique insight into their geological history of subduction as well as their deposition. In this thesis, the record of deformed metasediments from the lowermost tectonic units of the Cretan nappe pile in the Talea Ori, central Crete, is used to infer the deformation processes and stress and strain histories within subduction zones, aiming to better understand how rocks deform during burial and exhumation. The record of the metasediments additionally allows to gain information on the complex pre-Alpine tectonic development of the Eastern Mediterranean area.

Up to now, the location of contact between two HP-LT metamorphic nappes outcropping in the Talea Ori, the Talea Ori group and the overlying Phyllite-Quartzite unit *sensu stricto* (PQ s.str.) has been discussed controversially. This thesis resolves the location of contact and presents a new geological map of the area. The study confirms that siliciclastic metasediments in the contact area form the stratigraphic base of the lowermost tectonic unit, the Talea Ori group.

To gain information on the unknown basement of the Talea Ori group and the pre-Alpine relation to the overlying PQ s.str., the thesis analyses lithoclasts and U-Pb ages of detrital zircons. These new age spectra of the Talea Ori group differ markedly to those of the PQ s.str., indicating very different sedimentary source areas from Late Carboniferous/Early Permian to Olenekian times. Alternative tectonic models are discussed to reconcile the zircon age data and the geological record, including sediment transport from westerly and northerly sources, terrane-displacement and deposition of the Talea Ori group to the north of the PQ s.str.

The deformation record of the HP-LT metasediments reveals that the PQ s.str. and the Talea Ori group experienced a similar tectonometamorphic history during Alpine subduction. They show similar deformation structures with a main foliation developed at peak metamorphic temperatures (370–410 °C). In the area of the 20 km long contact between both nappes strain is localized in the siliciclastic metasediments of the Talea Ori group and the PQ s.str., forming a km-wide extensional ductile shear zone. This shear zone is characterized by shear bands, shear band cleavages (C′-type) and associated quartz veins crosscutting the main foliation. Microstructures in quartz veins associated to the ductile deformation indicate temperatures > 300–350 °C. During the onset of exhumation, strain localized in an extensional ductile shear zone at the contact between both nappes, with updoming of the Talea Ori group and relative downfaulting of the PQ s.str.

To infer the stress history during exhumation, the study analyses macro- and microstructures of quartz veins within the ductile shear zone. The structures indicate that deformation of the siliciclastic metasediments took place mainly by high strain-rate dissolution-precipitation creep and cyclic cracking and sealing under low bulk stress conditions of a few tens of MPa. The study concludes that the time scale of stress-loading to cause cyclic cracking and sealing is on the order of ten to hundred years. In contrast to the indicated

low bulk stress conditions, some quartz veins show microstructures indicative of dislocation glide-controlled crystal-plastic deformation (low-temperature plasticity) at transient high stresses of a few hundred MPa. Such high differential stresses in rocks at greenschist-facies conditions require fast stress-loading rates, presumably due to coseismic loading induced by seismic activity in the overlying upper crust.

In summary, the geological record of the Talea Ori firstly gives new insight into deformation processes during exhumation from peak metamorphic conditions from the subduction channel. In an early stage of exhumation deformation localized in an extensional ductile shear zone within the HP-LT metamorphic siliciclastic metasediments. The predominant deformation mechanisms are dissolution-precipitation creep and cyclic cracking and sealing, accompanied by local and transient high stresses induced by seismic activity in the overlying seismogenic zone. Secondly, the rock record gives insight into the pre-Alpine tectonic development of the eastern Mediterranean, suggesting a sediment source in the internal zones of the Variscan orogen delivering detritus to the Talea Ori group for $\sim$40 Ma, which can have an impact on further paleogeographic reconstructions.

Contents

1 Introduction

Understanding subduction zones is one main task in geosciences, because they are in many ways motors of the dynamic earth. Crustal material is transported to depth, where it undergoes high-pressure low-temperature (HP-LT) metamorphism and deformation. HP-LT metamorphic rocks can serve as the most direct witnesses of the processes at depth, which can have influences on the earth's surface, for example by volcanic eruptions and earthquakes. The processes in depth are otherwise unattainable or only indirectly measurable by geophysical methods.

HP-LT metamorphic rocks often indicate low strain and stress conditions throughout their subduction and exhumation history, with strain being localized in ductile shear zones deforming by dissolution-precipitation creep at low stresses and high strain (e.g., Guillot et al., 2009; Wassmann & Stöckhert, 2013). However, also structures associated to short-term high stresses of seismic events should be observable in exhumed HP-LT metamorphic rocks (e.g., Sibson et al., 1975; Sibson, 1977; Fagereng et al., 2011), since subduction zones are usually characterized by strong seismic activity, including earthquakes and seismic tremor (e.g., Obara, 2002; Schwartz & Rokosky, 2007; Rubinstein et al., 2009; Fagereng & Toy, 2011). To recognize the structures that were induced by seismic processes, and in general to decipher the deformation history of the exhumed rocks, is a task which needs detailed study of the macro- and microscopic deformation structures of rocks in connection with their metamorphic development (e.g. Küster & Stöckhert, 1999; Trepmann & Stöckhert, 2003; Trepmann et al., 2017; Fagereng et al., 2018; Ujiie et al., 2018b).

The geological record of HP-LT metamorphic sediments provides information not only on their young burial and exhumation history but potentially also on the earlier geologic history at the subduction zone. The lithologies and inferred depositional environment, their relation to different tectonic nappes and the information their detritus yields on their former basement or source area, can give insight on the regional tectonic development of the area at the subduction zone.

In this thesis, HP-LT metamorphic sediments in the Talea Ori, central Crete, are investigated, since they can yield information with respect to two main points: (1) the HP-LT metasediments provide insight into the Hellenic subduction zone and yield information on the stress- and strain history during their burial and exhumation. (2) the HP-LT metamorphic sediments in the Talea Ori belong to the lowest units of the Cretan nappe pile and potentially can provide information on the unknown basement. Such information leads to a better understanding of the paleogeographic relations of the HP-LT metamorphic lower units of the Cretan nappe pile and can thus contribute to a better understanding of the complex tectonic development of the Eastern Mediterranean.

1.1 The subduction history of the Eastern Mediterranean and Crete

The tectonic history of the Eastern Mediterranean is difficult to unravel as it involves subduction, accretion and exhumation of rocks reaching back to Paleozoic times. For several decades and still ongoing, research has been done to decipher the pre-Alpine tectonic development of the region (Şengör et al., 1984; Jacobshagen et al., 1986; Dercourt et al., 1993; Dornsiepen et al., 2001; Stampfli et al., 2003; Okay et al., 2006; Robertson, 2006; Anders et al., 2007; Papanikolaou, 2009; Robertson & Ustaömer, 2009; Robertson, 2012; Papanikolaou, 2013; Chatzaras et al., 2016; Gerogiannis & Xypolias, 2017; Zulauf et al., 2018, and many others). This research includes the reconstruction of paleogeographic configurations of different tectonic nappes of the Hellenides and their tectonometamorphic evolution, as well as the reconstruction of locations and directions of ancient subduction zones.

The younger subduction history of the Hellenic subduction zone is documented by HP-LT metamorphic rocks with ages spanning from ∼53 Ma in the northern Aegean to ∼20–25 Ma on the island of Crete, exhumed in compressional as well as in extensional settings (Ring et al., 2010). During the Alpine orogeny, HP-LT metamorphic rocks exposed on Crete were subducted to about 30 km depth, and in the last decades a main question has been whether exhumation of these rocks happened during regional extension or during regional compression (Lister et al., 1984; Fassoulas et al., 1994; Kilias et al., 1994; Jolivet et al., 1996; Thomson et al., 1999; Ring & Reischmann, 2002; Ring et al., 2010; Tortorici et al., 2010). On Crete, exhumation was relatively fast in geological times (Thomson et al., 1998b) and there is a still ongoing debate about the deformation mechanisms during exhumation as well as how low-angle detachment faults and brittle and/or ductile normal faults contribute to exhumation (e.g., Lister et al., 1984; Feldhoff et al., 1993; Kilias et al., 1994; Fassoulas et al., 1994; Jolivet et al., 1996; Thomson et al., 1999; Ring & Reischmann, 2002; Rahl et al., 2005; Chatzaras et al., 2006; Papanikolaou & Vassilakis, 2010; Ring et al., 2010; Klein et al., 2013; Ring & Yngwe, 2018). For example, in Western Crete, no deformation along retrograde pathways has been observed in the HP-LT metamorphic rocks, which are reported to conserve deformation at peak metamorphic conditions (Stöckhert et al., 1999). It is argued that most deformation is localized in ductile shear zones (e.g., Stöckhert et al., 1999; Thomson et al., 1999) that form the continuations of seismically active faults (Sibson, 1977). However, the nature of these ductile shear zones and their role during exhumation is still critically discussed (e.g., Chatzaras et al., 2006; Xypolias et al., 2007; Klein et al., 2008; Ring et al., 2010; Klein et al., 2013; Ring & Yngwe, 2018).

1.2 The lower tectonic units of the Cretan nappe pile, Talea Ori, central Crete

Among the best areas to study the HP-LT metamorphic sediments of the lower nappes of the Cretan nappe pile is the Talea Ori, central Crete. Here, it is the only place where the siliciclastic metasediments of the oldest and lowest known unit of the Cretan nappe pile are exposed (Talea Ori group, variously also called Plattenkalk unit/Ida unit/Crete-

Mani-Zone; Manutsoglu et al., 1995a). This lowest unit of the Cretan nappe pile, which is also the most external nappe of the Hellenides, usually comprises platy marbles with metacherts (Plattenkalk) and crops out in several places on Crete and the Peloponnesus, but the siliciclastic base of these marbles is only exposed in the Talea Ori. The Talea Ori therefore is important for two main points:

Firstly, the siliciclastic metasediments of the lowest unit crop out in contact to the structurally overlying nappe (Phyllite-quartzite unit *sensu lato* (PQ s.l.), Zulauf et al., 2016) which comprises HP-LT metamorphic phyllites and quartzites. Therefore, the contact between both nappes is exposed within lithologically similar rocks, whereas at other outcrops of the lowest unit, marbles are in contact with the phyllites and quartzites. Consequently, the Talea Ori offers the unique possibility to investigate and compare the deformation within both nappes, and to evaluate the deformation characterizing the contact, in rocks of similar rheology.

Secondly, the basement of the lowest unit of the Cretan nappe pile is not exposed and therefore unknown. The analyses of components of metasandstones and conglomerates at the stratigraphic base of the Talea Ori group can give information on the sediment sources and on the original basement. According to paleogeographic reconstructions, the metasediments of the Talea Ori group restore at the northern margin of Gondwana. However, since the basement is unknown, it is not clear if it is related to Gondwana or not. The analyses of the detrital components, therefore, can have an impact on paleogeographic reconstructions of the External Hellenides (Dornsiepen et al., 2001; Robertson, 2006; Kock et al., 2007; Robertson, 2012; Stampfli et al., 2013; Zulauf et al., 2016)

Interpreting field observations and microstructural analyses is complicated by the fact that the siliciclastic metasediments at the stratigraphic base of the Talea Ori group crop out in contact to lithologically very similar rocks of the overlying nappe: in earlier studies, rocks of the contact area have been associated either to the Talea Ori group (Kock et al., 2007; König & Kuss, 1980; Richter & Kopp, 1983) or the overlying Phyllite-Quartzite unit s.l. (Kuss & Thorbecke, 1974; Epting et al., 1972; Zulauf et al., 2016). In the existing maps the position of the contact between Talea Ori group and Phyllite-Quartzite unit s.l. shows quite a large variability, which is probably also due to the strong deformation of the siliciclastic metasediments in the contact area (e.g., Epting et al., 1972; König & Kuss, 1980; Richter & Kopp, 1983; Kock et al., 2007).

1.3 Aims of the study

The objective of this thesis is twofold: (1) The first aim is to resolve the regional geology of the Talea Ori. It is a prerequisite to understand the relations of the HP-LT metamorphic nappes, before evaluating the deformation structures in the light of the subduction history. To resolve the paleogeographic relations of the HP-LT metamorphic nappes, moreover can contribute to a better understanding of the general tectonic development of the Eastern Mediterranean. (2) The second aim is a better understanding of the deformation processes during subduction and exhumation, using the geologic record of the HP-LT metamorphic rocks exposed in the Talea Ori, central Crete. In order to reconstruct the stress-

and strain history during Alpine subduction and exhumation the deformation structures in the metasediments of the Talea Ori are analysed.

The approach of this study towards these two main goals is chosen as follows:

- A lithologic and structural mapping of the siliciclastic metasediments in the Talea Ori, resolving the location of the contact between the Talea Ori group and the overlying phyllites and quartzites
- Analyses of detrital components to infer on the unknown basement and the paleogeographic origin of the Talea Ori group
- Analyses of the deformation structures to infer on the tectonometamorphic history during subduction and exhumation
- Macro-and microstructural analyses of quartz veins associated to the ductile deformation to infer on the deformation mechanisms, timescales and stress-loading rates

2 Overview of the thesis

2.1 Outline

After the introduction, the regional geology of the study area is outlined (Chapter 3), providing the background for all subsequent chapters of the thesis. The chapter includes a brief outline of the geology of Crete, followed by a more detailed description of the geology of the Talea Ori based on findings from literature as well as new findings that resulted from the work done in course of this study. The new findings are shown in the modified geologic map of the study area, which is published in the work by Seybold et al. (2019). In Chapter 4, the regional geology is extended to the investigation about the unknown basement and paleogeographic origin of the Talea Ori group, using lithologic component analysis and U-Pb dating of detrital zircons. This chapter is based on a submitted work by Seybold et al. (in review). Chapter 5 and 6 both deal with the deformation structures in the Talea Ori: Chapter 5 focuses on the tectonometamorphic history and the exhumation mechanisms on larger scale, based on a structural mapping supported by macro- and microstructural analyses. This chapter is based on the published work by Seybold et al. (2019). Chapter 6 deals with the deformation mechanisms and the stress and strain history during exhumation of the metasediments in the Talea Ori, based on analysis of microstructures in quartz veins associated to the ductile deformation of the metasediments, using optical microscopy and electron-backscattered diffraction. This chapter is based on the published work by Trepmann & Seybold (2019). Chapter 7 summarizes and concludes the main findings.

2.2 Author publications and contributions

Parts of the thesis are based on manuscripts for publication as described above. In the following an overview on the manuscripts and the author contributions is given:

- Manuscript by Seybold et al. (in review): *"Seybold, L., Dörr, W., Trepmann, C. A., & Krahl, J. (in review) New constraints from U-Pb dating of detrital zircons on the paleogeographic origin of metasediments in the Talea Ori, central Crete. Geological Magazine."*

  Fieldwork, sampling and thin section analyses were carried out by LS under the supervision of CT. The sample preparation and separation of zircons was done by LS and WD. Zircon U–Pb isotope analysis by LA-ICP-MS was performed and evaluated by WD. Cathodoluminescence imaging was done by all authors. LS merged the data and drafted the manuscript. All authors contributed to data interpretation and discussions.
- Manuscript by Seybold et al. (2019): *"Seybold, L., Trepmann, C. A., & Janots, E. (2019). A ductile extensional shear zone at the contact area between HP-LT metamorphic units in the Talea Ori, central Crete, Greece: deformation during early*

stages of exhumation from peak metamorphic conditions. International Journal of Earth Sciences, 108(1), 213–227."

LS and CT designed the study. LS carried out the field work, microstructural analyses and EBSD measurements under the supervision of CT. The Raman measurements were carried out by LS and analysed with support of EJ. LS merged the data and drafted the manuscript. All authors contributed to the interpretation and discussions.

- Manuscript by Trepmann & Seybold (2019): *"Trepmann, C. A. & Seybold, L. (2019). Deformation at low and high stress-loading rates. Geoscience Frontiers, 10(1), 43 – 54."*

  CT and LS designed the study. Under the supervision of CT, LS carried out the field work and conducted microstructural analyses by optical microscopy and EBSD measurements. CT conducted the TEM measurements, merged the data and drafted the manuscript. Both authors contributed to the discussions and the final manuscript.

3 Regional Geology

3.1 The geology of Crete

The island of Crete forms a horst structure within the fore-arc region of the Hellenic subduction zone, where the African plate is subducted northwards beneath the Eurasian plate. It is located in the External Hellenides within the non-volcanic south Aegean island arc that spans from the Peloponnesus towards Rhodes (Fig. 3.1a). The geology of Crete is characterized by a pile of several tectonic nappes with different tectonic and metamorphic history that similarly occur along other islands of the arc and on the Peloponnesus. The island of Crete is presently undergoing uplift that started $\sim$4 Ma ago (Meier et al., 2007), which is documented by young normal faults and dominant graben structures with Neogene sediment fillings (Fig. 3.1b), shaping today's geomorphology of the island.

The Cretan nappe pile (Fig. 3.1b) formed during northward subduction of oceanic crust and subsequent collision of the northern margin of a microcontinent, belonging to the African Plate, with the southern margin of the Eurasian Plate in Late Oligocene to Miocene times (e.g., Fassoulas et al., 1994; Kilias et al., 1994; Jolivet et al., 1996; Robertson et al., 1996; Thomson et al., 1999; ten Veen & Kleinspehn, 2003; Meier et al., 2007; Ring et al., 2010). Parts of the sedimentary cover of the microcontinent were buried to HP-LT metamorphic conditions during collision and were rapidly exhumed during the Miocene (Thomson et al., 1998b, 1999; Seidel et al., 2007; Ring et al., 2010). These HP-LT metamorphic nappes form the lower part of the Cretan nappe pile and are classified as the Plattenkalk unit (variously also called Plattenkalk series, Ida-Zone, Crete-Mani-Zone or Talea Ori group, see Manutsoglu et al. (1995a)) and the Phyllite-Quartzite unit sensu lato (PQ s.l., Zulauf et al., 2008). The Plattenkalk unit is the lowest tectonic nappe exposed on Crete and the most external unit of the Hellenides (e.g., Bonneau 1984, Creutzburg and Seidel 1975, Manutsoglu et al. 1995; Soujon et al. 1998, Jacobshagen 1978, Jacobshagen et al. 1986; Kock et al. 2007). It is described as parautochthonous, which is in contrast to the HP-LT metamorphism that was identified based on mineral assemblages in metabauxites in the Talea Ori, central Crete (Seidel et al., 1982; Theye, 1988; Theye et al., 1992), and in phyllitic rocks stratigraphically underlying the Plattenkalk in the Taygetos, Peloponnesus (e.g., Kowalczyk & Dittmar, 1991; Blumor et al., 1994; Deckert et al., 1999). The Plattenkalk unit is overlain by the PQ s.l., which comprises from bottom to top: the Trypali unit, the Phyllite quartzite unit *sensu stricto* (PQ s.str.), a pre-Alpine basement unit and the Tyros unit (Dornsiepen & Manutsoglu, 1994; Zulauf et al., 2008). The HP-LT metamorphic nappes are overlain, in structurally ascending order, by the Tripolitza unit, the Pindos unit and the Uppermost unit (Fig. 3.1), which all do not show a comparable Alpine HP-LT metamorphism. The Tripolitza unit does show Alpine LT-metamorphism but there is no indication for high pressure (e.g., Feldhoff et al., 1993; Rahl et al., 2005; Klein et al., 2013; Ring & Yngwe, 2018).

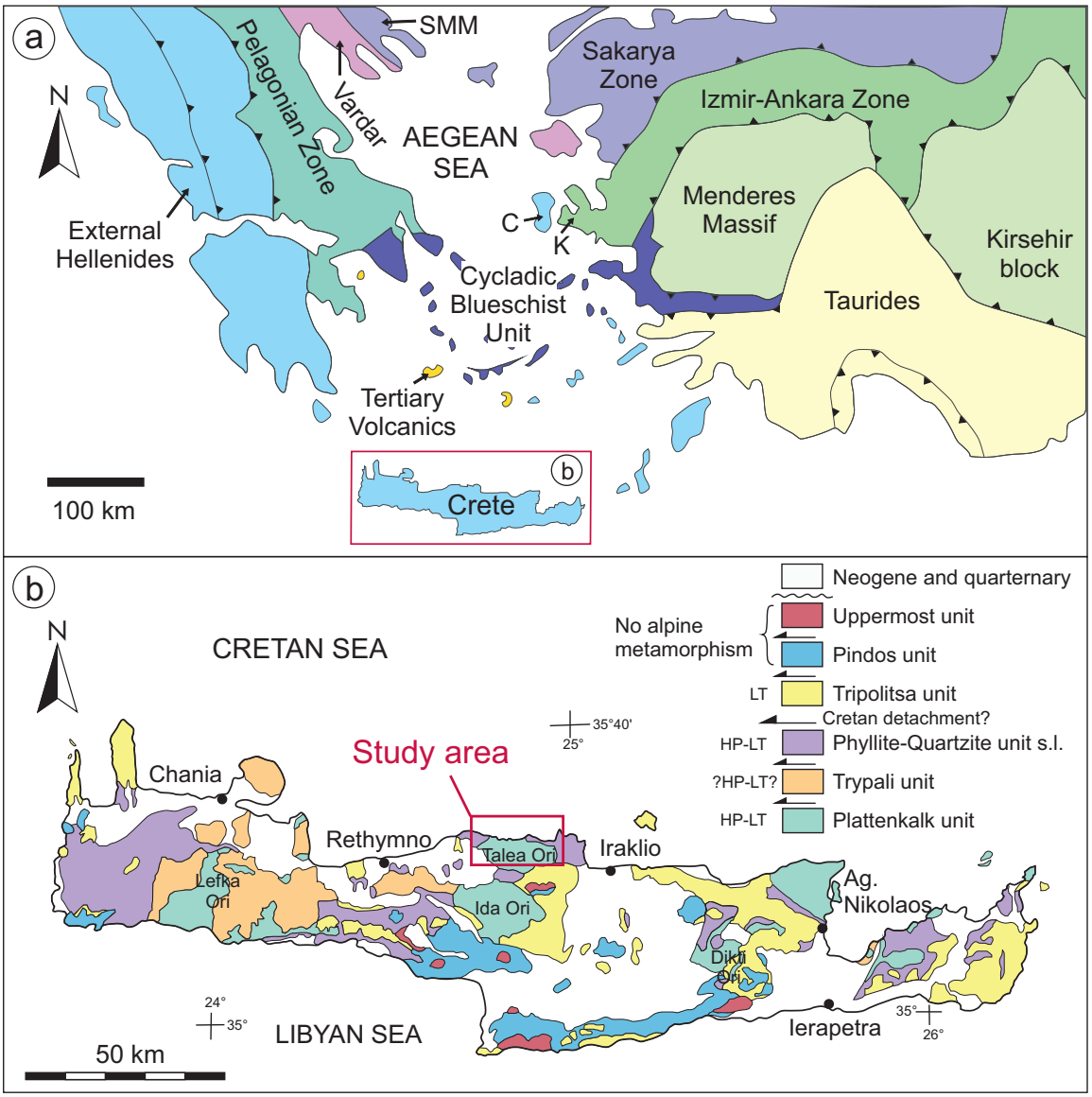

Fig. 3.1: Geologic map of (a) the Eastern Mediterranean modified after Zulauf et al. (2007), abbreviations: C = Chios, K = Karaburun, SMM = Serbo-Macedonian Massif, and (b) the island of Crete modified after Creutzburg & Seidel (1975)

3.2 Geology of the study area: the Talea Ori

The HP-LT metamorphic lower nappes of the Cretan nappe pile are well exposed in the Talea Ori, in the northern part of central Crete (Fig. 3.1b). There, the Upper Paleozoic to Lower Mesozoic metasediments of the Talea Ori group are tectonically overlain by the Phyllite-quartzite unit s.str. (e.g., Epting et al., 1972; Kuss & Thorbecke, 1974; Creutzburg & Seidel, 1975; Jacobshagen et al., 1978; König & Kuss, 1980; Bonneau, 1984; Jacobshagen et al., 1986; Kock et al., 2007; Robertson, 2012; Zulauf et al., 2016). The Talea Ori group is usually associated to the Plattenkalk unit because it comprises platy marbles with cherts at the stratigraphic top (Plattenkalk facies rocks) that are characteristic for the Plattenkalk unit, cropping out for example in the Ida Ori to the south or in the Lefka Ori in western Crete, as well as in the Taygetos mountains, Peloponnesus (e.g., Kuss & Thorbecke, 1974; Jacobshagen et al., 1978; Creutzburg & Seidel, 1975; Soujon et al., 1998; Deckert et al., 1999). However in the Talea Ori, these Plattenkalk-facies rocks are stratigraphically underlain by a siliciclastic/carbonatic rock sequence, which is not known from any other occurrence on Crete or the Peloponnesus. Therefore, in this thesis the term "Talea Ori group" is used for the siliciclastic/carbonatic succession cropping out in the Talea Ori and for other exposed platy marbles with chert on Crete and the Peloponnesus, for example in the Lefka Ori, the term "Plattenkalk unit" is used. Given the fact that in the Talea Ori such a unique HP-LT metamorphic siliciclastic/carbonatic sequence of the lowermost units of the Cretan nappe pile is exposed, it has been subject of several petrological and structural studies to unravel the Alpine subduction and exhumation history (e.g., Seidel et al., 1982; Hall & Audley-Charles, 1983; Richter & Kopp, 1983; Theye, 1988; Theye & Seidel, 1991; Theye et al., 1992; Trepmann et al., 2010). Several studies conducted lithologic mapping and biostratigraphic/geochronologic dating of the different units in the Talea Ori, not always coming to the same conclusions, regarding especially the base of the Talea Ori group and the location of the tectonic contact to the overlying PQ s.str. (Kuss, 1963; Epting et al., 1972; Kuss, 1973; Kuss & Thorbecke, 1974; König & Kuss, 1980; Krahl et al., 1988).

3.2.1 The tectonostratigraphic units in the Talea Ori

In the course of this study a detailed structural and lithological mapping was done of the area (Fig. 3.2) with special focus on the "Bali formation" cropping out at the contact between Talea Ori group and PQ s.str., to resolve if these siliciclastic metasediments belong to one or the other nappe (see also Chapter 1.2). The study confirmed that the Bali formation belongs to the Talea Ori group, cropping out in the center of the large-scale anticline (Fig. 3.2) and forming the lowest and oldest stratigraphic unit of the Talea Ori group (König & Kuss, 1980; Kock et al., 2007). The stratigraphic contacts of the different units of the Talea Ori group are often overprinted by younger normal faults, but the regular dipping of the layering and an at least locally still assessable sedimentary nature of the contacts indicates the stratigraphic relation of the different formations (e.g., Epting et al., 1972; Richter & Kopp, 1983; Kock et al., 2007).

The Bali formation is characterized by an alternation of black metasandstones/quartzites, black metacherts, meta-(quartz)conglomerates and black shales (Seybold et al., 2019). These rocks were formerly variously named, associated and mapped (e.g., Talea Ori phyl-

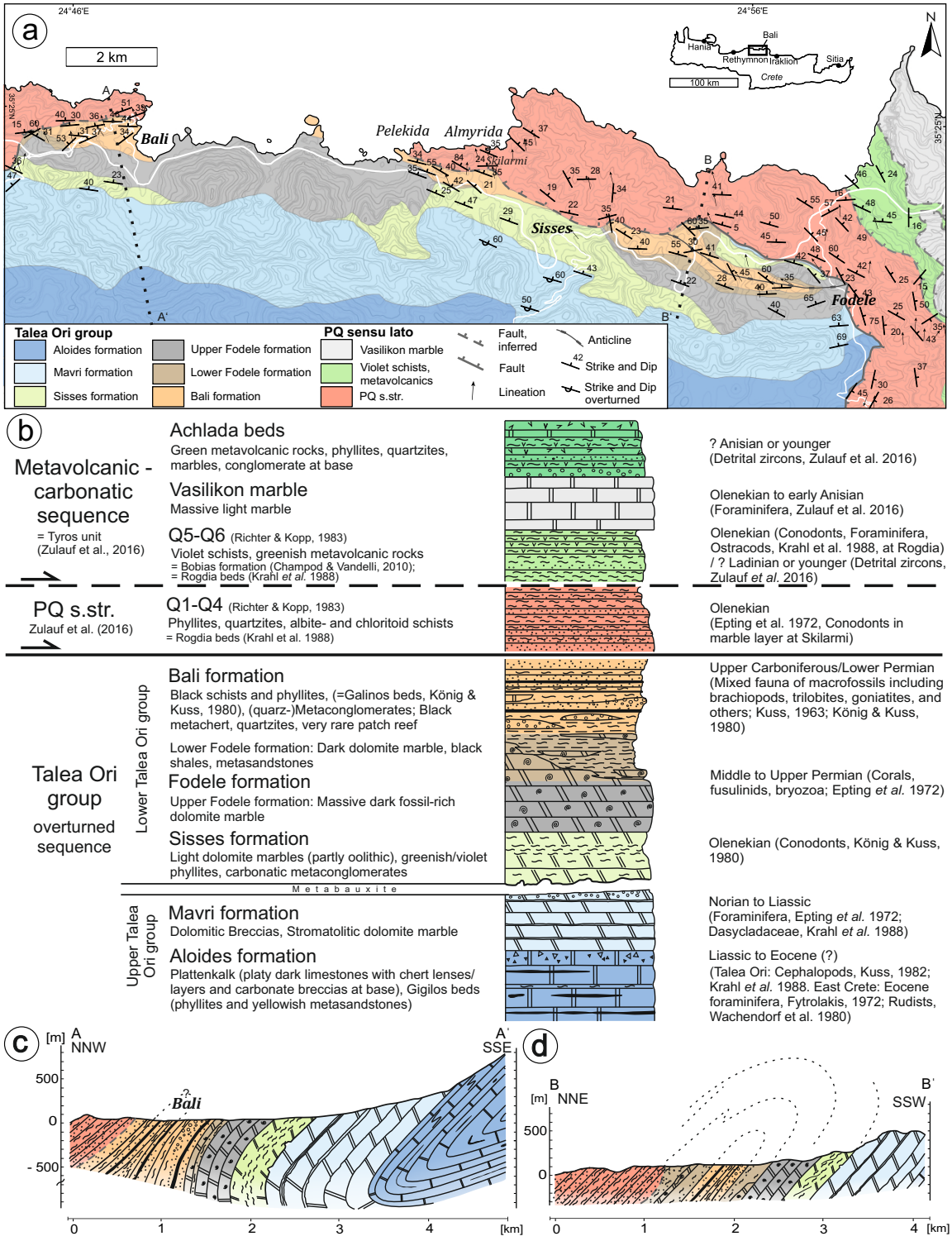

Fig. 3.2: a Geologic map of the Talea Ori modified after Epting et al. (1972), **b** tectonostratigraphic column of the different tectonostratigraphic units exposed in the Talea Ori. The given ages are biostratigraphic ages based on the macro- and microfossil records of the rocks. **c** Cross-section along line AA′, modified after Kock et al. (2007) and **d** along line BB′, modified after Richter & Kopp (1983) as marked in the map.

lite, Epting et al., 1972; Galinos shale, König & Kuss, 1980; lower Fodele formation, Richter & Kopp, 1983). The type locality of these rocks is at the beach of Bali village, and they can be found in their characteristic association in the western, central and eastern part of the northern Talea Ori (Fig. 3.2). The age of the formation has been determined by König & Kuss (1980) to be Late Carboniferous/Early Permian, based on a fauna of macrofossils including brachiopods, trilobites and goniatites. The Bali formation is stratigraphically overlain by the Fodele formation (Fig. 3.2 Epting et al., 1972; König & Kuss, 1980) characterized by 400–600 m thick dark dolomitic fossil-rich marbles (e.g., fusulinids, bryozoans, brachiopods, coral fragments), which in the lower part alternate with metasandstones and black shales (Fig. 3.2b). According to corals, fusulinids and bryozoans the Fodele formation is of Middle to Late Permian age (Epting et al., 1972; Kuss & Thorbecke, 1974; König & Kuss, 1980). The stratigraphically overlying Sisses formation (Fig. 3.2 Epting et al., 1972; König & Kuss, 1980) comprises greenish to buff coloured phyllites, light fine-grained dolomite marbles and carbonatic metaconglomerates. An Olenekian age has been determined for the dolomite marbles (conodonts, König & Kuss, 1980). The Bali, Fodele and Sisses formations are in this study grouped as the lower Talea Ori group (Fig. fig:geol-taleab). The contact to the stratigraphically overlying upper formations of the Talea Ori group (upper Talea Ori group, Fig. fig:geol-talead) is erosive with paleokarst filled by metabauxite (Epting et al., 1972; Kock et al., 2007), indicating tectonic uplift after deposition of the Sisses formation (Robertson, 2006; Stampfli et al., 2003). The Mavri formation of the upper Talea Ori group is characterized by stromatolitic dolomite marble, dated according to foraminifers and dasycladaceae to have a Norian to Liassic age (Epting et al., 1972; Krahl et al., 1988; Soujon et al., 1998). The stratigraphic top of the Talea Ori group is formed by the Aloides formation (Epting et al., 1972; Hall & Audley-Charles, 1983; Krahl et al., 1988; Soujon et al., 1998; Krahl & Kauffmann, 2004), a sequence of platy marbles with chert comprising coarse carbonate breccias at the base. In their upper part layers of greenish phyllite occur (Gigilos beds, Katsiavrias et al., 2008) and pelagic platy marbles with chert nodules or layers (Plattenkalk, Epting et al., 1972; Hall & Audley-Charles, 1983). Fossils, which are relevant for dating are rare in the formation, but cephalopods indicate an Early Jurassic age in the lower stratigraphic beds of the formation (Kuss, 1982; Krahl et al., 1988). The rock strata of the Plattenkalk unit exposed in several different outcrops on Crete are of Jurassic to Eocene age (foraminifers, east Crete, Fytrolakis (1972); rudists, east Crete Wachendorf et al. (1980); nummulites, Lefka Ori, Alexopoulos et al. (2000)), but in the Talea Ori the youngest member of the Plattenkalk unit, the Eocene Kalavros beds cropping out for example in the Ida Ori to the south, are missing (Fytrolakis, 1972; Krahl et al., 1988).

The siliciclastic/carbonatic succession of the lower Talea Ori group (Bali, Fodele and Sisses formations) is not known from any other outcrop of the Plattenkalk unit on Crete. In the Taygetos mountains, Peloponnesus, the Plattenkalk is underlain by the Kastania phyllites, but a correlation with the Talea Ori group is equivocal because the Kastania phyllites are mainly siliciclastic, containing only thin layers of carbonates (Kowalczyk & Dittmar, 1991) and are rather similar to the phyllites and quartzites of western Crete (Robertson, 2006).

The Talea Ori group is structurally overlain by the PQ s.str. (Fig. 3.2), comprising phyllites, quartzites, albite- and chloritoid schists (e.g., Zulauf et al., 2016; Creutzburg & Sei-

del, 1975; Bonneau, 1984). The PQ s.str. in the Talea Ori shows detrital zircon age patterns that are correlated with the PQ s.str. in eastern and western Crete and the Peloponnesus, with zircon ages being typically older than ∼400 Ma (Zulauf et al., 2016; Chatzaras et al., 2016). Known biostratigraphic ages of the PQ s.str. in western and eastern Crete are Late Carboniferous to Late Triassic (Krahl et al., 1983, 1986; Zulauf et al., 2018). In the Talea Ori, the sedimentation age of the PQ s.str. is uncertain because the only biostratigraphic age, determined by Epting et al. (1972) to be Olenekian, stems from a marble which is interpreted by other authors to belong to the Sisses formation of the Talea Ori group (e.g., Kuss & Thorbecke, 1974; Richter & Kopp, 1983). A conodont *Hindeodus parvus* (Kozur & Pjatakova, 1976), of the Permian-Triassic boundary was found at the southern border to the Talea Ori group.

The PQ s.str. in the eastern Talea Ori is overlain by an association of violet schists and greenish metavolcanic rocks and carbonatic rocks (Fig. 3.2a, b), which was variously named Q5–Q6 (Richter & Kopp, 1983), Rogdia beds (Krahl et al., 1988), Bobias formation (Champod & Vandelli, 2010) and upper Rogdia beds (Zulauf et al., 2016). The fossil record of samples in this metavolcanic/carbonatic sequence as well as in an overlying marble – the Vasilikon marble – give Olenekian/Anisian sedimentation ages (Krahl et al., 1988; Champod & Vandelli, 2010; Zulauf et al., 2016). Zulauf et al. (2016) attributed the metavolcanic/carbonatic sequence to the "Tyros unit" of eastern Crete (Zulauf et al., 2008). The detrital zircon patterns of this unit are characterized by a high amount of Variscan aged zircons and are similar to the zircon spectra of the Bali formation (Zulauf et al., 2016). Because of this similarity, Zulauf et al. (2016) inferred that the Bali formation and upper Rogdia beds can be associated to the Tyros unit of eastern Crete and deposited on the southern active margin of Eurasia. In eastern Crete, the Tyros unit is located above a pre-Alpine basement unit that is thrusted upon the PQ s.str. (Zulauf et al., 2008; Klein et al., 2013).

3.2.2 Deformation and metamorphism

All units in the Talea Ori experienced Alpine HP-LT conditions, as indicated by characteristic mineral assemblages (e.g., Mg-carpholite, sudoite, topaz, chloritoid, and lawsonite in the Sisses formation, and blue amphibole (crossite) in the metavolcanic rocks NW of Fodele, Seidel, 1978; Seidel et al., 1982; Theye, 1988; Theye & Seidel, 1991; Theye et al., 1992). From these studies, the metamorphic conditions were estimated around ∼0.9 GPa and 350 °C, converting in ∼30 km deep subduction. The temperature constraints are consistent with the degree of graphitization of carbonaceous material for central Crete, indicating temperatures around 400 °C (Rahl et al., 2005).

The main part of the Talea Ori group is structurally inverted, forming an overturned limb of a large-scale south-vergent fold structure with eastward plunging fold axis (Fig. 3.2 Epting et al., 1972; König & Kuss, 1980; Richter & Kopp, 1983; Krahl et al., 1988; Chatzaras et al., 2006; Kock et al., 2007). Due to the overturned fold structure of the Talea Ori group, its siliciclastic base is in contact to the PQ s.str. in the central and western Talea Ori (Fig. 3.2a). In the eastern Talea Ori, the strongly deformed and thinned non-inverted limb of the large-scale fold structure is marking the contact of higher formations of the Talea Ori group to the PQ s.str. (Epting et al., 1972; Richter & Kopp, 1983, Fig. 3.2a; "Schubfetzenzone" sensu). Because of the high strain and the similar lithology of

the siliciclastic metasediments at the base of the Talea Ori group and the PQ s.str. at their contact, there is quite a large variability in the reported position of the contact in existing maps, especially in the western Talea Ori (Epting et al., 1972; König & Kuss, 1980; Richter & Kopp, 1983; Kock et al., 2007). For both, the Talea Ori group and the PQ s.str., a common tectonic history has been described with a first deformation event represented by fold axes trending N–S to E–W (Krahl et al., 1988; Chatzaras et al., 2006; Zulauf et al., 2016). Chatzaras et al. (2006) related south-vergent folds with axes that are E-W trending and top-to-the-south shear senses to the overthrusting of the PQ s.str. onto the Talea Ori group. The early deformation is recorded by internal fabrics in albite and by isoclinal folding of a bedding-parallel first foliation (Krahl et al., 1988; Chatzaras et al., 2006; Zulauf et al., 2016). The dominant foliation is related to a second deformation event with top-to-the-north shear sense at HP-LT metamorphic conditions (Zulauf et al., 2016). Zulauf et al. (2016) distinguished a third deformation phase associated with north-vergent folds with E-W trending axes after peak metamorphic conditions at higher structural levels.

4 New constraints on the paleogeographic origin of the lowermost tectonic units of the Cretan nappe pile

This chapter is based on the manuscript *"Seybold, L, Dörr, W, Trepmann, C A, Krahl, J (in review) New constraints from U-Pb dating of detrital zircons on the paleogeographic origin of metasediments in the Talea Ori, central Crete. Geological Magazine"*.

4.1 Introduction

The Talea Ori is a key area to unravel the paleogeographic relationships between the lower nappes and the large-scale tectonic development of the eastern Mediterranean (e.g., Robertson, 2006; Stampfli et al., 2003; Kock et al., 2007; Zulauf et al., 2018). There are several alternative models discussed for example by Robertson (2006), including northward subduction, southward subduction and double subduction, in which the Talea Ori group and Plattenkalk unit restore either to a position at the northern margin of Gondwana (Dornsiepen et al., 2001; Robertson, 2006, 2012) or to the southern margin of the "Cimmerian" continent (Stampfli & Borel, 2002; Kock et al., 2007; Stampfli et al., 2013). The Cimmerian blocks started drifting northwards from Gondwana in Late Carboniferous to Early Permian times and collided with the southern Eurasian margin during the Eo-Cimmerian events in Middle Triassic times (Stampfli & Borel, 2002). According to Zulauf et al. (2018) the Plattenkalk unit restores to the northern passive margin of Gondwana. The paleogeographic origin of the structurally overlying PQ s.str. restores at the northern margin of Gondwana to the north of the Plattenkalk unit and Talea Ori group (e.g., Kozur & Krahl, 1987; Baud et al., 1993; Marcoux & Baud, 1995; Dornsiepen et al., 2001; Stampfli et al., 2003; Robertson, 2006, 2012; Stampfli & Kozur, 2006).

To further resolve the paleogeographic constellations, detrital zircon dating was carried out on several outcrops of the PQ s.l. on Crete and the Peloponnesus (Dörr et al., 2015; Zulauf et al., 2015; Chatzaras et al., 2016; Zulauf et al., 2018) and the Talea Ori group in central Crete (Kock et al., 2007; Zulauf et al., 2016). These authors revealed a large amount of Variscan aged zircons in the metasandstones at the stratigraphic base of the Talea Ori group (Bali formation, Seybold et al., 2019) and in the upper Rogdia beds on top of the PQ s.str., in contrast to detrital zircons from the PQ s.str., which systematically do not show Variscan ages. These findings challenge the interpretation that the Talea Ori group is associated to the Plattenkalk unit and deposited on the Panafrican crust of Gondwana (Dornsiepen et al., 2001) or Cimmeria (Stampfli et al., 2003; Kock et al., 2007; Moix et al., 2008). Therefore, Zulauf et al. (2016) suggested that the metasediments of the Bali formation were deposited at the active convergent margin of southern Eurasia, where the Paleotethys was subducted beneath Eurasia in Permo-Triassic times. In contrast, Kock et al. (2007) proposed that Variscan detritus was transported to the Bali formation, which

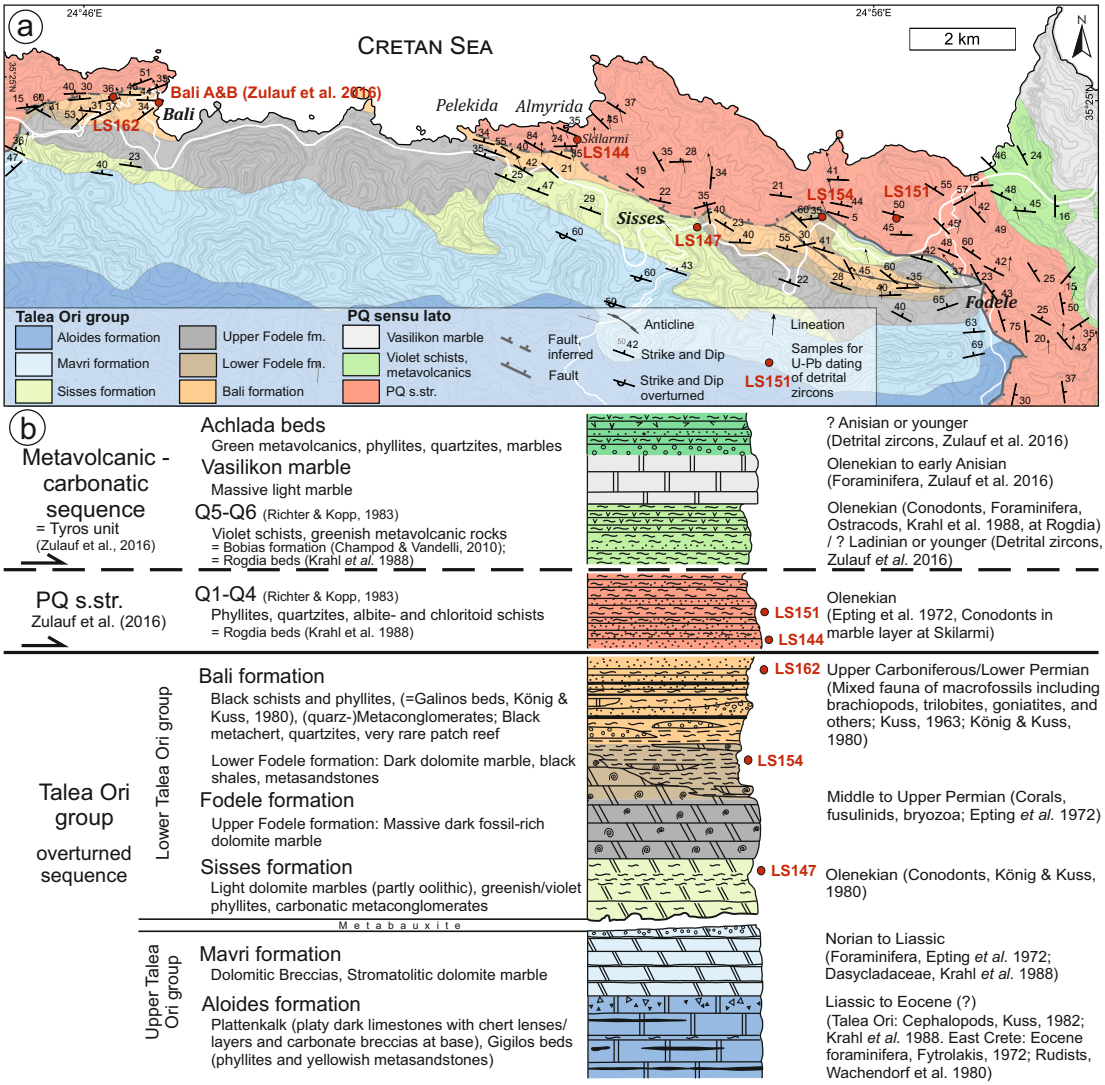

Fig. 4.1: a Geologic map of the Talea Ori, central Crete, modified after Epting et al. (1972) with sample locations for U-Pb dating. **b** Stratigraphic column with indicated samples for U-Pb dating, modified after Epting et al. (1972). The given ages are biostratigraphic ages based on the macro- and microfossil records of the rocks.

deposited in the rift between Gondwana and Cimmeria, by a river system from the Variscan belt in the West that was active during the Carboniferous.

In the following, new U-Pb ages of detrital zircons from the siliciclastic/carbonatic Upper Carboniferous/Lower Permian to Olenekian formations of the lower Talea Ori group (Fig. 4.1) and the structurally overlying PQ s.str. are presented, and the components of metaconglomerates at the base of the Talea Ori group are analysed. The paleogeographic origin of the Talea Ori group and its association to the Plattenkalk unit are critically discussed, including the approaches by Kock et al. (2007) and Zulauf et al. (2016), taking zircon data, lithofacies and structural viewpoints into account.

4.2 Analytical methods

Structural and lithological mapping in the northern area of the Talea Ori was carried out in field trips between 2016 and 2018. Samples from characteristic outcrops of the siliciclastic units were taken (Fig. 4.1) and standard petrographic thin sections (30 μm thickness) were prepared for microstructural characterization of the metasediments using polarized light microscopy. The thin sections were prepared perpendicular to the foliation and parallel to the stretching lineation, if present. U-Pb dating was performed on detrital zircons of five metasandstones and quartzites of the Bali (LS162), Fodele (LS154) and Sisses (LS147) beds as well as the PQ s.str. (LS144, LS151). For analysis by LA-ICPMS, samples were processed at the *Institut für Geowissenschaften* of the Goethe University, Frankfurt Main, using standard mineral separation techniques. These include crushing by hammer and grinding in a disk mill, followed by concentration of the heavy mineral fraction by wet shaking table, heavy liquids (bromoform, methylendiodide) and magnetic-separation with a Frantz isodynamic separator.

Hand-picked zircon grains were mounted in 25 mm-diameter circular epoxy mounts and polished to expose a section at their inner core. Prior and after LA-ICP-MS analysis, the grains were examined using cathodoluminescence (CL) imaging in order to recognize their internal structure and to identify cracks and mineral inclusions. Zircon U–Pb isotope analysis was performed by LA-ICP-MS technique using a Thermo-Finnigan Element II sector field ICPMS attached to a New Wave LUV213 laser ablation system ($\lambda = 213\ nm$). Ablation was carried out in a He carrier gas in a low volume (2.5 cm^3) cell; laser beam parameters used were 30 µm diameter; 5 Hz repetition rate 75 $\%$ power output. Isotope data were acquired in peak-jumping mode on eight masses; ^{202}Hg, ^{204}Pb, ^{206}Pb, ^{207}Pb, ^{208}Pb, ^{235}U and ^{238}U. Background and ablation data for each analysis were collected over 90 s, with background measurements (carrier gas, no ablation) being taken over the first 30 s prior to initiation of ablation. Data were collected at time-resolved mode allowing acquisition of the signal as a function of time (ablation depth), and subsequently recognition of isotopic heterogeneities within the ablated volume. Raw data were processed offline using an Excel® spreadsheet program (Frei & Gerdes, 2009). Mass discrimination of the MS, and elemental fractionation during laser ablation were corrected by calibration against the GJ-1 zircon standard (Jackson et al., 2004), which was analyzed routinely during analytical sessions (three standard analyses at the beginning and end of every session of 33 unknowns, and two standard analyses every 10 unknowns). Prior to this correction, the change of elemental fractionation (e.g. Pb/U and Pb/Th ratios as function of ablation time and thus depth) was corrected for each set of isotope ratios by applying a linear regression through all measured ratios versus time, excluding some outliers (> 2 s.e.), and taking the intercept $t = 0$ as the correct ratio. Changes in isotopic ratios arising from laser drilling into domains of distinct Pb/U ratio (core/rim), mineral inclusions, and zones affected by Pb loss (metamictization/cracks), can usually be detected by careful monitoring of the time-resolved signal, such analyses are normally rejected. Common Pb correction was applied only when the interference- and background-corrected ^{204}Pb signal was significantly higher than the detection limit of about 20 cps. The latter is limited by the amount of Hg in the carrier gas and the accuracy to which the ^{202}Hg and thus the interfering ^{204}Hg can be monitored. Corrections made were based on common Pb composition given by the

second stage growth curve of Stacey & Kramers (1975). Data presentation was made with Isoplot (Ludwig, 2001). In order to monitor the reproducibility and accuracy of our analytical procedure, the standard zircon 91500 (Wiedenbeck et al., 1995) has been reproduced with an age of 1063 $\pm$ 3 Ma.

4.3 Results

The U–Pb results obtained from the metasedimentary rocks are presented on density/relative probability plots (Ludwig, 2001) with a concordance ($^{207}Pb/^{206}Pb$ age / $^{206}Pb/^{238}U$ age * 100) from 90 to 110 %. To present the whole age spectrum of detrital zircons of a sample they were plotted with their $^{207}Pb/^{206}Pb$ ages. For a better comparison of the zircons younger than 1.1 Ga, they were plotted with their $^{206}Pb/^{238}U$ ages in a separate diagram. The relative probability plot of Ludwig (2001) was used, because it takes the analytical uncertainties into account. If not stated elsewhere, the age peaks are calculated with the concordant analyses (97 to 103 % concordance) as concordia age of a zircon population defined by Ludwig (2001). In most cases, the oscillatory-zoned parts between the core and rim of the zircons are measured, because these parts reflect the undisturbed zircon growth and thus an undisturbed U-Pb system of the zircons with no or minor lead loss. For tables and Concordia diagrams refer to Appendix 8.2 and 8.3. Lithologic and U-Pb analyses of detrital zircons are described for each sample in the following sections.

4.3.1 Bali formation

The type location of this formation is the bay of Bali (Fig. 4.1). There, the complete sequence of interlayered black quartz-metaconglomerates (Fig. 4.2a;) Trepmann et al., 2010), metasandstones, black shales, black metacherts (Fig. 4.2) is exposed, including and fossil-rich calcitic marbles, which are not exposed elsewhere in this formation. At Bali bay, graded bedding coarsening upwards can locally be observed (Fig. 4.2b), which is consistent with an overturned layering of the Talea Ori group (e.g., Epting et al., 1972). The association crops out also several times along the "New Road" between the villages Bali and Fodele and in the center of the anticline to the west of the village Fodele (Fig. 4.1). In the formation, the metacherts (Fig. 4.2c, d) and the black shales occur as several cm- to m-thick layers and as coarse intraformational metaconglomerate. The black shales can also contain black quartz-pebbles, comparable to the vein quartz pebbles in the quartz-metaconglomerate. Locally, recrystallized microfossils (radiolarians, ostracods) are preserved in the metachert, which are visible in thin section with reflected light (Fig. 4.2d, 4.3b); radiolarians are already mentioned by Kock et al. (2007). The metaconglomerates, metasandstones and shales compose a turbiditic sequence with strongly varying proportions of shale, chert and vein quartz components. The Bali quartz-metaconglomerate represents a quartz-component-rich endmember. Metasandstones are increasingly prominent towards the contact to the PQ s.str., where they vary from mica-rich metasandstones containing up to around 6 % feldspar to black quartzites. The feldspar as well as the mica in the metasandstones and in the quartz-metaconglomerate are partly of detrital nature but also metamorphic mica and albite porphyroblasts occur, the latter revealing aligned inclusions of white mica, biotite, quartz, graphite and rutile that form an internal foliation (Seybold

et al., 2019). Such albite blasts are also found in the Sisses formation and they typically occur in albite schists of the PQ s.str. (Zulauf et al., 2016; Seybold et al., 2019).

Clast lithologies of the Bali quartz-metaconglomerate

The Bali quartz-metaconglomerate contains mm- to several cm-large well-rounded pebbles of different lithologies (Figs. 4.2a, e, f and 4.3). The most frequent rock type are the black well-rounded quartz pebbles, derived from quartz veins (Fig. 4.2a, f; Trepmann et al., 2010). In the different layers of the metaconglomerate, the proportion of vein quartz clasts to lithic clasts varies between 100–80 % vein quartz and 0–20 % lithic clasts respectively.

Seven different rock types occur as clasts: vein quartz (Fig. 4.2a, f), quartzite (Fig. 4.3a), chert (Fig. 4.3b), pelitic/psammitic siliciclastic (meta-) sedimentary rocks (Fig. 4.3c), albite-quartz aggregates (Figs. fig:zirconsbalie, 4.3d), felsic volcanic rocks (Fig. 4.3e), and partly retrograde mica schists (Fig. 4.3f). The abundance of the different pebbles is shown in Figure 4.4. Whereas the metacherts and pelitic/psammitic metasediments crop out in the Talea Ori in close association to the Bali quartz-metaconglomerate, felsic volcanic rocks as well as the black vein quartz are not exposed anywhere in the Talea Ori.

The quartzite pebbles usually show an internal foliation characterized by the shape preferred orientation (SPO) of quartz and mica, and no crystallographic preferred orientation (CPO) of quartz (Fig. 4.3a). Pebbles originating from chert comprise foliated fine-grained quartz layers with random texture and dispersed opaque phases, which are commonly crosscut by coarser quartz veins (Fig. 4.3b). Pebbles containing aggregates of coarse-grained quartz and twinned albite are interpreted to be derived from hydrothermal albite-quartz veins (Fig. 4.3d) that similarly occur in the PQ s.str., however, also an igneous source is possible (Fig. 4.2f). Rare fine-grained light pebbles with up to dm-size comprise euhedral plagioclase with sericitization, quartz phenocrysts with embayments and a low amount of K-feldspar in a fine-grained sericite-quartz matrix (Fig. 4.3e). The source rock of these components is interpreted as volcanic rock of probably dacitic or rhyolitic composition. Foliated quartz- and mica-rich components can contain aggregates of fine-grained phyllosilicates replacing former minerals and are interpreted to be derived from mica schists (Fig. 4.3f), as are single detrital mica grains (Fig. 4.2f).

Coarse-grained metasandstone (LS162)

For U-Pb dating of detrital zircons, a foliated, coarse-grained metasandstone with elongate quartz clasts and lithic clasts of typically about several mm length and several hundreds of µm width (Fig. 4.2e, f) was sampled from the Bali formation west of Bali village close to the contact to the PQ s.str. (LS162, Fig. 4.1). The metasandstone is exposed in association with black shales and black metachert of the Bali formation. It contains rounded quartz clasts and lithic clasts within a matrix of fine-grained white mica, greenish biotite, quartz, albite and opaque phases (Fig. 4.2f). Micas are enriched at boundaries to clasts perpendicular to the foliation, forming strain caps around the elongate clasts (Fig. 4.2f). The long axis of the clasts is aligned parallel to the foliation of the metaconglomerate defined by a general SPO of all components (Fig. 4.2e, f). The clasts comprise coarse-grained quartz, fine-grained-sericite quartzites, elongated clasts of mica-schists, black shales and

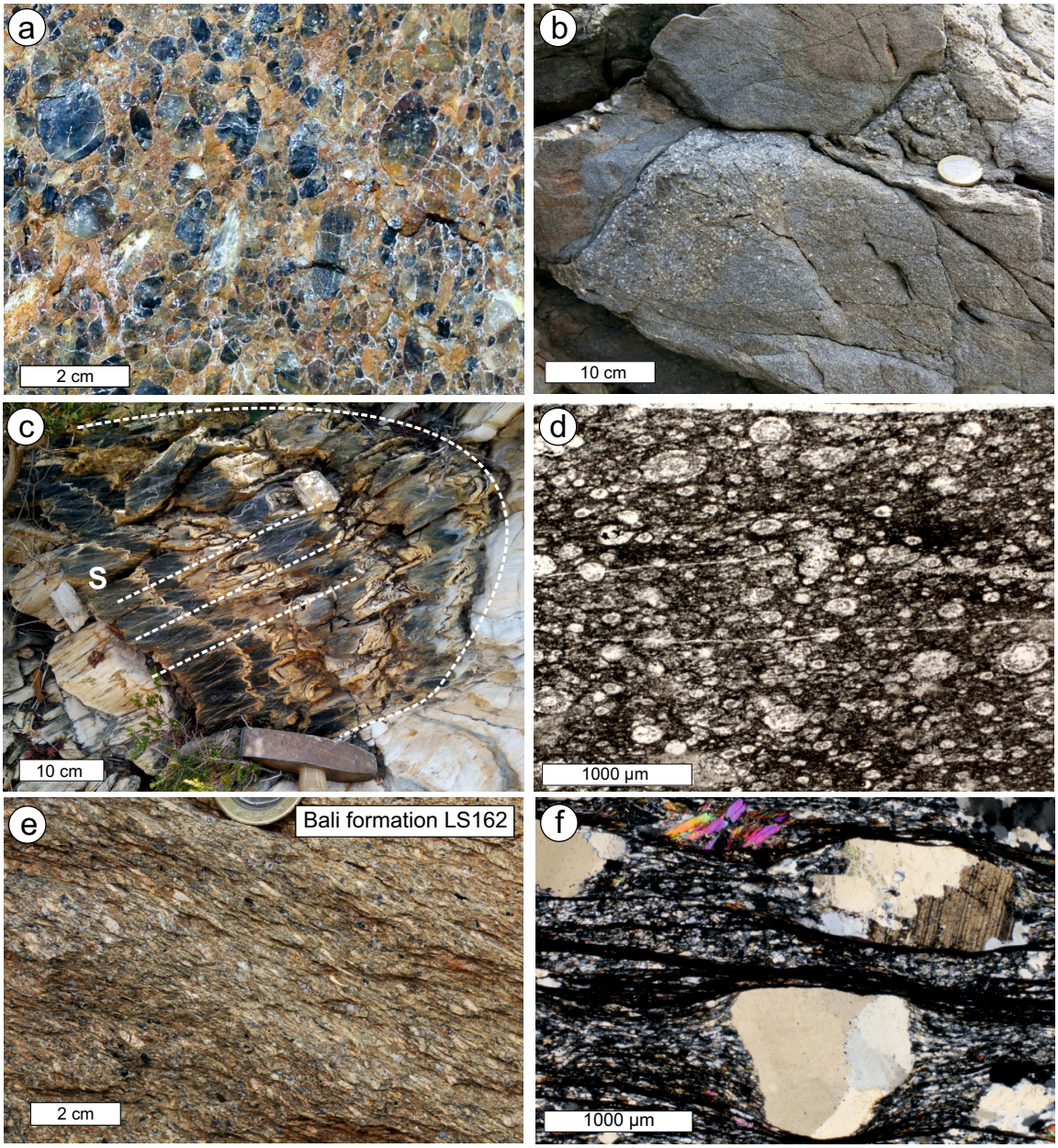

Fig. 4.2: Bali formation at the stratigraphic base of the Talea Ori group. **a** Quartz-metaconglomerate with > 90 % black vein quartz pebbles (Bali beach). **b** Inverted graded bedding in metasandstones associated to the quartz-metaconglomerate, south of the port of Bali, **c** Folded black metachert/shale interlayering with axial plane foliation, west of Galinos. **d** Metachert with fossil relicts (LS75, Bali beach). **e** and **f** coarse-grained metasandstone sampled for U-Pb dating of detrital zircons (LS162, west of Bali), (photomicrograph in **e** taken with crossed polarizers).

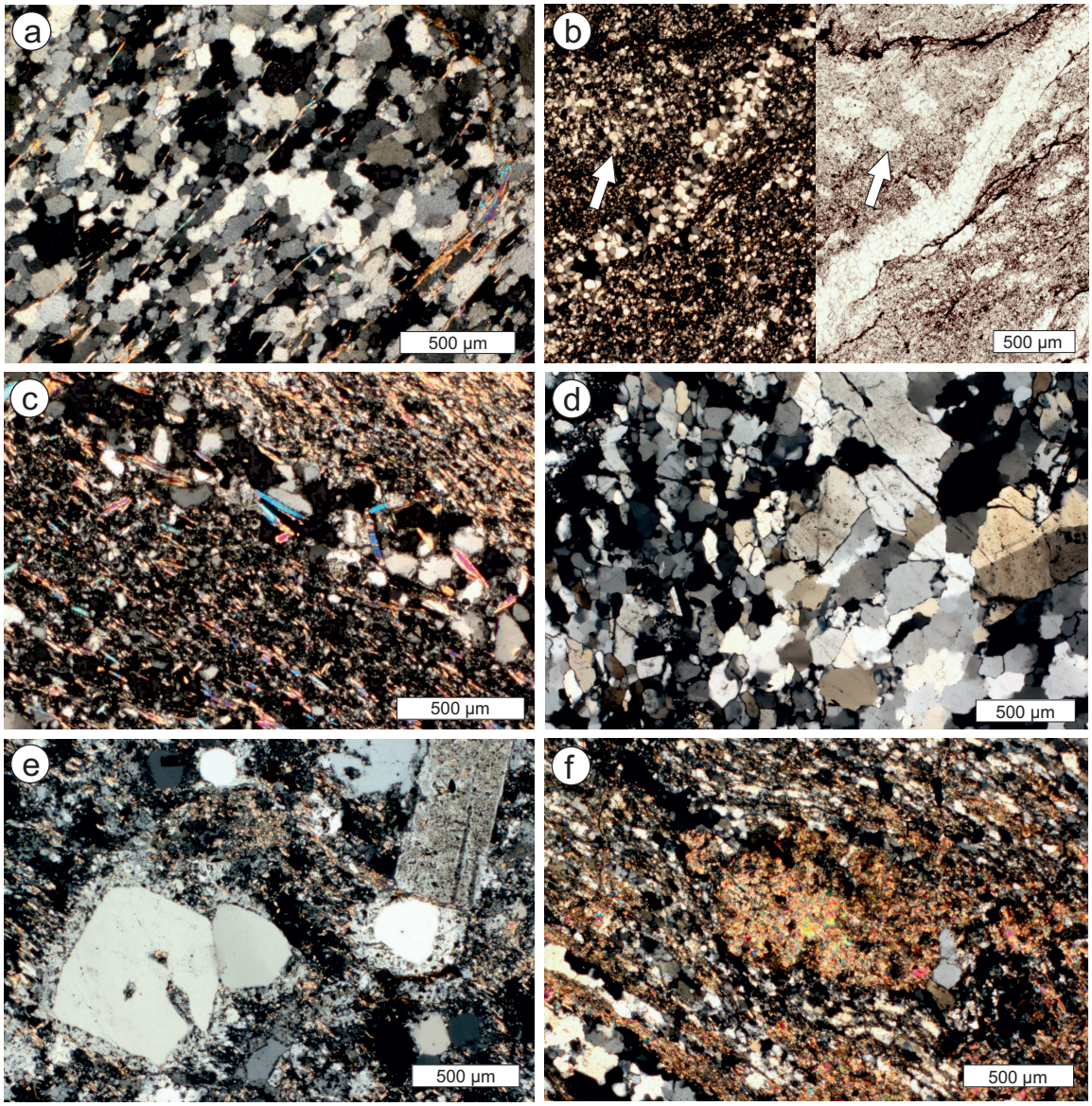

Fig. 4.3: Photomicrographs of the components of the Bali quartz-metaconglomerate and metasandstones. **a** Quartzite with mica flakes (crossed polarizers CT785). **b** Metachert with coarser quartz veins and ellipsoidial components visible mainly with plane polarized light (white arrows), CT785i, left: crossed polarizers, right: plane polarizers. **c** Metapelite with psammitic layer (LS70 crossed polarizers). **d** Albite-quartz aggregates, here also the finer grained matrix largely consists of small isometric grains of albite (LS261G crossed polarizers). **e** Felsic volcanic rock (LS261A crossed polarizers): euhedral quartz with resorption embayments and plagioclase with sericitization in fine grained quartz-plagioclase-sericite matrix, quartz shows overgrowth rims. **f** Retrograde mica schist with aggregate of fine grained phyllosilicates (LS261F crossed polarizers).

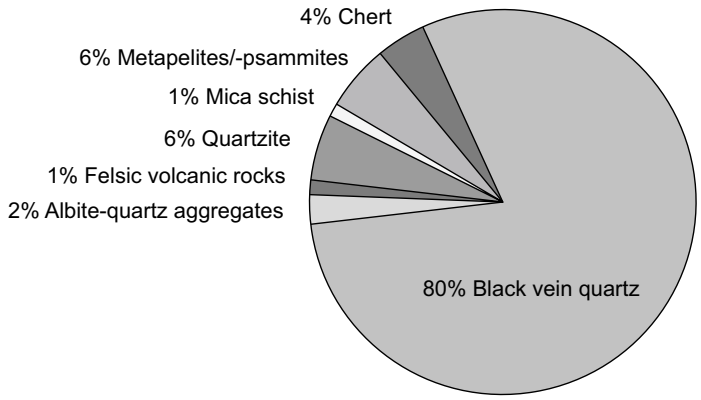

Fig. 4.4: Abundance of different pebbles of the Bali quartz-metaconglomerate.

black chert, as well as coarse-grained albite-quartz clasts. Metamorphic albite porphyroblasts occur with their internal foliation oriented oblique to the external foliation. The vein quartz clasts show large quartz grains with marked undulose extinction and subgrains and a high amount of fluid inclusions, often aligned as trails.

The sample contains 100 to 260 µm sized detrital zircons (Fig. 4.5) with a large amount of Precambrian U-Pb ages (Figs. 4.6, 4.7a, b, g). Most abundant are the Neoproterozoic detrital zircons (60 %, Fig. 4.7a, Appendix 8.2, 8.3). This age group is dominated by Ediacaran zircons (36 %) with age peaks at 562 ± 6 Ma and 611 ± 4 Ma, followed by 18 % Cryogenian detrital zircons (Figs. 4.7b, g). Only three zircons are Tonian in age. There is also a significant number of Paleozoic zircons (27 %) consisting of Early Carboniferous zircons (11 %, age peak at 343 ±7 Ma, Figs. 4.7a, g), Early Ordovician zircons (5 %, age peak at 484 ±6 Ma, Figs. 4.7a, g) and Late Cambrian zircons (9 %, age peak at 502 ±5 Ma; Figs. 4.7a, g). Only a small number of zircons (12 %) are between 1 Ga and 2.8 Ga old. The presence of Early Carboniferous zircons is consistent with a late Carboniferous/Early Permian age of the host rocks(König & Kuss, 1980). One zircon shows a younger age (271 ± 6 Ma), however, it is only 90 % concordant and the $^{207}Pb/^{206}Pb$ age is at 302 ± 3 Ma. The youngest concordant zircon is dated at 334 ± 7 Ma (Fig. 4.7a, Appendix 8.2, 8.3). The larger part of the zircons in all age groups is rounded or anhedral (Fig. 4.6). From the Paleozoic zircons about 40 % are euhedral, in the Neoproterozoic age group only approx. 20 % are euhedral and the zircons older than 1 Ga are generally well rounded (Fig. 4.6). Some of the zircons show pitted surfaces (Fig. 4.5a, zircon A85, 334 ± 7 Ma).

4.3.2 Lower Fodele formation

The Fodele formation in their lower part consist of metasandstones and black shales interlayered with dark dolomite marbles. In the upper part, mainly dark dolomite marble occurs, which is typically rich in fossil relics (e.g., Epting et al., 1972; König & Kuss, 1980). For U-Pb analysis a metasandstone (LS154) was sampled in the central Talea Ori at Pera Galinos, which is the largest outcrop of the lower Fodele formation, located within the non-inverted (normal) limb of the large-scale fold structure of the Talea Ori group (Fig. 4.1 Richter & Kopp, 1983; Seybold et al., 2019). The metasandstone is foliated in an angle to the bedding and forms several dm-thick layers interlayered with phyllitic rocks (Fig. 4.8a).

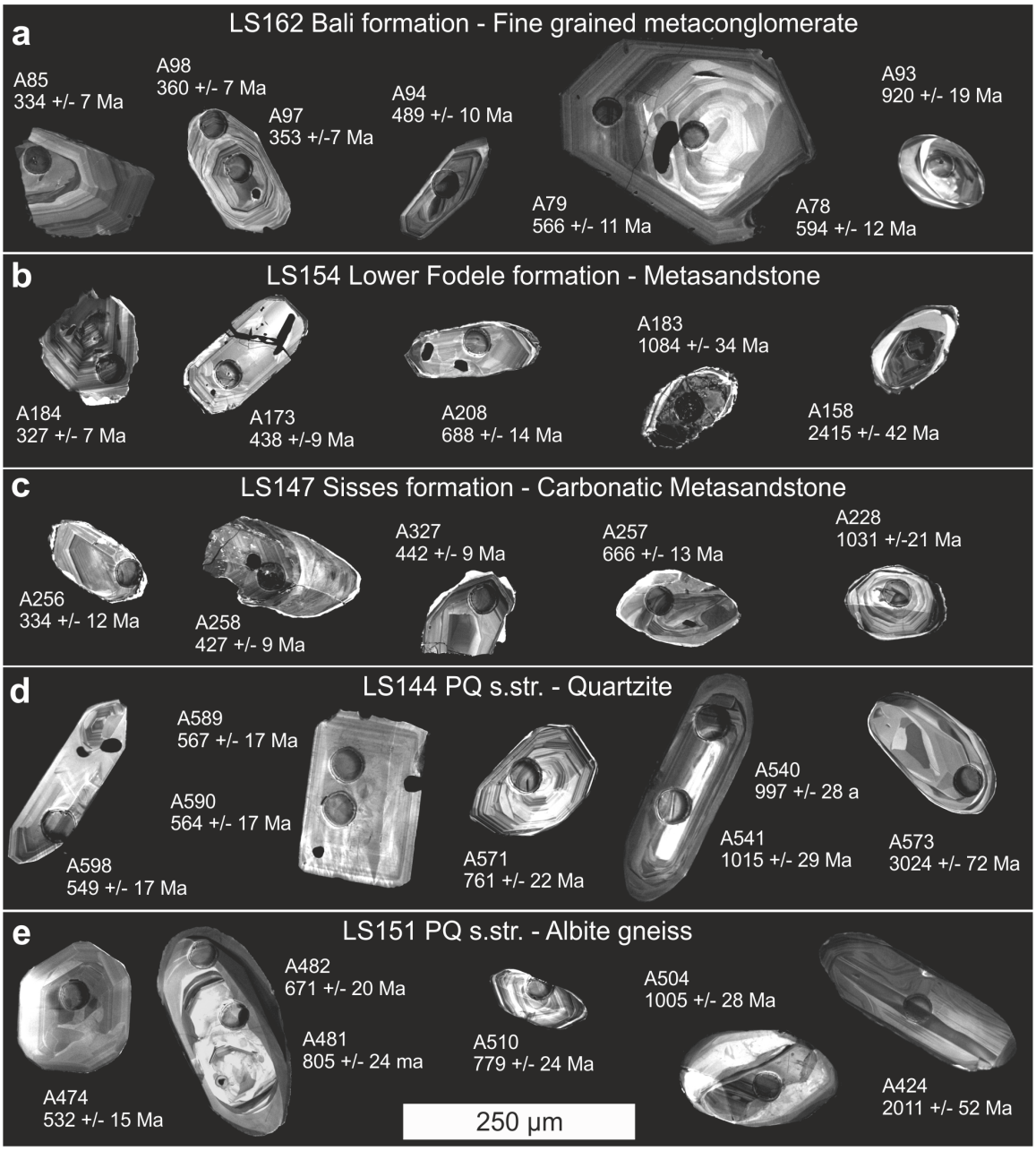

Fig. 4.5: Representative cathodoluminescence (CL) images of analyzed zircons. Apparent ^{206}Pb /^{238}U-Ages are reported with $2sigma$ uncertainty.

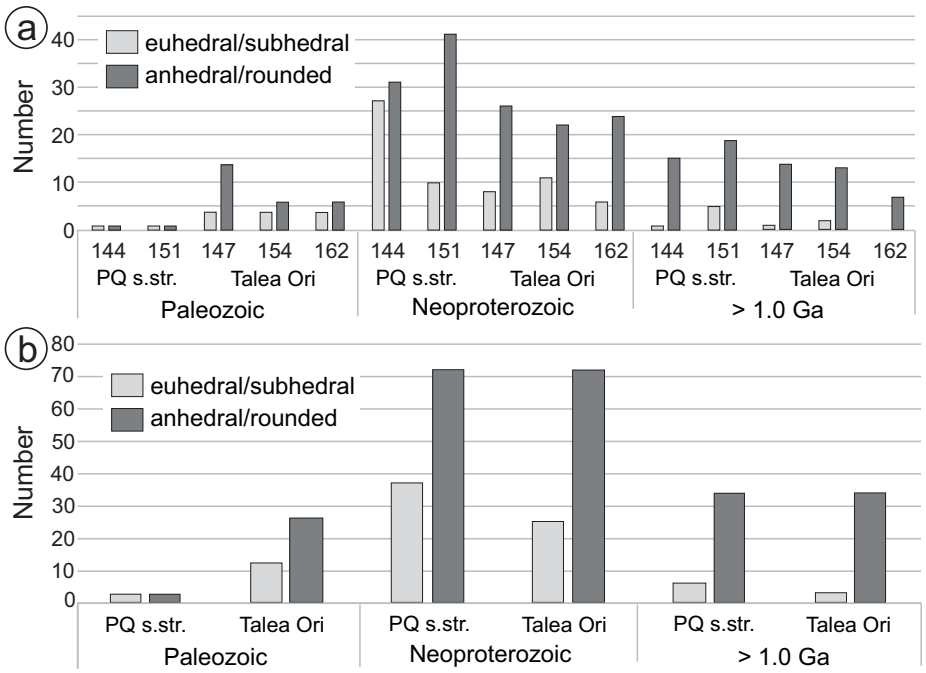

Fig. 4.6: Number of euhedral and subhedral vs. anhedral and rounded zircons within **a** each of the five different samples LS144, LS151, LS162, LS147, LS154 and **b** within the PQ s.str. (LS144 & LS151) and the Talea Ori group (LS162, LS147, LS154).

It comprises angular quartz grains that are 200 to 400 µm in diameter and surrounded by a phyllosilicate-rich matrix (Fig. 4.8b). A minor amount (about 1 %) of angular albite clasts of a few hundred µm in diameter occurs (Fig. 4.8b). On microscopic scale, bedding and foliation are hardly recognizable (Fig. 4.8b).

The metasandstone of the lower Fodele formation contains 80 to 200 µm sized detrital zircons with mainly Precambrian ages (80 %, Fig. 4.6a, 4.7c, Appendix 8.2, 8.3). The dominant Neoproterozoic age group (57 %) is split into three equal parts (Fig. 4.7d; 20 % Ediacaran, 1 % Cryogenian, 20 % Tonian zircons). There are 9 % zircons with Stenian age. The age peak at 611 $\pm$ 4 Ma is similar to the Ediacaran age peak of the Bali formation (Fig. 4.7g, h). In contrast to the Bali formation, there are also age peaks at 678 $\pm$ 6 Ma (n = 5) in the Cryogenian, and at 878 $\pm$ 10 Ma (n = 3) and 977 $\pm$ 11 Ma (n = 6) in the Tonian (Fig. 4.7g, h). Paleoproterozoic and Archean zircons are less abundant (13 %) and are mostly rounded (approx. 90 %, Fig. 4.5b, 4.6a). From the Paleozoic zircons (20 %) the highest age peak is at the Silurian/Devonian boundary, dated at 414 $\pm$ 4 Ma (n = 4). The analysis of the two youngest zircons defines a U-Pb age at 326 $\pm$ 5 Ma (Carboniferous) which is compatible with the Middle Permian biostratigraphic age of the Fodele formation (Pseudofusulina and Parafusulina zones, (Epting et al., 1972), corresponding to Artinskian to Kungurian (Zhang & Wang, 2018; Kozur & Krahl, 1987)). The zircons of the lower Fodele formation sample often show pitted surfaces, but in general the proportions of rounded/angular to euhedral or subhedral zircons is similar to the proportions within the Bali formation sample, of around 60 % anhedral/ rounded zircons within the Paleozoic group and $>$ 70 % in the Neoproterozoic age group (Fig. 4.6).

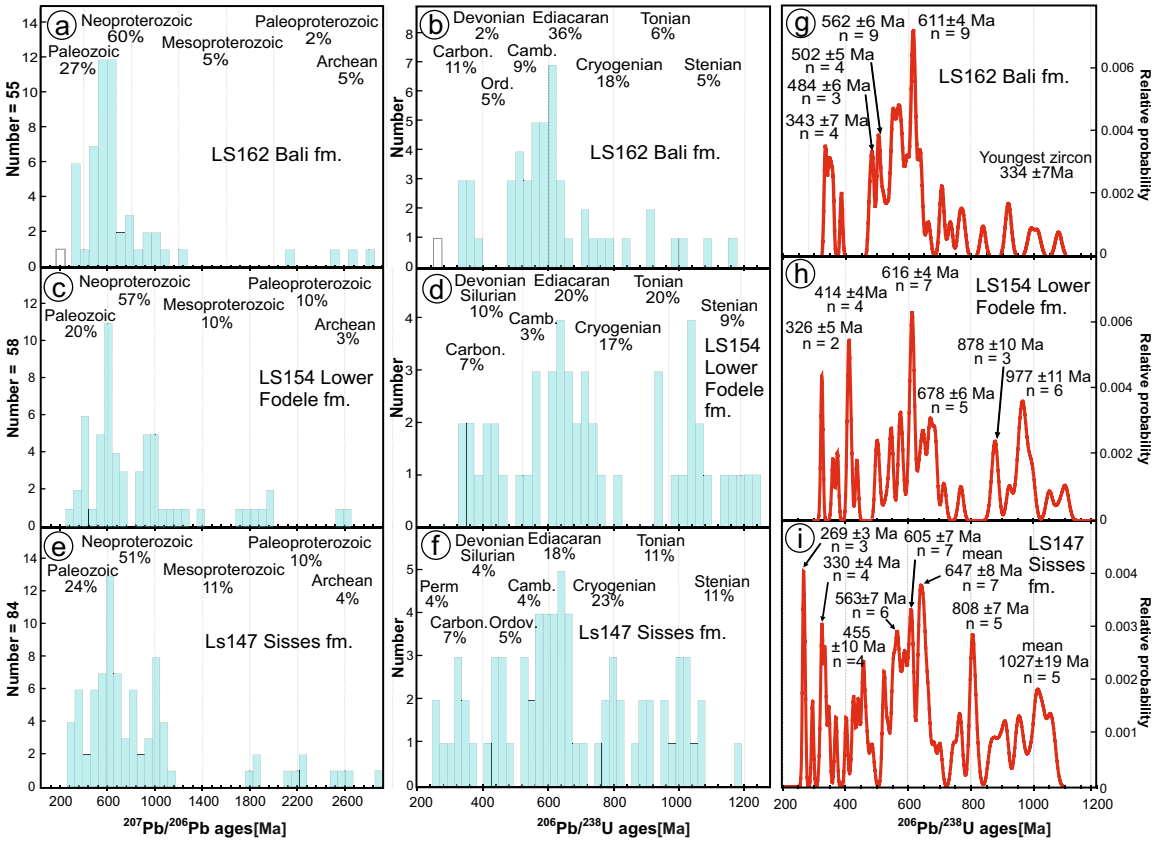

Fig. 4.7: a-f Density plots of detrital zircons separated from the Bali formation (LS162), lower Fodele formation (154) and Sisses formation (LS147) of the Talea Ori group. Complete ranges are plotted against the $^{207}Pb/^{206}Pb$ age and for younger zircons the ^{206}Pb /^{238}U-age is shown. Bin width = 40, concordance is between 90 % to 110 %. **g-i** Probability curves with age peaks of Bali formation, lower Fodele formation and Sisses formation of the Talea Ori group.

4.3.3 Sisses formation

The Sisses formation comprises marbles and violet to greenish phyllites interlayered with meta-sandstones and carbonatic metaconglomerates (Fig. 4.8c–f). Epidote (Fig. 4.8f) and albite blasts occur with a high amount of inclusions forming internal fabrics usually oblique to the external foliation of the rock, which is typical for porphyroblast formation in the Talea Ori, as described for example for albite (Theye, 1988; Zulauf et al., 2016; Seybold et al., 2019) and chloritoid (Chatzaras et al., 2006). The carbonatic metaconglomerates comprise carbonatic clasts up to ∼5 cm in diameter with strain caps and strain shadows (Fig. 4.8e, f). The strain shadows form as complex pressure fringes composed by elongate calcite and quartz grains ± mica (Fig. 4.8f). The carbonatic clasts contain various relic shapes of recrystallized fossil material, which was investigated in a metaconglomerate by Kock et al. (2007). For U-Pb analysis, a sample from a carbonatic metasandstone was collected close to the contact to the Fodele formation (LS147, Fig. 4.1, Appendix 8.2, 8.3). The metasandstone is foliated oblique to the bedding, which is apparent by darker layers enriched in opaque phases (Fig. 4.8c, d). It consists mainly of quartz and calcite and a small amount of albite, with grain diameters of 200–500 µm (Fig. 4.8d).

Sample LS147 contains, like the samples from the Bali formation and Fodele formation,

a high amount of Precambrian detrital zircons (76 %). Half of the detrital zircons (51 %) show Neoproterozoic ages with 17 % Ediacaran, 23 % Cryogenian and 11 % Tonian detrital zircons (Fig. 4.7e, f). The Ediacaran age peaks are similar to the samples described above at 563 ± 7 Ma (n = 6) and 605 ± 7 Ma (n = 7). The other Neoproterozoic age peaks are different in the Cryogenian at 647 ± 8 Ma (n = 7) and at 808 ± 7 Ma (n = 5). The Stenian aged zircons (11 %) are the only Mesoproterozoic input (Fig. 4.7e, f). Together with the Tonian zircons they define an age peak at the Neoproterozoic/Mesoproterozoic boundary at 1027 ± 19 Ma (n = 5, Fig. 4.7i) which is typical for zircon ages of the Grenvillian orogeny. A smaller amount (14 %) of the zircons is older than 1.6 Ga (Fig. 4.7e). The Paleozoic detrital zircons (24 %) display similar age peaks like in the Fodele and Bali formation in the Ordovician at 455 ± 10 Ma (n = 5) and in the Early Carboniferous at 330 ± 4 Ma (n = 4). Early Permian detrital zircons occur with the youngest age peak at 269 ± 3 Ma (n = 3, Fig. 8), which is compatible with the Olenekian deposition age of the Sisses formation (König & Kuss, 1980). An analysis of an angular zircon yield a $^{206}Pb/^{238}U$ age of 118 ± 2 Ma (concordance of 96 %, Appendix 8.2, 8.3) which is too young compared to the deposition age. This analysis could be influenced by low temperature Ca-rich fluids which caused a strong lead loss. Seven discordant zircons with U-Pb ages from ∼70 to 190 Ma point also to a later lead loss. The sample of the Sisses formation contains the smallest amount of euhedral zircons from all three samples of the Talea Ori group. Especially in the Paleozoic age group there is a larger amount of anhedral/rounded zircons (Fig. 4.6a) than in LS154 (Fodele formation) and LS162 (Bali formation).

4.3.4 Phyllite Quartzite unit s.str.

From the PQ s.str., a quartzite from the central Talea Ori (LS144) and an albite gneiss from the eastern Talea Ori (LS151) were collected (Fig. 4.1).

Quartzite (LS144)

The quartzite (LS144, Fig. 1, Appendix 8.2, 8.3) interlayered with phyllites, crops out a few meters south and structurally below a marble at the hill of Skilarmi, SE of the village Almyrida. Conodonts in the marble indicated the biostratigraphic age to be Olenekian (Epting et al., 1972; König & Kuss, 1980). It has been discussed whether this marble at Skilarmi rather belongs to the Olenekian Sisses formation instead of being part of the PQ s.str. In the discussion, Kuss & Thorbecke (1974) proposed that the marble was tectonically emplaced within the phyllites and quartzites, whereas Richter & Kopp (1983) suggested that the metasediments south of the marble also belong to the Sisses formation. According to our observations, the marble layers are strongly deformed (just like the phyllites and quartzites next to it) but they represent sedimentary layers: Marble layers with cm-thickness to 0.5 m thickness and calcitic phyllites are interlayered with the phyllites and quartzites.

The quartzite is composed by elongate quartz grains of variable diameter (100 µm to 1 mm) forming a weak foliation by their shape preferred orientation (Fig. 4.9a, b). The grain boundaries of quartz grains are coated with fine-grained iron oxides and mica (< 1 %) and small amounts of tourmaline (< 1 %) occur. Euhedral zircon grains up to ∼80 µm

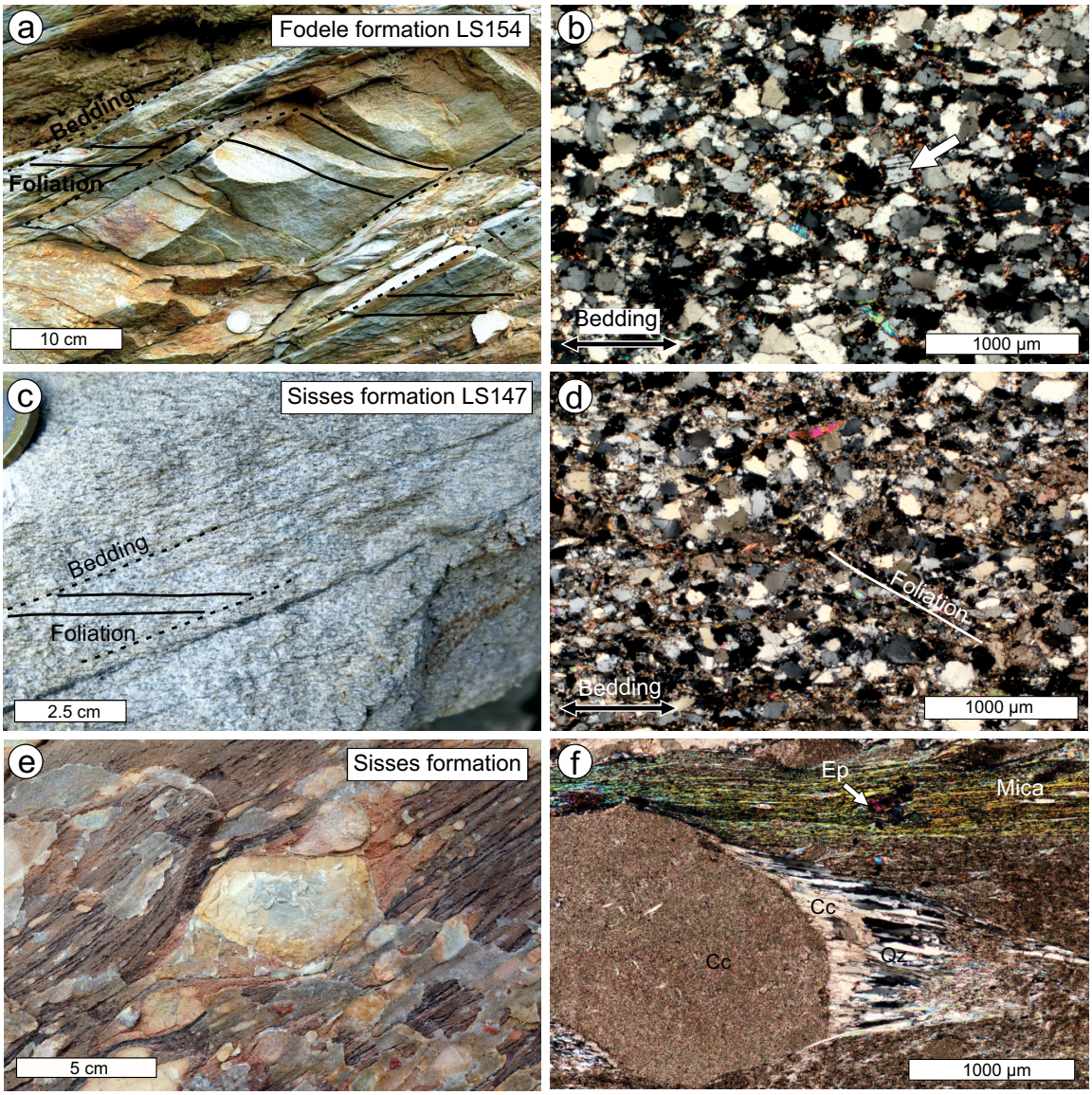

Fig. 4.8: Lower Fodele formation and Sisses formation of the Talea Ori group. **a-b** Metasandstone of the lower Fodele formation at Pera Galinos, the sample in b was collected for U-Pb dating of detrital zircons. It is composed mainly of quartz and smaller amounts of mica, iron oxides and albite (arrow), **c-d** Carbonatic metasandstone of the Sisses formation, collected for U-Pb dating of detrital zircons, the foliation forms an angle to the bedding. **e-f** Carbonatic metaconglomerate of the Sisses formation (New Road east of Sisses). Carbonate clasts form complex strain shadows composed of calcite (Cc), quartz (Qz) and mica. In the mica-rich layers of the matric epidote blasts with a high amount of inclusions occur.

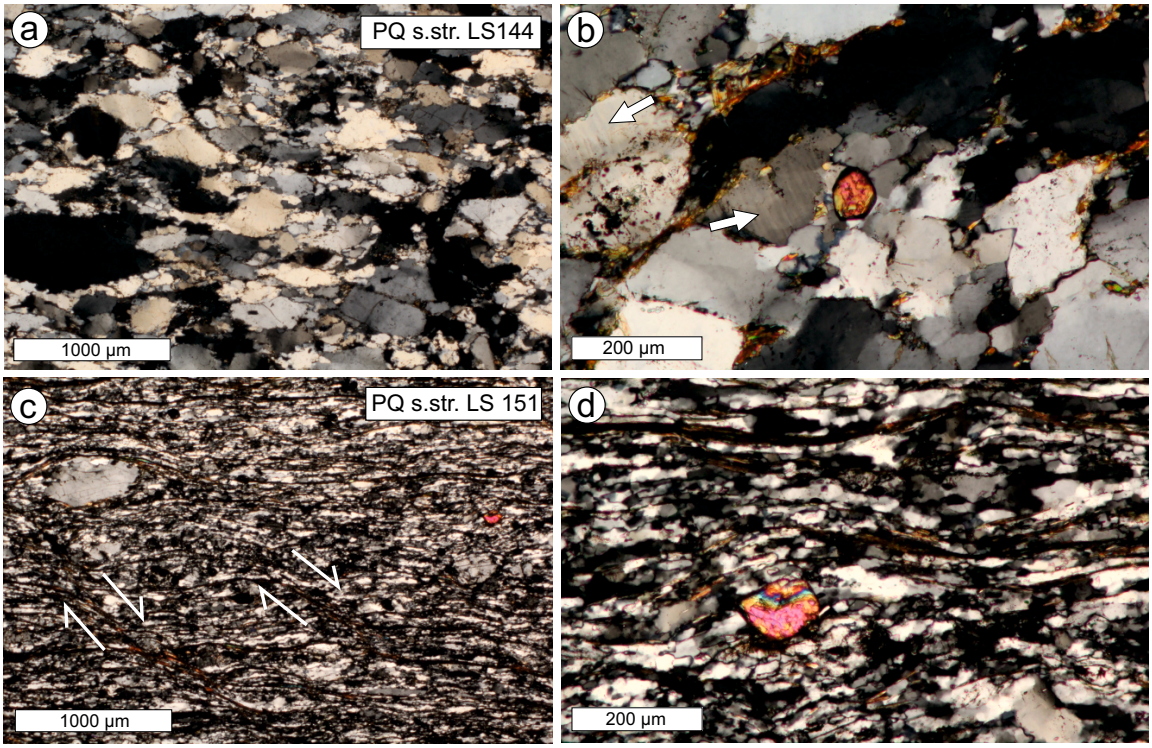

Fig. 4.9: Photomicrographs of samples from the PQ s.str. collected for U-Pb dating of detrital zircons (crossed polarizers). **a-b** Quartzite LS144 (Skilarmi) shows irregular shaped elongate quartz grains with sutured grain boundaries. Close up (**b**) shows deformation lamellae in quartz grains (white arrows) and euhedral zircon grain. **c-d** Albite-gneiss NW of Fodele shows layers with fine-grained quartz and larger albite-clasts as well as subhedral to euhedral zircon grains.

size are visible in thin section (Fig. 4.9b). The quartz grains show undulatory extinction and locally deformation lamellae (Fig. 4.9b), however, it is not clear if these features are inherited from a deformed host rock or if this is due to Alpine deformation.

The quartzite contains mainly Precambrian zircons (99 %). The main U-Pb age group of the detrital zircons is the Neoproterozoic group (80 %), which is dominated by the Ediacaran zircons (37 %, Fig. 4.10a-c) with age peaks at 571 ± 9 Ma (n = 9), 599 ± 4 Ma (n =13), 624 ± 5 Ma (n = 8) and by the subhedral to euhedral Cryogenian zircons (32 %) with smaller age peaks at 661 ± 6 Ma (n = 6) and at 794 ± 8 Ma (n = 6). Only 11 % Tonian zircons occur with a tiny peak at 972 ± 8 Ma (n = 4). Stenian (5 %) zircons are the only Mesoproterozoic zircons (Fig. 4.10c). There are 14 % zircons with U-Pb ages larger than 1.6 Ga, which are mostly rounded (Fig. 4.6a). Two concordant analysis of one Ordovician zircon yield a U-Pb age at 466 ± 10 Ma (see Appendix 8.3) which is the youngest zircon. The quartzite contains the highest number of euhedral zircons from all samples analyzed in this study, from which most occur in the Neoproterozoic age group (∼45 %, Fig. 4.6a).

Albite gneiss (LS151)

Sample LS151 is an albite gneiss, collected NE of Fodele (Fig. 1, Appendix 8.2, 8.3). The albite gneiss is interlayered with dark greenish albite schists, characteristic for the PQ s.str. It is composed of several mm-thick layers comprising lense-shaped larger quartz and

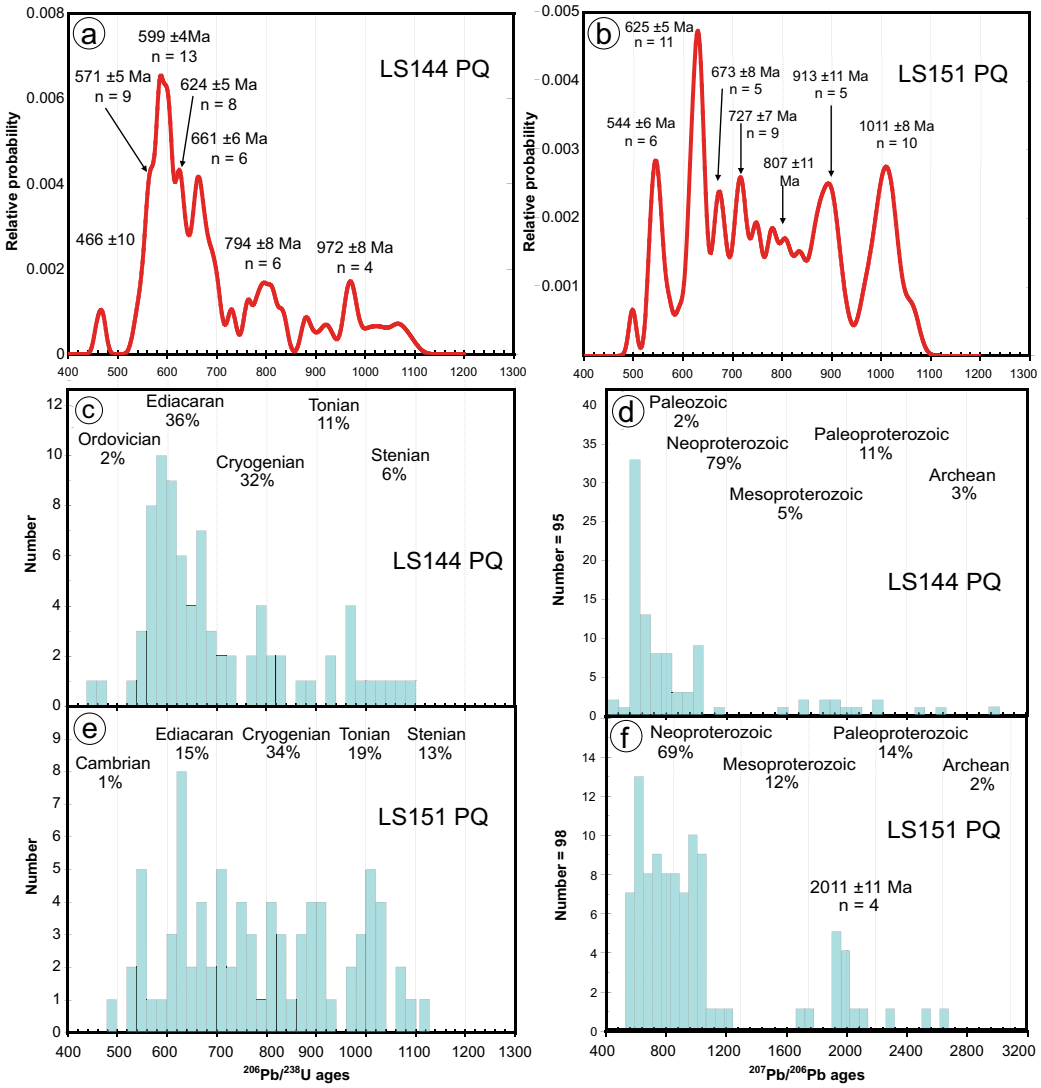

Fig. 4.10: 11 Probability curves (**a**, **d**) and density plots (**b-c**, **e-f**) of detrital zircons from quartzite (LS144) and albite-gneiss (LS151) of the PQ s.str.

albite grains (typically 500–700 µm in diameter, Fig. 4.9c) within a fine-grained (typically ∼50 µm in diameter, Fig. 4.9d) matrix of quartz, albite, iron oxides and micas. Layers rich in larger clasts occur interlayered with mm-thick layers devoid of larger clasts, comprised purely of fine-grained elongate quartz and mica (Fig. 4.9c, d). Subhedral isometric zircons with up to ∼140 µm size are visible in thin section (Fig. 4.9d). The larger grains show strain caps and strain shadows, with their long axis and the alignment of the micas forming a pronounced foliation. A second cleavage (shear band cleavage, compare Seybold et al., 2019) with enrichment of micas along the shear band boundaries is present (Fig. 4.9c).

The albite gneiss (LS151) contains two zircons with Early Cambrian age and otherwise only Precambrian zircons (Fig. 4.10d-f). The prominent U-Pb age group of the detrital zircons is the Neoproterozoic group (70 %), which is dominated by Cryogenian zircons (35 %) and the highest age peak is in the Ediacaran (Fig. 4.10d) at the boundary to the Cryogenian at 625 ± 5 Ma (n = 11). The age peaks at 673 ± 6 Ma (n = 5) and at 807 ± 11 Ma (n = 8) are similar to the Cryogenian age peaks of the sample LS144 and there is and ad-

ditional age peak at 727 ± 7 Ma (n = 9). The Ediacaran zircons (15 %) are less abundant with a prominent age peak close to the Cambrian boundary at 544 ± 6 Ma (n = 6), which is the youngest concordant zircon population of the sample. In the Tonian age group (20 %) there is an age peak at 913 ± 11 Ma (n = 5). The Stenian zircons (13 %), together with the early Tonian zircons, define a prominent age peak at the Neoproterozoic/Mesoproterozoic boundary (Fig. 4.10d) at 1011 ± 8 Ma (n = 11) which is typical for zircon ages of the Grenvillian orogeny. The Paleoproterozoic zircons occur with 14 %, which is the highest percentage of all samples. They define an age peak at 2011 ± 11 Ma (n = 4). Archean zircons (2 %) are scarce (Fig. 4.10f). The zircons are mostly anhedral or rounded and a small number of zircons is euhedral to subhedral (Fig. 4.6a).

4.4 Discussion

Our data show characteristically different zircon age spectra of the metasediments in the Talea Ori of central Crete. Including the detrital zircon age spectra obtained by Zulauf et al. (2016) and Kock et al. (2007), three different zircon age spectra are distinguished (Fig. 4.11). (1) The Carboniferous to Triassic quartzites of the PQ s.str. are dominated by Precambrian zircons (LS151 and LS144, Fig. 4.11). (2) The metasandstones of the Upper Carboniferous/Lower Permian Bali formation, sampled at south of the port of Bali (Zulauf et al., 2016; Kock et al., 2007), have a prominent U-Pb zircon age peak in the Late Carboniferous with scarce older Paleozoic (< 3 %) input (Bali A, Fig. 4.11). (3) The Lower Permian coarse-grained metasandstone of the Bali formation, sampled west of Bali village, the metasandstones of the Middle Permian Fodele formation and the Olenekian Sisses formation all show similar age spectra, with Early Paleozoic and Early Carboniferous age peaks together with a high amount of Neoproterozoic zircons (LS162, LS154, LS147, Fig. 4.11).

In the following, we discuss the provenance of the siliciclastic metasediments in the PQ s.str. and in the Talea Ori group. All available data will be balanced with respect to the provenance of the siliciclastic metasediments. The different detrital zircon U-Pb age spectra and our lithological analyses lead to four alternative models for the paleogeographic and tectonic configurations of the nappes of the External Hellenides.

4.4.1 Zircon age spectra of the PQ s.str.

Stratigraphic age of the PQ s.str. in central Crete

The youngest concordant zircon population defines an Upper Ordovician maximum sedimentation age. The only fossil record for a biostratigaphic age, conodonts from a marble at Skilarmi, point to a Olenekian deposition age in central Crete (Epting et al., 1972). It was, however, suggested that this marble is associated to the Sisses formation, which is Olenekian in age (Kuss & Thorbecke, 1974; König & Kuss, 1980; Richter & Kopp, 1983). Here, we refute this suggestion since the age spectrum obtained by U-Pb dating of detrital zircons in the quartzite (LS144, Fig. 4.11), which is located few meters structurally below and south of the Skilarmi marble, is characteristic of the PQ s.str. (Chatzaras et al., 2016,

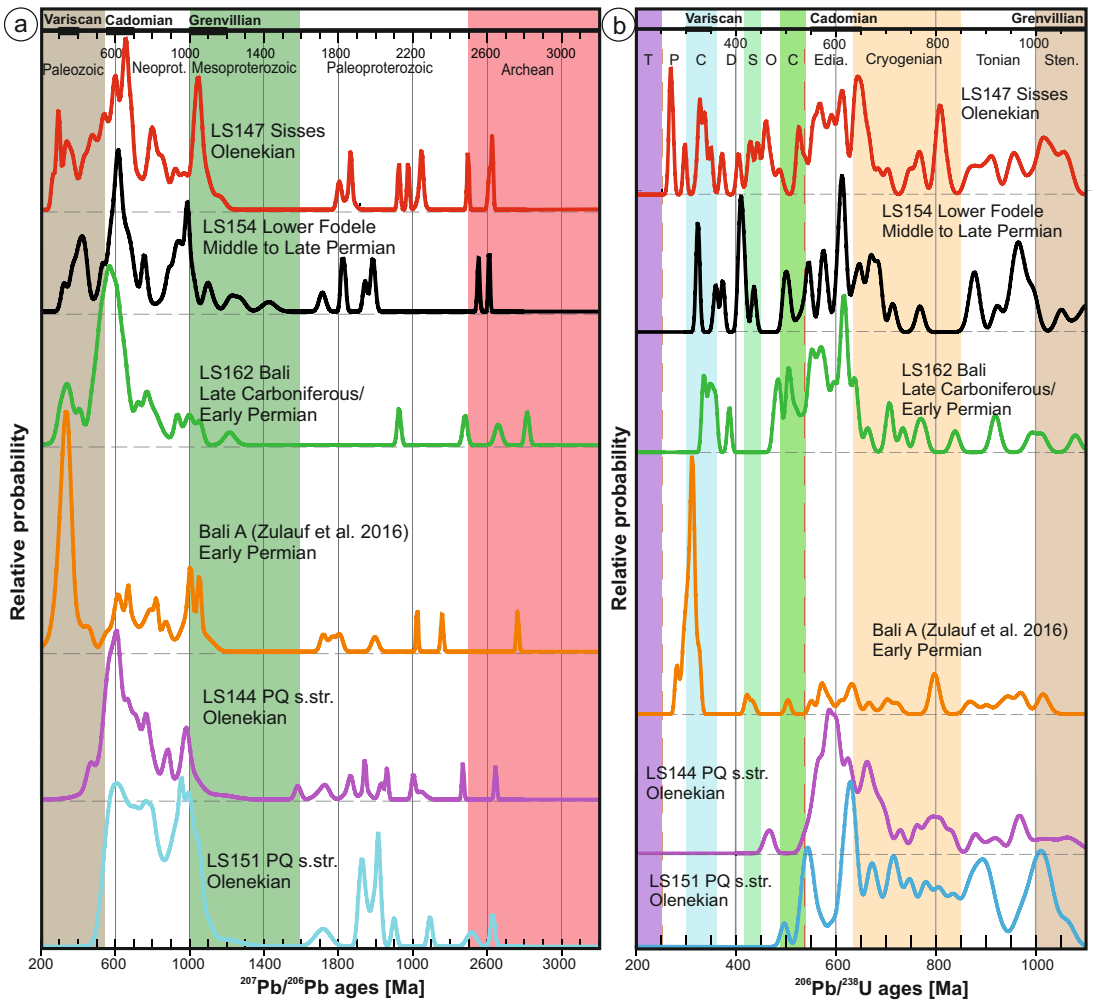

Fig. 4.11: Comparison of the probability curves of the samples of the Talea Ori group and the PQ s.str. (**a**) data from 200–3200 Ma, (**b**) data from 200–1200 Ma.

this study) and differs clearly from that of the Talea Ori group. This implies that the rocks exposed south of the Skilarmi marble are part of the PQ s.str. and the Olenekian age of the marble (Epting et al., 1972) can be taken as valid biostratigraphic age of the PQ s.str. in central Crete. This age is consistent to Carboniferous to Triassic biostratigraphic ages known for the PQ s.str. in western and eastern Crete (Krahl et al., 1983, 1986; Zulauf et al., 2018).

U-Pb ages and source regions of the PQ s.str. detrital zircons

The samples from the phyllites and quartzites in the Talea Ori are dominated by 96 % (Cr114, Zulauf2016) to 99 % (LS151, LS144 this study) Precambrian zircons with a small amount of Cambrian (533 ± 6 Ma, n = 4) to Ordovician (479 ± 10 Ma, n = 5) zircons (Concordia diagrams in supplementary material). There are similar high numbers of zircons with Ediacaran and Cryogenian ages (Fig. 4.10). The amount of Tonian aged zircons is variable from 11–26 % and it is sometimes higher than the amount of the Ediacaran zircons (LS151, Fig. 4.10). There are a pronounced Early Ediacaran age peaks around

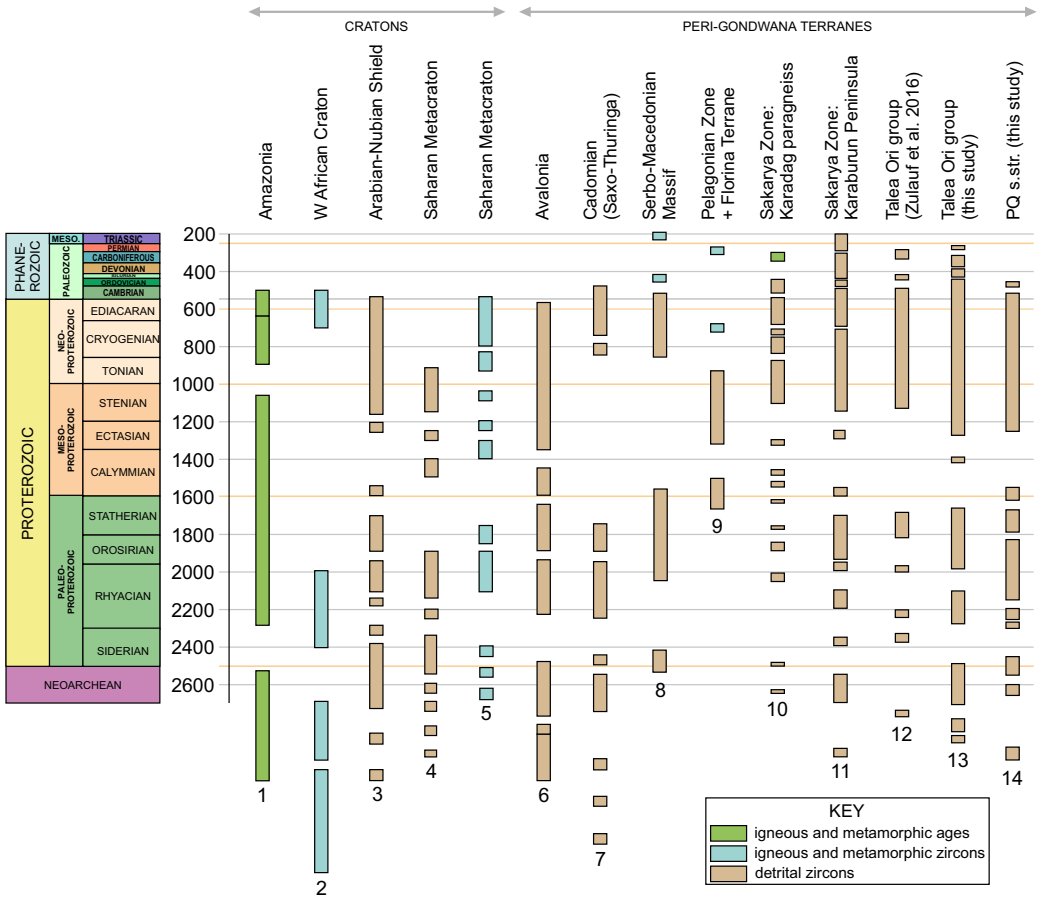

Fig. 4.12: Distribution of detrital/igneous/metamorphic zircon ages and igneous/metamorphic events known from major cratons and peri Gondwana terranes, modified after Ustaömer et al. (2013), in comparison to data from the Talea Ori (12-14). Data sources: 1, Friedl et al. (2004); Nance et al. (2008); 2, Friedl et al. (2004); Linnemann et al. (2004); Murphy et al. (2004a,b); 3, Drost et al. (2011) and references therein; 4, Drost et al. (2011) and references therein, Meinhold et al. (2011); 5-7, Drost et al. (2011) and references therein; 8, Himmerkus et al. (2007, 2009), Meinhold et al. (2010), Pirgadikia and Vertiskos Terranes belonging to the Serbo-Macedonian Massif; 9, Himmerkus et al. (2007) and references therein; 10, Ustaömer et al. (2013); 11, Löwen et al. (2017); 12, Zulauf et al. (2016); 13-14, this study.

600 Ma and high Tonian/Stenian age peaks at ∼1000 Ma, the latter pointing to a strong input of zircons formed at the Grenvillian orogeny (Fig. 4.11). Typical for the zircon age spectrum is a Mesoproterozoic age gap between 1.12 and 1.6 Ga (Fig. 4.11a) and the high amount of Cryogenian zircons. This excludes the Amazonian craton (West Gondwana) and related Avalonian type terranes, like the Pelagonian Zone, as the source area for the studied metasediments, because these do not show an age gap in the Mesoproterozic (Fig. 4.12).

Instead, the Sahara Metacraton (SMC, Fig. 4.12) is suggested as one of the possible sources of the detrital zircons analyzed from the PQ s.str. in central Crete. The SMC is built up of Neoarchean to Paleoproterozoic domains, which were overprinted in Neoproterozoic time (e.g., Meert & Van Der Voo, 1997; Abdelsalam et al., 2002; Johnson & Woldehaimanot, 2003, and references therein). The Neoproterozoic detrital zircons of the present study (Fig. 4.10) correlate with the orogenic events associated with the assembly of the SMC, the Arabian-Nubian Shield and East Gondwana (e.g., Stern, 1994; Abdelsalam et al., 2002; Kröner & Stern, 2005; Küster et al., 2008; Morag et al., 2011a,b). In the

West African Craton some of the Neoproterozoic events and the age gap from 1.1 Ga to 1.6 Ga described above are also known. However, there are no latest Mesoproterozoic (Stenian)/Early Neoproterozoic (Tonian) events, which are yet significant for the zircon spectra of the sediments from the PQ s.str. Tonian and Stenian zircons are known from the eastern margin of the SMC at the contact to the Arabian–Nubian Shield in northern Sudan (Küster et al., 2008), from xenocrysts in Pan-African granites of the western Desert of Egypt (Bea et al., 2010) and from the Sa'al metamorphic complex in South Sinai (Be'eri-Shlevin et al., 2009b, 2012). These ages correspond well with the Tonian/Stenian age peak at ∼1000 Ma of the PQ s.str. of central Crete. The rounded Neoproterozoic (50 %) and Tonian/Stenian (90 %) zircons in the metasediments of the PQ s.str. can also be explained by the recycling of Cambrian to Devonian sediments from Libya (Meinhold et al., 2011), Egypt and Middle East (Israel and Jordan, Be'eri-Shlevin et al., 2009b). The Cambrian detrital zircons and the latest Ediacaran age peak of euhedral zircons at 547 ± 5 Ma (n = 9) from the three PQ s.str. samples of central Crete (Zulauf et al., 2016, this study) are pointing to the Cadomian arc as possible source area, which occurs along the north Gondwana margin (Zlatkin et al., 2013, granitoids in the Menderes Massif,). The Cadomian magmatic arc was partly detached from the northern margin of Gondwana and survived inside the Minoan terranes (Zulauf et al., 2007), described for example in NE Sicily (Williams et al., 2012), Peloponnesus (Dörr et al., 2015) and Crete (Romano et al., 2004). East Africa and Middle East are unlikely source regions for the numerous 540–555 Ma old zircons, because igneous activity younger than 570 Ma was extremely rare in this region (Be'eri-Shlevin et al., 2009a; Avigad et al., 2012; Morag et al., 2011a,b). Thus, the latest Ediacaran and Cambrian zircons most probably stem from the remaining Cadomian arc. A possible source region of the metasediments of the PQ s.str., thus, is the former northern passive margin of East Gondwana with the SMC and the Arabian–Nubian Shield together with their Paleozoic cover sediments.

In comparison to detrital zircon age spectra of sandstones from northern Africa (e.g., Avigad et al., 2003; Kolodner et al., 2006; Linnemann et al., 2011; Meinhold et al., 2011; Avigad et al., 2012), the detrital zircon age spectra of the quartzites of the PQ s.str. from central Crete correlate well with the age spectra of the Carboniferous and Triassic sandstones of Libya (Meinhold et al., 2011). These Libyan sandstones contain also the same young zircons from the Ordovician (3 %) and Cambrian (7 %) together with 540 Ma age peaks (Meinhold et al., 2011). The Neoproterozoic age group displays the same composition as the quartzites of the PQ s.str. with 22 % Ediacaran, 23 % Cryogenian and 11 % Tonian zircons. The Stenian detrital zircons are with 17 % present. There is also an age gap between 1.1 Ga and 1.6 Ga, typical for East Gondwana, with only 17 % zircons older than 1.6 Ga. Because of this similarity of the detrital zircon age spectra of the unmetamorphosed Libyan cover sediments and the PQ s.str., both should have shared the same source area at the northern passive margin of Gondwana until the PQ s.str. was detached during Triassic times from Gondwana (e.g., Zulauf et al., 2018).

In summary, the age spectra of detrital zircons of the Olenekian quartzites of the PQ s.str. of central Crete correlate well with known age spectra of the PQ s.str. (Fig. 4.13) from other occurrences on Crete (Chatzaras et al., 2016; Zulauf et al., 2016, 2018), Kythira and Peloponnesus (Marsellos et al., 2012; Kydonakis et al., 2014; Chatzaras et al., 2016) and Samos (Löwen et al., 2015). The inferred paleogeographic position of the PQ s.str. is at

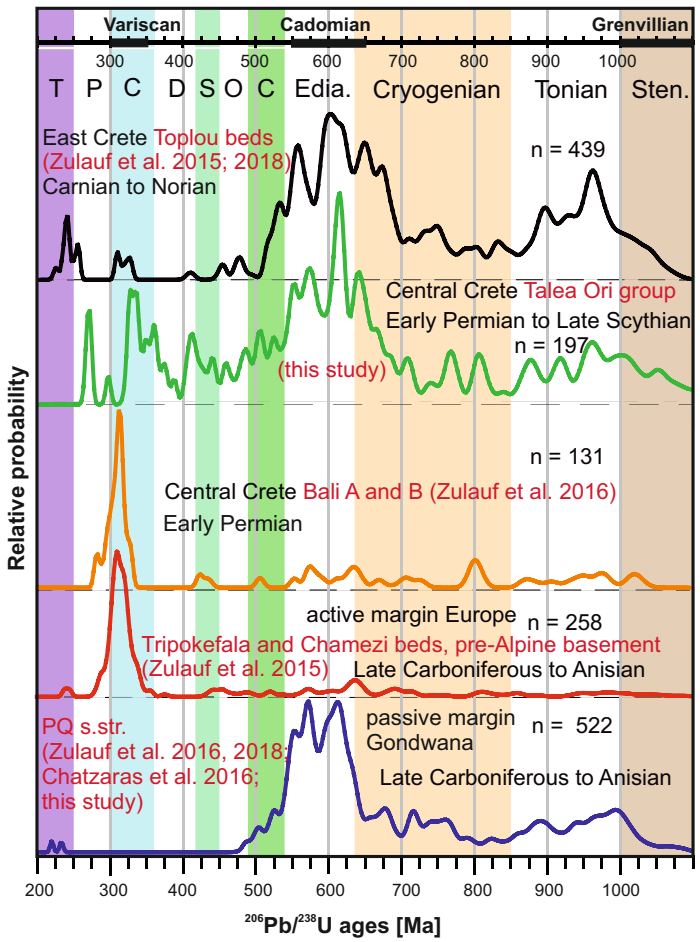

Fig. 4.13: Comparison of probability curves from different units exposed on Crete.

the northern passive margin of East Gondwana (Fig. 4.14; Zulauf et al., 2015, 2016, 2018; Chatzaras et al., 2016). This is consistent with what is expected based on sedimentological, structural and regional arguments (e.g., Kozur & Krahl, 1987; Dornsiepen & Manutsoglu, 1994; Dornsiepen et al., 2001; Stampfli et al., 2003; Robertson, 2006).

4.4.2 Zircon age spectra and sedimentary source regions of the Talea Ori group

The detrital zircon age patterns of three metasandstones sampled south of the Bali port close to the contact to the PQ s.str., analysed by (Zulauf et al., 2016) and Kock et al. (2007), show a distinctly different pattern compared to the PQ s.str. (representative sample Bali A by Zulauf et al., 2016, is shown in Fig. 4.11,). The highest age peak is in the Late Carboniferous and older Paleozoic zircon ages are scarce (< 3 %), whereas in the PQ s.str. there are no zircon ages < 450 Ma. Concerning the amount of Precambrian zircons, the three samples are heterogeneous: The samples from Zulauf et al. (2016) contained 55 % (Bali A, Fig. 4.11) and 17 % (Bali B) of Precambrian zircons. The sample from Kock et al. (2007) with only 23 analysed zircons, contains a similar amount of 26 % Precambrian zircons. The Proterozoic age spectrum resembles the age spectrum of the PQ s.str., with the

Neoproterozoic zircons having similar high amounts of Ediacaran and Cryogenian ages, an age peak at around 1 Ga and a Mesoproterozoic age gap (Fig. 4.11a). Such zircon-spectra were suggested to be characteristic for the "Minoan terranes", as introduced by Zulauf et al. (2007), who derived them from East Gondwana. According to Zulauf et al. (2015) these Minoan terranes collided prior to the Carboniferous with Eurasia along the Eurasian margin. In general, the Minoan terrane-type zircon spectra are zircon spectra that can be correlated with East Gondwana i.e., NE Africa–Arabia, which nowadays are known from Iberia, the Pyrenees, the Alps, the Serbomacedonian Massif and Turkey (Stephan et al., 2019). The Late Carboniferous/Early Permian zircons (33 to 65 %) in the metasandstones are commonly euhedral (Kock et al., 2007; Zulauf et al., 2016), suggesting a proximal source. According to Zulauf et al. (2016) the metasandstones south of the Bali port are derived from the Late Variscan orogen situated at the southern active margin of Eurasia (see discussion in Zulauf et al., 2016, 2018, and references therein).

The detrital zircon age spectra of the samples from the Bali formation west of Bali (LS162), the Fodele formation (LS154) and the Sisses formation (LS147), analyzed in this study (Figs. 4.11), are similar to each other but strikingly different to the detrital zircon age spectra of the samples south to the port of Bali (Kock et al., 2007; Zulauf et al., 2016), as well as different to those from the PQ s.str. (Fig. 4.11). Compared to the metasandstones from south of the Bali port, the change of the highest age peak from the Late Carboniferous to the Ediacaran is one of the main differences (Fig. 4.11). The amount of Late Carboniferous zircons drops from a maximum of 66 % (Kock et al., 2007; Zulauf et al., 2016) to 0–1 % in the samples of the Bali, Fodele and Sisses formations. The Paleozoic age record is dominated by Early Palaeozoic input rather than Late Paleozoic (Fig. 4.11b). Only a small proportion of the Paleozoic zircons are euhedral, similar to the proportion within the Neoproterozoic group (Fig. 4.6b). In general, the samples of the Talea Ori group show an even higher proportion of anhedral/rounded zircons vs. euhedral zircons than the samples of the PQ s.str. (Fig. 4.6b) and a large part of them are rounded to angular, partly with pitted surfaces (especially in the Fodele formation, sample LS154, Fig. 4.5b). This is in contrast to the Late Carboniferous zircons of the Bali formation from south of the Bali port, that are dominated by euhedral zircons (Kock et al., 2007; Zulauf et al., 2016). The Neoproterozoic age group varied in the metasandstones south of Bali port between 5 % to 45 %, whereas in the new samples it is constant around 55 %. The Proterozoic zircons show, like in all other samples from the Talea Ori, a NE Africa–Arabia-type age spectrum, with the Neoproterozoic zircons having similar amounts of zircons with Ediacaran and Cryogenian ages with age peaks at around 0.6 Ga and 1 Ga (Figs. 4.7, 4.11) and a considerable amount of Tonian/ Stenian zircons (Fig. 4.11).

Despite the differences in age spectra, the samples south of the port and the sample of the Bali formation analyzed in this study belong to a the same sedimentary sequence (Kock et al., 2007). All samples from the Bali formation are located close to the contact to the PQ s.str. (Fig. 4.1; Kock et al., 2007; Zulauf et al., 2016). The samples of the Bali formation west of Bali (this study), are probably of slightly higher stratigraphic position compared to the samples from the thick black metasandstones south of the port analyzed in the former studies. This is indicated on one hand by their respective structural positions within the overturned fold limb, but due to the strong tectonic overprint within the shear zone (Seybold et al., 2019) it is ambiguous to derive a relative age from the structural

position between two samples. The heterogeneity of the different zircon spectra within the Talea Ori group, and especially within the Bali formation, is suggested to be due to sediment delivery from different source areas. This assumption is supported by the high lithological diversity of components within the siliciclastic rocks of the Bali formation (Figs. 4.2-4.4).

Origin of lithoclasts, Bali formation

The component analysis of the quartz-metaconglomerate of the Bali formation indicates that the pebbles are derived from several different source areas. The black metachert (approx. 4 % of the pebbles) as well as metapelitic and metapsammitic clasts (approx. 6 % of the pebbles) are most probably derived from a local source, as the Bali formation itself are to a large part made up of metasandstones, shales and metachert. The elongate shapes and similarity of the black metachert clasts to the stratiform chert layers within the Bali formation, as well as the low resistance to weathering and transport of the metapelitic and metapsammitic clasts, are consistent with a proximal and presumably intraformational source. These types of pebbles make up less than 10 % in the conglomerate (Fig. 4.4). In contrast, the pebbles derived from felsic volcanic rocks, mica schists and black vein quartz have a very good rounding (Fig. 4.2a), indicating a rather distal source, consistent with the observation that such rocks are not exposed anywhere in the Talea Ori. Despite the indicated distal source, these pebbles form more than 80 % of the components. This high amount of "exotic" components reveals a complex source of detritus. The proportions of the different types of pebbles varies greatly in different outcrops of the conglomerate, from pure metaquartzconglomerates to pure intraformational meta-conglomerates/breccias, indicating an active environment in a slope setting with ongoing change in deposition conditions, in Late Carboniferous to Early Permian times. The metaconglomerates and metasandstones indicate a strong terrigenous influx while the contemporaneous black metachert with radiolarians points to pelagic conditions. The rare patch reefs (cropping out exclusively at Bali beach) in contrast point to a shallow marine environment. The sequence is consistent with a tectonically unstable setting in which sediments were deposited by turbiditic currents.

Zircon age spectra and lithological comparison to Eastern Crete

The Bali formation metasandstones south of the Bali port (Fig. 4.13, yellow colour, Zulauf et al., 2016) and the upper Rogdia Beds from the eastern Talea Ori show a similar detrital zircon age pattern as a coeval Early Permian black quartzite of pre-Alpine basement from eastern Crete, interpreted as active margin signature of Europe (Fig. 4.13, red colour, Zulauf et al., 2015). Zulauf et al. (2016) therefore suggested that in the Late Carboniferous/Early Permian a similar Late Variscan basement fed the Bali formation in central Crete and the pre-Alpine basement observed in eastern Crete.

The overlying Upper Carboniferous/Lower Permian to Olenekian formations of the lower Talea Ori group, analysed in our study, show a similar zircon age spectrum (Fig. 4.13, green probability curve) to that of the upper beds of the Tyros units, the Toplou beds (Fig. 15, black probability curve, Zulauf et al., 2015): A high amount of Neoproterozoic zircons together with Grenvillian input points in both cases to the Minoan terranes as source areas.

However, the Upper Triassic Toplou beds of eastern Crete cannot be correlated to the lower Talea Ori group because the Toplou beds display only few Ordovician to Devonian zircons with no age peaks and their stratigraphic age is much younger than the age of the metasediments of the lower Talea Ori group. The U-Pb age spectrum of detrital zircons from the Talea Ori group in general contains more Early Palaeozoic zircons than the other spectra from Crete. Therefore, despite some similarities in the zircon spectra of the Talea Ori group and the Tyros unit, there are significant differences in the zircon spectra, indicating different source areas.

Both units are different in tectonic position, with the Talea Ori group structurally below and the Tyros group structurally above the PQ s.str. They have different stratigraphic ages as well as metamorphic grade (amphibolite facies metamorphism of pre-Alpine basement quartzite). Furthermore, the lithologies of the siliciclastic/carbonatic sequence of the Talea Ori group and the metavolcanic Tyros unit are very different.

The differences in zircon spectra, lithologies and structural position suggest that the deposition area of the Talea Ori group was different from that of the Tyros unit. The source region for the Lower Permian metasandstones south of Bali port and pre-Alpine basement quartzite of Eastern Crete was similar (Late Variscan basement), but from the Early Permian to the Olenekian, the source region of the Talea Ori group cannot be correlated with the source region of the Tyros unit.

Source regions of the detrital zircons in the lower Talea Ori group

The Ordovician U-Pb age peaks of the detrital zircon of the Talea Ori group at 455 $\pm$ 10 Ma (n = 4) and 484 $\pm$ 6 Ma (n = 3) can be correlated with Ordovician granitoids of the basements dated with U-Pb analyses on zircons from the West Sakarya Zone (Biga Peninsula; 462 $\pm$ 6 Ma Özmen & Reischmann, 1999), from Armutlu Peninsula (Boundary to the Istanbul Zone; 470 Ma; Okay et al., 2008a), from the Tavşanli Zone correlated with the Taurides (446 $\pm$ 8 Ma,Özbey et al. (2013) and 467 $\pm$ 5 Ma, Okay et al. (2008b)) and from the Serbo-Macedonian Massif (460 $\pm$ 8 Ma, Titorenkova et al. (2003); 452 $\pm$ 5 Ma, Meinhold et al. (2010). The Silurian age peak of the Bali, Fodele and Sisses formations at 435 $\pm$ 5 Ma (n = 4, mean age) can be correlated to the Silurian basement with orthogneisses of the Serbo-Macedonian Massif (U-Pb analyses on zircons at 425 Ma to 443 Ma, Himmerkus et al., 2006, 2009). The Early Devonian age peak at 414 $\pm$ 4 Ma (n = 4) of the U-Pb analyses of detrital zircons of the Talea Ori group (central Crete) is similar to the Devonian ages of the NW Turkey of metagranodiorite from the Biga peninsula (390 to 400 Ma, Okay et al., 1996, 2006). Aysal et al. (2012b) and Sunal (2012) dated five granitoids of the West Sakarya Zone (NW Turkey) with U-Pb zircon ages from 390–401 Ma. Their wall rocks are metasediments which contain an U-Pb age spectrum of detrital zircons with a dominant Ediacaran age peak and two age peaks during the Tonian and one at 1 Ga. Aysal et al. (2012a) interpreted the amount of 6 % Mesoproterozoic zircons of the age spectrum of the detrital zircons of the wall rock as Avalonian/Amazonian related, but if we consider the Tonian and Stenian aged zircons as one age group (11 %, Grenvillian) then only 3 % zircons with an age between 1.15 Ga and 1.6 Ga are left. Tonian and Stenian zircons are common in the Central and East Sakarya Zone and are similar to the U-Pb age spectra of NE Africa–Arabia (Stephan et al., 2019) and East Gondwana derived ter-

ranes (Zulauf et al., 2007). Late Devonian granitic–granodioritic gneisses, dated at around 370 Ma from the northern (Sea of Marmara) and southern (Aegean Sea) part of the Biga peninsula (Özmen & Reischmann, 1999, Pb/Pb single-zircon), are slightly older than the U-Pb age peak at 362 ± 4 Ma (n = 4, mean age) of the Upper Devonian detrital zircons of the Talea Ori group. Ustaömer et al. (2012) dated a granitoid with a similar U-Pb age at the Devonian/Carboniferous boundary (358 ± 5 Ma) of the Eastern Sakarya Zone which intruded into the Karadağ paragneiss.

Late Carboniferous to Early Permian (325 to 280 Ma) granitoids are abundant in the Eastern Mediterranean region and have been reported from the Hellenides, the Cycladic islands and the Sakarya Zone (see compilation in Meinhold et al., 2008; Löwen et al., 2017) whereas plutons of the Early Carboniferous age (325 to 355 Ma) are not known from the Eastern Mediterranean region. The oldest Carboniferous plutons have zircon ages around 325 Ma described from orthogneisses of the central Cyclades (Engel & Reischmann, 1998, 1999), of the External Hellenides (Kithira Island, Xypolias et al., 2006) and the Central- and East Sakarya Zone (Ustaömer et al., 2012, 2013). The only U-Pb ages of zircons from the basement of the Eastern Mediterranean region, which correlates with U-Pb ages of the Early Carboniferous detrital zircons of the Talea Ori group, are metamorphic rims with an age of 344 ± 4 Ma and 337 ± 4 Ma grown around Late Devonian and Ediacaran zircons from the Karadağ paragneiss of the Eastern Sakarya Zone (Ustaömer et al., 2013).

The Karadağ paragneiss from the Variscan high grade overprinted basement reveals also a similar detrital zircon age spectrum (Ustaömer et al., 2013) like the Talea Ori group. Taking the approx. 335 Ma old metamorphic zircons not into account, the U-Pb age spectrum of the detrital zircons of the Karadağ paragneiss displays again Precambrian zircons with zircon ages of NE Africa–Arabia affinity (Grenvillian zircons up to 32 %) with dominant Ediacaran/Cryogenian input (46 %). The rounded Palaeozoic zircons are similar to those of the Talea Ori group with only 27 % abundance. Mainly Cambrian and Ordovician zircons (18 %) together with the few Devonian zircons (8 %) point to a distal position to the Devonian source.

Early Palaeozoic to Early Carboniferous ages (500 to 340 Ma) as mentioned above of the Eastern Mediterranean region are typical for the internal Zones of the Variscan belt from central Europe. Late Cadomian, Cambrian and rift related Ordovician granitoids are described from the Saxothuringian Zone (Vesser Complex and the Polish West Sudetes; Kröner et al., 2001; Linnemann et al., 2007, 2008, and references therein), the Moldanubian Zone (Teplá-Barrandian Unit and Mariánské Lázně Complex Bowes & Aftalion, 1991; Dörr et al., 1998; Timmermann et al., 2006; Teufel, 1988), the French Massif Central, the Armorican Massif and of the Allochthonous Complex in Spain (Da Silva et al., 2016, and references therein). Early Variscan Silurian and Devonian ages are known from granodiorite-gneisses of the northern Saxothuringian Zone (Böllstein Odenwald and Spessart; Reischmann et al., 2001; Lippolt, 1986; Dombrowski et al., 1995; Brätz, 2000; Zeh et al., 2000, 2003) from Saxothuringian/Moldanubian boundary (Teufel, 1988) and from Moldanubian basement (Teplá-Barrandian Unit and Mariánské Lázně Complex; Timmermann et al., 2004, 2006). The Devonian thermal event from 370 to 390 Ma is widespread in crystalline basement of the Central European Variscides. Devonian monazite and zircon U-Pb ages are known from the allochthonous units of the Saxothuringian Zone (Münchberger nappe pile metamorphic grown zircons at 390 ± 3 Ma, Koglin et al., 2018), from Moldanu-

bian Zone (Tepla-Barrandian Unit and the Mariánské Lázně Complex; 380 to 387 ± 3 Ma, ID-TIMS, Timmermann et al., 2004, 2006), from Central Armorican Domain (Armorican Massif, Schulz, 2013).

Early Variscan granitic rocks are also known from the Slavonian mountains (NE Croatia), Tisia unit (Tisza unit), with cooling ages between 423.7 ± 12.9 to 321.5 ± 8 Ma (Pamić & Jurković, 2002). There, also metamorphic rocks of Ordovician to Silurian age are exposed with monazite ages of 444 ± 19 Ma and 421 ± 1 Ma (Pamić & Jurković, 2002; Balen et al., 2006). However age data and outcrops of the concerning rocks seem to be rare and also the paleogeographic position during Permian time seems not to be well constrained so far (Pamić & Jurković, 2002). Moreover the dated pre-Variscan Metamorphism was low-grade (350–400 °C), therefore a delivery of Paleozoic pre-Variscan aged zircons from this region is ambiguous.

The Sakarya Zone and Serbo-Macedonian Massif of the Eastern Mediterranean and Slavonian mountains of NE Croatia are equivalent to the internal zones of the Variscides of central Europe whereas the Cycladic islands and parts of the Hellenides are suggested to represent a Late Carboniferous to Early Permian active margin at the southern margin of Eurasia (Zulauf et al., 2015, 2016, 2018). Based on the comparison of the zircon data, in the Talea Ori group one of the source areas during the Early Permian might be the active margin, which fed the Bali formation with euhedral Late Carboniferous zircons (50 to 80 %, 300 to 315 Ma). The second source area during the Early Permian until Olenekian (Bali, Fodele and Sisses formations) could be represented by the Sakarya Zone with East-Gondwana derived basement and early Paleozoic granitoids, which formed the hinterland of the active margin.

Similar zircon age spectra as in the lower Talea Ori group have also been detected to the Karaburun Peninsula and Chios island. The Upper Carboniferous to Permian Küçükbahçe Formation of the Karaburun Peninsula contains also pre-Cambrian zircons with a NE Africa–Arabia-type age spectrum, but more Palaeozoic zircons (35–45 %) than the Talea Ori group. There are mainly Early Carboniferous zircons (10–16 %) and Devonian zircons (8–12 %). The Cambrian zircons have a similar amount (7–12 %) like that of the Talea Ori group (9 %). The Early Triassic sample of the Gerence Formation contains 55 % Devonian detrital zircons (Löwen et al., 2017). These authors, therefore, suggested that the Sakarya Zone represents the Devonian basement acting as proximal source for the Karaburun sediments, because of the similarities of the zircon spectra. However, recent analyses show that the ε_{Hf} values of the Devonian zircon populations differ significantly from the ε_{Hf} values of the Devonian granites in the Sakarya Zone (Ustaömer et al., 2019). Accordingly, Ustaömer et al. (2019) suggested westerly sources such as granitic rocks of the Aegean or central Europe, rather than the Sakarya Zone, for the Karaburun sediments, which are suggested to restore to the northern margin of Gondwana.

In summary, the zircon age spectra and the lithological characteristics of the lower Talea Ori group indicate that different sedimentary source areas have to be assumed. One source area delivered Late Carboniferous euhedral zircons (300 to 320 Ma, Kock et al., 2007; Zulauf et al., 2016), which point to a late Variscan basement as source area, similar to the pre-Alpine basement of the Tyros unit from East Crete (Zulauf et al., 2015). This late Variscan basement was proximal to the deposition of the Bali formation in Late Carboniferous/Early Permian times. From the Late Carboniferous/Early Permian onwards to the

Olenekian, however, sediment transport to the Talea Ori group was dominated by zircons with Cambrian to Early Carboniferous ages and Neoproterozoic ages indicating East Gondwana derivation (NE Africa–Arabia affinity). The good rounding of these zircons points to a distal source region. The comparison of the zircon age spectra of the Talea Ori group to currently existing zircon data reveals that the Sakarya Zone and southern active margin of Eurasia have to be discussed as probable source regions. Also a yet unspecified westerly source in the Aegean region or central Europe needs to be considered, which was suggested by Ustaömer et al. (2019), as source for the Karaburun sediments, which reveal similar zircon age spectra. Based on lithological and structural observations, we will further discuss the source areas and the implications for the paleogeographic positions.

4.4.3 Implications for the paleogeographic position of the Talea Ori group and its association to the Plattenkalk unit

In the following, we discuss four alternative models to reconcile the sedimentological and structural arguments with the zircon data of the Talea Ori group (Fig. 4.14). The first alternative considers sediment transport from westerly sources other than the Sakarya Zone, consistent with a paleogeographic position of the Talea Ori group at the northern margin of Gondwana in the western Paleotethys, as it is also assumed for the Plattenkalk unit to which the Talea Ori group is generally associated (e.g., Soujon et al., 1998; Dornsiepen et al., 2001; Stampfli et al., 2003; Kock et al., 2007; Robertson, 2006, 2012). If the Sakarya Zone, however, represents the main distal source region for the Talea Ori group, the sediment transport to the Talea Ori group needs to be discussed, as in most Late Carboniferous to Early Triassic paleogeographic reconstructions of the Eastern Mediterranean, the Sakarya Zone restores to the southern margin of Eurasia to the east of the Pelagonian Zone and Rhodope (e.g., Stampfli et al., 2003; Okay et al., 2006). Therefore, the second and third alternatives discuss a sediment current from the Sakarya Zone at the southern margin of Eurasia and terrane-displacement of the Sakarya Zone to the east. The fourth alternative is that the Talea Ori group was deposited to the north of the PQ s.str. and, therefore, might not be associated to the Plattenkalk unit.

Sediment transport from westerly sources

Consistent with sedimentological studies (Robertson & Pickett, 2000; Robertson & Ustaömer, 2009; Okay et al., 2006), Ustaömer et al. (2019) suggested a westerly sediment source for the Karaburun sediments, which have similar zircon age spectra compared to the Talea Ori group. Sediment transport from westerly sources to the Talea Ori group at the northern margin of Gondwana has been suggested already by Kock et al. (2007); however, the suggested sources – Spain, Calabria, Algeria or Morocco – almost exclusively provide zircons of Late Carboniferous/Early Permian age, apart from central Iberia where a small number of Early Carboniferous zircon ages were reported (Montero et al., 2004). The rounded zircons of Devonian and Silurian age in the Talea Ori group, therefore, cannot be explained by transport from Spain, Calabria, Algeria or Morocco, but they should be derived from more internal zones of the Variscan orogen. Ustaömer et al. (2019) suggested still unidentified sources in the west, such as the Aegean or central Europe to explain the

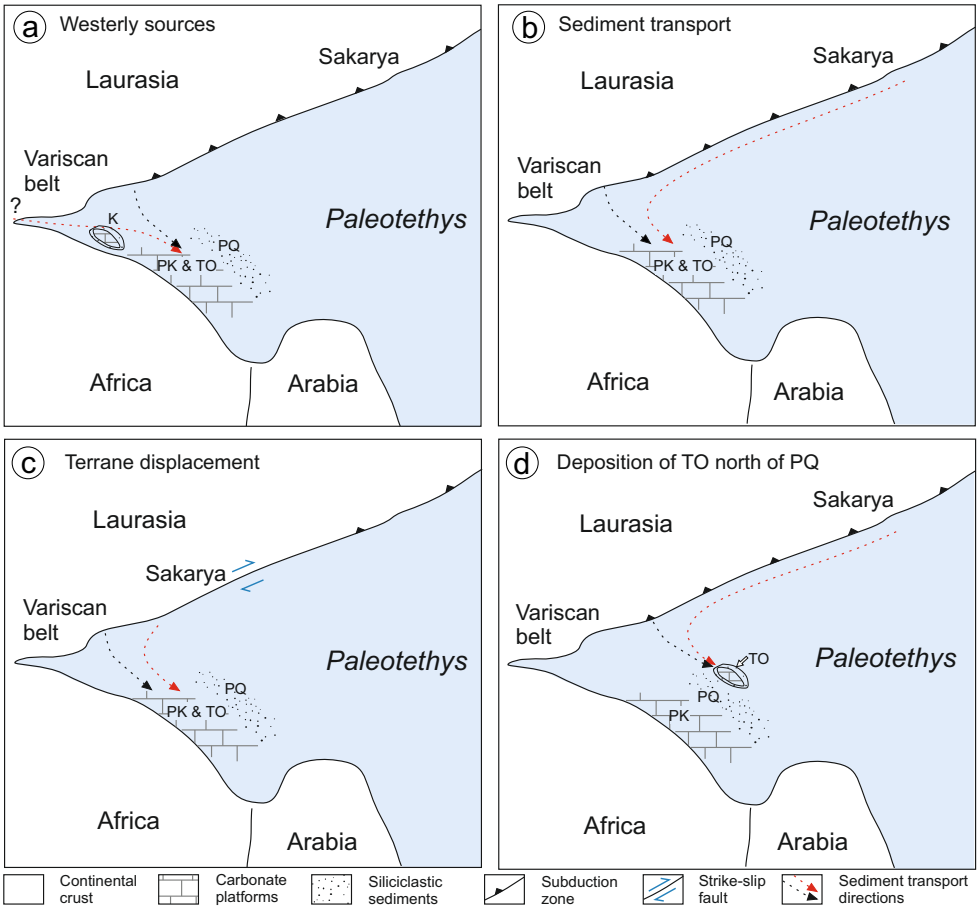

Fig. 4.14: Alternatives for the paleogeographic configurations of the lower tectonic nappes of the Cretan nappe pile from Late Carboniferous/Early Permian to Olenekian times. Dashed arrows indicate directions of sediment transport (black arrows = transport of euhedral variscan aged zircons; red arrows = transport of rounded zircons with Silurian, Devonian and Early Carboniferous U-Pb ages). (**a**) Distal sediment transport from westerly yet unspecified sources, modified after Ustaömer et al. (2019). (**b**) Distal sediment transport from the Sakarya Zone. (**c**) Eastward terrane-displacement of the Sakarya Zone after deposition of the lower Talea Ori group. Blue arrows indicate dextral displacement that should have happened after Olenekian times. (**d**) Deposition of the Talea Ori group north of the PQ s.str. Abbreviations are: Sakarya Zone (Sk), Phyllite-Quartzite unit s.str. (PQ), Plattenkalk unit (PK), Talea Ori (TO), Karaburun sediments (K).

Devonian zircons in the Karaburun sediments. In this alternative, sediments were eroded in the west, transported eastwards and deposited by turbidity currents up to several hundreds of kilometres to the east (Ustaömer et al., 2019). Such a setting may be possible also for the Talea Ori metasediments (Fig. 4.14a). However, the euhedral Variscan aged zircons in the metasediments of the Bali formation rather point to a proximal source and are not consistent with such a long-distance sediment transport. Furthermore, the unknown westerly sediment sources are not yet specified by zircon age spectra and as the similarity of the zircon age pattern of the Talea Ori group to the Sakarya zone is quite striking, the Sakarya Zone as source region and its paleographic implications will be explored in the following three alternatives.

Sediment transport from sources at the southern margin of Eurasia

Sources at the southern margin of Eurasia were considered possible by Kock et al. (2007) under the condition of southward subduction of the Paleotethys Ocean (Şengör et al., 1984). Even if during Permian and Triassic times rather northward subduction is assumed (e.g., Stampfli & Borel, 2002), southward subduction (or double subduction) has been inferred at least during Carboniferous times for some regions in the South Aegean (e.g., Xypolias et al., 2006; Romano et al., 2006; Zulauf et al., 2008) and Turkey (e.g., Goncuoglu et al., 2007; Robertson & Ustaömer, 2009; Candan et al., 2016). Transport from northerly sources to the Talea Ori group was also considered possible under the condition that the PQ s.str. is interpreted as post-Variscan rift basin that filled near sea level by Late Triassic times (Robertson, 2012). Assuming a paleogeographic model in which the Paleotethys was closed by Late Carboniferous times (e.g., Robertson, 2006; Ustaömer et al., 2019) and deep troughs existed in N-S direction (e.g., Crasquin-Soleau et al., 2006), sediment transport from a northerly origin may be plausible (Fig. 4.14b). However, a main problem with sediment transport from north to south is that the PQ s.str., which restores to the north of the Talea Ori group (e.g., Dornsiepen et al., 2001), systematically lacks Middle to Late Paleozoic ages and Variscan zircons (Chatzaras et al., 2016; Zulauf et al., 2016, 2018). Therefore, currents bringing sediment from the north should have transported sediment exclusively to the Talea Ori group and not to the PQ s.str., to which, in contrast, only sediment was delivered from Gondwana in the south.

Terrane displacement

In a tectonically active setting like the Eastern Mediterranean, tectonic processes must be considered for paleogeographic reconstructions. In several paleogeographic reconstructions the assumed source rocks for the Talea Ori group in the Sakarya Zone, as well as the Karaburun sediments, restore far to the East, which would imply that a wide ocean separating Gondwana and Eurasia was located to the south, since the Paleotethys opened up to the East (e.g., Stampfli et al., 2003; Stampfli & Kozur, 2006; Löwen et al., 2017). Eastward terrane displacement by strike-slip faults (possibly also combined with southward subduction) was suggested to provide an alternative in which the Karaburun sediments and Sakarya Zone were located more in the West during Permian times, and only later, due to reassembly of Pangea, were transported hundreds of km to the East (Robertson & Ustaömer, 2009). In such a paleogeographic situation, the Sakarya Zone should have been located more in the western Paleotethys closer to the northern margin of Gondwana (e.g., Şengör et al., 1984; Golonka et al., 2006). Considering a position of the source areas for the siliciclastic metasediments of the lower Talea Ori group in the West, where the Paleotethys had much smaller N-S extent, sediment transport to a location at the northern margin of Gondwana might be more likely (Fig. 4.14).

Deposition of the Talea Ori group north of the PQ s.str.

Based on the zircon spectra with a high amount of euhedral Variscan aged zircons, Zulauf et al. (2016) proposed deposition of the siliciclastic dominated lower base of the Talea Ori

group, the Bali formation, at the southern active margin of Eurasia, which would be in accordance with the new zircon age spectra pointing to the Sakarya Zone as a source. A paleogeographic origin of the Talea Ori group to the north of the PQ s.str. (Fig. 4.14d), however, contradicts the association of the Talea Ori group to the Plattenkalk unit, which restores to the northern margin of Gondwana (Baud et al., 1993; Marcoux & Baud, 1995; Dornsiepen et al., 2001; Stampfli et al., 2003; Robertson, 2006, 2012). The main argument for the general association is that the lithofacies of the upper Talea Ori group closely resembles the lithofacies of the Plattenkalk unit at other locations on Crete and the Peloponnesus, indicating a similar paleogeographic environment (e.g., Creutzburg & Seidel, 1975; Hall & Audley-Charles, 1983; Bonneau, 1984; Jacobshagen et al., 1986; Krahl et al., 1988; Soujon et al., 1998; Krahl & Kauffmann, 2004; Kock et al., 2007; Robertson, 2012). The sequence of stromatolitic dolomite marbles (Mavri formation) overlain by a sequence of platy marbles interlayered with chert (Aloides formation) that are interrupted by phyllitic layers (Gigilos beds, Fytrolakis, 1972) is found in the Lefka Ori like in the Talea Ori (e.g., Krahl et al., 1988; Soujon et al., 1998). The sedimentary succession – with carbonate breccias at the base and platy marbles that are increasingly interlayered with chert towards the stratigraphic top – indicate subsidence and collapse of the carbonate platform in the Late Triassic/Liassic, which is consistent with a pulse of rifting at the northern margin of Gondwana during the Late Triassic (e.g., Robertson, 2006).

Yet, the siliciclastic lower Talea Ori group, the Sisses, Fodele and Bali formation are not exposed in any other outcrop of the Plattenkalk unit on Crete and the Peloponnesus. Also, the younger pelitic parts of the Plattenkalk unit, the Kalavros beds, are missing in the Talea Ori (e.g., Epting et al., 1972; Hall & Audley-Charles, 1983; Papanikolaou & Vassilakis, 2010). On the Peloponnesus, the siliciclastic base of the platy marbles and cherts of the Taygetos mountains is lithologically different to that of the Talea Ori group (Kowalczyk & Dittmar, 1991) and similar to the phyllites and quartzites of western Crete (Robertson, 2012). The Plattenkalk unit and continuous siliciclastic sediment sequences of Carboniferous to Triassic age, as the phyllites and quartzites of central and western Crete, are typical pelagic sequences of the southern Paleotethys (e.g., Krahl et al., 1983; Kozur & Krahl, 1987; Baud et al., 1993; Marcoux & Baud, 1995; Dornsiepen et al., 2001; Stampfli et al., 2003; Robertson, 2006, 2012; Stampfli & Kozur, 2006). In contrast to the pelagic setting of the Plattenkalk unit, the sedimentary sequence of the lower Talea Ori group can be interpreted as a tectonically unstable shallow-marine setting with terrifeneous influx (Epting et al., 1972; Kuss & Thorbecke, 1974; König & Kuss, 1980; Robertson, 2006). Therefore, the lower Talea Ori group would be compatible with deposition in a shallow marine environment as it is assumed for the Eurasian shelf. The Aloides formation of the upper Talea Ori group, comprising platy marbles with chert commonly also described as Plattenkalk, are interpreted usually as pelagic sequence (e.g., Epting et al., 1972; Krahl et al., 1988; Krahl & Kauffmann, 2004; Robertson, 2006, 2012), but in contrast a shallow marine facies was inferred for the similar platy marbles with chert of the Ida Ori based on lithistid demosponges (e.g., Manutsoglu et al., 1995b; Soujon et al., 1998). Even a pelagic setting of the Aloides formation may be reconciled with a paleogeographic origin in the northern Paleotethys, since smaller pelagic carbonate platforms existed also at the Eurasian continental margin during the Middle to Late Jurassic (e.g., Haas et al., 2011).

Furthermore, the structural position of the Plattenkalk unit and the Talea Ori group that

are structurally underlying the PQ s.str. must be taken into account. The Plattenkalk unit forms the lowermost unit of the Cretan nappe pile and is commonly described as "parautochthonous" (e.g., Creutzburg & Seidel, 1975; Hall & Audley-Charles, 1983; Bonneau, 1984; Jacobshagen et al., 1986; Krahl & Kauffmann, 2004). Assuming a nappe stacking process during N–S compression in course of the Alpine orogeny with nappe transport from north to south and the southern nappes at the base and the more northern nappes at the top, the structural position is consistent with a paleogeographic origin of the Plattenkalk unit to the south of the PQ s.str. (e.g., Dornsiepen et al., 2001; Robertson, 2006). The parautochthonous character of the Talea Ori group, however, is obsolete, because the geological record is revealing a similar Alpine deformation and metamorphic history as the PQ s.str., evidencing burial to 30 km depth and rapid exhumation (e.g., Seidel, 1978; Seidel et al., 1982; Theye, 1988; Theye et al., 1992; Rahl et al., 2005; Seybold et al., 2019). A paleogeographic origin to the north of the PQ s.str. might be reconciled with the structural position below the PQ s.str., assuming the variety of tectonic processes that are possible during subduction. For example, the Talea Ori group located to the north of the PQ s.str. may have entered the subduction channel first and both units were superimposed to each other during early exhumation, consistent with field observations of an extensional shear zone contact between both units (Seybold et al., 2019).

In summary, it cannot be excluded that the Talea Ori group was deposited further north than the PQ s.str. and thus, might not be associated to the Plattenkalk unit (Fig. 4.14d). However, since the lithologies of the upper Talea Ori group closely resemble the Plattenkalk unit in other outcrops of Crete, this alternative is considered to be ambiguous. The three alternatives in which the Talea Ori group restores to the northern margin of Gondwana, do not exclude each other and combinations might be considered, i.e. sediment transport from different source areas in combination with terrane-displacement. The suggested alternatives taking zircon data, structural and lithological arguments into account, have further to be tested. For example, more lithological and tectonic constraints as well as new ε_{Hf} data may help to distinguish if the Sakarya Zone is indeed a probable source region for the siliciclastic metasediments of the Talea Ori group.

4.5 Conclusions

- The siliciclastic sediments of the Bali, Fodele and Sisses formations of the lower Talea Ori group are derived by mainly two different source areas: (1) A distal source, characterized by zircon age spectra with Early Paleozoic and Early Carboniferous age peaks together with a high amount of Neoproterozoic zircons, a Mesoproterozoic age gap and a low amount of Paleoproterozoic and Archean aged zircons. (2) A proximal source characterized by dominating Late Variscan zircon ages and euhedral zircons (Kock et al., 2007; Zulauf et al., 2016).
- During the Late Carboniferous/Early Permian, sediments from the proximal Variscan source were delivered and deposited on a shelf slope, possibly close to a pelagic realm (black metachert). Still during the Late Carboniferous/Early Permian, there was a change to recycled Early Palaeozoic to Early Carboniferous ($>$ 325 Ma) zircons together with a high amount of recycled zircons with U-Pb ages indicating East

Gondwana affinity (70 %), pointing to a distal source area, the hinterland of the shelf. The U-Pb age spectrum of detrital zircons typical for the distal hinterland was prolongating 40 Ma until the Olenekian.

- Based on the detrital zircons with Neoproterozoic ages, consistent with an East Gondwana derivation, and Cambrian to Devonian and Variscan ages, the Sakarya Zone is the most probable distal sediment source for the lower Talea Ori group, which was located in the hinterland of the shelf at the southern active margin of Eurasia. Another possible source region would be westerly sources; however, these sources are not yet specified. Despite their Variscan plutons and metamorphism, the West African related terranes (Morocco, Algerian), the Amazonian and the Avalonian/Baltic terranes (Pelagonian terrane) can be excluded as source areas, because their metamorphic and/or detrital age patterns are not compatible with the Mesoproterozoic age gap combined with a high amount of Tonian/Stenian zircons, which are both significant for the lower Talea Ori group detrital zircon age patterns.
- A paleogeographic position of the Talea Ori group at the northern margin of Gondwana as it is so far assumed can be reconciled with the zircon data assuming a combination of different alternatives. These include sediment transport from still unspecified westerly sources in the Aegean region and central Europe as well as the Sakarya Zone at the southern active margin of Eurasia as important source area. Long-distance sediment transport through the Paleotethys from the Sakarya Zone and eastward terrane-displacement allowing for shorter sediment transport distances are suggested to bring sediment to the paleogeographic origin of the Talea Ori group at the northern margin of Gondwana. The alternative that the Talea Ori group deposited north of the PQ s.str. is not excluded, but in this case the association of the Talea Ori group to the Plattenkalk unit must be reconsidered in combination with lithological, structural and biofacial investigations.

Detrital zircon age spectra in close combination with lithological and structural observations are a powerful tool to characterize provenance and to constrain the paleogeographic origin of the metamorphic rocks in the Talea Ori, an important area for paleotectonic reconstruction in the complicated Eastern Mediterraenean region.

5 The tectonometamorphic history of the Talea Ori, central Crete: extensional shearing during early stages of exhumation

This Chapter is based on the manuscript "*Seybold, L., Trepmann, C. A., & Janots, E. (2019). A ductile extensional shear zone at the contact area between HP-LT metamorphic units in the Talea Ori, central Crete, Greece: deformation during early stages of exhumation from peak metamorphic conditions. International Journal of Earth Sciences, 108(1), 213–227. https://doi.org/10.1007/s00531-018-1650-6.*".

5.1 Introduction

The role of ductile shear zones, normal faults and low-angle detachment faults on the exhumation of high-pressure low-temperature (HP-LT) metamorphic rocks is discussed controversially, regarding the amount of exhumation localized on these faults and their relation to crustal scale extension or syncompressional normal faulting in extrusion wedges (e.g., Lister et al., 1984; Fassoulas et al., 1994; Kilias et al., 1994; Jolivet et al., 1996, 2013; Thomson et al., 1999; Doutsos et al., 2000; Ring & Reischmann, 2002; Rahl et al., 2005; Chatzaras et al., 2006; Klein et al., 2008, 2013; Ring et al., 2010). For the island of Crete and the Peloponnesus, the model of syncompressional exhumation in an extrusion wedge was proposed, in which deformation is localized on two bounding faults and the extruded rocks are exhumed as one coherent block (Thomson et al., 1999; Doutsos et al., 2000; Ring & Reischmann, 2002). Earlier studies favoured exhumation during crustal scale extension, and described ductile extensional shear zones also within the exhumed HP-LT metamorphic rocks on Crete (Fassoulas et al., 1994; Jolivet et al., 1996). The boundary between the HP-LT metamorphic PQ s.l. and the overlying Tripolitza unit, the so-called "Cretan detachment", was in both cases suggested to have played a major role for exhumation of the Miocene HP-LT metamorphic rocks (e.g., Jolivet et al., 1996; Ring & Reischmann, 2002). Based on the small difference in metamorphic peak temperature of the PQ s.l. below, and the Tripolitza unit above the detachment, however, Rahl et al. (2005) estimated that the detachment accounts for only $\sim$ 5 to 7 km of exhumation of the underlying HP-LT metamorphic rocks from $\sim$ 35 km depths. In recent publications, several contacts between the PQ s.l. and the Tripolitza unit have been recognized as thrust faults rather than normal faults (Klein et al., 2013; Ring & Yngwe, 2018). Therefore it is assumed that the HP-LT metamorphic rocks were exhumed during compression (Ring & Yngwe, 2018) and the activation of more than one single detachment/normal fault was suggested (Papanikolaou & Vassilakis, 2010; Ring et al., 2010), which may also be located within the lower HP-LT metamorphic group and rather of ductile character (Klein et al., 2013). The nature of such ductile normal faults is however still unclear, since for example in Western Crete, deformation is limited to peak metamorphic conditions and nor deformation during exhumation was observed.

In this Chapter, the deformation structures in HP-LT metamorphic rocks in the Talea Ori, central Crete are described, presenting a new structural mapping of the siliciclastic base of the Talea Ori group and the overlying PQ s.str. supported by microfabric analyses. Based on these observations the deformation conditions are discussed with respect to the subduction and exhumation history of the HP-LT metamorphic rocks in the Talea Ori.

5.2 Methods

During field campaigns between 2015 and 2017 lithological and structural mapping of the 20 km long contact area between the base of the Talea Ori group and PQ s.str. was carried out. About 300 samples (Appendix 8.1) were collected and analysed microscopically to thoroughly distinguish between the deformed HP-LT metasediments of the two units as well as to distinguish between deformation related to the main fabric formed at peak metamorphic conditions and the ductile shear zone. For structural analysis, the samples were taken oriented in the field. Polished thin sections (with approximately 25 µm thickness) were prepared from cuts oriented parallel to the lineation and perpendicular to the foliation. The microfabrics were analysed by polarized light microscopy and scanning electron microscopy (SEM), including electron backscattered diffraction (EBSD) measurements and energy dispersive spectroscopy (EDS) using a field emission microscope (SU5000 Hitachi) at Ludwig-Maximilians University, Munich, Department of Earth and Environmental Sciences. The sections for EBSD measurements were polished by an alkaloid colloidal suspension (Syton) prior to carbon coating. EDS and EBSD signals were acquired using the Aztec software (Oxford technology). For EDS measurements a working distance of 10 mm and for EBSD a working distance of 20–25 mm was applied at an acceleration voltage of 20 kV. For EBSD measurements we used a pre-tilted holder with the specimen at an angle of 70° to the beam. Processing of the data was performed with the Channel 5 software (Oxford technology). Grain size is given as the diameter of a circle of equal area applying a misorientation threshold value of 10°. Crystallographic orientations are presented by stereographic projections of the lower hemisphere.

Raman spectroscopical investigations on carbonaceous material (CM) were made on polished petrographic thin sections, using a Horiba Xplora integrated confocal micro Raman system on an Olympus BX51 microscope (Mineralogical state collection, Munich). For the measurements a Nd-YAG 532 nm laser source was used and the laser was focused on the sample with a 300 nm confocal hole. Laser power on the sample surface was 8.4 mW. The laser was focused, using a 100×LW objective (with larger working distance), on spots of CM below the surface beneath translucent grains as quartz, to avoid bias due to polishing of the sample surface. Ten to twelve spots were measured per sample with an acquisition time of 5 s. Background correction and peak fitting of the G band (1580 cm^{-1}), D1 band (1350 cm^{-1}) and D2 band (1620 cm^{-1}) was performed using the software Peakfit (Version 4.06). Since we used a similar setting for the measurements as Rahl et al. (2005) temperatures were calculated by their equation using R1, which is the ratio of peak heights (D1/G), and R2, the ratio of peak areas (D1/(G + D1 + D2)). By this method, metamorphic peak temperatures can be predicted to ± 50 °C (Rahl et al., 2005). A comparison with temperatures calculated using only R2 after Beyssac et al. (2002), showed no significant differences for the four samples measured (Appendix 8.4). The standard deviation of the

obtained temperatures from ten measurements per sample was generally higher using the equation by Rahl et al. (2005), than using the equation of citetBeyssac2002.

For chemical in situ U-Th-Pb chemical dating, monazite grains were first identified on thin sections using backscatter electron (BSE) images by SEM. Quantitative analyses were acquired on a Jeol JXA-8230 at ISTerre laboratory (Grenoble, France). The analytical conditions follow a slightly modified protocol of (Janots et al., 2008), with a beam diameter of 1 µm, an accelerating voltage of 15 kV and a beam current of 200 nA. Natural minerals and synthetic glass standards, including Smithsonian REE phosphates, were used for calibration, with the following X-ray lines: SiKα, UMβ, ThMα, CaKα, PKα, YLα, DyLβ, GdLβ, SmLβ, PrLβ, NdLα, CeLα, LaLα, PbMβ. Counting times of 80 (40), 150 (75) and 240 (120) were used for Th, U and Pb on peak and background, respectively. A calibrated overlap correction of 0.0079 was applied for peak interference of ThMγ on UMβ. Standardization and age calculations were checked before and after the analysis session using the Manangotry monazite standard (555 $\pm$ 2 Ma, ID-TIMS; Paquette & Tiepolo, 2007). All analysed monazite grains have a Pb content below the detection limit (< 100 ppm, Appendix 8.5).

5.3 Results

The area around the contact between the Talea Ori group and the PQ s.str. (dashed area in Fig. 5.1) is characterized by shear bands, extensional shear band cleavages, kink bands, asymmetric boudinage and a high amount of quartz veins that are associated to these structures (Figs. 5.2, 5.3). The abundance of these deformation structures increases within the Talea Ori group towards the contact to the PQ s.str., where the deformation structures occur within a width of $\sim$1 km and more, along the $\sim$20 km long contact between the two units. In the following, we firstly describe the mesoscopic deformation structures that characterize the shear zone in the field and subsequently the microfabrics. To distinguish between deformation related to the ductile shear zone and the deformation at peak metamorphic conditions, we describe the relation between porphyroblast growth, foliation and shear band formation. The degree of graphitization of carbonaceous material in the hanging wall (PQ s.str.) and footwall (Talea Ori group) of the shear zone is analyzed to infer peak metamorphic temperatures.

5.3.1 Macroscopic deformation structures of the shear zone

In the western and central Talea Ori, the main foliation of the rocks, in the Talea Ori group and the PQ s.str., dips generally towards N (Fig. 5.1; Epting et al., 1972; König & Kuss, 1980; Richter & Kopp, 1983; Krahl et al., 1988). In the east, where the shear zone contact between Talea Ori group and PQ s.str. crosscuts the large-scale fold structure of the Talea Ori group, the foliation in the Talea Ori group is steadily N-dipping, whereas the siliciclastic metasediments of the PQ s.str. are dipping towards E and SE, following the strike of the contact (Fig. 5.1).

The shear zone is macroscopically characterized mainly by the occurrence of extensional shear bands, where the foliation is transected and deflected at the shear band boundaries

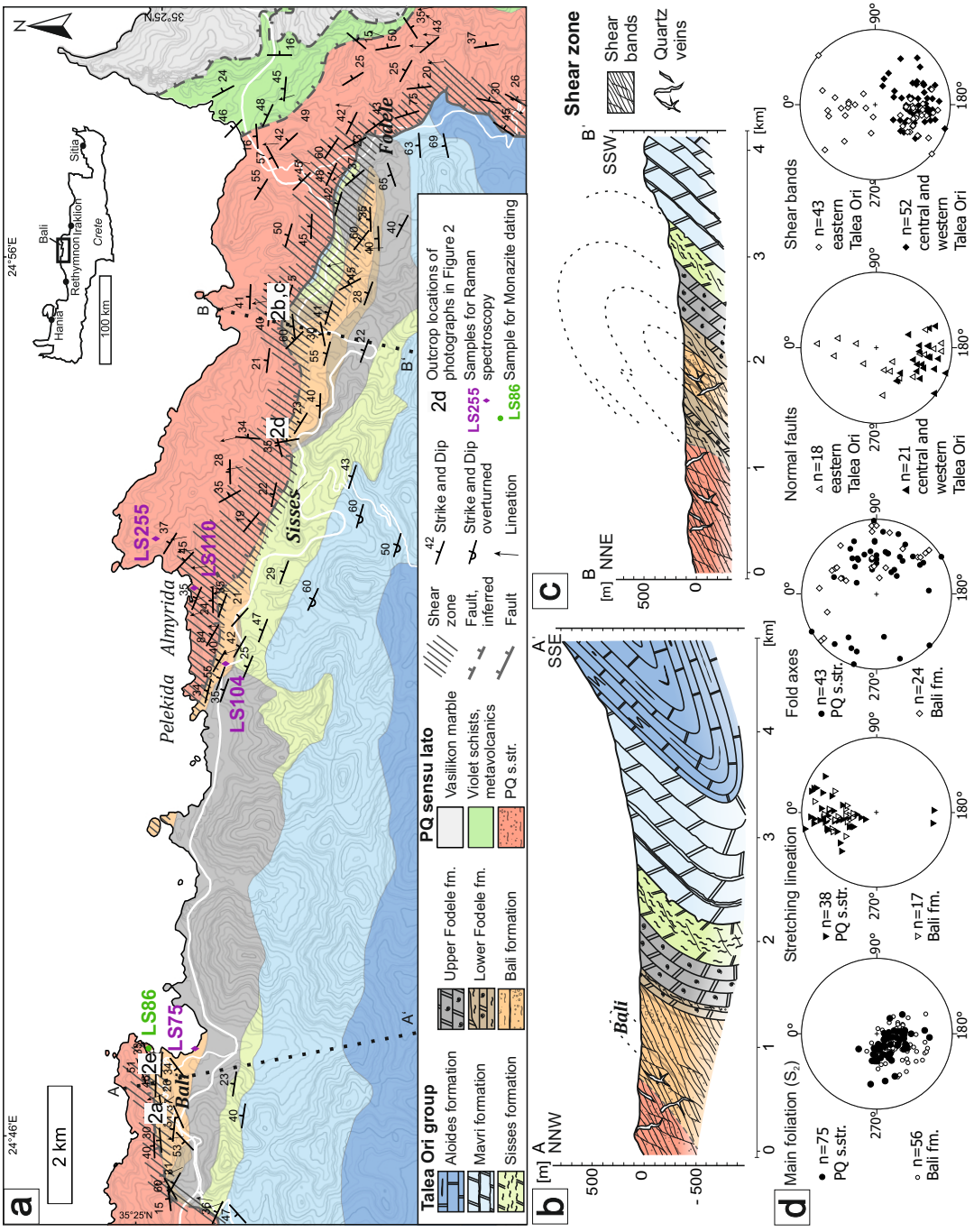

Fig. 5.1: Geologic map of the Talea Ori modified after Epting et al. (1972), Richter & Kopp (1983) and Kock et al. (2007). The dashed area marks the position of the extensional shear zone. **b** Cross-section along line AA′, modified after Kock et al. (2007) and **c** along line BB′, modified after Richter & Kopp (1983) as marked in the map. **d** Stereographic projections, lower hemisphere, of deformation structures.

(Figs. 5.2, 5.3). The shear band boundaries show a spacing on the scale of several centimeters to meters, and are commonly associated with quartz veins (Figs. 5.2, 5.3). In the western and central Talea Ori, exclusively one set of extensional shear bands occurs, with shear band boundaries dipping typically with 40°–70° towards N (perpendicular to the contact between Talea Ori group and PQ s.str.), with the northern block being systematically downfaulted (Figs. 5.1d, 5.2). In contrast, in the eastern Talea Ori, where the contact to the PQ s.str. is dipping to the E and SE, also conjugated sets of shear bands occur (Figs. 5.1d, 5.3a).

In the shear zone, quartz veins discordant to the foliation form m-wide networks (Figs. 5.2a, c, e, 5.3). The quartz veins commonly occur along boundaries of mesoscopic shear bands (Figs. 5.2c, d, 5.3a), in the necks of (asymmetric) boudins (Fig. 5.3b, c) and in the necks of foliation boudinage (Fig. 5.3d-f; Platt & Vissers, 1980; Birtel & Stöckhert, 2008). Small (cm-wide) wedge-shaped and wing-shaped veins occur associated to the boudin necks or shear band boundaries (Fig. 5.3c). Shear bands and quartz veins are systematically more abundant in the Talea Ori group towards the contact to the PQ s.str., whereas they are rare within the central part of the Talea Ori. Brittle normal faults occur with similar strike and dip like the ductile shear bands (Figs. 5.1d, 5.2a), locally overprinting the shear band boundaries.

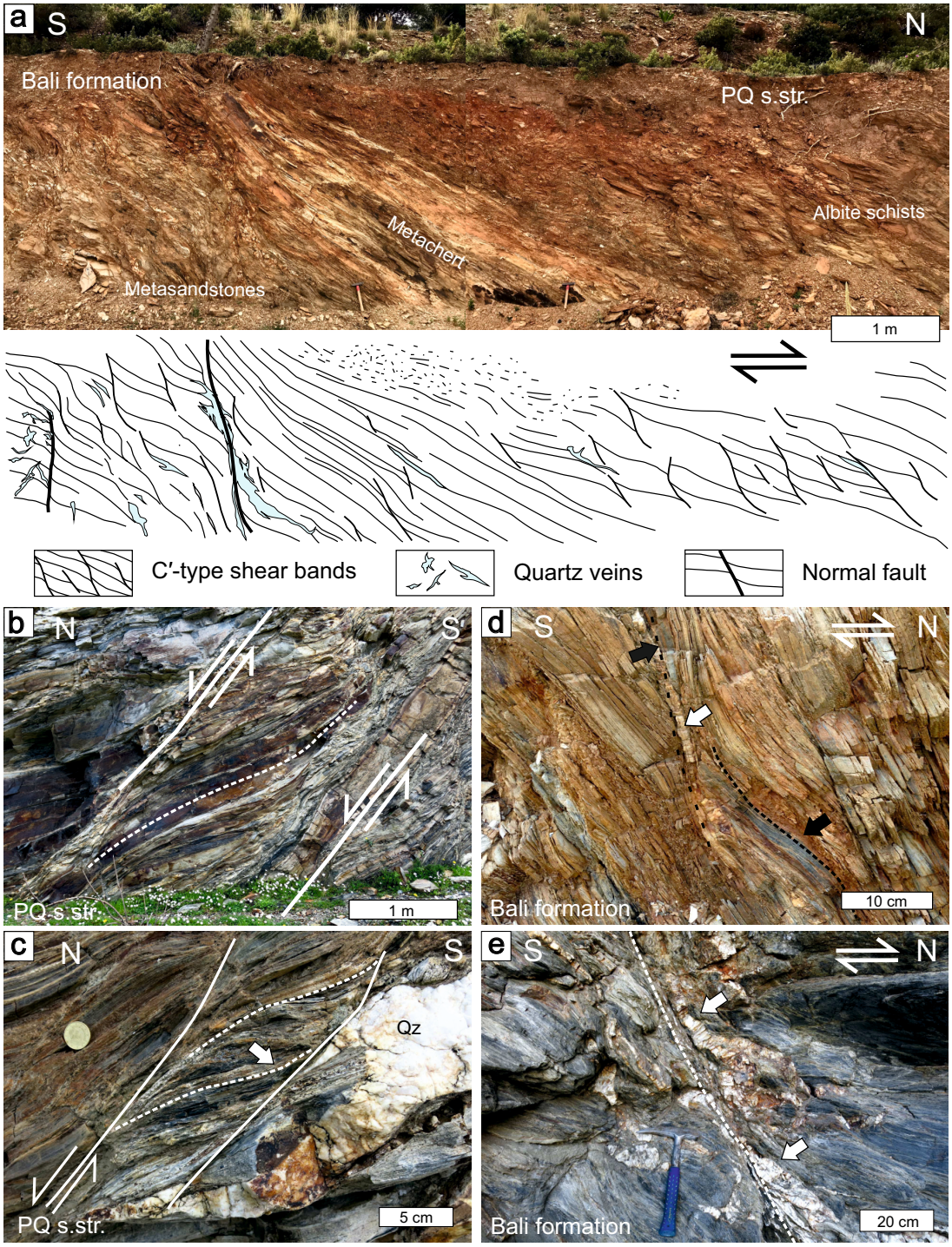

Fig. 5.2: Mesoscopic shear band cleavages at the contact between the base of the Talea Ori group and PQ s.str., locations of photograph within the shear zone are indicated in Fig.5.1. **a** Shear zone at the contact between Bali formation (Talea Ori group) and PQ s.str. west of the village of Bali; the ductile shear bands are overprinted by brittle normal faults. **b** Shear bands in phyllites and quartzites of the PQ s.str. at Pera Galinos. **c** Shear bands and associated quartz vein in phyllites of the PQ s.str. at Pera Galinos. **d** Shear band in schists interlayered with black chert, Bali formation east of Sisses; the black chert layer (black arrows) marks the top-down-to-the-north shear sense at the shear band. Quartz veins along the shear band boundary are indicated by white arrow. **e** Shear band in black schists of the Bali formation with associated quartz vein network, Bali port.

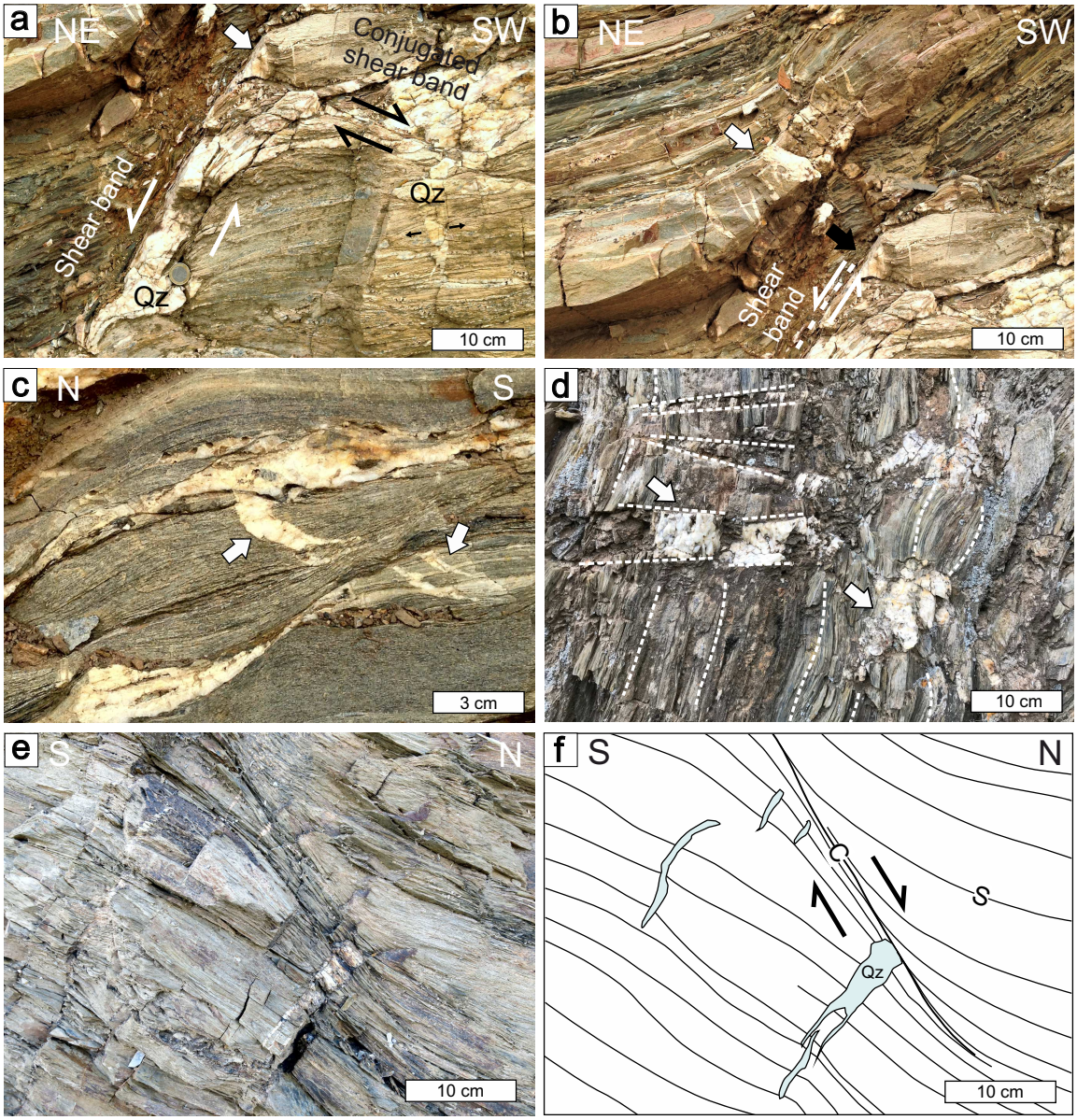

Fig. 5.3: Quartz veins associated to deformation structures of the extensional shear zone. **a** Quartz vein in asymmetric boudin neck of quartzite boudin (white arrow) along a shear band boundary with top-down-to-the-north shear sense; conjugated shear band with small displacement; quartz vein associated to foliation boudinage (tiny black arrows). **b** Asymmetric boudinage with quartz veins in boudin neck and wedge-shaped veins. **c** Wing-shaped quartz veins associated to boudinage and shearing of phyllitic host rocks. d Foliation boudinage (white arrow) and quartz veins along kink band boundaries (dashed horizontal lines) **e**, **f** Shear band with branching quartz veins formed perpendicular to foliation.

5.3.2 Microstructures

The mesoscopic shear bands are related to shear band cleavages (Fig. 5.4a-d), which are of C′-type, also referred to as extensional crenulation cleavage (Platt & Vissers, 1980; Passchier & Trouw, 2005; Mukherjee, 2013a, 2014a). The shear band cleavages have typical spacings on the order of a few hundred µm to mm, dependent on the grain size of the rocks (Fig. 5.4a, b). The cleavage planes are defined by a relative enrichment of mica and opaque minerals, whereas quartz has been dissolved (Fig. 5.4a, b). The cleavage planes are at an angle of 30°–60° to the main foliation. Quartz precipitated at sites of dilation such as strain shadows and veins (Figs. 5.4b, c, 5.5, 5.6). Antitaxial strain shadows are developed usually around hematite crystals that are pseudomorphs after pyrite (Lougheed & Mancuso, 1973) containing elongate quartz grains (late precipitates) and white mica (early precipitates, Fig. 5.4b). In strain shadows around albite porphyroblasts, quartz and albite are present (Fig. 5.5). In albite gneisses, sutured passively enriched stylolytic seams of opaque phases occur along shear band boundaries (Fig. 5.4d).

Albite porphyroblasts occur frequently in the metasediments of the PQ s.str. (Figs. 5.4d, f, 5.5) and more rarely also in the Bali and Sisses formation of the Talea Ori group (Fig. 5.4e). These porphyroblasts typically show a high amount of mineral inclusions in the center, leading to a macroscopically black colour of albite, and an inclusion-free rim (Fig. 5.4e, f). They have anhedral elongated shapes, strain caps and (asymmetric) strain shadows forming a SPO parallel to the main foliation (Figs. 5.4f, 5.5). The albite blasts do neither show any compositional zoning nor internal misorientations (Fig. 5.5a).

The inclusions in albite porphyroblasts mainly comprise quartz, graphite, rutile and Fe-oxides. Tourmaline, calcite, ankerite, phengite, apatite, zircons, monazite, and allanite can also occur depending on the mineralogy of the host rock (Figs. 5.5a, b, 5.7). The small prismatic to ellipsoidal inclusions with sizes of a few µm up to $\sim$ 40 µm are aligned with their long axis, forming an internal fabric (S_1). The internal fabric can be subparallel to the external foliation of the host rock (S_2), representing a former foliation which was overgrown by the albite blast (S_1, Figs. 5.4e, f, 5.5). In most albite-schists, the internal foliation is curved and oblique to the external foliation.

In general, quartz and albite in the rocks do not show a crystallographic preferred orientation (CPO), neither in the external foliation of the rocks nor in the inclusions or in the strain shadows (Fig. 5.5c–f). In the young quartz veins discordant to the foliation (Fig. 5.6a), as well as in monophase quartz layers concordant to the foliation (Fig. 5.6b), crystal-plastic deformation is evident by undulatory extinction, deformation lamellae and sutured grain boundaries (Fig. 5.6c) occurring in the Talea Ori group and the PQ s.str. (Trepmann & Seybold, 2019).

Monazite crystals occur as inclusions in albite and ilmenite, as well as in the matrix of albite schists (Fig. 5.7a). The crystals are elongate parallel to the foliation (Fig. 5.7a). Monazite shows the same inclusions as albite blasts and is interpreted to have grown at the same time (Fig. 5.7). Monazite is zoned in light rare earth elements (Appendix 8.5): a Nd-rich core (with La/Nd as low as 0.4) is surrounded by a La-rich rim (with La/Nd up to 1.3). The low Pb contents (below EMP detection limit < 100 ppm) of monazite with Th up to 5–7 wt. % show that monazite crystallization age is younger than 60–80 Ma.

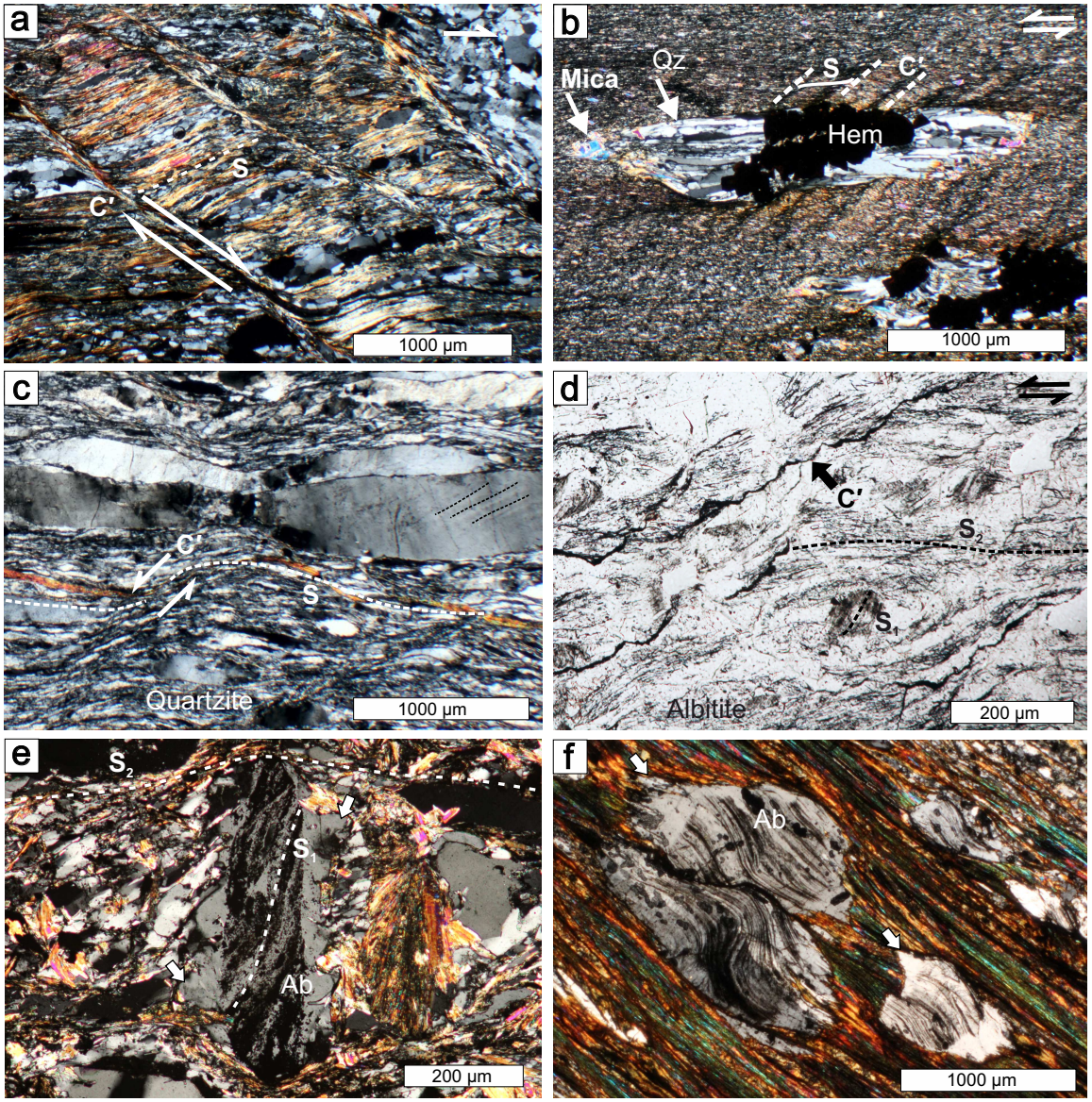

Fig. 5.4: Thin section micrographs of deformation structures in the Bali formation (Talea Ori group, **a**, **b**, **e**) and the PQ s.str. (**c**, **d**, **f**). **a** C′-type shear band cleavage in phyllites (CT83). **b** Antitaxial strain shadow around hematite pseudomorphs after pyrite and C′-type shear band cleavage in black schist (LS22). Shear sense is derived from shear band cleavage, since pressure fringes are symmetric. Stretching of hematite aggregate is consistent with sinistral shear sense. **c** C′-type shear bands in quartzite with deformation lamellae in deformed quartz grains and discordant quartz vein (LS48). **d** Albitite (LS51) with stylolites marked by enrichment of opaque phases along shear band boundaries (C′); albite grains have a high amount of opaque inclusions in the core that are aligned (S_1) oblique to the external foliation of the rocks (S_2). **e** Albite blast in metasandstone of the Bali formation (LS46). The internal foliation and long axis of the blast is perpendicular to the external foliation of the conglomerate (S_2), the inclusion-free rim bulges in the direction of S_2. **f** Albite schist of the PQ s.str. (LS148) with curved internal foliation in albite grains and inclusion free rims, bulging into the external foliation.

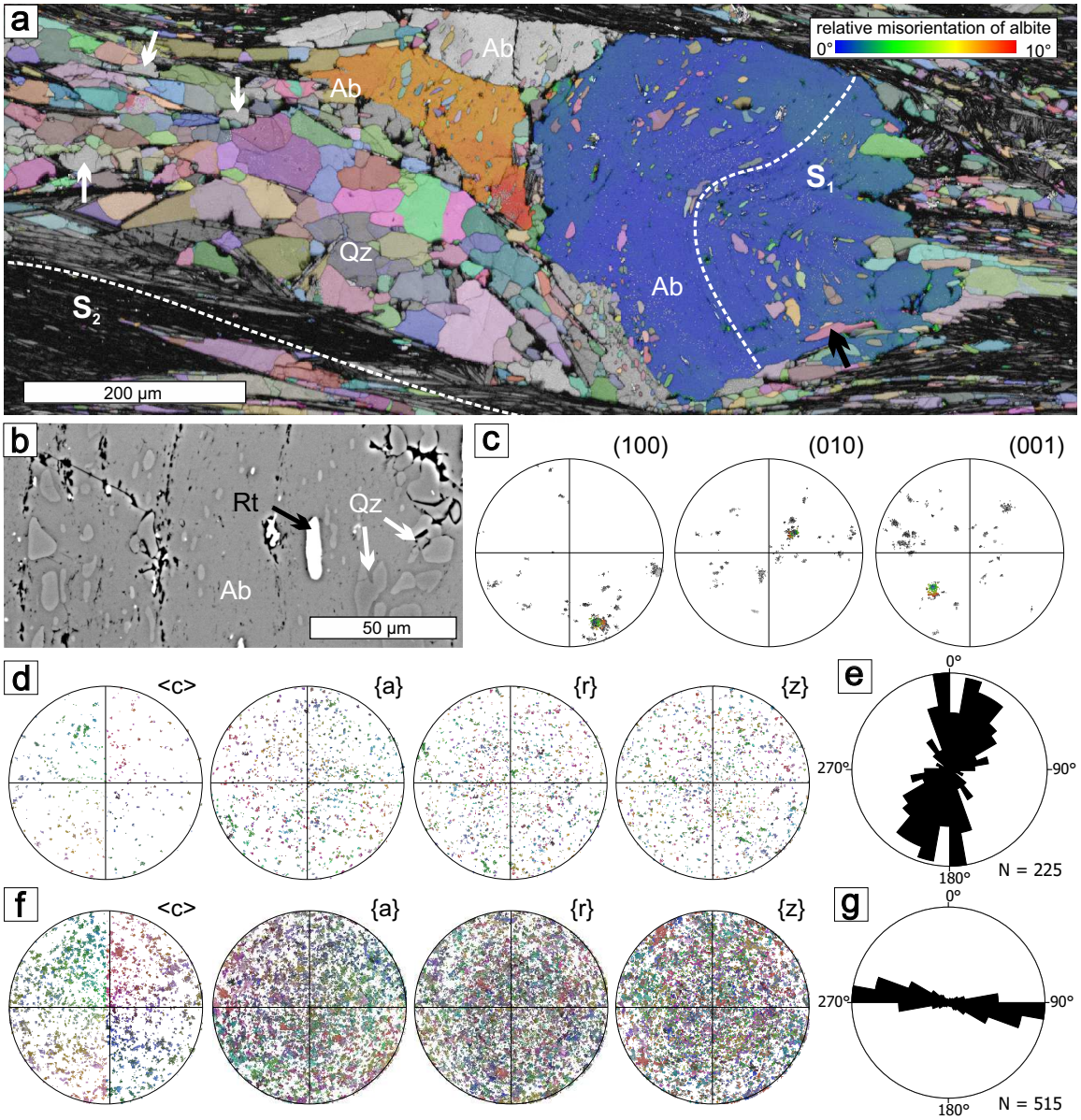

Fig. 5.5: a EBSD map of albite and quartz with internal foliation (S_1) oblique to the external foliation (S_2) of the schist (LS116, stepsize 0.6 µm). Colour coding of quartz by all Euler angles, large albite grain is coloured by relative misorientation with respect to blue orientation (blue to red 10° misorientation angle). Note also isolated albite grains in the strain shadow (white arrows). **b** BSE-image of aligned inclusion of rutile and quartz in albite. **c** Stereographic projections of poles to (100), (010), (001) of albite. **d**, **f** Stereographic projections of c- and a- axes and of the r and z planes of quartz in albite forming the internal fabric and in the matrix, respectively. **e**, **g** 2-D orientation of azimuth of long axis of quartz inclusions and quartz in the matrix, respectively.

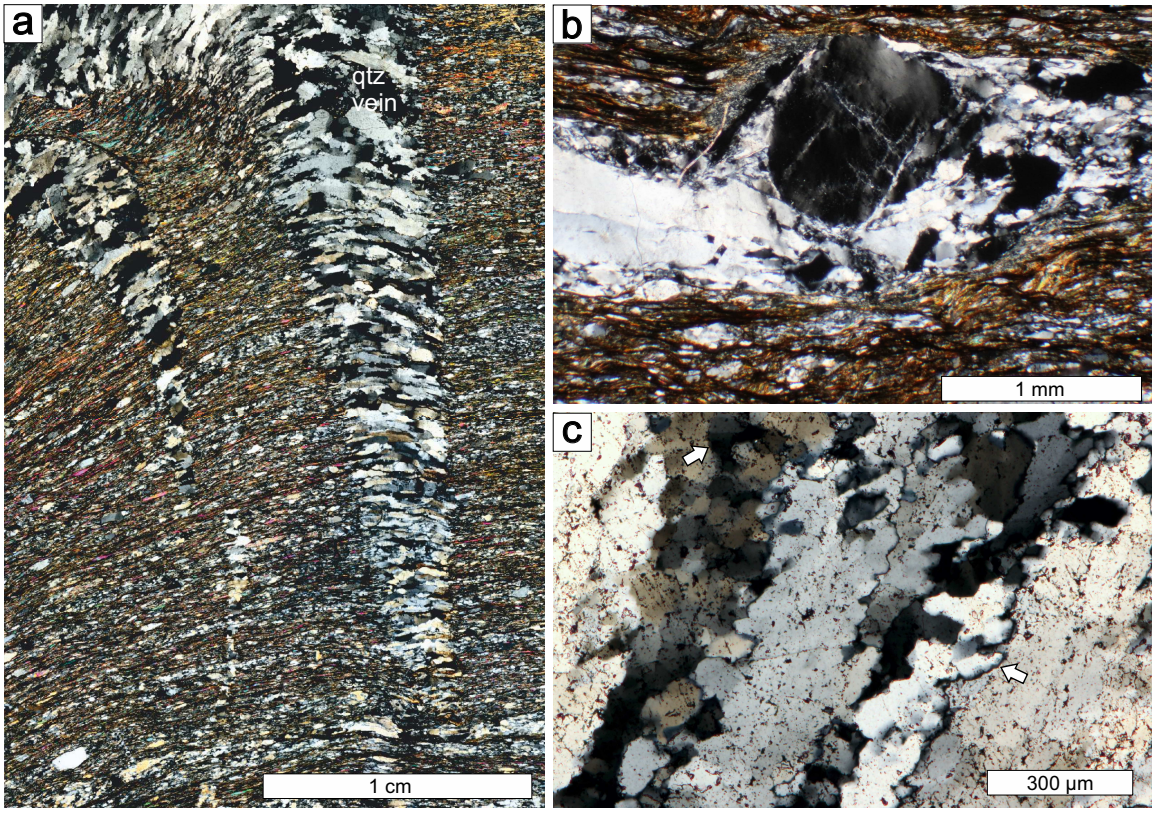

Fig. 5.6: Thin section scan (**a**) and photomicrographs (**b**, **c**) of quartz microstructures in the shear zone, crossed polarizers. **a** Wedge-shaped quartz vein discordant to the foliation in metasandstone (MS1). **b** Deformed quartz pebble in metaconglomerate (CT83). **c** Sutured grain boundaries and subgrains indicating crystal–plastic deformation of quartz in quartz ribbons of wedge-shaped quartz vein (PM4)

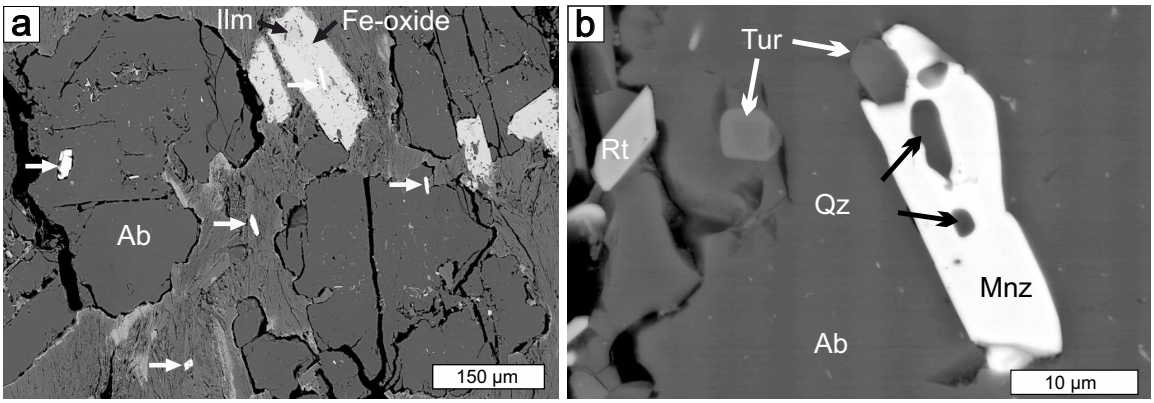

Fig. 5.7: BSE micrographs of monazite grains in albite schist (LS86). **a** Monazite grains (white arrows) as inclusions in poikiloblasts of ilmenite/Fe-oxide and albite and in the mica-rich matrix. **b** Monazite inclusion in albite, which itself has similar quartz inclusions. Mineral abbreviations used after Whitney & Evans (2010)

5.3.3 Peak metamorphic temperatures of footwall and hanging wall of the shear zone

The degree of graphitization of carbonaceous material, analyzed by Raman spectroscopy, depends on the peak distinguish the thermal peak recorded by the Talea Ori group in the footwall and the PQ s.str. in the hanging wall, Raman spectroscopy was carried out on four samples close to the contact of the two units (Fig. 5.1). From the Bali formation a black metachert (LS75) and a black shale (LS104) and from the PQ s.str. a fine grained dark quartzite (LS110) and an albite schist (LS255) were measured. On each of the four samples, several measurements of CM were collected in at least ten different spots, to get ten reliable Raman spectra per sample, which were analyzed to calculate temperatures. For each sample, from these ten calculated temperatures, the mean temperature and standard deviation were determined. For comparison, temperatures were determined after Rahl et al. (2005) as well as after Beyssac et al. (2002). Following the procedure of Rahl et al. (2005), for the Bali formation mean temperatures of 382 °C (LS104) and 403 °C (LS75) were obtained, and for the PQ s.str. 404 °C (LS110) and 408 °C (LS255). Calculation of the mean temperatures after Beyssac et al. (2002) showed a lower standard deviation within the 10 measurements per sample, with mean temperatures of 374 °C (LS104) and 397 °C (LS75) of the Bali formation and 381 °C (LS110) and 400 °C (LS255) of the PQ s.str. (Appendix 8.4).

5.4 Discussions

In the following, we discuss the deformation, related to the formation of the extensional shear zone, and the tectonometamorphic history of the Talea Ori group and the PQ s.str.

5.4.1 The extensional shear zone

The shear bands with associated quartz veins and shear band cleavages that characterize the shear zone, are summarized in a synoptic sketch, showing that on macro- to microscopic scale the hanging block is systematically downfaulted at shear bands and shear band cleavages (Fig. 5.8). In the western and central Talea Ori, where the contact of the Talea Ori group to the PQ s.str. is striking E-W, the movement is consistent with a top-to-the-north shear sense. In the eastern Talea Ori, where the contact strikes N-S and cuts the fold structure of the Talea Ori group, conjugate sets of extensional shear bands occur. The occurrence of both simple and conjugate shear bands dependent on the strike of the shear zone indicates combinations of coaxial and noncoaxial deformation (Mukherjee, 2013b). The extensional character of the shear zone is evident by the shear bands, with boundaries inclined at about 40°–70° and normal drag (Figs. 5.2, 5.8), the frequent quartz veins formed at dilational sites parallel to the shear band boundaries (Figs. 5.2c-e, 5.3a, 5.8), asymmetric boudinage with quartz filled boudin necks (Figs. 5.3b-f, 5.8) as well as shear band cleavages on microscopic scale (Figs. 5.4, 5.8). No indication of any substantial later rotation is present. Younger brittle normal faults overprint the ductile deformation structures (Figs. 5.1, 5.2a, 5.8).

The main deformation mechanism forming the shear bands and shear band cleavages was dissolution-precipitation creep, as indicated by the relative enrichment of mica and opaque minerals in C′-type shear band cleavage planes (Fig. 5.4a, b), by quartz and albite precipitated in asymmetric strain shadows (Fig. 5.5) and in veins, by albite growth rims bulging parallel to the foliation (Figs. 5.4e, f, 5.5a, 5.8) and by stylolites in albitites (Fig. 5.4d). The albite growth rims show that the metamorphic conditions did not markedly differ during the onset of shear band formation with respect to the main foliation development. EBSD maps show that there is no CPO of quartz, as well as no internal deformation of albite (Fig. 5.5a), which indicates that crystal-plastic deformation did not play a major role for accumulating the main strain at any stage. Yet, monophase quartz layers parallel to the foliation as well as younger quartz veins discordant to the foliation related to the extensional shear bands, show microfabrics that indicate deformation by dislocation creep at temperatures of at least 300–350 °C (Trepmann & Seybold, 2019). This indicates firstly that the extensional shear zone at the contact between Talea Ori group and PQ s.str. was activated at almost peak metamorphic conditions (consistent with the microfabrics in the metasediments) and secondly, that stresses were only locally and transiently high enough to cause crystal-plastic deformation.

The importance of dissolution-precipitation creep at peak metamorphic conditions has been reported for the PQ s.str. in Western Crete (e.g., Greiling, 1982; Fassoulas et al., 1994; Schwarz & Stöckhert, 1996; Stöckhert et al., 1999). Deformation related to the shear zone, however, is not pervasive and continuous. Instead, strain is localized within the shear zone forming shear bands. The abundant associated quartz veins discordant to the foliation and in association to the shear bands (Figs. 5.3, 5.6, 5.8) were interpreted by Trepmann & Seybold (2019) to have developed dominantly by crack-seal increments during flow of the metasediments at high strain rates on the order of 10^{-9} to 10^{-10} s^{-1}. Although the shear zone itself is not interpreted to be seismically active, the high strain rates and the locally recorded high stress crystal-plastic deformation at few hundred of MPa are probably related to seismic stress pulses introduced by near-by seismic active faults in the overlying seismogenic zone (Trepmann & Seybold, 2019). The deformation related to the shear zone, therefore is episodic with transient stages of flow at changing stress and strain rate conditions. The documented deformation, localized in the area at the contact between the base of the Talea Ori unit and the PQ s.str. in shear bands associated with quartz veins, is markedly different from that typically recorded from HP-LT metamorphic rocks indicating low stress deformation at HP-LT metamorphic conditions within subduction zones (Stöckhert et al., 1999; Wassmann & Stöckhert, 2013). The relation of the recorded deformation to the subduction and exhumation history is discussed in the following.

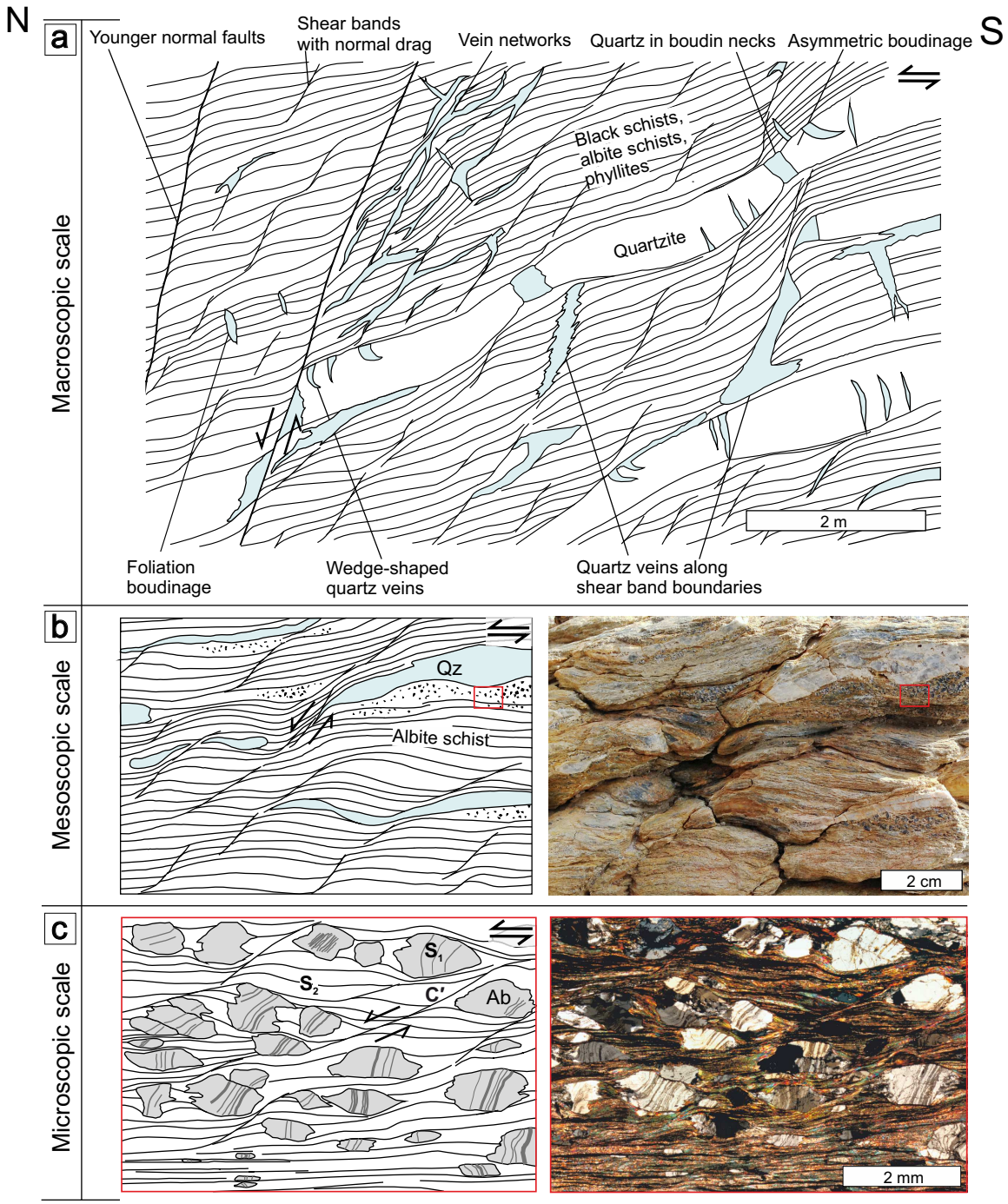

Fig. 5.8: Synoptic sketch of deformation structures in the extensional shear zone linking macroscopic, mesoscopic and microscopic scales. **a** Macroscopic view on deformation structures on outcrop scale. **b** Mesoscopic view on shear band cleavage on cm-scale in albite schist. **c** Microscopic view on same albite schist (red rectangle), showing S_1 (internal foliation in albite) and S_2 (main foliation of the schist) overprinted by C′-type shear band cleavage (LS238). Several of the albite blasts show symmetric shape (Mukherjee, 2017)

5.4.2 Shear zone development in relation to metamorphism and earlier deformation in the Talea Ori

The extensional ductile shear zone crosscuts all earlier deformation structures in the PQ s.str. and the Talea Ori group. The albite porphyroblasts internal fabrics in the Talea Ori group and the PQ s.str. (Figs. 5.4d–f, 5.8) show that albite porphyroblast formation started overgrowing a first foliation in both units. This first foliation and early isoclinal folds most probably developed during top-to-the-south shearing (Zulauf et al., 2016), whereas the dominant foliation is related to a second deformation event with top-to-the-north shear sense at HP-LT metamorphic conditions (Zulauf et al., 2016, this study). This is consistent with the ongoing growth of albite porphyroblasts, evident by their bulging inclusion-free rims and elongation parallel to the stretching direction of the main foliation as well as by the formation of asymmetric strain shadows indicating top-to-the-north shear sense (Figs. 5.4e, f, 5.5, 5.8). Albite formed during Alpine metamorphism, as shown by the low Pb content of monazite inclusions, indicating an age younger than 60–80 Ma. This excludes a possible pre-Alpine origin of the monazite and the host albite porphyroblast. The observed monazite zoning with a LREE fractionation and elongation along the foliation are consistent with a metamorphic growth at (sub)greenschist-facies temperature (Janots et al., 2008). The degree of graphitization of carbonaceous material in the Talea Ori group and the PQ s.str. indicates that both units experienced the same metamorphic peak temperatures of 380–400 °C (Rahl et al., 2005, this study). These metamorphic conditions are consistent with the mineral assemblages (Seidel, 1978; Seidel et al., 1982; Theye, 1988; Theye & Seidel, 1991; Theye et al., 1992). Overall, the Talea Ori group and the PQ s.str. show similar peak metamorphic temperatures and the same characteristics of porphyroblast growth, indicating that both units experienced a similar tectonometamorphic history (at least from the metamorphic peak temperatures). This is consistent with generally similar deformation history of the Talea Ori group and the PQ s.str. as described previously (Krahl et al., 1988; Chatzaras et al., 2006; Zulauf et al., 2016).

The south-vergent map-scale fold structure with E-W trending fold axis in the Talea Ori has been related by Chatzaras et al. (2006) to late compressional extrusion at high crustal levels and temperatures < 300°C. We argue, however, that this fold structure formed before the ductile deformation structures related to the extensional shear zone at the contact between PQ s.str. and Talea Ori group because of two main reasons. Firstly, the ductile shear zone crosscuts the fold structure (Fig. 5.1). The deflection of the dip direction of the foliation parallel to the strike of the shear zone in the east (Fig. 5.1), a kind of flanking structure (Mukherjee, 2014b), is most probably related to the updoming of the Talea Ori group and related downfaulting of the PQ s.str. Secondly, the C′-type shear band cleavages and quartz veins described here developed after peak metamorphism, but still at temperatures > 300 °C. They show an extensional character and – in the central Talea Ori – a top-to-the-north shear sense, which cannot be reconciled to south-vergent folding. It is likely that the south-vergent fold structure with W-E trending fold axis is related to the early nappe stacking and thrusting of the PQ s.str. onto the Talea Ori group (Chatzaras et al., 2006).

In former maps of the Talea Ori, the contact between the PQ s.str. and the Talea Ori group is displayed as thrust fault (e.g., Epting et al., 1972; Richter & Kopp, 1983; Kock

et al., 2007; Zulauf et al., 2016), although it is in the field rather related by steeply northward dipping normal faults (e.g., Richter & Kopp, 1983). Xypolias et al. (2007) supposed that the contact between the PQ s.str. and the Talea Ori group is part of a 600 km long thrust-sense shear zone. The documented deformation – the extensional shear bands, C′-type shear band cleavage and associated quartz veins – characterizing the contact between Talea Ori group and PQ s.str., however, gives evidence that it is related to exhumation and downfaulting of the PQ s.str.

5.4.3 Implications for the exhumation history of the HP-LT metamorphic rocks in the Talea Ori

The ductile extensional shear zone developed at an early stage of exhumation, close to peak metamorphic temperatures (Fig. 5.9), marked by high strain rate dissolution-precipitation creep of the metasediments and vein formation at temperatures higher than 300 °C. The onset of exhumation was probably accompanied by seismic activity, suggested by the quartz microstructures that indicate transiently high stresses (Trepmann & Seybold, 2019). Strain localized within the siliciclastic metasediments of the base of the Talea Ori group and PQ s.str., eventually resulting in the updoming of the Talea Ori group. The extensional character of the shear zone associated with vein formation suggests that the shear zone involves dilation. Normal faults overprinting the ductile shear bands at similar orientation indicate that extensional deformation in this area may have lasted during exhumation of the rocks until reaching a depth of less than 10 km.

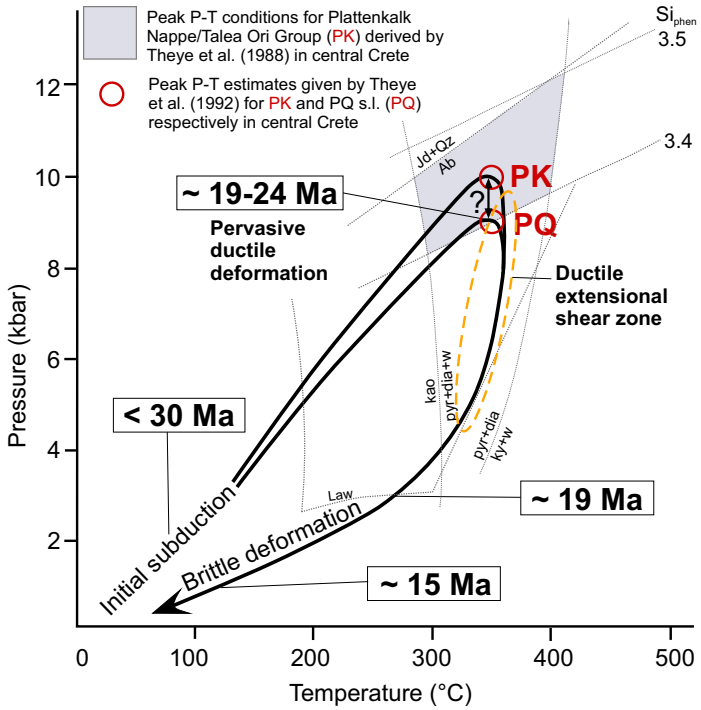

Fig. 5.9: PTt-Diagram for central Crete modified after Thomson et al. (1998b) and Theye (1988). For the Talea Ori group (here taken together with the Plattenkalk unit) and the PQ s.str. (part of the PQ s.l.) a similar PTt-path can be inferred with an unknown but, if present, rather small difference in peak metamorphic pressure

The degree of graphitization in the graphite schists of the Talea Ori group and the PQ s.str. did not reveal a marked temperature gradient over the extensional ductile shear zone, which might be due to the limited resolution of this technique, predicting temperatures to $\pm$ 50 °C (Rahl et al., 2005). However, a large temperature gradient along the shear zone within HP-LT metamorphic rocks that experienced peak temperatures of only 380–400 °C cannot be expected (Fig. 5.9). Furthermore, the vertical offset might not be characterized by temperature, but rather by pressure, since the exhumation of the HP-LT metamorphic rocks was fast and close to adiabatic, with temperatures remaining higher than 300 °C up to approximately 10 km depth ((Fig. 5.9); Thomson et al., 1998a). Constraints on a pressure gradient are not available. The microfabrics in both units show growth of albite during deformation at peak metamorphic conditions as well as during early stages of exhumation (Figs. 5.4e, f, 5.5a, 5.8) without evidence for the presence of jadeite at any stage. Thus, the vertical offset along the shear zone cannot be constrained, for which detailed data on the decompression and/or cooling path of both units would be required. For Crete, the model of syncompressional extrusion in a subduction wedge, with a basal thrust fault and an upper normal sense fault is widely accepted (e.g., Chatzaras et al., 2006; Xypolias et al., 2007; Ring et al., 2010; Jolivet et al., 2013), where strain and exhumation is supposed to be localized into the two main bounding faults (Ring & Reischmann, 2002). From Western Crete dissolution-precipitation creep is found to be important during deformation at peak conditions, but evidence for deformation during exhumation was not recorded (Greiling, 1982; Schwarz & Stöckhert, 1996; Stöckhert et al., 1999). This study shows that deformation during early stages of exhumation can localise in wide shear zones and that high strain rate deformation by dissolution-precipitation creep associated with vein formation are the dominant deformation processes.

5.4.4 Summary

Based on the documented deformation (micro)structures characterizing the several hundred meter up to kilometre wide area at the contact between the base of the Talea Ori group and the PQ s.str. on map-scale down to the grain scale, the conclusions are summarized as follows.

- The ductile extensional shear zone is documented by extensional shear bands with boundaries dipping at 40–70°, where the hanging blocks are systematically down-faulted, C′-type shear band cleavages, asymmetric boudinage, foliation boudinage and associated quartz veins.
- Deformation characterizing the shear zone is by high strain rate dissolution-precipitation creep (evident by albite growth rims, mica along shear band cleavage, stylolites, strain shadows) and associated vein formation at temperatures close to peak metamorphic temperatures ($\geq$ 300–350 °C).
- The shear zone overprints the main foliation in both units. The similarities of paragenesis (albite), peak metamorphic temperatures and structural inventory in the PQ s.str. and Talea Ori group, indicate the common tectonometamorphic history.
- No change in peak metamorphic temperatures (380–400 °C) across the shear zone is apparent by the degree of graphitization and the mineral assemblage in the graphite-

and albite-bearing schists of both units.

- The vertical offset along the extensional shear zone is difficult to estimate, given the same inferred peak metamorphic temperatures for both units. Due to the fast exhumation of the rocks, temperatures higher than 300 °C were maintained during uplift up to a depth of 10 km, and the vertical offset would be characterized rather by the pressure than by the temperature. The decompression path of the rocks would be required to give information on the amount of exhumation.

The high strain rate dissolution-precipitation creep accompanied by vein formation resulting in the extensional ductile shear zone is interpreted to mark the onset of exhumation from peak metamorphic conditions, finally resulting in the updoming of the HP-LT metamorphic rocks in the Talea Ori.

6 Transient deformation at low and high stress-loading rates

The following chapter is based on the manuscript "*Trepmann, C. A. & Seybold, L. (2019). Deformation at low and high stress-loading rates. Geoscience Frontiers, 10(1), 43–54. https://doi.org/10.1016/j.gsf.2018.05.002.*".

6.1 Introduction

Rocks correspond to stress by deformation. The stress conditions and their evolution with time in the lithosphere are of vital interest for all geodynamic processes. Early works of Sibson (1977) and Scholz (1988) indicated that shear zones can be characterized as deep continuations of seismic active faults, where the affected rocks deform controlled by stress loading and stress relaxation of the seismic cycle. Especially quartz veins have been found to be able to record the deep response of changes in stress and fluid pressure related to the seismic cycle (Henderson & McCaig, 1996; Famin et al., 2004; Nüchter & Stöckhert, 2007, 2008; Birtel & Stöckhert, 2008; Fagereng et al., 2018). Characteristic deformation microstructures that form at transient high stresses and subsequent modification at low stresses below the seismogenic zone, i.e., the plastosphere sensu Scholz (2002), have been identified from the geological record (e.g., Küster & Stöckhert, 1999; Trepmann & Stöckhert, 2003; Trepmann et al., 2017) in combination with experimental vein quartz deformation (Trepmann et al., 2007; Trepmann & Stöckhert, 2013). In these studies, the inferred transient high stresses in the plastosphere have been explained by "external stress" loading from seismic faulting in the overlying upper crust (Ellis & Stöckhert, 2004; Ellis et al., 2006; Nüchter & Ellis, 2010, 2011). Yet, stress loading in the plastosphere can also be related to "internal" processes, for example ductile instabilities with strain hardening (e.g., Hobbs et al., 1986; White, 1996, 2012). Local stress concentrations can occur in high-viscosity particles in a low-viscosity matrix during boudinage and folding (e.g., Masuda et al., 1989; Trepmann & Stöckhert, 2009; Peters et al., 2016). Dehydration reactions during metamorphism have recently been described to result in quartz vein formation along the deep, tremorgenic subduction interface (Fagereng et al., 2018). Stress concentrations in the plastosphere by such internal processes lead to enhanced strain rates, which might load the seismogenic zone. Resulting earthquakes can again reload the plastosphere, which is characterizing the seismic cycle (e.g., Scholz, 2002). Here, the question is addressed, whether the microstructural record can distinguish between external stress loading of the plastosphere related to seismic activity in the upper crust and internal stress loading related to enhanced flow within the plastosphere.

In this Chapter, quartz microstructures in veins of HP-LT metamorphic sediments from the Talea Ori, Crete, are presented, which are interpreted to reflect deformation at different stress-loading rates during exhumation of the metasediments. It is proposed that the

recorded rapid loading to high stresses requires external coseismic stress loading, whereas slow stress loading rates resulted from high strain-rate dissolution-precipitation creep.

6.2 Methods

Rock samples were collected on field campaigns between 2015 and 2017 (for coordinates and description of samples refer to Appendix 8.1). Thin sections for transmitted light microscopy were prepared perpendicular to the foliation and parallel to the lineation. Sections used for analyses by electron backscatter diffraction (EBSD) at a scanning electron microscope (SEM) were polished by an alkaloid colloidal suspension (Syton) and coated with carbon. A field emission SEM (SU5000, Hitachi) equipped with EBSD facilities (NordlysNano Detector) at Ludwig-Maximilians University Munich, Department of Earth and Environmental Sciences, was used. An acceleration voltage of 20 kV and a working distance of 20–25 mm were applied on samples tilted at an angle of 70° with respect to the beam. EBSD patterns were automatically measured (step size of 0.7–1 µm) with the AZtec software (Oxford Technology) and postprocessed using the software CHANNEL 5 (Oxford Technology). To present crystallographic orientations of the grains, stereographic projections of the lower hemisphere are used. The software also provides information about grain size and shape. For grain detection, a threshold value of 10° for the misorientation angle was used. The misorientation of silicates may be > 10 (White, 1977). However, a higher threshold value of e.g. 15° did not change our results. Grain size is given as the diameter of a circle of equal area. TEM samples were prepared by ion thinning (GATAN PIPS) of 30 µm thin sections glued onto a copper grid. The TEM samples were thinned at voltages of 3–4 kV and an Ar-beam at an angle of 6°–8° with respect to the sample. TEM samples were analysed using bright field conditions at a Tecnai G2 (FEI) microscope operated at 200 kV at Ludwig-Maximilians University Munich, Department of Chemistry.

6.3 Results

6.3.1 Deformation structures and quartz veins

The deformation structures in the shear zone at the contact between the PQ s.str. and the Talea Ori group include extensional shear bands, shear band cleavages, kink bands and boudins (Figs. 6.1b–e, 6.2a, b; Seybold et al., 2019). Quartz veins discordant to the foliation and with a relative high ratio of aperture to length (typically around 1:6 to 1:10) are associated to these structures. Such aperture-to-length ratios exceed the elastic limit of fracture aperture, indicating that inelastic host rock deformation contributed to relief stresses concentrating at the fracture tips to keep the fracture arrested during aperture growth (e.g., Vermilye & Scholz, 1995; Olson, 2003). This is consistent with the relation of the quartz veins to ductile deformation structures of the host rocks, i.e. shear bands, boudins and kink bands within the shear zone (Fig. 6.1b–e). An older generation of quartz veins is concordant to the foliation (Fig. 6.1c, e). Discordant wedge-shaped quartz veins can occur in arrays (Fig. 6.1e). The quartz veins can contain minor amounts of albitic feldspar and chlorite may be present. In quartzites, the spacing between the foliation,

characterized by layers rich in opaque minerals and mica, decreases towards quartz-sealed boudin necks (Fig. 6.2a). This microstructure indicates a relative enrichment of insoluble minerals caused by selective dissolution of quartz at sites of shortening, indicating dissolution-precipitation creep. In mica-rich layers of metasandstones and shales, C′-type shear band cleavage, also referred to as extensional crenulation cleavage (e.g., Platt & Vissers, 1980; Passchier & Trouw, 2005), is common (Fig. 6.2b). The shear band cleavage is characterized by a passive enrichment of micas and opaque minerals, whereas quartz has been removed by dissolution, indicating dissolution-precipitation creep. At the sites of dilation, quartz is precipitated forming the observed quartz veins discordant to the cleavage, resembling an asymmetric foliation boudinage (Platt & Vissers, 1980). The metasediments generally show a shape preferred orientation (SPO) but no crystallographic preferred orientation (CPO) (Fig. 6.2a, c), revealing a low amount of strain accumulated by dislocation glide. These microstructures indicate vein formation by fracturing and sealing during dissolution-precipitation creep of the host rock.

6.3.2 Vein quartz microstructures

Three types of vein quartz microstructure are distinguished by the recorded strain and are presented in the following.

The type A microstructure is exclusively present in quartz veins discordant to the foliation (Fig. 6.2c–e). It is the most common vein microstructure. Elongate to blocky grains with long axes perpendicular to the vein wall characterize it. The crystallographic orientation of the grains indicates epitactic growth from the vein wall (Fig. 6.2c–f). Common fluid inclusion trails subparallel to the vein wall represent healed microcracks (Fig. 6.2d, f). This microstructure is characteristic of stretching veins, indicating formation by multiple crack-seal increments (e.g., Durney, 1973; Ramsay, 1980; Cox & Etheridge, 1983; Fisher & Byrne, 1990; Fisher & Brantley, 1992; Fisher et al., 1995; Nollet et al., 2005; Bons et al., 2012). Along the vein boundaries, the foliation in the host rock can be displaced (Fig. 6.1c). The curved shape of elongate grains is commonly not corresponding to a respective change of crystallographic orientation (Fig. 6.2e), indicating that they grew epitactically during deformation of the host rock, instead of being deformed after growth. Such bent elongate quartz grains can track the shear-offset during vein widening (Durney, 1973; Ramsay & Huber, 1983; Urai et al., 1991). Yet, some crystal-plastic deformation and strain-induced grain-boundary migration after growth are indicated by the presence of undulatory extinction and sutured high-angle grain boundaries (Fig. 6.2d–f). TEM investigations show tiny grains with diameter of a few mm, abundant fluid inclusions along grain boundaries, a relative low free dislocation density and common low angle grain boundaries (Fig. 6.3a–c).

The type B microstructure occurs in the centre of veins discordant to the foliation, showing otherwise a type A microstructure at the area close to the vein wall. Towards the centre of these veins, grain sizes can increase, indicating growth competition of the fast growth direction parallel to the quartz c-axis (e.g., Durney, 1973; Fisher & Brantley, 1992; Fisher et al., 1995; Hilgers & Urai, 2002; Nollet et al., 2005; Bons et al., 2012). The type B microstructure is characterized by rational boundaries of quartz grains, representing crystallographic planes (Fig. 6.2f). These hypidiomorphic quartz grains are almost devoid of

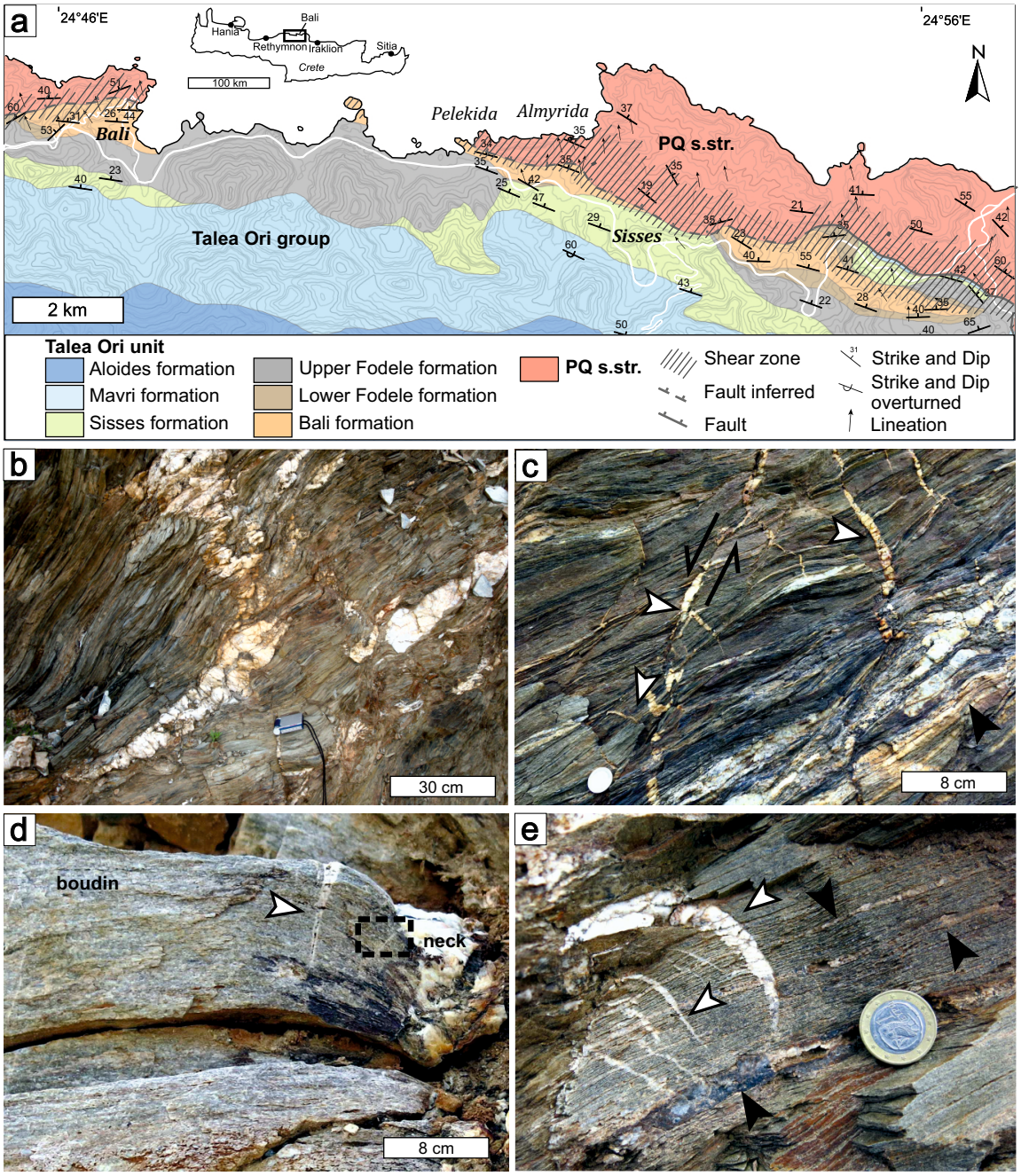

Fig. 6.1: **a** Geologic map of the Talea Ori modified after Epting et al. (1972),Richter & Kopp (1983), and Kock et al. (2007). **b** Slaty cleavage of black shales in shear zone with quartz veins (Bali beds). **c** Extensional shear bands in schists with quartz precipitated along shear band boundaries (white arrows, PQ s.str.). Quartz veins concordant to the foliation are indicated by black arrow. **d** Quartzite boudin with a few cm-wide quartz vein in the boudin neck and mm-wide quartz veins (white arrow). Thin section micrographs from this sample, MB2 (PQ s.str.), are shown in Fig. 6.2a, f (dashed line). **e** Array of bent wedge-shaped discordant quartz veins (white arrows, PQ s.str.). Black arrows indicate quartz veins concordant to the foliation.

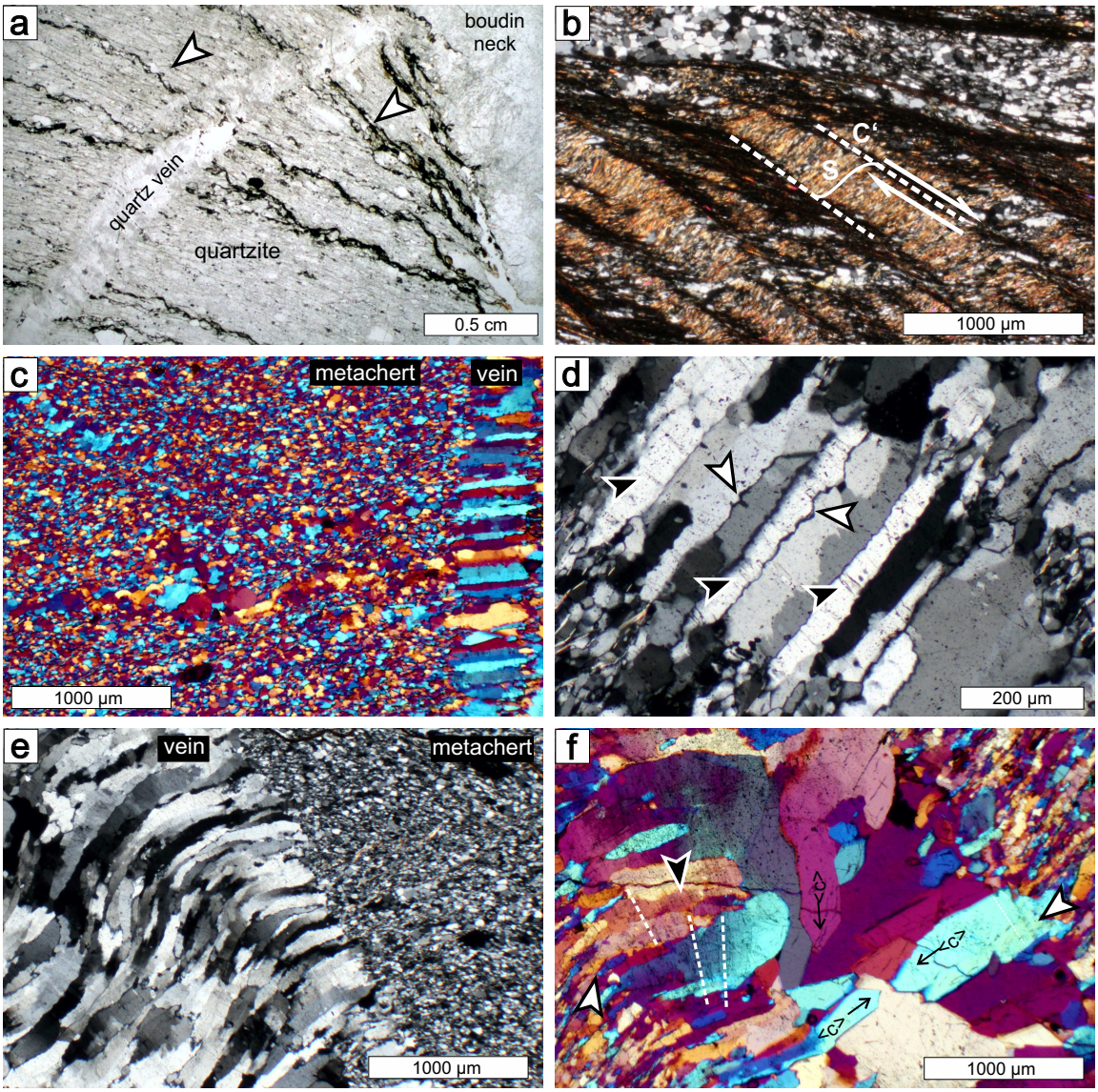

Fig. 6.2: a Transmitted light micrographs of quartz vein in quartzite boudin displayed in Fig. 6.1c (dashed line), sample MB2 (PQ s.str.). The distance between layers enriched in opaque phases decreases towards the boudin neck (arrows). **b** Polarized light micrograph (crossed polarizers) showing shear band cleavage (C'-type) in black shale at Bali harbour (sample LS82). **c** Metachert and vein with elongate quartz grains of type A microstructure (crossed polarizers, compensator plate, sample LS128, Bali formation). Note that the optical characteristics do not reveal a CPO in the metachert. **d** Polarized light micrograph (crossed polarizers, sample LS128, Bali formation) of type A quartz vein microstructure characterized by elongate grains and fluid inclusion trails subparallel to the vein wall (black arrows). White arrow marks sutured grain boundaries. **e** Polarized light micrograph (crossed polarizers, sample LS128, Bali formation) of type A quartz vein microstructure. Note bent elongate grains, indicating growth during deformation of the host rock. **f** Polarized light micrograph (crossed polarizers, compensator plate, sample MB2, PQ s.str.) with type A microstructure close to the veinwall. In the centre of the vein, grains with rational boundaries are marked by the orientation of the c-axis. These grains are poor in fluid inclusions and show no undulatory extinction, characterising the type B microstructure.

fluid inclusions and internal deformation structures as undulatory extinction and sutured grain boundaries, in strong contrast to the type A microstructure. The hypidiomorphic quartz crystals are elongate, with their long axis parallel to the c-axis, consistent with the quartz c-axis being the fast growth axis and growth in open cavities (Fisher & Brantley, 1992; Ague, 1995; Nollet et al., 2005; Bons et al., 2012). Consistently, associated veins can be partly open.

The heterogeneous type C microstructure can occur in the old generation of quartz veins concordant to the foliation of the host metasediments (Figs. 6.4 and 5) and rarely also in the young discordant veins associated to shear bands (Fig. 6.6). Sub-basal deformation lamellae, a marked short-wavelength undulatory extinction (SWUE) and micro-shear zones in conjugate sets (Figs. 6.4, 6.5, 6.6) characterize the type C microstructure. Deformation lamellae sub-parallel to the basal plane can occur in concordant veins and in host rocks (Fig. 6.4c, d). They show a slight difference in refractive index and a low oscillating change in misorientation angle of <1 at the detection limit of the EBSD technique. Such sub-basal deformation lamellae are common in quartz deformed at high stresses and greenschist facies conditions (e.g., McLaren et al., 1970; McLaren & Hobbs, 1972; White, 1973, 1977; Christie & Ardell, 1974; Drury, 1993; Trepmann & Stöckhert, 2003, 2013). An oscillatory change in misorientation angle of a few degrees is characterizing the SWUE (Fig. 6.5a, e). Along micro-shear zones, the orientation abruptly changes with misorientation angles being generally smaller than 10° (Fig. 6.5a, e). The micro-shear zones in conjugate sets are sub-parallel to one r and one z rhombohedral planes of the host orientation (Figs. 6.4b and 5a, c). They show a systematic difference in crystallographic orientation, indicating a dextral or sinistral rotation of the c-axes with respect to the host orientation in micro-shear zones parallel to the z and r planes, respectively (Figs. 6.4b and 5a, e). The angle between the c-axes in the micro-shear zone and the host grain is within average 5° very similar in both micro-shear zones. Similar conjugate micro-shear zones with systematically different crystallographic orientations are described for example by van Daalen et al. (1999), Kjøll et al. (2015), Ceccato et al. (2017) and Trepmann et al. (2017), where both brittle and crystal-plastic mechanisms are discussed to be involved in their formation. Dauphiné twin orientations are common along the micro-shear zones (Fig. 6.5a–c). Mechanical Dauphiné twinning of quartz is observed in quartz mylonites (e.g., Pehl & Wenk, 2005; Wenk et al., 2006, 2011; Kjøll et al., 2015). Dauphiné twin boundaries can be modified during recrystallization of quartz, resulting in HAGBs with large misorientation angles (Lloyd, 2004; Menegon et al., 2011). Most new grains (about 70 %) in micro-shear zones have diameters of smaller than 8 mm, as indicated by EBSD-measurements (Fig. 6.5b, d, f). Recrystallized grains can also occur restricted to high angle grain boundaries or intragranular cracks (Fig. 6.6b, d, e). There, most newgrains (ca. 70 %) have a grain diameter smaller than 10 mm with an expected value of 9 mm (Fig. 6.6e). Subgrains similar in shape and size are common close to recrystallized areas (Fig. 6.6c). New grains show similar grain orientations as the deformed host (Fig. 6.6g, f). TEM observations of quartz from the vein in Fig. 6.6 show high dislocation densities (Fig. 6.3d–i). Sutured high angle grain boundaries (Fig. 6.3d) and grain boundaries decorated by fluid inclusions (Fig. 6.3e), as well as low angle grain boundaries (Fig. 6.3f, h) are common.

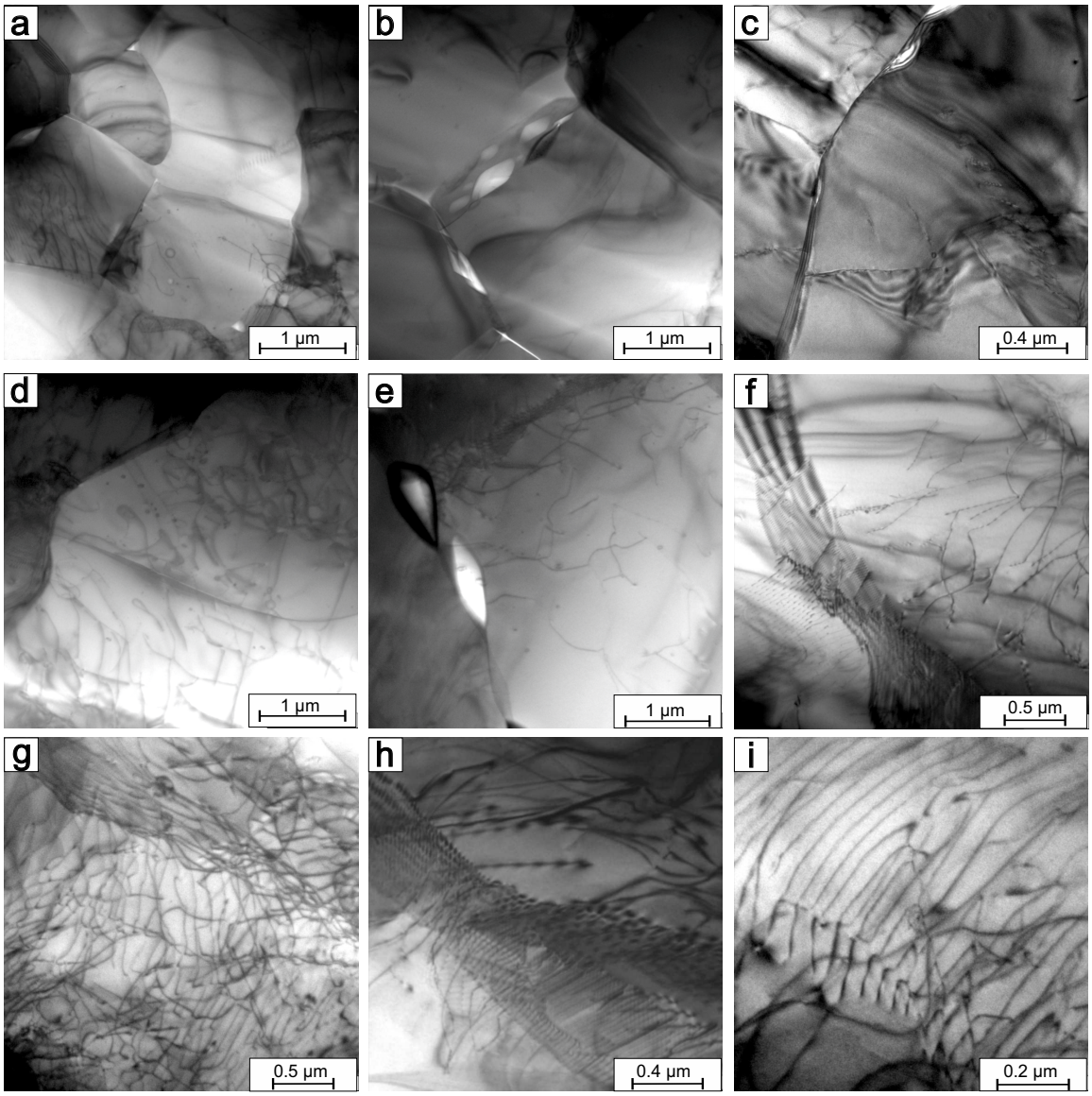

Fig. 6.3: TEM bright field images of vein quartz from samples discordant to foliation. **a–c** Type A microstructure (sample MS 1, Bali formation, compare with Fig. 6.2e) showing new grains with low dislocation density, a high amount of fluid inclusions along grain boundaries and low angle grain boundaries. **d–i** Sample MB 1, PQ s.str. (type C microstructure, compare Fig. 6.6). **d** Curved high angle grain boundaries in grains with high dislocation density. **e** Fluid inclusions along high-angle grain boundary. **f–i** Low-angle grain boundaries and networks of tangled dislocations.

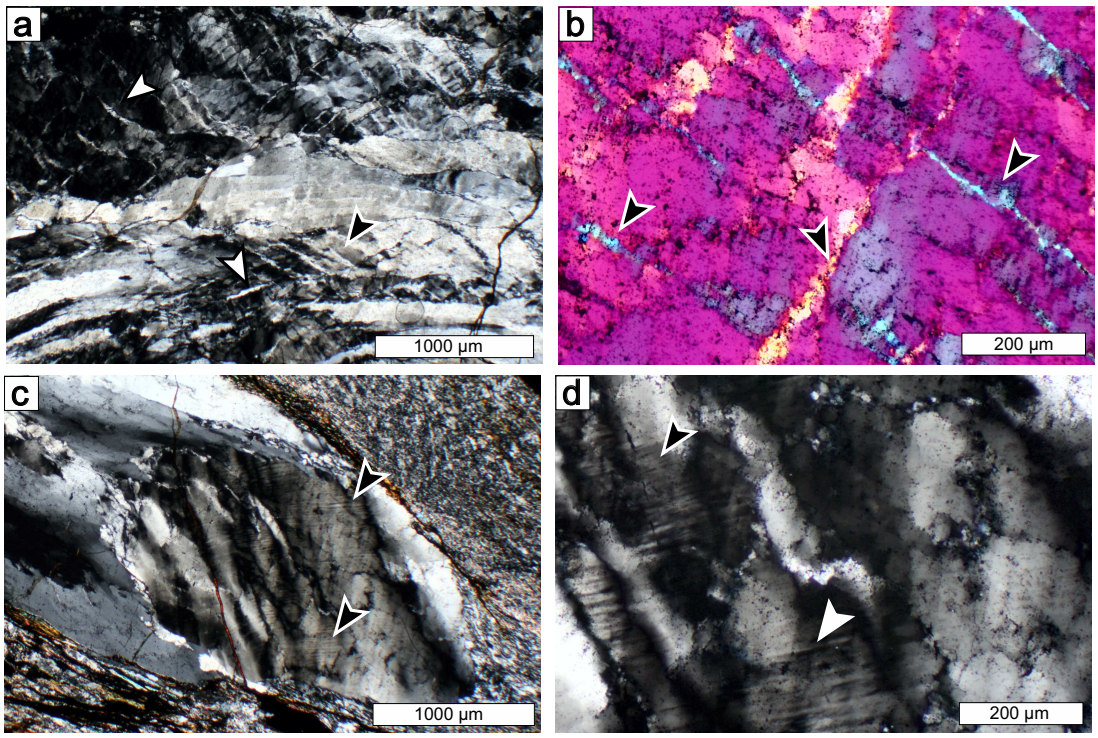

Fig. 6.4: Transmitted light micrographs with crossed polarizers of vein quartz microstructure type C revealing high stress, dislocation glide-controlled deformation. **a** Vein quartz concordant to the foliation showing elongate grains and micro shear zones, in conjugate sets (arrows) (CT83). **b** Close-up of micro-shear zones. Micrograph is taken with compensator plate inserted, indicating systematic rotation of the quartz c-axes with respect to the host orientation (sample LS12 Bali formation, compare with Fig. 6.5). **c, d** Quartz vein showing short wavelength undulatory extinction and deformation lamellae (black arrows, LS12, Bali formation).

6.4 Discussion

The three different types of vein quartz microstructure are interpreted to represent deformation at different stress conditions, which is discussed in the following.

6.4.1 Growth of quartz in open cavities at quasi-isostatic stress conditions

The type B microstructure with hypidiomorphic grains and no internal deformation microstructures, exclusively occurring in discordant quartz veins, represents the latest stage of veining, after which the temperature-stress conditions were too low to allow for crystal-plastic deformation of quartz. The rational grain boundaries together with the associated partly open fractures indicate that vein opening was fast compared to the precipitation rates (e.g., Fisher & Byrne, 1990; Fisher & Brantley, 1992; Ague, 1994, 1995; Fisher et al., 1995; Hilgers et al., 2003; Nollet et al., 2005). This suggests that ductile deformation of the host rocks by dissolution-precipitation creep was ongoing, forming the cavities. The fluid pressure remained high enough to keep the veins open against the lithostatic pressure. These microstructures indicate that stresses relaxed and became quasi-isostatic after precipitation of the crystals into the residual cavities and completion of the veins.

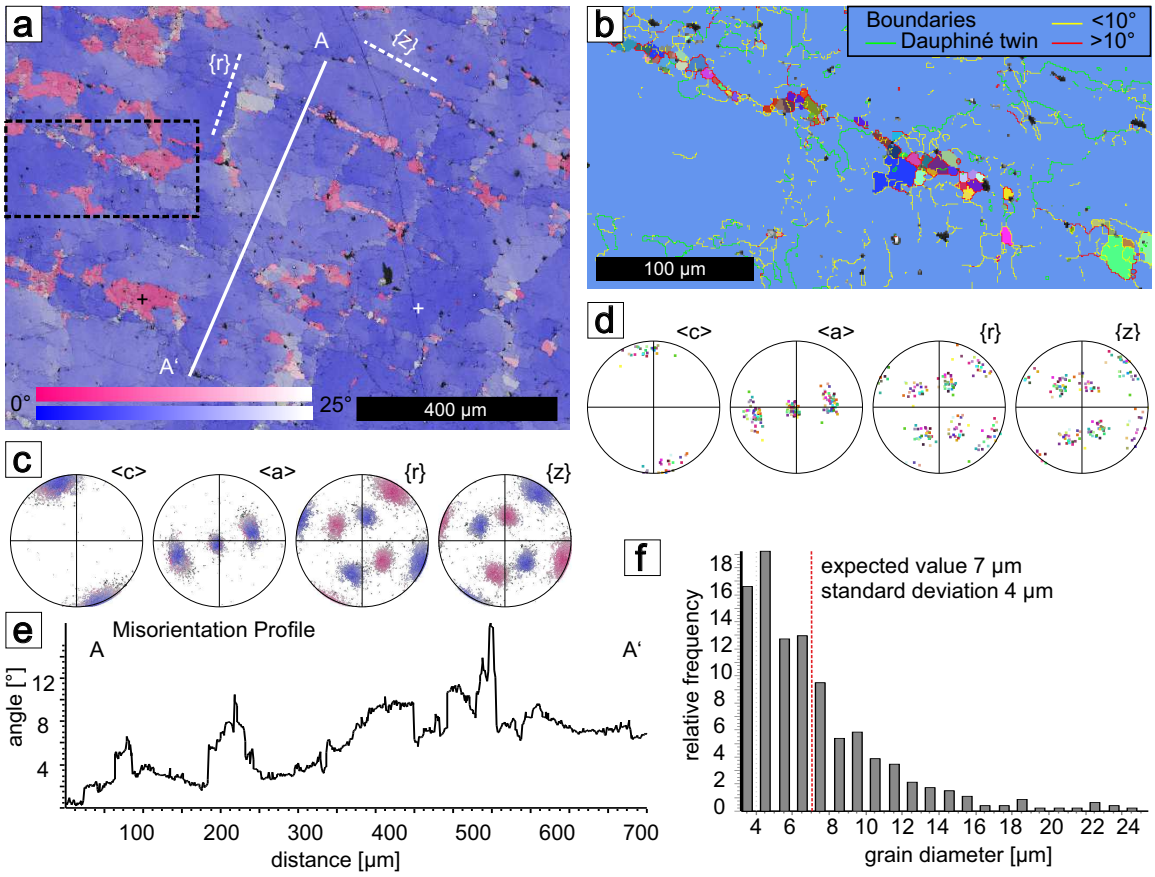

Fig. 6.5: EBSD data of optical microstructure shown in Fig. 6.4, (sample LS12). **a** EBSD map, colour coding is by misorientation angle of up to 25° to a reference orientation of the host grain (white cross) and Dauphiné twin domains (black cross). Host orientations are in dominating blue colour, Dauphiné twins in red colour, compare with (c). Orientation of misorientation profile (AA') is indicated by white line. Dashed white lines indicate traces of one r and one z rhombohedral plane, compare with (c). Black dashed box indicates close-up in (b). **b** Close-up of a micro-shear zone with new grains in random colours (neglecting Dauphiné twins). Grain boundaries are indicated by yellow (low-angle grain boundaries with misorientation angle <10°) and red lines (high-angle grain boundaries with misorientation angle >10°). **c, d** Corresponding pole figures to old grains (a) and corresponding pole figures for new grains (one point per grain) in (b), stereographic projection of the lower hemisphere. **e** Misorientation profile to line displayed in (a). **f** Grain size distribution for new grains.

6.4.2 Vein formation by crack-and-seal increments – deformation at low stress-loading rates

The curved shape of elongate grains characteristic of the type A microstructure, which is not corresponding to a change of crystallographic orientation (Fig. 6.2e and f), indicates deformation of the host rock during sealing (Durney, 1973; Ramsay & Huber, 1983; Urai et al., 1991). The elongate grains epitactically growing from quartz grains in the host rock with healed microcracks parallel to the vein wall indicate formation by crack-seal increments, where the average vein opening velocity is smaller than the growth velocity of the crystals as indicated from numerical simulation (e.g., Hilgers et al., 2001; Nollet et al., 2005). The observation that the crack-seal microstructures exclusively occurs in discordant veins located at sites of dilation along shear band boundaries, kink band boundaries

and boudin necks (Fig. 1b–e) shows that vein formation by cracking and sealing is related to dissolution-precipitation creep of the metasediments. Undulatory extinction, subgrains, sutured high-angle grain boundaries (Fig. 6.2c–f) and tiny dislocation-free new grains observed in TEM (Fig. 6.3a) indicate that most of the veins formed at temperatures sufficiently high to allow for dislocation climb and strain-induced grain boundary migration, i.e. temperatures of at least 300–350 °C. These temperatures are close to the peak metamorphic conditions for the rocks of central Crete (about 0.9 GPa, 350 °C after Seidel et al., 1982; Theye et al., 1992). Given the extensional character of the shear bands and boudins, the veins formed most probable during exhumation from depth of maximal 30 km within the subduction channel. The generally low amount of strain accumulated by dislocation creep of quartz in most veins and host rocks implies that stresses in these rocks were too low to result in relevant strain rates of dislocation creep at the given temperatures. Thus, flow laws for dislocation creep of quartz can be used as lower bound of the differential stress (e.g., Stöckhert, 2002; Trepmann & Stöckhert, 2009; Wassmann & Stöckhert, 2013). For temperatures of 300–350 °C and a strain rate of 10^{-15} s^{-1}, the flow law of Paterson & Luan (1990), equation (1), predicts differential stresses below a few tens of MPa.

$$d_\varepsilon/d_t = A \cdot exp(-Q/RT) \cdot \sigma^n \tag{6.1}$$

with the parameters $A = 6.5 \times 10^{-}8$ MPa$^{-n}/s$; Q $= 135 \pm 15$ kJ mol^{-1}; n $= 3.1$.

Applying different creep parameters for a rheology controlled by dislocation creep of quartz (e.g., Ranalli, 1995, Chapter 10), yields the same order of magnitude. These differential stress conditions of less than few tens of MPa are consistent with the record of static recrystallization of quartz in HP-LT metamorphic conglomerates from related tectonic units in the Talea Ori (Trepmann et al., 2010). Generally, the record of rocks exhumed from subduction zones indicate low bulk stress conditions and a long-term rheology dominated by dissolution-precipitation creep over crystal-plastic deformation in subduction zones (e.g., Stöckhert et al., 1999; Wassmann & Stöckhert, 2013). Consistently, the expected brittle strength of the host rock at the given P-, T-conditions and the indicated high pore fluid pressures would not require higher stress conditions for the crack-seal processes. As vein opening is related to dissolution-precipitation creep in the metasediments, the time interval for the crack-seal episodes depends on the effective viscosity of the metasediments. Dissolution-precipitation creep is a deformation mechanism, which allows for the accumulation of high strain at low bulk stress conditions characterized by relatively low viscosities on the order of 10^{19}–10^{20} Pa s (e.g., Trepmann & Stöckhert, 2009; Wassmann & Stöckhert, 2013). Considering a Maxwell rheology, the time required to dissipate the imposed stress can be expressed by the relaxation time λ_R (e.g., Ranalli, 1995, Chapter 4), which is defined as the viscosity (η) divided by the shear modulus, G (6.2).

$$\lambda_R = \eta/G \tag{6.2}$$

For viscosities, η, of 10^{19}–10^{20} Pa s and a typical shear modulus, G, for schists of 19 GPa (Johnson & DeGraff, 1988) it is on the order of a few tens to hundred years. The time scales of stress build up for cracking and sealing can be assumed lower than the Maxwell relaxation time of the metasediments undergoing dissolution-precipitation creep. Progressive vein formation might cause increasing bulk strength of the rocks, representing high-

viscosity layers in a low-viscosity matrix. The Deborah number, *De*, relates relaxation time and the characteristic time of a deformation process (e.g., Poole, 2012). For our purpose, *De* can be considered as Maxwell relaxation time multiplied with strain rate, d_ε/d_t (6.3).

$$De = \lambda_R \cdot d_\varepsilon/d_t \tag{6.3}$$

When De becomes >1, i.e. the Maxwell relaxation time is higher than the reciprocal of the strain rate, d_ε/d_t, the material cannot dissipate the imposed stress. Assuming a viscosity of 10^{19} Pa s for the metasediments undergoing dissolution-precipitation creep, a strain rate of 2.5×10^{-9} s^{-1} would be required for this critical behaviour, and 3.5×10^{-10} s^{-1} would be required for a viscosity of 10^{20} Pa s. Such high strain rates are predicted along the plate interface in subduction zones, which depend on relative plate velocity and cumulative shear zone width (e.g., Fagereng & Sibson, 2010). For a convergence of about 4.5 cm/yr for the Hellenic subduction zone (McClusky et al., 2000), and 10 m cumulative shear zone width, for example, the predicted strain rates are on the order of 10^{-10} s^{-1}.

6.4.3 High-stress dislocation glide-controlled deformation

The heterogeneous type C microstructure occurs sporadically in older vein generations concordant to the foliation (Figs. 6.4 and 5) and few young discordant veins related to the extensional shear zone (Fig. 6.6). Sub-basal deformation lamellae and SWUE (Figs. 6.4c, d, 6.5a, e and 6b) reflect high-stress dislocation glide-controlled deformation with subsequent modification by recovery (e.g., McLaren & Hobbs, 1972; Christie & Ardell, 1974; Drury, 1993; Trepmann & Stöckhert, 2003, 2013; Vernooij & Langenhorst, 2005). Micro-shear zones in conjugate sets (Figs. 6.4a, b and 5) involve brittle and crystal-plastic mechanisms with formation of new grains by nucleation and growth (Trepmann et al., 2007; Kilian & Heilbronner, 2017) associated with subgrain rotation and strain-induced grain boundary migration (van Daalen et al., 1999; Ceccato et al., 2017; Trepmann et al., 2017) at greenschist facies conditions. In the type C microstructure, recrystallized grains are generally restricted to sites of localised high strain (i.e., along intragranular cracks and pre-existing grain boundaries, Figs. 6.5 and 6). Abundant low angle grain boundaries (Fig. 6.3e, f, h), subgrains of similar shape and size close to recrystallized grains (Fig. 6.6c) and new grain orientations scattering around the orientation of the host grain (Fig. 6.6f and g) indicate recrystallization with subgrain rotation and strain-induced grain-boundary migration (e.g., Stipp & Kunze, 2008; Ceccato et al., 2017; Trepmann et al., 2017). The sequence of dislocation glide-controlled and associated brittle deformation of quartz producing highly damaged zones, which are sites of subsequent formation of new grains is interpreted to reflect initially high and then relaxing stresses (Trepmann & Stöckhert, 2003; Trepmann et al., 2017), consistent to microstructures produced in deformation experiments at such stress histories (Hobbs, 1968; Trepmann et al., 2007). During high-stress dislocation glide controlled deformation (low-temperature plasticity, Peierls stress controlled glide), strain rates are too high at given temperature for effective concomitant dislocation climb, causing dislocation pile up with strain hardening and associated microcracking (e.g., Hobbs, 1968; Drury, 1993; White, 1996). The resulting localized high strain zones are sites of recrystallization during dislocation creep at subsequently relaxing stresses (e.g., Hobbs, 1968; Trepmann & Stöckhert, 2003; Trepmann et al., 2007, 2017). Because of the transient

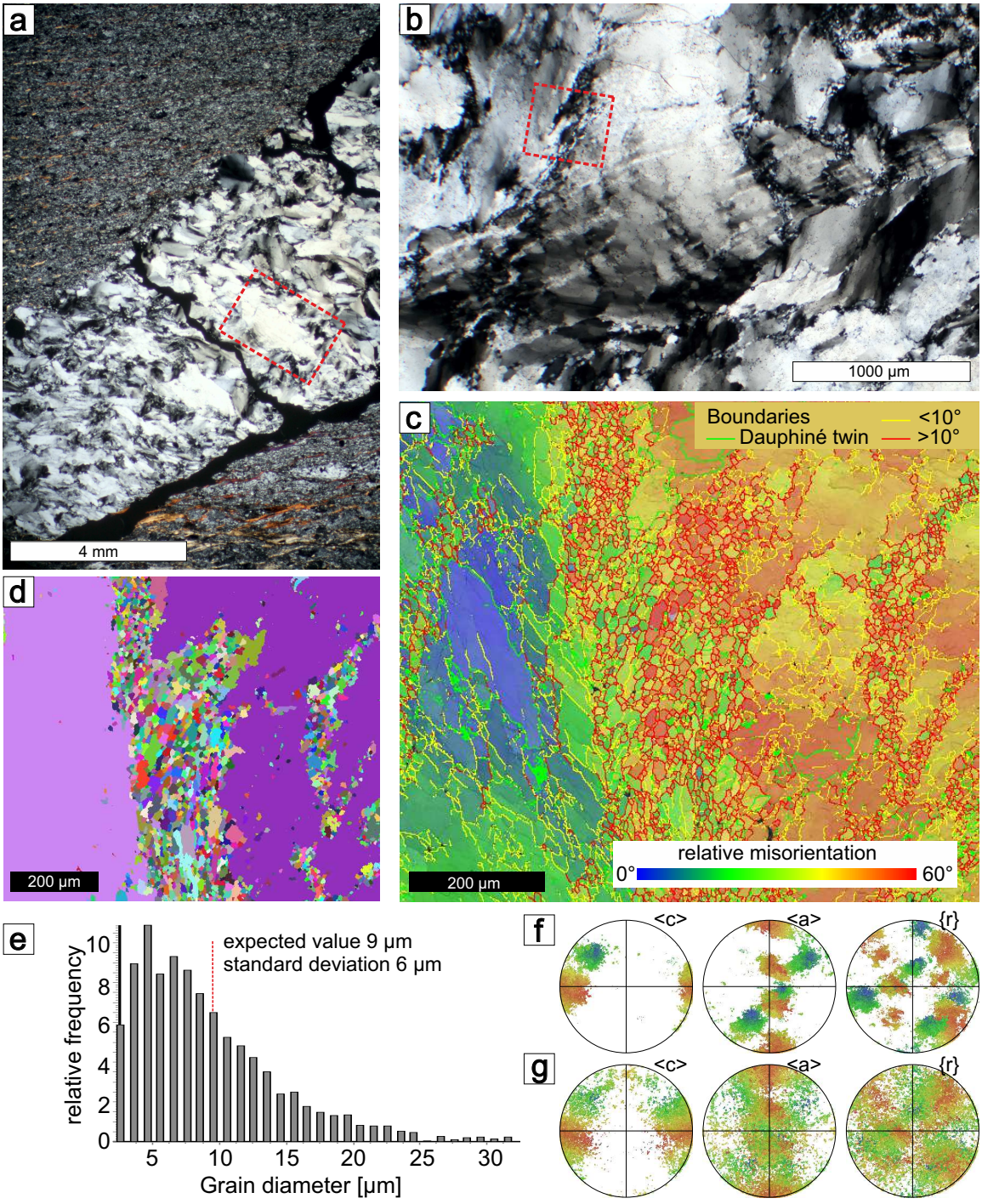

Fig. 6.6: Type C quartz microstructure of vein discordant to foliation in metasandstone (sample MB1, PQ s.str.). **a, b** Cross polarized light micrographs showing short-wavelength undulatory extinction and localized zones of recrystallized grains. Box in (a) shows close-up photograph in **b**, box in (b) is indicating area of the EBSD map in (c) and (d). **c** EBSD map with colour coding by relative misorientation angle (up to 60°) with respect to blue colour. Lines indicate Dauphiné twin boundaries (green), low-angle (yellow) and highangle (red) grain boundaries. **d** EBSD map of same area showing new grains in random colours. **e** Histogram of grain sizes of new grains. **f, g** Lower hemisphere stereographic projection of host grains and new grains, respectively.

nature of this deformation and relatively low strain, paleopiezometers are difficult to apply and they can at best record some arbitrary stage of stress relaxation after peak stresses (e.g., Trepmann & Stöckhert, 2003). However, at least as a very rough indicator of a lower stress bound, we can use the grain diameters of new grains in the micro-shear zones within the range of 7–10 mm (Figs. 6.5f and 6e). Following the paleopiezometer of Stipp & Tullis (2003), these grain diameters would indicate differential stresses within the given error range between 45 MPa and 400 MPa for the stage of recrystallization at already relaxed stresses. Initial dislocation-glide controlled deformation with the formation of deformation lamellae (Christie & Ardell, 1974; Drury, 1993; Trepmann & Stöckhert, 2003, 2013; Vernooij & Langenhorst, 2005), micro-shear zones (Trepmann et al., 2017) and Dauphiné twins (e.g., Pehl & Wenk, 2005; Wenk et al., 2006, 2011; Kjøll et al., 2015)would consistently indicate stresses of a few hundred MPa.

6.4.4 High (coseismic) stress-loading rates

The dominating microstructures indicative of low-stress, high-strain dissolution-precipitation creep of the host rocks and type A and B vein quartz microstructures are in marked contrast to the type C microstructure indicating high-stress, glide-controlled deformation. To explain the locally present evidence of high stresses we discuss two possibilities: (1) Stresses concentrated in monophase quartz layers representing high-viscosity layers in a low-viscosity matrix (e.g., Masuda et al., 1989; Trepmann & Stöckhert, 2009; Peters et al., 2016). If this would be the case, the type C microstructure should be much more common and dependent on the strain accumulated within the metasediments. This, however, has not been observed: The type C microstructure is not as common as the type A microstructure and can occur in veins both, concordant and discordant to the foliation. As such, it is not directly related to the high strain-rate by dissolution-precipitation creep of the metasediments in contrast to the crack-seal deformation indicated by the type A microstructure. (2) Stress-loading in the flowing metasediments occurred as consequence of seismic rupture in the overlying seismogenic zone (e.g., Sibson, 1977; Scholz, 1988, 2002), as simulated in numerical models by Ellis & Stöckhert (2004) and Nüchter & Ellis (2010, 2011). We argue that loading of the middle crust, which relieves shear stress by creep on the long term, to high differential stresses must be achieved rapidly, presumably by seismic activity in the overlying upper crust (Küster & Stöckhert, 1999; Trepmann & Stöckhert, 2003). Slow stress-built-up at the given temperatures and lithologies would result in high strain-rate dissolution-precipitation creep with type A crack-seal microstructures before reaching the stresses required for low-temperature plasticity of monophase quartz layers. During fast stress-loading rates, dissolution-precipitation creep of the metasediments cannot relax the stresses sufficiently fast, so that transient peak stresses can build up causing dislocation glide-controlled deformation and associated microcracking in the monophase quartz veins. The time scale of stress loading is characterized by the duration of the slip event along a fault, i.e., a few seconds to minutes, depending on the size of the fault and the seismic event (e.g., Wald & Heaton, 1994). Unfortunately, the microstructures in the Talea Ori do not provide good constraints on the peak stresses for coseismic deformation. In metagranites from the Sesia zone, Western Alps, peak stresses at the base of the seismogenic zone were estimated based on mechanical twinning of jadeite to be about 0.5 GPa or even higher

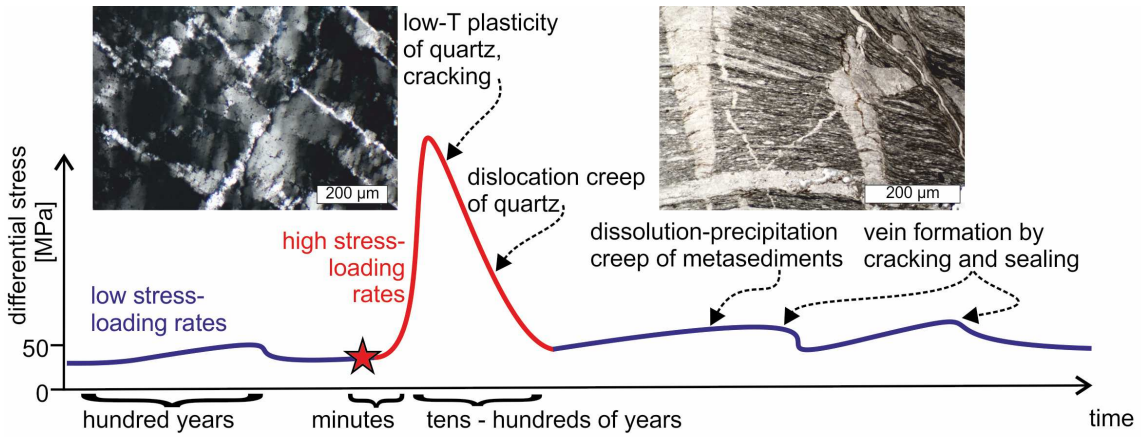

Fig. 6.7: Conceptual sketch showing the stress history during deformation of the host rock, see text for discussion.

(Trepmann & Stöckhert, 2001). Whereas the quartz microstructures in the associated metagranites (Trepmann & Stöckhert, 2003) are quite similar to the type C microstructure, the tectonic setting and the lithologies are very different. Yet, to our knowledge, it is the only estimate on the peak differential stress related to coseismic loading in the plastosphere at greenschist facies conditions. The microstructures suggest that dislocation creep with localized recrystallization of quartz is dominating stress relaxation after coseismic glide-controlled deformation at peak differential stress. Therefore, a flow law for dislocation creep can be used to infer the time scale of stress and strain rate relaxation assuming temperatures between 300 °C and 350 °C and initial peak stresses of for example 300 MPa to 500 MPa. For these temperature and stress conditions, strain rates suggested by the flow law of Paterson & Luan (1990), Eq. (6.1), are on the order of 10^{-11} s^{-1} to 10^{-12} s^{-1}. Assuming a Maxwell rheology, the relaxation time (2) for these conditions is between ten to few hundred years (Fig. 6.7). Although strain rates during initial dislocation glide-controlled deformation might have been transiently higher, the rapidly relaxing strain rates cause that the overall amount of strain by dislocation glide and creep is low in comparison to the low-stress, high-strain rate dissolution-precipitation creep of the host rock.

6.4.5 Quartz veins and the seismic cyle

Quartz veins with a high ratio of aperture to length have been attributed to coseismic deformation and sealing during postseismic creep (Henderson & McCaig, 1996; Nüchter & Stöckhert, 2007, 2008; Birtel & Stöckhert, 2008). There, however, vein formation is monogenetic and crystallization occurred in an open cavity as opposed to the crack-seal microstructures, observed here (Fig. 6.2c–e). Fagereng et al. (2018) discussed the occurrence of quartz veins formed by dehydration reactions during metamorphism at 470–550 °C to reflect tremors along the subduction thrust interface. Dissolution-precipitation creep at high strain rates causing internal stress loading and thus multiple crack-seal episodes, is not contradictory to such scenarios, on the contrary, it might be triggered or at least amplified by seismic stress pulses.

6.5 Conclusions and summary

The quartz microstructures type A and type B in veins associated to boudins, kink bands and shear bands in metasediments (Figs. 6.1, 6.2, 6.3a–c) reflect episodes of cracking and sealing during dissolution-precipitation creep of the host rock at temperatures close to peak metamorphic conditions of around 350 °C. The time scale to cause cyclic cracking and sealing is assumed lower than the Maxwell relaxation time of the metasediments undergoing dissolution-precipitation creep at strain rates of 10^{-10} s^{-1} to 10^{-9} s^{-1}, which are a few tens to hundred years (Fig. 6.7). The generally low amount of strain accumulated by dislocation creep of quartz in the host rock indicates that bulk stresses stayed below a few tens of MPa at the given temperature conditions on a long term. In some veins concordant or discordant to the foliation, the heterogeneous type C quartz microstructure is characterized by micro-shear zones, SWUE, sub-basal deformation lamellae and recrystallized grains restricted to high strain zones (Figs. 6.3d–f, 6.4, 6.5, 6.6). These microstructures indicate local and transient highstress dislocation-glide controlled deformation (low-T plasticity, Peierls stress-controlled glide) and subsequent dislocation creep at relaxing stresses. The indicated stresses of a few hundred MPa are explained by fast (coseismic) stress-loading rates resulting from a seismic slip event in the overlying seismogenic layer, i.e. on the time scale of seconds to minutes (Fig. 6.7). Stress relaxation is controlled by dislocation creep at rapidly decaying strain rates from initially about 10^{-11} s^{-1} to 10^{-12} s^{-1} at time scales of tens to hundred years. The overall amount of strain by dislocation glide and creep is low in comparison to the low-stress, high-strain rate dissolution-precipitation creep of the host rock. The study demonstrates that quartz microstructures are a powerful tool to distinguish different stress histories during deformation and to detect transient deformation caused by seismic activity.

7 Summary and conclusions

In this thesis, the deformation processes during burial and exhumation at subduction zones were investigated at the example of the HP-LT metamorphic sediments in the Talea Ori, central Crete, which belong to the lowermost tectonic units of the Cretan nappe pile. A detailed structural and lithologic mapping of the Talea Ori was carried out, supported by microstructural analysis and U-Pb dating of detrital zircons. As a prerequisite to interpret the deformation structures in the Talea Ori, the regional geology was resolved. A special focus was on controversially discussed siliciclastic metasediments in the contact area between the Talea Ori group – the lowermost nappe – and the overlying PQ s.str. Resolving the location of the contact between both nappes was problematic, since the rocks in the contact area are lithologically very similar and strongly deformed.

The mapping and U-Pb dating of detrital zircons confirm that the controversial association of black meta-quartzconglomerates, metasandstones, black shales and black metacherts (Bali formation), cropping out in the contact area to the PQ s.str., forms the stratigraphic base of the Talea Ori group. Main evidence is that the rock sequence with its type locality at Bali in the western Talea Ori is also exposed in the center of the large-scale anticline formed by the Talea Ori group in the eastern Talea Ori (Fig. 3.2). Consistently, U-Pb age data of detrital zircons showed that the Bali formation as well as the overlying Fodele and Sisses formations all show similar age spectra, which are systematically different from the age spectra of the PQ s.str. By the detailed mapping, sampling and analysis of approx. 300 thin-sections, the slight lithologic differences between the metasediments of the PQ s.str. and the Bali formation could be identified and the location of the contact between the PQ s.str. and the Talea Ori group could be resolved, shown in a new comprehensive geological map of the Talea Ori (Chapter 3, Fig. 3.2). The thesis confirms the so far ambiguously interpreted Olenekian biostratigraphic age of the PQ s.str. in central Crete, based on characteristic detrital zircon spectra of a quartzite of the PQ s.str. structurally underlying an Olenekian marble layer (Chapter 4, Section 4.4.1).

7.1 Ductile shear zone at the contact between Talea Ori group and PQ s.str.

The structural mapping of the area at the resolved contact between Talea Ori group and PQ s.str. showed that the deformation structures in the siliciclastic metasediments are very similar on both sides of the contact. The orientations of the main foliation, stretching lineation and fold axes are similar in both nappes and there are similar albite porphyroblasts with internal fabrics oblique to the external foliation. The main foliation developed at peak metamorphic conditions, which is indicated by aligned metamorphic muscovite and albite. Peak metamorphic temperatures on both sides of the contact are similar ranging from 370–410 °C according to the degree of graphitization of carbonaceous material, analysed by Raman spectroscopy. This is consistent with PT-determinations based on the mineral para-

genesis in earlier studies (Seidel et al., 1982; Theye, 1988; Theye et al., 1992). The similar structural inventory and peak metamorphic temperatures indicate a similar tectonometamorphic history of the Talea Ori group and the PQ s.str.

In the contact area, the main foliation is crosscut by extensional shear bands, normal faults, asymmetric boudinage and a high number of quartz veins associated to these structures, forming a kilometer-wide ductile shear zone along the ∼20 km long contact. At shear bands and normal faults the hanging block is systematically downfaulted. This is in contrast to earlier studies in which the deformation at the contact is associated to thrusting of the PQ s.str. onto the Talea Ori group (e.g., Chatzaras et al., 2006; Xypolias et al., 2007). The new observations show that deformation at the contact is characterized by an extensional ductile shear zone, along which the PQ s.str. is downfaulted with respect to the Talea Ori group.

The main strain in the shear zone is accommodated by dissolution-precipitation creep of mica-rich siliciclastic metasediments. In quartz veins and quartz-rich metasediments, locally microstructures indicate dislocation-creep but the overall amount of strain by dislocation-creep is low in comparison to the amount of strain taken up by dissolution-precipitation creep. This finding indicates low bulk stress conditions, which is consistent with findings from other exhumed HP-LT metamorphic rocks (e.g., Wassmann & Stöckhert, 2013). The high number of quartz veins within the ductile shear zone are associated to the ductile deformation (Section 6.3.1), indicating that high strain-rate dissolution precipitation creep was accompanied by cyclic cracking and sealing in timescales on the order of ten to hundred years, according to their Maxwell relaxation time (Section 6.4.2; Trepmann & Seybold, 2019). This is consistent with observations by Ujiie et al. (2018a) who determined a minimum time interval of a few years for the recurrence of crack-seal events that formed quartz veins coeval to deformation of the host rock by dissolution-precipitation creep. The authors determined the recurrence time based on a kinetic model for quartz precipitation and the width between inclusion bands, indicating different crack-seal intervals.

The shear zone was activated after peak metamorphism but still at elevated temperatures. This is indicated firstly because the main foliation, which developed at peak metamorphic conditions, is crosscut by the ductile shear bands and shear band cleavages. Secondly, near peak metamorphic temperatures (300–350 °C) during formation of the shear bands are indicated by microstructures in some of the associated quartz veins, recording recovery and strain-induced grain boundary migration. In conclusion this means that the shear zone was activated in an early stage of exhumation from ∼30 km depth. Since also a high number of discordant quartz veins do not indicate temperatures > 300 °C and there is a gradual transition between ductile shear bands and brittle normal faults, with normal faulting in the same orientation as the shear bands, the shear zone activity may also have continued under brittle conditions.

The ductile deformation structures of HP-LT metamorphic rocks in Western Crete are reported to have formed during peak metamorphic conditions, whereas ductile deformation during burial or during exhumation has not been observed so far (Stöckhert et al., 1999). In contrast, in the Talea Ori, the deformation during exhumation is recorded, with strain localizing during the early stages of exhumation in a km-wide ductile shear zone within the HP-LT metamorphic rocks.

7.2 High stresses in a low bulk stress environment

In contrast to the main deformation by dissolution-precipitation creep under low bulk stress conditions, microstructures in some of the quartz veins as well as in quartz rich host rocks locally indicate high stresses. These microstructures are micro-shear zones in conjugated sets, subbasal deformation lamellae and short-wavelength undulatory extinction, indicating dislocation-glide controlled deformation and microcracking associated to high stresses with subsequent stress-relaxation and recrystallization. An internal stress loading causing these high stresses, by for example stress concentration due to viscosity contrast, is unlikely because the microstructures in question occur in several quartz veins, but not in all quartz veins, and independent from the rheology and accumulated strain within the host rock. Therefore, the high-stress-microstructures are interpreted to result from external coseismic stress-loading induced by seismicity in the overlying seismogenic zone. In conclusion, assuming the time-scale of an earthquake the time-scale for stress-loading would be on the order of several minutes. According to the concepts of Sibson (1977) and Scholz (1988), the ductile extensional shear zone is interpreted to represent the deep level of seismically active faults.

According to the record from HP-LT metamorphic rocks e.g. in western Crete, stress is supposed to be low in subduction channels, where deformation is dominated by dissolution-precipitation creep (e.g., Stöckhert et al., 1999; Wassmann & Stöckhert, 2013). The quartz microstructures in the Talea Ori indicate that, at least temporarily and locally restricted, high stresses occurred associated to rapid coseismic loading. This kind of episodic deformation leading to microcracking within a regime governed by dissolution-precipitation creep is consistent with frequent observations of mixed brittle-ductile behaviour in shear zones (e.g., Henderson & McCaig, 1996; Küster & Stöckhert, 1999; Trepmann et al., 2017; Fagereng et al., 2018; Ujiie et al., 2018a). Also, the observation of microstructures induced by stress-loading rate dependent episodic deformation is consistent with the high seismicity observed at subduction zones today.

7.3 Role of the ductile shear zone for exhumation

This study shows that the HP-LT metamorphic rocks in the Talea Ori were deformed by dissolution-precipitation creep, cracking and high-stress dislocation glide controlled deformation during exhumation. This is in contrast to existing exhumation models for Crete, in which all deformation during exhumation is supposed to be localized on two major faults at the bottom and top of an extruded coherent block of HP-LT metamorphic rocks (e.g., Ring & Reischmann, 2002). On Crete, the "Cretan detachment" was assumed to be the major normal sense shear zone at the top of the extruded block. However, this assumption has been questioned in recent studies (e.g. Klein et al., 2013; Ring & Yngwe, 2018). These studies report that the tectonic contact between the HP-LT metamorphic PQ s.l. and the overlying non-HP-metamorphic Tripolitza unit is a younger thrust fault post-dating the exhumation of the HP-LT metamorphic rocks. Klein et al. (2013) concluded that deformation during exhumation therefore may be localized within the lower HP-LT metamorphic nappes and proposed a combination of ductile thinning and ductile extrusion. This would be consistent with ductile shear zones that were active during exhumation within the HP-LT

metamorphic lower nappes, as observed in this study in the Talea Ori.

The amount of exhumation localized on the ductile shear zone in the Talea Ori, however, was probably rather low, since the nappes on both sides of the shear zone experienced similar peak metamorphic conditions and therefore a similar depth of burial. A small difference in burial is possible but lacking detailed information on metamorphic pressures, it cannot be detected.

Mineral paragenesis in the Talea Ori do not yield such detailed information on metamorphic pressures, but Raman-measurements of quartz inclusions may provide a possibility to collect information on the pressure development during subduction and exhumation, which could be interesting to pursue in future studies. Metamorphic albite grains in albite schists comprise quartz-inclusions in the discordant internal fabrics as well as inclusions concordant to the external foliation in their outer growth rims. Accordingly it may be possible to derive (1) the metamorphic pressure during early growth of the albite porphyroblasts and (2) the metamorphic pressure during later formation of the outer growth rims that took place during deformation by dissolution-precipitation creep and formation of the main foliation. Pressure determination by Raman-measurements has been done on quartz inclusions in garnet (Ashley et al., 2014) and may be possible in albite too, although the optical detection of inclusions is more difficult there because of the small difference in refraction index between albite and quartz.

7.4 Pre-Alpine tectonic development of the HP-LT metamorphic lower nappes

The metasediments in the Talea Ori record not only Alpine deformation, but they also yield information on the pre-Alpine tectonic development of the Eastern Mediterranean. Lithologically similar rocks to the upper carbonatic formations of the Talea Ori group crop out in several places on Crete and the Peloponnesus and therefore the Talea Ori group is usually correlated with these units (Plattenkalk unit). The Plattenkalk unit is the most external unit of the Hellenides and its basement is unknown. The similar litho- and biofacies of the respective platy marbles with cherts indicate that the rocks of the Plattenkalk unit and the upper Talea Ori group formed in a similar depositional environment in Jurassic to Eocene times. The deposition area for these carbonatic rocks is generally assumed to restore at the northern margin of Gondwana in the southwestern Paleotethys.

The new detrital zircon data of the Talea Ori group indicate, however, a source in the internal zones of the Variscan orogen, delivering sediment from Late Carboniferous/Early Permian to Olenekian times. Therefore, a possible source region for the Talea Ori group metasediments is the southern margin of Eurasia (Sakarya Zone) but also still unknown westerly sources may be possible. Sediment transport to an origin at the northern margin of Gondwana is nevertheless possible assuming different alternatives or a combination of them, including long-distance sediment transport and eastward terrane-displacement. Also, a more northerly paleogeographic origin of the Talea Ori group cannot be excluded, however in this case the association of the Talea Ori group to the Plattenkalk unit has to be reconsidered.

These new data and suggested alternatives of the paleogeographic configuration of the

lower nappes of the Cretan nappe pile can have an impact on further paleogeographic reconstructions, as the Talea Ori group is an important area for paleotectonic reconstruction in the complicated Eastern Mediterranean region.

7.5 Conclusions

The geological record of the Talea Ori gives new insight into an Alpine subduction wedge as well as into the pre-Alpine tectonic development of the Eastern Mediterranean. The main conclusions from this record can be summarized as follows:

- The Alpine deformation record in the Talea Ori differs characteristically from Western Crete, where only ductile deformation at peak metamorphic conditions has been observed so far. In contrast, in the Talea Ori, additionally to deformation at peak metamorphic conditions also ductile deformation during exhumation is recorded.
- The Talea Ori group and the PQ s.str. have a similar tectonometamorphic history and the deformation at their contact is mainly due to downfaulting of the PQ s.str. during exhumation and updoming of the Talea Ori group.
- The main deformation mechanism in the siliciclastic metasediments is dissolution-precipitation creep accompanied by cyclic cracking and sealing. Transient local high stresses were induced in the ductile shear zone in an early stage of exhumation, presumably by coseismic stress loading due to seismic activity in the overlying seismogenic zone.
- From the Late Carboniferous/Early Permian to Olenekian times, sediment was transported from source areas in the internal zones of the Variscan orogen. Based on possible source areas at the southern amrgin of Eurasia and unidentified westerly sources, different alternative scenarios are possible for the paleogeographic origin of the Talea Ori group, which have to be tested further.

Bibliography

Abdelsalam, M. G., Liégeois, J.-P., & Stern, R. J. (2002). The Saharan metacraton. *Journal of African Earth Sciences*, 34(3-4), 119–136.

Ague, J. (1995). Deep crustal growth of quartz, kyanite and garnet into large-aperture, fluid-filled fractures, north-eastern Connecticut, USA. *Journal of Metamorphic Geology*, 13(2), 299–314.

Ague, J. J. (1994). Mass transfer during Barrovian metamorphism of pelites, south-central Connecticut; II, Channelized fluid flow and the growth of staurolite and kyanite. *American Journal of Science*, 294(9), 1061–1134.

Alexopoulos, A., Hang, H., & Krahl, J. (2000). First Nummulites from the "Plattenkalk" sequence in the Lefka Ori, west Crete. *Ann. Geol. Pays Hell*, 38, 117–121.

Anders, B., Reischmann, T., & Kostopoulos, D. (2007). Zircon geochronology of basement rocks from the Pelagonian Zone, Greece: constraints on the pre-Alpine evolution of the westernmost Internal Hellenides. *International Journal of Earth Sciences*, 96(4), 639–661.

Ashley, K. T., Steele-MacInnis, M., & Caddick, M. J. (2014). QuIB Calc: A MATLAB® script for geobarometry based on Raman spectroscopy and elastic modeling of quartz inclusions in garnet. *Computers & geosciences*, 66, 155–157. https://doi.org/10.1016/j.cageo.2014.01.005.

Avigad, D., Gerdes, A., Morag, N., & Bechstädt, T. (2012). Coupled U–Pb–Hf of detrital zircons of Cambrian sandstones from Morocco and Sardinia: implications for provenance and Precambrian crustal evolution of North Africa. *Gondwana Research*, 21(2-3), 690–703.

Avigad, D., Kolodner, K., McWilliams, M., Persing, H., & Weissbrod, T. (2003). Origin of northern Gondwana Cambrian sandstone revealed by detrital zircon SHRIMP dating. *Geology*, 31(3), 227–230.

Aysal, N., Öngen, S., Peytcheva, I., & Keskin, M. (2012a). Origin and evolution of the Havran Unit, Western Sakarya basement (NW Turkey): new LA-ICP-MS U-Pb dating of the metasedimentary-metagranitic rocks and possible affiliation to Avalonian microcontinent. *Geodinamica Acta*, 25(3-4), 226–247.

Aysal, N., Ustaömer, T., Öngen, S., Keskin, M., Köksal, S., Peytcheva, I., & Fanning, M. (2012b). Origin of the Early-Middle Devonian magmatism in the Sakarya Zone, NW Turkey: Geochronology, geochemistry and isotope systematics. *Journal of Asian Earth Sciences*, 45, 201 – 222, doi:https://doi.org/10.1016/j.jseaes.2011.10.011.

Balen, D., Horvath, P., Tomljenović, B., Finger, F., Humer, B., Pamic, J., & Arkai, P. (2006). A record of pre-Variscan Barrovian regional metamorphism in the eastern part of the Slavonian Mountains (NE Croatia). *Mineralogy and Petrology*, 87(1-2), 143–162.

Baud, A., Marcoux, J., Guiraud, R., Ricou, L., & Gaetani, M. (1993). *Late Murgabian (266 to 264 Ma) Paleoenvironment Map, explanatory notes*, (pp. 9–20). Gauthier-Villars, Paris.

Bea, F., Montero, P., Talavera, C., Abu Anbar, M., Scarrow, J. H., Molina, J. F., & Moreno, J. A. (2010). The palaeogeographic position of Central Iberia in Gondwana during the Ordovician: evidence from zircon chronology and Nd isotopes. *Terra Nova*, 22(5), 341–346.

Be'eri-Shlevin, Y., Eyal, M., Eyal, Y., Whitehouse, M. J., & Litvinovsky, B. (2012). The Sa'al volcano-sedimentary complex (Sinai, Egypt): a latest Mesoproterozoic volcanic arc in the northern Arabian Nubian Shield. *Geology*, 40(5), 403–406.

Be'eri-Shlevin, Y., Katzir, Y., & Whitehouse, M. (2009a). Post-collisional tectonomagmatic evolution in the northern Arabian–Nubian Shield: time constraints from ion-probe U–Pb dating of zircon. *Journal of the Geological Society*, 166(1), 71–85.

Be'eri-Shlevin, Y., Katzir, Y., Whitehouse, M. J., & Kleinhanns, I. C. (2009b). Contribution of pre Pan-African crust to formation of the Arabian Nubian Shield: New secondary ionization mass spectrometry U-Pb and O studies of zircon. *Geology*, 37(10), 899–902.

Beyssac, O., Goffé, B., Chopin, C., & Rouzaud, J. (2002). Raman spectra of carbonaceous material in metasediments: a new geothermometer. *Journal of metamorphic Geology*, 20(9), 859–871.

Birtel, S. & Stöckhert, B. (2008). Quartz veins record earthquake-related brittle failure and short term ductile flow in the deep crust. *Tectonophysics*, 457(1-2), 53–63.

Blumor, T., Dollinger, J., Mutter, A., Zarda, S., Kowalczyk, G., et al. (1994). Plattenkalk Series and Kastania phyllites of the Taygetos Mts.: New results on structure and succession= Οι σειρές πλακωδών ασβεστολίθων και οι φυλλίτες της Καστανιάς του όρους Ταϋγετος: νέα αποτελέσματα επί της δομής και διαδοχής. *Δελτίον της Ελληνικής Γεωλογικής Εταιρίας*, 30(2), 83–92.

Bonneau, M. (1984). Correlation of the Hellenide nappes in the south-east Aegean and their tectonic reconstruction. *Geological Society, London, Special Publications*, 17(1), 517–527.

Bons, P. D., Elburg, M. A., & Gomez-Rivas, E. (2012). A review of the formation of tectonic veins and their microstructures. *Journal of Structural Geology*, 43, 33–62.

Bowes, D. & Aftalion, M. (1991). U-Pb zircon isotopic evidence for early Ordovician and late Proterozoic units in the Mariánské Lázně Complex, Central-European Hercynides. *Neues Jahrbuch fur Mineralogie-Monatshefte*, 7, 315–326.

Brätz, H. (2000). *Radiometrische Altersdatierungen und geochemische Untersuchungen von Orthogneisen, Graniten und Granitporphyren aus dem Ruhlaer Kristallin, Mitteldeutsche Kristallinzone*. Thesis, Julius-Maximilians-Universität Würzburg.

Candan, O., Akal, C., Koralay, O., Okay, A., Oberhänsli, R., Prelević, D., & Mertz-Kraus, R. (2016). Carboniferous granites on the northern margin of Gondwana, Anatolide-Tauride Block, Turkey–Evidence for southward subduction of Paleotethys. *Tectonophysics*, 683, 349–366.

Ceccato, A., Pennacchioni, G., Menegon, L., & Bestmann, M. (2017). Crystallographic control and texture inheritance during mylonitization of coarse grained quartz veins. *Lithos*, 290-29, 210 – 227. `https://doi.org/10.1016/j.lithos.2017.08.005`.

Champod, E. & Vandelli, A. (2010). Stampfli field CourSe Tectonostratigraphy and plate tectonics of Crete.

Chatzaras, V., Dörr, W., Gerdes, A., Krahl, J., Xypolias, P., & Zulauf, G. (2016). Tracking the late Paleozoic to early Mesozoic margin of northern Gondwana in the Hellenides: paleotectonic constraints from U–Pb detrital zircon ages. *International Journal of Earth Sciences*, 105(7), 1881–1899.

Chatzaras, V., Xypolias, P., & Doutsos, T. (2006). Exhumation of high-pressure rocks under continuous compression: a working hypothesis for the southern Hellenides (central Crete, Greece). *Geological Magazine*, 143(6), 859–876.

Christie, J. & Ardell, A. (1974). Substructures of deformation lamellae in quartz. *Geology*, 2(8), 405–408.

Cox, S. & Etheridge, M. (1983). Crack-seal fibre growth mechanisms and their significance in the development of oriented layer silicate microstructures. *Tectonophysics*, 92(1-3), 147–170.

Crasquin-Soleau, S., Vaslet, D., & Le Nindre, Y.-M. (2006). Ostracods of the Permian-Triassic Khuff Formation, Saudi Arabia: palaeoecology and palaeobiogeography. *GeoArabia*, 11(1), 55–76.

Creutzburg, N. & Seidel, E. (1975). Zum Stand der Geologie des Präneogens auf Kreta. *Neues Jahrbuch für Geologie und Paläontologie Abhandlungen*, 198, 363–383.

Da Silva, Í. D., Fernández, R. D., Díez-Montes, A., Clavijo, E. G., & Foster, D. A. (2016). Magmatic evolution in the N-Gondwana margin related to the opening of the Rheic Ocean—evidence from the Upper Parautochthon of the Galicia-Trás-os-Montes Zone and from the Central Iberian Zone (NW Iberian Massif). *International Journal of Earth Sciences*, 105(4), 1127–1151.

Deckert, C., Plank, M., Seidel, M., & Zacher, W. (1999). Die metamorphen Decken des Taygetos-Gebirges (Peloponnes) und ihre Korrelation mit den metamorphen Einheiten auf Kreta–Neugliederung, Vergleiche und Denkmodelle. *Zeitschrift der Deutschen Geologischen Gesellschaft*, (pp. 133–158).

Dercourt, J., Ricou, L. E., & Vrielynck, B., Eds. (1993). *Atlas Tethys Palaeoenvironmental Maps: Explanatory Notes. Liste Des Articles, Communications, Cartes Et Thèses. Programme GS-Téthys, 1986-1993*. Gauthier-Villars.

Dombrowski, A., Okrusch, M., Richter, P., Henjes-Kunst, F., Höhndorf, A., & Kröner, A. (1995). Orthogneisses in the Spessart Crystalline Complex, north-west Bavaria: Silurian granitoid magmatism at an active continental margin. *Geologische Rundschau*, 84(2), 399–411.

Dornsiepen, U. F. & Manutsoglu, E. (1994). Zur Gliederung der Phyllit-Decke Kretas und des Peloponnes. *Zeitschrift der Deutschen Geologischen Gesellschaft*, 145, 286–304.

Dornsiepen, U. F., Manutsoglu, E., & Mertmann, D. (2001). Permian–Triassic palaeogeography of the external Hellenides. *Palaeogeography, Palaeoclimatology, Palaeoecology*, 172(3), 327–338.

Dörr, W., Fiala, J., Vejnar, Z., & Zulauf, G. (1998). U–Pb zircon ages and structural development of metagranitoids of the Teplá crystalline complex: evidence for pervasive Cambrian plutonism within the Bohemian massif (Czech Republic). *Geologische Rundschau*, 87(1), 135–149.

Doutsos, T., Koukouvelas, I., Poulimenos, G., Kokkalas, S., Xypolias, P., & Skourlis, K. (2000). An exhumation model of the south Peloponnesus, Greece. *International Journal of Earth Sciences*, 89(2), 350–365.

Drost, K., Gerdes, A., Jeffries, T., Linnemann, U., & Storey, C. (2011). Provenance of Neoproterozoic and early Paleozoic siliciclastic rocks of the Teplá-Barrandian unit (Bohemian Massif): evidence from U–Pb detrital zircon ages. *Gondwana Research*, 19(1), 213–231.

Dörr, W., Zulauf, G., Gerdes, A., Lahaye, Y., & Kowalczyk, G. (2015). A hidden Tonian basement in the eastern Mediterranean: Age constraints from U–Pb data of magmatic and detrital zircons of the External Hellenides (Crete and Peloponnesus). *Precambrian Research*, 258, 83 – 108. `https://doi.org/10.1016/j.precamres.2014.12.015`.

Drury, M. (1993). Deformation lamellae in metals and minerals. *Defects and processes in the solid state: Geoscience applications: McLaren volume: Amsterdam, The Netherlands, Elsevier*, (pp. 195–212).

Durney, D. (1973). Incremental strains measured by syntectonic crystal growths. *Gravity and tectonics*, (pp. 67–96).

Ellis, S., Beavan, J., Eberhart-Phillips, D., & Stöckhert, B. (2006). Simplified models of the Alpine Fault seismic cycle: stress transfer in the mid-crust. *Geophysical Journal International*, 166(1), 386–402.

Ellis, S. & Stöckhert, B. (2004). Elevated stresses and creep rates beneath the brittle-ductile transition caused by seismic faulting in the upper crust. *Journal of Geophysical Research: Solid Earth*, 109(B5).

Engel, M. & Reischmann, T. (1998). Single zircon geochronology of orthogneisses from Paros, Greece. *Δελτίον της Ελληνικής Γεωλογικής Εταιρίας*, 32(3), 91–99.

Engel, M. & Reischmann, T. (1999). Geochronology of the pre-alpine basement of the central Cyclades, Greece. In *Journal of Conference Abstracts*, volume 4 (pp. 806).

Epting, M., Kudrass, H., Leppig, U., & Schäfer, A. (1972). Geologie der Talea Ori/Kreta. *Neues Jahrbuch für Geologie und Paläontologie, Abhandlungen*, 141(3), 259–285.

Fagereng, Å., Remitti, F., & Sibson, R. (2011). Incrementally developed slickenfibers — Geological record of repeating low stress-drop seismic events? *Tectonophysics*, 510(3), 381 – 386. `https://doi.org/10.1016/j.tecto.2011.08.015`.

Fagereng, Å. & Toy, V. G. (2011). Geology of the earthquake source: an introduction. *Geological Society, London, Special Publications*, 359(1), 1–16.

Fagereng, k., Diener, J. F., Meneghini, F., Harris, C., & Kvadsheim, A. (2018). Quartz vein formation by local dehydration embrittlement along the deep, tremorgenic subduction thrust interface. *Geology*, 46(1), 67–70.

Fagereng, k. & Sibson, R. H. (2010). Melange rheology and seismic style. *Geology*, 38(8), 751–754.

Famin, V., Philippot, P., Jolivet, L., & Agard, P. (2004). Evolution of hydrothermal regime along a crustal shear zone, Tinos Island, Greece. *Tectonics*, 23(5).

Fassoulas, C., Kilias, A., & Mountrakis, D. (1994). Postnappe stacking extension and exhumation of high-pressure/low-temperature rocks in the island of Crete, Greece. *Tectonics*, 13(1), 127–138.

Feldhoff, R., Theye, T., & Richter, D. (1993). Coal rank versus illite crystallinity and estimated P-T conditions: some problems concerning the Pindos, Tripolitza and phyllite-quartzite series in Crete. *Bulletin of the Geological Society of Greece*, 28(3), 603.

Fisher, D. & Byrne, T. (1990). The character and distribution of mineralized fractures in the Kodiak Formation, Alaska: implications for fluid flow in an underthrust sequence. *Journal of Geophysical Research: Solid Earth*, 95(B6), 9069–9080.

Fisher, D. M. & Brantley, S. L. (1992). Models of quartz overgrowth and vein formation: deformation and episodic fluid flow in an ancient subduction zone. *Journal of Geophysical Research: Solid Earth*, 97(B13), 20043–20061.

Fisher, D. M., Brantley, S. L., Everett, M., & Dzvonik, J. (1995). Cyclic fluid flow through a regionally extensive fracture network within the Kodiak accretionary prism. *Journal of Geophysical Research: Solid Earth*, 100(B7), 12881–12894.

Frei, D. & Gerdes, A. (2009). Precise and accurate in situ U–Pb dating of zircon with high sample throughput by automated LA-SF-ICP-MS. *Chemical Geology*, 261(3-4), 261–270.

Friedl, G., Finger, F., Paquette, J.-L., von Quadt, A., McNaughton, N. J., & Fletcher, I. R. (2004). Pre-Variscan geological events in the Austrian part of the Bohemian Massif deduced from U–Pb zircon ages. *International Journal of Earth Sciences*, 93(5), 802–823.

Fytrolakis, N. (1972). Die Einwirkung gewisser orogener Bewegungen und die Gipsbildung in Ostkreta (Prov. Sitia). *Neues Jahrbuch für Geologie und Palaontologie, Abhandlungen*, 9, 81–100.

Gerogiannis, N. & Xypolias, P. (2017). Retroward extrusion of high-pressure rocks: An example from the Hellenides (Pelion Blueschist Nappe, NW Aegean). *Terra Nova*, 29, doi:10.1111/ter.12297.

Golonka, J., Gahagan, L., Krobicki, M., Marko, F., Oszczypko, N., et al. (2006). *Plate-tectonic evolution and paleogeography of the circum-Carpathian region*, chapter 2, (pp. 11–46). AAPG Special Volumes.

Goncuoglu, M. C., et al. (2007). The Mississippian in the Central and Eastern Taurides (Turkey): constraints on the tectonic setting of the Tauride-Anatolide Platform. *Geologica Carpathica Bratislava*, 58(5), 427.

Greiling, R. (1982). The metamorphic and structural evolution of the Phyllite-Quartzite nappe of western Crete. *Journal of Structural Geology*, 4(3), 291–297.

Guillot, S., Hattori, K., Agard, P., Schwartz, S., & Vidal, O. (2009). Exhumation processes in oceanic and continental subduction contexts: a review. In *Subduction zone geodynamics* (pp. 175–205). Springer, 978-3-540-87971-8.

Haas, J., et al. (2011). Jurassic Evolution of the Tectonostratigraphic Units of the Circum-Pannonian Region. *Jahrbuch der Geologischen Bundesanstalt, Wien*, 151(3-4), 281–354.

Hall, R. & Audley-Charles, M. (1983). The structure and regional significance of the Talea Ori, Crete. *Journal of Structural Geology*, 5(2), 167–179.

Henderson, I. & McCaig, A. (1996). Fluid pressure and salinity variations in shear zone-related veins, central Pyrenees, France: implications for the fault-valve model. *Tectonophysics*, 262(1-4), 321–348.

Hilgers, C., Dilg-Gruschinski, K., & Urai, J. L. (2003). Microstructures grown experimentally from advectivesupersaturated solution and their implication for natural vein systems. *Journal of Geochemical Exploration*, 78, 221–225.

Hilgers, C., Koehn, D., Bons, P., & Urai, J. (2001). Development of crystal morphology during unitaxial growth in a progressively widening vein: II. Numerical simulations of the evolution of antitaxial fibrous veins. *Journal of Structural Geology*, 23(6-7), 873–885.

Hilgers, C. & Urai, J. L. (2002). Experimental study of syntaxial vein growth during lateral fluid flow in transmitted light: first results. *Journal of Structural Geology*, 24(6-7), 1029–1043.

Himmerkus, F., Anders, B., Reischmann, T., & Kostopoulos, D. (2007). Gondwana-derived terranes in the northern Hellenides. *MEMOIRS-GEOLOGICAL SOCIETY OF AMERICA*, 200, 379.

Himmerkus, F., Reischmann, T., & Kostopoulos, D. (2006). Late Proterozoic and Silurian basement units within the Serbo-Macedonian Massif, northern Greece: the significance of terrane accretion in the Hellenides. *Geological Society, London, Special Publications*, 260(1), 35–50.

Himmerkus, F., Reischmann, T., & Kostopoulos, D. (2009). Serbo-Macedonian revisited: a Silurian basement terrane from northern Gondwana in the Internal Hellenides, Greece. *Tectonophysics*, 473(1-2), 20–35.

Hobbs, B. (1968). Recrystallization of single crystals of quartz. *Tectonophysics*, 6(5), 353–401.

Hobbs, B., Ord, A., & Teyssier, C. (1986). Earthquakes in the ductile regime? *Pure and Applied Geophysics*, 124(1-2), 309–336.

Jackson, S. E., Pearson, N. J., Griffin, W. L., & Belousova, E. A. (2004). The application of laser ablation-inductively coupled plasma-mass spectrometry to in situ U–Pb zircon geochronology. *Chemical Geology*, 211(1-2), 47–69.

Jacobshagen, V., Dürr, S., Kockel, F., Kopp, K., Kowalczyk, G., Berckhemer, H., & Büttner, D. (1978). *Structure and geodynamic evolution of the Aegean region*, volume 38, (pp. 455–477). Schweizerbart Stuttgart, 3510650832.

Jacobshagen, V., Dürr, S., Kockel, F., Makris, J., Dornsiepen, U. F., Giese, P., & Wallbrecher, E. (1986). *Geologie von Griechenland*. Beiträge zur regionalen Geologie der Erde, Band 19. Borntraeger Berlin-Stuttgart, 3443110192.

Janots, E., Engi, M., Berger, A., Allaz, J., Schwarz, J.-O., & Spandler, C. (2008). Prograde metamorphic sequence of REE minerals in pelitic rocks of the Central Alps: implications for allanite–monazite–xenotime phase relations from 250 to 610 C. *Journal of Metamorphic Geology*, 26(5), 509–526.

Johnson, P. R. & Woldehaimanot, B. (2003). Development of the Arabian-Nubian Shield: perspectives on accretion and deformation in the northern East African Orogen and the assembly of Gondwana. *Geological Society, London, Special Publications*, 206(1), 289–325.

Johnson, R. B. & DeGraff, J. V. (1988). *Principles of engineering geology*. Wiley, 0471034363.

Jolivet, L., et al. (2013). Aegean tectonics: Strain localisation, slab tearing and trench retreat. *Tectonophysics*, 597, 1–33.

Jolivet, L., Goffé, B., Monié, P., Truffert-Luxey, C., Patriat, M., & Bonneau, M. (1996). Miocene detachment in Crete and exhumation P-T-t paths of high-pressure metamorphic rocks. *Tectonics*, 15(6), 1129–1153.

Katsiavrias, N., Papazeti, E., Tsaila-Monopoli, S., Lappas, I., & Antonakos, A. (2008). Geological map of Anoyia, Crete, 1:50.000.

Kilian, R. & Heilbronner, R. (2017). Analysis of crystallographic preferred orientations of experimentally deformed Black Hills Quartzite. *Solid Earth*, 8(5), 1095–1117. `https://doi.org/10.5194/se-8-1095-2017`.

Kilias, A., Fassoulas, C., & Mountrakis, D. (1994). Tertiary extension of continental crust and uplift of Psiloritis metamorphic core complex in the central part of the Hellenic Arc (Crete, Greece). In *Active Continental Margins—Present and Past* (pp. 417–430). Springer, 3662377093.

Kjøll, H., Viola, G., Menegon, L., & Sørensen, B. (2015). Brittle-viscous deformation of vein quartz under fluid-rich lower greenschist facies conditions. *Solid Earth*, 6(2), 681.

Klein, T., Craddock, J., & Zulauf, G. (2013). Constraints on the geodynamical evolution of Crete: insights from illite crystallinity, Raman spectroscopy and calcite twinning above and below the 'Cretan detachment'. *International Journal of Earth Sciences*, 102(1), 139–182.

Klein, T., Reichhardt, H., Klinger, L., Grigull, S., Wostal, G., Kowalczyk, G., & Zulauf, G. (2008). Reverse slip along the contact Phyllite-Quartzite Unit/Tripolitsa Unit in eastern Crete: implications for the geodynamic evolution of the External Hellenides. [Kontraktive Tektonik entlang des Kontakts von Phyllit-Quarzit-und Tripolitsa-Einheit in Ostkreta: Folgen für die geodynamische Entwicklung der Externen Helleniden.]. *Zeitschrift der deutschen Gesellschaft füer Geowissenschaften*, 159(3), 375–398.

König, H. & Kuss, S. (1980). Neue Daten zur Biostratigraphie des permotriadischen Autochthons der Insel Kreta (Griechenland). *Neues Jahrbuch für Geologie und Paläontologie, Monatshefte*, 9, 525–540.

Kock, S., Martini, R., Reischmann, T., & Stampfli, G. (2007). Detrital zircon and micropalaeontological ages as new constraints for the lowermost tectonic unit (Talea Ori unit) of Crete, Greece. *Palaeogeography, Palaeoclimatology, Palaeoecology*, 243(3), 307–321.

Koglin, N., Zeh, A., Franz, G., Schüssler, U., Glodny, J., Gerdes, A., & Brätz, H. (2018). From Cadomian magmatic arc to Rheic ocean closure: the geochronological-geochemical record of nappe protoliths of the Münchberg Massif, NE Bavaria (Germany). *Gondwana Research*, 55, 135–152.

Kolodner, K., Avigad, D., McWilliams, M., Wooden, J., Weissbrod, T., & Feinstein, S. (2006). Provenance of north Gondwana Cambrian–Ordovician sandstone: U–Pb SHRIMP dating of detrital zircons from Israel and Jordan. *Geological Magazine*, 143(3), 367–391.

Kowalczyk, G. & Dittmar, U. (1991). The metamorphics underlying the plattenkalk carbonates in the Taygetos mts (Southern Peloponnese). *Bulletin of the Geological Society of Greece*, 25(1), 455–467.

Kozur, H. & Krahl, J. (1987). Erster Nachweis von Radiolarien im tethyalen Perm Europas. *Neues Jahrbuch für Geologie und Paläontologie, Abhandlungen*, 174, 357–372.

Kozur, H. & Pjatakova, M. (1976). Die Conodontenart Anchignathodus parvus n. sp., eine wichtige Leitform der basalen Trias. *Koninklijk Nederlands Akademie van Wetenschappen-Amsterdam, Series B*, 79(2), 123–128.

Krahl, J. & Kauffmann, G. (2004). New aspects for a palinspastic model of the External Hellenides on Crete. In *5th Int. Symp. on Eastern Mediterranean Geology, Thessaloniki, Greece* (pp. 14–20).

Krahl, J., Kauffmann, G., Kozur, H., Richter, D., Förster, O., & Heinritzi, F. (1983). Neue Daten zur biostratigraphie und zur tektonischen lagerung der Phyllit-Gruppe und der Trypali-Gruppe auf der Insel Kreta (Griechenland). *Geologische Rundschau*, 72(3), 1147–1166.

Krahl, J., et al. (1986). Neue Fossilfunde in der Phyllit-Gruppe Ostkretas (Griechenland). *Zeitschrift der deutschen geologischen Gesellschaft*, (pp. 523–536).

Krahl, J., Richter, D., Förster, O., Kozur, H., & Hall, R. (1988). Zur Stellung der Talea Ori im Bau des kretischen Deckenstapels (Griechenland). *Zeitschrift der deutschen geologischen Gesellschaft*, (pp. 191–227).

Kröner, A., Jaeckel, P., Hegner, E., & Opletal, M. (2001). Single zircon ages and whole-rock Nd isotopic systematics of early Palaeozoic granitoid gneisses from the Czech and Polish Sudetes (Jizerské hory, Krkonoše Mountains and Orlice-Sněžník Complex). *International Journal of Earth Sciences*, 90(2), 304–324.

Kröner, A. & Stern, R. (2005). AFRICA| Pan-African orogeny. In *Encyclopedia of geology*, volume 1 (pp. 1–12). Amsterdam, Elsevier.

Küster, M. & Stöckhert, B. (1999). High differential stress and sublithostatic pore fluid pressure in the ductile regime—microstructural evidence for short-term post-seismic creep in the Sesia Zone, Western Alps. *Tectonophysics*, 303(1-4), 263–277.

Kuss, S. (1963). Erster Nachweis von permischen Fusulinen auf der Insel Kreta. *Praktika tēs Akadēmias Athēnōn*, 38, 431–436.

Kuss, S. (1973). Neue Fusulinenfunde in den Talea Ori/Kreta (Griechenland). *Berichte der Naturforschenden-Gesellschaft zu Freiburg im Breisgau*, 63, 73–79.

Kuss, S. (1982). Ein erster Ammonitenfund aus der Plattenkalk-Formation der Insel Kreta/Griechenland. *Bericht der Naturforschenden Gesellschaft zu Freiburg in Breisgau*, 71(72), 35–38.

Kuss, S. & Thorbecke, G. (1974). Die präneogenen Gesteine der Insel Kreta und ihre Korrelierbarkeit im ägäischen Raum. *Ber. Naturf. Ges. Freiburg I Br*, 64, 39–75.

Küster, D., Liégeois, J.-P., Matukov, D., Sergeev, S., & Lucassen, F. (2008). Zircon geochronology and Sr, Nd, Pb isotope geochemistry of granitoids from Bayuda Desert and Sabaloka (Sudan): evidence for a Bayudian event (920–900 Ma) preceding the Pan-African orogenic cycle (860–590 Ma) at the eastern boundary of the Saharan Metacraton. *Precambrian Research*, 164(1-2), 16–39.

Kydonakis, K., Kostopoulos, D., Poujol, M., Brun, J.-P., Papanikolaou, D., & Paquette, J.-L. (2014). The dispersal of the Gondwana Super-fan System in the eastern Mediterranean: New insights from detrital zircon geochronology. *Gondwana Research*, 25(3), 1230–1241.

Linnemann, U., Gerdes, A., Drost, K., & Buschmann, B. (2007). *The continuum between Cadomian orogenesis and opening of the Rheic Ocean: Constraints from LA-ICP-MS U-Pb zircon dating and analysis of plate-tectonic setting (Saxo-Thuringian zone, northeastern Bohemian Massif, Germany)*, volume 423, (pp. 61–96). Boulder, Colo.; Geological Society of America; 1999.

Linnemann, U., McNaughton, N. J., Romer, R. L., Gehmlich, M., Drost, K., & Tonk, C. (2004). West African provenance for Saxo-Thuringia (Bohemian Massif): did Armorica ever leave pre-Pangean Gondwana?–U/Pb-SHRIMP zircon evidence and the Nd-isotopic record. *International Journal of Earth Sciences*, 93(5), 683–705.

Linnemann, U., Ouzegane, K., Drareni, A., Hofmann, M., Becker, S., Gärtner, A., & Sagawe, A. (2011). Sands of West Gondwana: an archive of secular magmatism and plate interactions—a case study from the Cambro-Ordovician section of the Tassili Ouan Ahaggar (Algerian Sahara) using U–Pb–LA-ICP-MS detrital zircon ages. *Lithos*, 123(1-4), 188–203.

Linnemann, U., Pereira, F., Jeffries, T. E., Drost, K., & Gerdes, A. (2008). The Cadomian Orogeny and the opening of the Rheic Ocean: the diacrony of geotectonic processes constrained by LA-ICP-MS U–Pb zircon dating (Ossa-Morena and Saxo-Thuringian Zones, Iberian and Bohemian Massifs). *Tectonophysics*, 461(1-4), 21–43.

Lippolt, H. J. (1986). Nachweis altpaläozoischer Primäralter (Rb-Sr) und karbonischer Abkühlungsalter (K-Ar) der muskovit-biotit-gneise des Spessarts und der biotit-gneise des Böllsteiner Odenwaldes. *Geologische Rundschau*, 75(3), 569–583.

Lister, G. S., Banga, G., & Feenstra, A. (1984). Metamorphic core complexes of Cordilleran type in the Cyclades, Aegean Sea, Greece. *Geology*, 12(4), 221–225.

Lloyd, G. E. (2004). Microstructural evolution in a mylonitic quartz simple shear zone: the significant roles of dauphine twinning and misorientation. *Geological Society, London, Special Publications*, 224(1), 39–61.

Lougheed, M. & Mancuso, J. (1973). Hematite Framboids in the Negaunee Iron Formation, Michigan; evidence for Their Biogenic Origin. *Economic geology*, 68(2), 202–209.

Löwen, K., Bröcker, M., & Berndt, J. (2015). Depositional ages of clastic metasediments from Samos and Syros, Greece: results of a detrital zircon study. *International Journal of Earth Sciences*, 104(1), 205–220.

Löwen, K., Meinhold, G., Güngör, T., & Berndt, J. (2017). Palaeotethys-related sediments of the Karaburun Peninsula, western Turkey: constraints on provenance and stratigraphy from detrital zircon geochronology. *International Journal of Earth Sciences*, 106(8), 2771–2796.

Ludwig, K. (2001). Users manual for Isoplot/Ex (rev. 2.49): a geochronological toolkit for Microsoft Excel. *Berkeley Geochronology Center, Special Publication*, 1, 55.

Manutsoglu, E., Mertmann, D., Soujon, A., Dornsiepen, U., & Jacobshagen, V. (1995a). Zur Nomenklatur der Metamorphite auf der Insel Kreta, Griechenland. *Berliner geowiss. Abh E*, 16, 579–588.

Manutsoglu, E., Soujon, A., Reitner, J., & Dornsiepen, U. (1995b). Relics of lithistid demosponges from the metamorphic Plattenkalk Series of Crete island (Greece) and their paleobathymetric significance. *Neues Jahrbuch für Geologie und Paläontologie, Monatshefte*, (pp. 235–235).

Marcoux, J. & Baud, A. (1995). Late Permian to Late Triassic, Tethyan Paleoenvironments. In *The Tethys Ocean* (pp. 153–190). Springer.

Marsellos, A., Foster, D. A., Kamenov, G., & Kyriakopoulos, K. (2012). Detrital zircon U-Pb data from the Hellenic South Aegean belts: constraints on the age and source of the South Aegean basement. *Journal of the Virtual Explorer*, 42, 1–12.

Masuda, T., Shibutani, T., Igarashi, T., & Kuriyama, M. (1989). Microboudin structure of piedmontite in quartz schists: a proposal for a new indicator of relative palaeodifferential stress. *Tectonophysics*, 163(1-2), 169–180.

McClusky, S., et al. (2000). Global Positioning System constraints on plate kinematics and dynamics in the eastern Mediterranean and Caucasus. *Journal of Geophysical Research: Solid Earth*, 105(B3), 5695–5719.

McLaren, A. & Hobbs, B. (1972). Transmission electron microscope investigation of some naturally deformed quartzites. *Flow and fracture of rocks*, (pp. 55–66).

McLaren, A., Turner, R., Boland, J., & Hobbs, B. (1970). Dislocation structure of the deformation lamellae in synthetic quartz; a study by electron and optical microscopy. *Contributions to Mineralogy and Petrology*, 29(2), 104–115.

Meert, J. G. & Van Der Voo, R. (1997). The assembly of Gondwana 800-550 Ma. *Journal of Geodynamics*, 23(3-4), 223–235.

Meier, T., Becker, D., Endrun, B., Rische, M., Bohnhoff, M., Stöckhert, B., & Harjes, H.-P. (2007). A model for the Hellenic subduction zone in the area of Crete based on seismological investigations. *Geological Society, London, Special Publications*, 291(1), 183–199.

Meinhold, G., Kostopoulos, D., Frei, D., Himmerkus, F., & Reischmann, T. (2010). U–Pb LA-SF-ICP-MS zircon geochronology of the Serbo-Macedonian Massif, Greece: palaeotectonic constraints for Gondwana-derived terranes in the Eastern Mediterranean. *International Journal of Earth Sciences*, 99(4), 813–832.

Meinhold, G., et al. (2011). Evidence from detrital zircons for recycling of Mesoproterozoic and Neoproterozoic crust recorded in Paleozoic and Mesozoic sandstones of southern Libya. *Earth and Planetary Science Letters*, 312(1-2), 164–175.

Meinhold, G., Reischmann, T., Kostopoulos, D., Lehnert, O., Matukov, D., & Sergeev, S. (2008). Provenance of sediments during subduction of Palaeotethys: detrital zircon ages and olistolith analysis in Palaeozoic sediments from Chios Island, Greece. *Palaeogeography, Palaeoclimatology, Palaeoecology*, 263(3-4), 71–91.

Menegon, L., Piazolo, S., & Pennacchioni, G. (2011). The effect of Dauphiné twinning on plastic strain in quartz. *Contributions to Mineralogy and Petrology*, 161(4), 635–652.

Moix, P., Beccaletto, L., Kozur, H. W., Hochard, C., Rosselet, F., & Stampfli, G. M. (2008). A new classification of the Turkish terranes and sutures and its implication for the paleotectonic history of the region. *Tectonophysics*, 451(1-4), 7–39.

Montero, P., Bea, F., Zinger, T., Scarrow, J., Molina, J., & Whitehouse, M. (2004). 55 million years of continuous anatexis in Central Iberia: single-zircon dating of the Pena Negra Complex. *Journal of the Geological Society*, 161(2), 255–263.

Morag, N., Avigad, D., Gerdes, A., Belousova, E., & Harlavan, Y. (2011a). Crustal evolution and recycling in the northern Arabian-Nubian Shield: New perspectives from zircon Lu–Hf and U–Pb systematics. *Precambrian Research*, 186, 101–116, doi:10.1016/j.precamres.2011.01.004.

Morag, N., Avigad, D., Gerdes, A., Belousova, E., & Harlavan, Y. (2011b). Long-distance transport of North Gondwana Cambro-Ordovician sandstones: Evidence from detrital zircon Hf isotopic composition. In *Goldschmidt Conference Abstracts Mineralogical Magazine www.minersoc.org*.

Mukherjee, S. (2013a). *Deformation microstructures in rocks*. Springer, 3642256082.

Mukherjee, S. (2013b). Higher Himalaya in the Bhagirathi section (NW Himalaya, India): its structures, backthrusts and extrusion mechanism by both channel flow and critical taper mechanisms. *International Journal of Earth Sciences*, 102(7), 1851–1870.

Mukherjee, S. (2014a). *Atlas of shear zone structures in meso-scale*. Springer, 3319000888.

Mukherjee, S. (2014b). Review of flanking structures in meso-and micro-scales. *Geological Magazine*, 151(6), 957–974.

Mukherjee, S. (2017). Review on symmetric structures in ductile shear zones. *International Journal of Earth Sciences*, 106(5), 1453–1468.

Murphy, J. B., FernÁndez-SuÁrez, J., Jeffries, T., & Strachan, R. (2004a). U–Pb (LA–ICP-MS) dating of detrital zircons from Cambrian clastic rocks in Avalonia: erosion of a Neoproterozoic arc along the northern Gondwanan margin. *Journal of the Geological Society*, 161(2), 243–254.

Murphy, J. B., Fernández-Suárez, J., & Jeffries, T. E. (2004b). Lithogeochemical and Sm-Nd and U-Pb isotope data from the Silurian–Lower Devonian Arisaig Group clastic rocks, Avalon terrane, Nova Scotia: A record of terrane accretion in the Appalachian-Caledonide orogen. *Geological Society of America Bulletin*, 116(9-10), 1183–1201.

Nance, R. D., et al. (2008). Neoproterozoic-early Palaeozoic tectonostratigraphy and palaeogeography of the peri-Gondwanan terranes: Amazonian v. West African connections. *Geological Society, London, Special Publications*, 297(1), 345–383.

Nüchter, J.-A. & Ellis, S. (2010). Complex states of stress during the normal faulting seismic cycle: Role of midcrustal postseismic creep. *Journal of Geophysical Research: Solid Earth*, 115(B12).

Nüchter, J.-A. & Ellis, S. (2011). Mid-crustal controls on episodic stress-field rotation around major reverse, normal and strike-slip faults. *Geological Society, London, Special Publications*, 359(1), 187–201.

Nüchter, J.-A. & Stöckhert, B. (2007). Vein quartz microfabrics indicating progressive evolution of fractures into cavities during postseismic creep in the middle crust. *Journal of Structural Geology*, 29(9), 1445–1462.

Nüchter, J.-A. & Stöckhert, B. (2008). Coupled stress and pore fluid pressure changes in the middle crust: Vein record of coseismic loading and postseismic stress relaxation. *Tectonics*, 27(1).

Nollet, S., Urai, J. L., Bons, P. D., & Hilgers, C. (2005). Numerical simulations of polycrystal growth in veins. *Journal of Structural Geology*, 27(2), 217–230.

Obara, K. (2002). Nonvolcanic deep tremor associated with subduction in southwest Japan. *Science*, 296(5573), 1679–1681.

Okay, A., Satir, M., Maluski, H., Siyako, M., Monie, P., Metzger, R., & Akyüz, S. (1996). Paleo-and Neo-Tethyan events in northwestern Turkey: geologic and geochronologic constraints. *World and Regional Geology*, (pp. 420–441).

Okay, A., Satir, M., & Siebel, W. (2006). Pre-Alpide Palaeozoic and Mesozoic orogenic events in the Eastern Mediterranean region. *Geological Society, London, Memoirs*, 32(1), 389–405.

Okay, A. I., Bozkurt, E., Satır, M., Yiğitbaş, E., Crowley, Q. G., & Shang, C. K. (2008a). Defining the southern margin of Avalonia in the Pontides: geochronological data from the Late Proterozoic and Ordovician granitoids from NW Turkey. *Tectonophysics*, 461(1-4), 252–264.

Okay, A. I., Satır, M., & Shang, C. K. (2008b). Ordovician metagranitoid from the Anatolide-Tauride Block, northwest Turkey: geodynamic implications. *Terra Nova*, 20(4), 280–288.

Olson, J. E. (2003). Sublinear scaling of fracture aperture versus length: an exception or the rule? *Journal of Geophysical Research: Solid Earth*, 108(B9).

Özbey, Z., Ustaömer, T., Robertson, A. H., & Ustaömer, P. A. (2013). Tectonic significance of Late Ordovician granitic magmatism and clastic sedimentation on the northern margin of Gondwana (Tavşanlı Zone, NW Turkey). *Journal of the Geological Society*, 170(1), 159–173.

Özmen, F. & Reischmann, T. (1999). The age of the Sakarya continent in W Anatolia: implications for the evolution of the Aegean region. In *Journal of Conference Abstracts*, volume 4 (pp. 805).

Pamić, J. & Jurković, I. (2002). Paleozoic tectonostratigraphic units of the northwest and central Dinarides and the adjoining South Tisia. *International Journal of Earth Sciences*, 91(3), 538–554.

Papanikolaou, D. (2009). Timing of tectonic emplacement of the ophiolites and terrane paleogeography in the Hellenides. *Lithos*, 108(1-4), 262–280.

Papanikolaou, D. (2013). Tectonostratigraphic models of the Alpine terranes and subduction history of the Hellenides. *Tectonophysics*, 595-596, 1 – 24. `https://doi.org/10.1016/j.tecto.2012.08.008`.

Papanikolaou, D. & Vassilakis, E. (2010). Thrust faults and extensional detachment faults in Cretan tectonostratigraphy: implications for Middle Miocene extension. *Tectonophysics*, 488(1), 233–247.

Paquette, J.-L. & Tiepolo, M. (2007). High resolution (5 μm) U–Th–Pb isotope dating of monazite with excimer laser ablation (ELA)-ICPMS. *Chemical Geology*, 240(3-4), 222–237.

Passchier, C. W. & Trouw, R. A. (2005). *Microtectonics*, volume 1. Springer Science & Business Media, 3540293590.

Paterson, M. & Luan, F. (1990). Quartzite rheology under geological conditions. *Geological Society, London, Special Publications*, 54(1), 299–307.

Pehl, J. & Wenk, H.-R. (2005). Evidence for regional Dauphiné twinning in quartz from the Santa Rosa mylonite zone in Southern California. A neutron diffraction study. *Journal of Structural Geology*, 27(10), 1741–1749.

Peters, M., Herwegh, M., Paesold, M. K., Poulet, T., Regenauer-Lieb, K., & Veveakis, M. (2016). Boudinage and folding as an energy instability in ductile deformation. *Journal of Geophysical Research: Solid Earth*, 121(5), 3996–4013.

Platt, J. & Vissers, R. (1980). Extensional structures in anisotropic rocks. *Journal of Structural Geology*, 2(4), 397–410.

Poole, R. (2012). The deborah and weissenberg numbers. *British Soc. Rheol. Rheol. Bull*, 53, 32–39.

Rahl, J. M., Anderson, K. M., Brandon, M. T., & Fassoulas, C. (2005). Raman spectroscopic carbonaceous material thermometry of low-grade metamorphic rocks: calibration and application to tectonic exhumation in Crete, Greece. *Earth and Planetary Science Letters*, 240(2), 339–354.

Ramsay, J. & Huber, M. (1983). Strain analysis, The techniques of modern structural geology, Vol. 1. *Strain Analysis. Academic Press, London*.

Ramsay, J. G. (1980). The crack–seal mechanism of rock deformation. *Nature*, 284(5752), 135.

Ranalli, G. (1995). *Rheology of the Earth*. Springer Science & Business Media, 0412546701.

Reischmann, T., Anthes, G., Jaeckel, P., & Altenberger, U. (2001). Age and origin of the Böllsteiner Odenwald. *Mineralogy and Petrology*, 72(1-3), 29–44.

Richter, D. & Kopp, K. (1983). Zur Tektonik der untersten geologischen Stockwerke auf Kreta. *N Jb Geol Paläont Monatsh*, 1983, 27–46.

Ring, U., Glodny, J., Will, T., & Thomson, S. (2010). The Hellenic subduction system: high-pressure metamorphism, exhumation, normal faulting, and large-scale extension. *Annual Review of Earth and Planetary Sciences*, 38, 45–76.

Ring, U. & Reischmann, T. (2002). The weak and superfast Cretan detachment, Greece: exhumation at subduction rates in extruding wedges. *Journal of the Geological Society*, 159(3), 225–228.

Ring, U. & Yngwe, F. (2018). "To Be, or Not to Be, That Is the Question"–The Cretan Extensional Detachment, Greece. *Tectonics*. `https://doi.org/10.1029/2018TC005179`.

Robertson, A. (2006). Sedimentary evidence from the south Mediterranean region (Sicily, Crete, Peloponnese, Evia) used to test alternative models for the regional tectonic setting of Tethys during Late Palaeozoic-Early Mesozoic time. *Geological Society, London, Special Publications*, 260(1), 91–154.

Robertson, A., et al. (1996). Alternative tectonic models for the Late Palaeozoic-Early Tertiary development of Tethys in the Eastern Mediterranean region. *Geological Society, London, Special Publications*, 105(1), 239–263.

Robertson, A. H. (2012). Late Palaeozoic–Cenozoic tectonic development of Greece and Albania in the context of alternative reconstructions of Tethys in the Eastern Mediterranean region. *International Geology Review*, 54(4), 373–454.

Robertson, A. H. & Pickett, E. A. (2000). Palaeozoic-Early Tertiary Tethyan evolution of mélanges, rift and passive margin units in the Karaburun Peninsula (western Turkey) and Chios island (Greece). *Geological Society, London, Special Publications*, 173(1), 43–82.

Robertson, A. H. & Ustaömer, T. (2009). Formation of the Late Palaeozoic Konya Complex and comparable units in southern Turkey by subduction–accretion processes: Implications for the tectonic development of Tethys in the Eastern Mediterranean region. *Tectonophysics*, 473(1-2), 113–148.

Romano, S., Brix, M., Dörr, W., Fiala, J., Krenn, E., & Zulauf, G. (2006). The Carboniferous to Jurassic evolution of the pre-Alpine basement of Crete: constraints from U-Pb and U-(Th)-Pb dating of orthogneiss, fission-track dating of zircon, structural and petrological data. *Geological Society, London, Special Publications*, 260(1), 69–90.

Romano, S. S., Dörr, W., & Zulauf, G. (2004). Cambrian granitoids in pre-Alpine basement of Crete (Greece): evidence from U-Pb dating of zircon. *International Journal of Earth Sciences*, 93(5), 844–859.

Rubinstein, J. L., Shelly, D. R., & Ellsworth, W. L. (2009). Non-volcanic tremor: A window into the roots of fault zones. In *New Frontiers in Integrated Solid Earth Sciences* (pp. 287–314). Springer. `https://doi.org/10.1007/978-90-481-2737-5_8`.

Scholz, C. (1988). The brittle-plastic transition and the depth of seismic faulting. *Geologische Rundschau*, 77(1), 319–328.

Scholz, C. H. (2002). *The mechanics of earthquakes and faulting*. Cambridge university press, 0521655404.

Schulz, B. (2013). Monazite EMP-Th-U-Pb age pattern in Variscan metamorphic units in the Armorican Massif (Brittany, France)[Monazit-Altersmuster (EMS-Th-U-Pb) in den variskischen metamorphen Einheiten des Armorikanischen Massivs (Bretagne, Frankreich)]. *Zeitschrift der Deutschen Gesellschaft für Geowissenschaften*, 164(2), 313–335.

Schwartz, S. Y. & Rokosky, J. M. (2007). Slow slip events and seismic tremor at circum-Pacific subduction zones. *Reviews of Geophysics*, 45(3).

Schwarz, S. & Stöckhert, B. (1996). Pressure solution in siliciclastic HP-LT metamorphic rocks—Constraints on the state of stress in deep levels of accretionary complexes. *Tectonophysics*, 255(3-4), 203–209.

Seidel, E. (1978). *Zur Petrologie der Phyllit-Quarzit-Serie Kretas*. Thesis, Technische Universität, Braunschweig.

Seidel, E., Kreuzer, H., & Harre, W. (1982). A late Oligocene/early Miocene high pressure belt in the external Hellenides. *Geologisches Jahrbuch*, E 23, 165–206.

Seidel, M., Seidel, E., & Stöckhert, B. (2007). Tectono-sedimentary evolution of lower to middle Miocene half-graben basins related to an extensional detachment fault (western Crete, Greece). *Terra Nova*, 19(1), 39–47.

Şengör, A., Yılmaz, Y., & Sungurlu, O. (1984). Tectonics of the Mediterranean Cimmerides: nature and evolution of the western termination of Palaeo-Tethys. *Geological Society, London, Special Publications*, 17(1), 77–112.

Seybold, L., Doerr, W., Trepmann, C. A., & Krahl, J. (in review). New constraints from U-Pb dating of detrital zircons on the paleogeographic origin of metasediments in the Talea Ori, central Crete. *Geological Magazine*, xx, xxx.

Seybold, L., Trepmann, C. A., & Janots, E. (2019). A ductile extensional shear zone at the contact area between HP-LT metamorphic units in the Talea Ori, central Crete, Greece: deformation during early stages of exhumation from peak metamorphic conditions. *International Journal of Earth Sciences*, 108(1), 213–227. `https://doi.org/10.1007/s00531-018-1650-6`.

Sibson, R. (1977). Fault rocks and fault mechanisms. *Journal of the Geological Society*, 133(3), 191–213.

Sibson, R., Moore, J. M. M., & Rankin, A. (1975). Seismic pumping—a hydrothermal fluid transport mechanism. *Journal of the Geological Society*, 131(6), 653–659.

Soujon, A., Jacobshagen, V., & Manutsoglu, E. (1998). A lithostratigraphic correlation of the Plattenkalk occurences of Crete (Greece). *Bulletin of the Geological Society of Greece*, 32(1), 41–48.

Stacey, J. t. & Kramers, J. (1975). Approximation of terrestrial lead isotope evolution by a two-stage model. *Earth and planetary science letters*, 26(2), 207–221.

Stampfli, G., Hochard, C., Vérard, C., & Wilhem, C. (2013). The formation of Pangea. *Tectonophysics*, 593, 1–19.

Stampfli, G. M. & Borel, G. (2002). A plate tectonic model for the Paleozoic and Mesozoic constrained by dynamic plate boundaries and restored synthetic oceanic isochrons. *Earth and Planetary Science Letters*, 196(1), 17–33.

Stampfli, G. M. & Kozur, H. W. (2006). Europe from the Variscan to the Alpine cycles. *MEMOIRS-GEOLOGICAL SOCIETY OF LONDON*, 32, 57.

Stampfli, G. M., Vavassis, I., De Bono, A., Rosselet, F., Matti, B., & Bellini, M. (2003). Remnants of the Paleotethys oceanic suture-zone in the western Tethyan area. *Stratigraphic and structural evolution on the Late Carboniferous to Triassic continental and marine successions in Tuscany (Italy): regional reports and general correlation. Bolletino della Società Geologica Italiana, Volume speciale*, 2, 1–24.

Stöckhert, B. (2002). Stress and deformation in subduction zones: insight from the record of exhumed metamorphic rocks. *Geological Society, London, Special Publications*, 200(1), 255–274.

Stöckhert, B., Wachmann, M., Küster, M., & Bimmermann, S. (1999). Low effective viscosity during high pressure metamorphism due to dissolution precipitation creep: the record of HP–LT metamorphic carbonates and siliciclastic rocks from Crete. *Tectonophysics*, 303(1-4), 299–319.

Stephan, T., Kroner, U., & Romer, R. L. (2019). The pre-orogenic detrital zircon record of the Peri-Gondwanan crust. *Geological Magazine*, 156(2), 281–307.

Stern, R. J. (1994). Arc assembly and continental collision in the Neoproterozoic East African Orogen: implications for the consolidation of Gondwanaland. *Annual Review of Earth and Planetary Sciences*, 22(1), 319–351.

Stipp, M. & Kunze, K. (2008). Dynamic recrystallization near the brittle-plastic transition in naturally and experimentally deformed quartz aggregates. *Tectonophysics*, 448(1), 77 – 97. `https://doi.org/10.1016/j.tecto.2007.11.041`.

Stipp, M. & Tullis, J. (2003). The recrystallized grain size piezometer for quartz. *Geophysical Research Letters*, 30(21).

Sunal, G. (2012). Devonian magmatism in the western Sakarya Zone, Karacabey region, NW Turkey. *Geodinamica Acta*, 25(3-4), 183–201.

ten Veen, J. & Kleinspehn, K. (2003). Incipient continental collision and plate-boundary curvature: Late Pliocene-Holocene transtenstional Hellenic forearc, Crete, Greece. *Journal of the Geological Society (London)*, 160, 1–21.

Teufel, S. (1988). *Vergleichende U-Pb-und Rb-Sr-Altersbestimmungen an Gesteinen des Übergangsbereiches Saxothuringikum/Moldanubikum, NE–Bayern*. 35. Im Selbstverlag der Geologischen Institute der Georg-August-Universität.

Theye, T. (1988). *Aufsteigende Hochdruckmetamorphose in Sedimenten der Phyllit-Quarzit-Einheit Kretas und des Peloponnes*. Thesis, Technische Universität, Braunschweig.

Theye, T. & Seidel, E. (1991). Petrology of low-grade high-pressure metapelites from the External Hellenides (Crete, Peloponnese) A case study with attention to sodic minerals. *European Journal of Mineralogy*, (pp. 343–366).

Theye, T., Seidel, E., & Vidal, O. (1992). Carpholite, sudoite, and chloritoid in low-grade high-pressure metapelites from Crete and the Peloponnese, Greece. *European Journal of Mineralogy*, (pp. 487–508).

Thomson, S., Stöckhert, B., Rauche, H., & Brix, M. (1998a). Apatite fission-track thermochronology of the uppermost tectonic unit of Crete, Greece: implications for the post-Eocene tectonic evolution of the Hellenic subduction system. In *Advances in Fission-Track Geochronology* (pp. 187–205). Springer.

Thomson, S. N., Stöckhert, B., & Brix, M. R. (1998b). Thermochronology of the high-pressure metamorphic rocks of Crete, Greece: implications for the speed of tectonic processes. *Geology*, 26(3), 259–262.

Thomson, S. N., Stöckhert, B., & Brix, M. R. (1999). Miocene high-pressure metamorphic rocks of Crete, Greece: rapid exhumation by buoyant escape. *Geological Society, London, Special Publications*, 154(1), 87–107.

Timmermann, H., Dörr, W., Krenn, E., Finger, F., & Zulauf, G. (2006). Conventional and in situ geochronology of the Teplá Crystalline unit, Bohemian Massif: implications for the processes involving monazite formation. *International Journal of Earth Sciences*, 95(4), 629–647.

Timmermann, H., Štědrá, V., Gerdes, A., Noble, S., Parrish, R. R., & Dörr, W. (2004). The problem of dating high-pressure metamorphism: a U–Pb isotope and geochemical study on eclogites and related rocks of the Mariánské Lázně Complex, Czech Republic. *Journal of Petrology*, 45(7), 1311–1338.

Titorenkova, R., Macheva, L., Zidarov, N., Von Quadt, A., & Peytcheva, I. (2003). Metagranites from SW Bulgaria as a part of the Neoproterozoic to Early Paleozoic system in Europe: new insight from zircon typology, U-Pb isotope data and Hf-tracing. In *EGS-AGU-EUG Joint Assembly*.

Tortorici, L., Caputo, R., & Monaco, C. (2010). Late Neogene to quaternary contractional structures in Crete (Greece). *Tectonophysics*, 483(3), 203–213.

Trepmann, C., Lenze, A., & Stöckhert, B. (2010). Static recrystallization of vein quartz pebbles in a high-pressure–low-temperature metamorphic conglomerate. *Journal of Structural Geology*, 32(2), 202–215.

Trepmann, C. & Stöckhert, B. (2001). Mechanical twinning of jadeite–an indication of synseismic loading beneath the brittle–plastic transition. *International Journal of Earth Sciences*, 90(1), 4–13.

Trepmann, C. & Stöckhert, B. (2009). Microfabric of folded quartz veins in metagreywackes: dislocation creep and subgrain rotation at high stress. *Journal of Metamorphic Geology*, 27(8), 555–570.

Trepmann, C. & Stöckhert, B. (2013). Short-wavelength undulatory extinction in quartz recording coseismic deformation in the middle crust-an experimental study. *Solid Earth*, 4(2), 263.

Trepmann, C. A., Hsu, C., Hentschel, F., Döhler, K., Schneider, C., & Wichmann, V. (2017). Recrystallization of quartz after low-temperature plasticity–The record of stress relaxation below the seismogenic zone. *Journal of Structural Geology*, 95, 77–92.

Trepmann, C. A. & Seybold, L. (2019). Deformation at low and high stress-loading rates. *Geoscience Frontiers*, 10(1), 43 – 54. https://doi.org/10.1016/j.gsf.2018.05.002.

Trepmann, C. A. & Stöckhert, B. (2003). Quartz microstructures developed during non-steady state plastic flow at rapidly decaying stress and strain rate. *Journal of Structural Geology*, 25(12), 2035–2051.

Trepmann, C. A., Stöckhert, B., Dorner, D., Moghadam, R. H., Küster, M., & Röller, K. (2007). Simulating coseismic deformation of quartz in the middle crust and fabric evolution during postseismic stress relaxation—an experimental study. *Tectonophysics*, 442(1-4), 83–104.

Ujiie, K., Saishu, H., Fagereng, Å., Nishiyama, N., Otsubo, M., Masuyama, H., & Kagi, H. (2018a). An explanation of episodic tremor and slow slip constrained by crack-seal veins and viscous shear in subduction mélange. *Geophysical Research Letters*, 45(11), 5371–5379.

Ujiie, K., Saishu, H., Fagereng, k., Nishiyama, N., Otsubo, M., Masuyama, H., & Kagi, H. (2018b). An Explanation of Episodic Tremor and Slow Slip Constrained by Crack-Seal Veins and Viscous Shear in Subduction Mélange. *Geophysical Research Letters*, 45(11), 5371–5379. https://doi.org/10.1029/2018GL078374.

Urai, J., Williams, P., & Van Roermund, H. (1991). Kinematics of crystal growth in syntectonic fibrous veins. *Journal of Structural Geology*, 13(7), 823–836.

Ustaömer, P. A., Ustaömer, T., & Robertson, A. (2012). Ion probe U-Pb dating of the Central Sakarya basement: a peri-Gondwana terrane intruded by late Lower Carboniferous subduction/collision-related granitic rocks. *Turkish Journal of Earth Sciences*, 21(6), 905–932.

Ustaömer, T., Robertson, A. H., Ustaömer, P. A., Gerdes, A., & Peytcheva, I. (2013). Constraints on Variscan and Cimmerian magmatism and metamorphism in the Pontides (Yusufeli–Artvin area), NE Turkey from U–Pb dating and granite geochemistry. *Geological Society, London, Special Publications*, 372(1), 49–74.

Ustaömer, T., Ustaömer, P. A., Robertson, A. H., & Gerdes, A. (2019). U-Pb-Hf isotopic data from detrital zircons in late Carboniferous and Mid-Late Triassic sandstones, and also Carboniferous granites from the Tauride and Anatolide continental units in S Turkey: implications for Tethyan palaeogeography. *International Geology Review*, (pp. 1–28).

van Daalen, M., Heilbronner, R., & Kunze, K. (1999). Orientation analysis of localized shear deformation in quartz fibres at the brittle–ductile transition. *Tectonophysics*, 303(1-4), 83–107.

Vermilye, J. M. & Scholz, C. H. (1995). Relation between vein length and aperture. *Journal of structural geology*, 17(3), 423–434.

Vernooij, M. & Langenhorst, F. (2005). Experimental reproduction of tectonic deformation lamellae in quartz and comparison to shock-induced planar deformation features. *Meteoritics & Planetary Science*, 40(9-10), 1353–1361.

Wachendorf, H., Gralla, P., Koll, J., & Schulze, I. (1980). Geodynamik des mittelkretischen Deckenstapels-(nördliches Dikti-Gebirge). *Geotektonische Forschungen*, 59, 1–71.

Wald, D. J. & Heaton, T. H. (1994). Spatial and temporal distribution of slip for the 1992 Landers, California, earthquake. *Bulletin of the Seismological Society of America*, 84(3), 668–691.

Wassmann, S. & Stöckhert, B. (2013). Rheology of the plate interface—dissolution precipitation creep in high pressure metamorphic rocks. *Tectonophysics*, 608, 1–29.

Wenk, H.-R., Janssen, C., Kenkmann, T., & Dresen, G. (2011). Mechanical twinning in quartz: shock experiments, impact, pseudotachylites and fault breccias. *Tectonophysics*, 510(1-2), 69–79. https://doi.org/10.1016/j.tecto.2011.06.016.

Wenk, H.-R., Rybacki, E., Dresen, G., Lonardelli, I., Barton, N., Franz, H., & Gonzalez, G. (2006). Dauphiné twinning and texture memory in polycrystalline quartz. Part 1: experimental deformation of novaculite. *Physics and chemistry of minerals*, 33(10), 667. https://doi.org/10.1007/s00269-006-0115-9.

White, J. C. (1996). Transient discontinuities revisited: pseudotachylyte, plastic instability and the influence of low pore fluid pressure on deformation processes in the mid-crust. *Journal of Structural Geology*, 18(12), 1471 – 1486. https://doi.org/10.1016/S0191-8141(96)00059-4.

White, J. C. (2012). Paradoxical pseudotachylyte – Fault melt outside the seismogenic zone. *Journal of Structural Geology*, 38, 11 – 20. Physico-Chemical Processes in Seismic Faults. https://doi.org/10.1016/j.jsg.2011.11.016.

White, S. (1973). Syntectonic recrystallization and texture development in quartz. *Nature*, 244(5414), 276.

White, S. (1977). Geological significance of recovery and recrystallization processes in quartz. *Tectonophysics*, 39(1-3), 143–170.

Whitney, D. L. & Evans, B. W. (2010). Abbreviations for names of rock-forming minerals. *American mineralogist*, 95(1), 185–187.

Wiedenbeck, M., et al. (1995). Three natural zircon standards for U-Th-Pb, Lu-Hf, trace element and REE analyses. *Geostandards newsletter*, 19(1), 1–23.

Williams, I. S., Fiannacca, P., Cirrincione, R., & Pezzino, A. (2012). Peri-Gondwanan origin and early geodynamic history of NE Sicily: a zircon tale from the basement of the Peloritani Mountains. *Gondwana Research*, 22(3-4), 855–865.

Xypolias, P., Chatzaras, V., & Koukouvelas, I. (2007). Strain gradients in zones of ductile thrusting: Insights from the External Hellenides. *Journal of Structural Geology*, 29(9), 1522–1537.

Xypolias, P., Dorr, W., & Zulauf, G. (2006). Late Carboniferous plutonism within the pre-Alpine basement of the External Hellenides (Kithira, Greece): evidence from U–Pb zircon dating. *Journal of the Geological Society*, 163(3), 539–547.

Zeh, A., Cosca, M., Brätz, H., Okrusch, M., & Tichomirowa, M. (2000). Simultaneous horst-basin formation and magmatism during Late Variscan transtension: evidence from 40 Ar/39 Ar and 207 Pb/206 Pb geochronology in the Ruhla Crystalline Complex. *International Journal of Earth Sciences*, 89(1), 52–71.

Zeh, A., Williams, I. S., Brätz, H., & Millar, I. L. (2003). Different age response of zircon and monazite during the tectono-metamorphic evolution of a high grade paragneiss from the Ruhla Crystalline Complex, central Germany. *Contributions to Mineralogy and Petrology*, 145(6), 691–706.

Zhang, Y.-C. & Wang, Y. (2018). Permian fusuline biostratigraphy. *Geological Society, London, Special Publications*, 450(1), 253–288, doi:10.1144/SP450.14. https://sp.lyellcollection.org/content/450/1/253.

Zlatkin, O., Avigad, D., & Gerdes, A. (2013). Evolution and provenance of Neoproterozoic basement and Lower Paleozoic siliciclastic cover of the Menderes Massif (western Taurides): coupled U–Pb–Hf zircon isotope geochemistry. *Gondwana Research*, 23(2), 682–700.

Zulauf, G., Dörr, W., Marko, L., & Krahl, J. (2018). The late Eo-Cimmerian evolution of the external Hellenides: constraints from microfabrics and U–Pb detrital zircon ages of Upper Triassic (meta) sediments (Crete, Greece). *International Journal of Earth Sciences*, 107(8), 2859–2894. https://doi.org/10.1007/s00531-018-1632-8.

Zulauf, G., Dörr, W., Fisher-Spurlock, S., Gerdes, A., Chatzaras, V., & Xypolias, P. (2015). Closure of the Paleotethys in the External Hellenides: constraints from U–Pb ages of magmatic and detrital zircons (Crete). *Gondwana Research*, 28(2), 642–667.

Zulauf, G., Dörr, W., Krahl, J., Lahaye, Y., Chatzaras, V., & Xypolias, P. (2016). U–Pb zircon and biostratigraphic data of high-pressure/low-temperature metamorphic rocks of the Talea Ori: tracking the Paleotethys suture in central Crete, Greece. *International Journal of Earth Sciences*, 105(7), 1901–1922.

Zulauf, G., Klein, T., Kowalczyk, G., Krahl, J., & Romano, S. S. (2008). The Mirsini Syncline of eastern Crete, Greece: a key area for understanding pre-Alpine and Alpine orogeny in the eastern Mediterranean [Die Mulde von Mirsini in Ostkreta, Griechenland: ein Schlüsselgebiet zum Verständnis präalpiner und alpiner Orogenese im östlichen Mittelmeerraum.]. *Zeitschrift der deutschen Gesellschaft fuer Geowissenschaften*, 159(3), 399–414.

Zulauf, G., Romano, S., Dorr, W., & Fiala, J. (2007). Crete and the Minoan terranes: Age constraints from U-Pb dating of detrital zircons. *SPECIAL PAPERS-GEOLOGICAL SOCIETY OF AMERICA*, 423, 401.

8 Appendix

8.1 Sample list

Name	Unit	Description	Locality	Orientation	Latitude	Longitude	Thin Sec.
LS3	Sisses	Metabauxit	Südwesthang Koufotos		35° 23' 21'' N	24° 50' 39'' E	2
LS7	U.- Fodele	Glimmerschiefer	New Road SW Almyrida	025/30	35° 24' 8'' N	24° 51' 44'' E	1
LS10	Bali	Tonschiefer	Küste W von Almyrida	020/30	35° 24' 28'' N	24° 50' 56'' E	2
LS12	Bali / PQ	Quarzitboudin mit Qz-Gängen	Pera Galinos	080/65	35° 23' 51'' N	24° 51' 23,5'' E	1
LS14b	Bali / PQ	keilförmiger Qz-Gang diskordant	im Norden von Bali	332/35	35° 24' 59'' N	24° 47' 4'' E	1
LS15	Bali	Scherkörper aus Quarzit	im Norden von Bali	318/25	35° 25' 1'' N	24° 47' 00'' E	
LS17	Sisses	heller Schiefer	Mülldeponie	010/67	35° 23' 25'' N	24° 55' 32,5'' E	
LS18	Sisses	heller Schiefer	Mülldeponie		35° 23' 25'' N	24° 55' 32,5'' E	1
LS21	Bali	Chert	Mülldeponie	062/45	35° 23' 9'' N	24° 55' 52'' E	1
LS22	Bali	Schwarzer Schiefer	Mülldeponie		35° 23' 2'' N	24° 55' 39'' E	
LS23	Bali	Grobklast. Metasediment	Mülldeponie		35° 23' 12'' N	24° 55' 53'' E	1
LS24	Bali	Qz-Konglomerat	Mülldeponie		35° 23' 3,5'' N	24° 55' 38'' E	1
LS25	Bali	Schwarzschiefer mit Qz-Gängen	W Almyrida	040/35	35° 24' 14,6'' N	24° 51' 28,4'' E	1
LS27	Bali	Grober Metasandstein	W Almyrida	016/70	35° 24' 19'' N	24° 51' 32'' E	1
LS31	PQ	Glimmerschiefer mit Quarzgang	W Almyrida	010/25	35° 24' 19,6'' N	24° 51' 43,7'' E	1
LS32	PQ	Phyllit mit Quarzgängen	W Almyrida		35° 24' 24'' N	24° 51' 53'' E	2
LS33	PQ	Quarzit	W Almyrida	354/56	35° 24' 27,7'' N	24° 51' 56,3'' E	
LS36	PQ	Glimmerreicher	W Almyrida	341/31	35° 24' 29,3'' N	24° 51' 52,5'' E	1
LS39	Bali	Qz-Gang in schwarzem Schiefer	Bali Hafen	002/15	35° 24' 50'' N	24° 46' 59'' E	1
LS41	PQ	Glimmerschiefer mit Qz-Gang	Bali	310/30	35° 24' 49'' N	24° 46' 49,3'' E	1
LS42	PQ	Glimmerschiefer mit Qz-Gang	Bali	350/15	35° 24' 49'' N	24° 46' 49,3'' E	
LS43	PQ	Schiefer mit Boudin-neck?	Bali	291/20	35° 24' 49'' N	24° 46' 49,3'' E	
LS44	Bali/PQ	Qz-Konglomerat	Bali		35° 24' 39'' N	24° 46' 22'' E	1
LS46	Bali	glimmerreicher Metapsammit	Bucht südlich des Hafens Bali		35° 24' 40'' N	24° 46' 21,9'' E	3
LS48	PQ	Quarzit mit Qz-Gängen	Schweinezucht	294/61	35° 23' 42'' N	24° 55' 41'' E	1
LS51	PQ	Qz-Brekzie	Schweinezucht an der Küste		35° 24' 10'' N	24° 55' 43'' E	1
LS52	PQ	keilförmiger Qz-Gang	Schweinezucht		35° 24' 06'' N	24° 55' 43'' E	
LS53	Bali	Glimmerschiefer mit Qz-Gang	New Road Mülldeponie	042/41	35° 23' 21'' N	24° 55' 15'' E	1
LS54	PQ	Qz-Gang in Glimmerschiefer	Schweinezucht		35° 23' 39,7'' N	24° 55' 42,2'' E	1
LS56	Bali	Qz-Gang in Metasandstein	New Rd O. F zu Bali W	180/70	35° 24' 33'' N	24° 46' 05'' E	1
LS57	Bali	Metasandstein	New Rd O. F zu Bali W		35° 24' 33'' N	24° 46' 05'' E	1
LS58	Bali	Schwarzer Schiefer	New Rd O. F zu Bali W		35° 24' 33'' N	24° 46' 05'' E	1
LS59	Bali	Metasandstein	New Rd O. F zu Bali W		35° 24' 33'' N	24° 46' 05'' E	1
LS61	Bali	Verfalteter Chert	E Sisses	042/40	35° 23' 35,1'' N	24° 54' 18,7'' E	1
LS62	Sisses	Calcitmarmor	Nordhang des Koufotos		35° 23' 45'' N	24° 51' 10,3'' E	
LS63	Sisses	Dolomitmarmor serizitisch	Nordhang des Koufotos		35° 23' 45'' N	24° 51' 10,3'' E	
LS64	Sisses	dunkler Dolomitmarmor	Nordhang des Koufotos		35° 23' 45'' N	24° 51' 10,3'' E	
LS65	Sisses	Dolomitmarmor gemischt	Nordhang des Koufotos		35° 23' 45'' N	24° 51' 10,3'' E	1
LS66	Sisses	Dolomit-Konglomerat	Nordhang des Koufotos		35° 23' 45'' N	24° 51' 10,3'' E	1
LS67	Sisses	Dolomit-Konglomerat	Nordhang des Koufotos		35° 23' 45'' N	24° 51' 10,3'' E	
LS68	Sisses	grauer Dolomitmarmor	Nordhang des Koufotos		35° 23' 45'' N	24° 51' 10,3'' E	
LS69	Stromatoli	Fe-Mineralisation	SSW von Fodele		35° 22' 03'' N	24° 57' 06'' E	
LS70	Bali	Bali Qz-Kongo	Bali beach		35°24'31.8"N	24°47'00.2"E	1+1(Dia)
LS71	PQ	grünlicher Schiefer	N Fodele		35.39786653	24.95283228	
LS72	PQ	bunter Schiefer	N Fodele		35.39821346	24.95286229	
LS73	PQ	grüner Schiefer	N Fodele		35.40243911	24.95793703	2
LS74	PQ	bunter Schiefer mit Qz-Gang	N Fodele		35.40243911	24.95793703	1
LS75	Bali	Chert	Bali		35.40784175	24.78372521	1
LS76	Bali	Chert	Bali		35.40784175	24.78372521	1
LS77	Bali	Chert	Bali		35.40784175	24.78372521	
LS78	Bali	Schwarzschiefer	Bali		35.4091179	24.78317393	
LS79	Bali	Metasandstein	Bali		35.40970576	24.78318097	1
LS80	Bali	Schwarzschiefer	Bali		35.4098328	24.78311438	
LS81	Bali	Schwarzschiefer	Bali		35.41126555	24.78340837	1

Name	Unit	Description	Locality	Orientation	Latitude	Longitude	Thin Sec.
LS82	Bali	Schwarzschiefer	Bali		35.41384219	24.78320925	1
LS83	Bali	Schwarzschiefer	Bali	296/20	35.41277451	24.78342834	1
LS84	Bali	Schwarzschiefer	Bali		35.41426878	24.78391648	1
LS85	Bali	Schiefer	Bali		35.41582962	24.78469189	
LS86	Bali	toniger Sandstein	Bali		35.41582962	24.78469189	1
LS87	Bali	Schwarzschiefer	Pelekida		35.40735568	24.84876987	1
LS88	Bali	grünlich anwitternder Schiefer	Pelekida		35.40542596	24.85617813	1
LS89	Bali	laminierter Chert	Pelekida	020/55	35.40553325	24.85632422	1
LS90	Bali	Metasandstein	Pelekida		35.40580111	24.85668709	1
LS91	Bali	Schwarzschiefer	Pelekida		35.407252	24.8567776	1
LS92	Bali	dunkler Sandstein	Pelekida		35.4074828	24.85714724	1
LS93	Bali	heller Sandstein	Pelekida		35.4074828	24.85714724	1
LS94	Bali	Metapsammit/pelit	Pelekida		35.40801764	24.85605466	1
LS95	Bali	bunter Schiefer	Pelekida		35.4074435	24.85499703	1
LS96	Bali	Schwarzschiefer	Pelekida	000/24	35.4087123	24.85245413	1
LS97	Bali	Metapsammit/pelit	Pelekida	014/34	35.40892805	24.85213017	
LS98	Bali	grüner Schiefer mit Qz-Lagen	Pelekida		35.40969746	24.8520202	
LS99	Bali	Schwarzschiefer	Pelekida		35.40859319	24.85188894	
LS100	Bali	Sandstein	Pelekida		35.40859	24.85165	1
LS101	Bali	Schiefer mit Chloritoid?	Pelekida		35.40825	24.85122	1
LS102	Bali	lagiger Sandstein/Schiefer	Pelekida		35.40783	24.85059	1
LS103	Bali	Chert/Schwarzschiefer	SW Almyrida New Road		35.40349	24.85724	
LS104	Bali	Schwarzschiefer	SW Almyrida New Road		35.40363	24.85722	1
LS105	Bali	sandiger Schwarzschiefer	Almyrida Straße von W		35.40403	24.85795	
LS106	Bali	Schwarzschiefer	Almyrida Straße von W		35.40395	24.85815	1
LS107	Bali	heller Schiefer	Almyrida Straße von W		35.40550	24.86035	1
LS108	Bali	heller Schiefer	Almyrida Straße von W		35.40531	24.86336	
LS109	Bali	roter Schiefer	Almyrida Straße von W		35.40844	24.86534	
LS110	PQ	Schwarzschiefer	Almyrida Küste		35.40951	24.87097	1
LS111	PQ	Q1-Quarzit	Almyrida Küste		35.40951	24.87097	1
LS112	PQ	Marmor bei Skilarmi	Skilarmi		35.40680	24.87130	2(Dia)
LS113	Bali	Schwarzschiefer	E von Galinoskirche		35.39093	24.91888	
LS114	Bali	Schwarzschiefer	NE von Galinoskirche		35.39448	24.92075	1
LS115	PQ	gefältelter Schwarzschiefer	NE von Almyrida		35.41094	24.88141	
LS116	PQ	Albit-Schiefer	NE von Almyrida	032/41	35.41406	24.88186	1
LS117	Bali	Zerscherter Chert mit Qz-Gang	E Sisses		35.39168	24.90821	
LS118	Bali	Tonschieferkonglomerat	E Sisses		35.39433	24.90094	1
LS119	PQ	Falte aus Quarzit mit Schiefern	E Sisses		35.40124	24.90107	2
LS121	PQ	Quarzlinse	E Sisses		35.40089	24.90096	
LS122	PQ	Quarzit mit schwarzem Quarz	E Sisses	354/35	35.39572	24.90038	1
LS123	Bali	Quarz-Komponente in Schiefer	Skilarmi		35.40387	24.86820	1
LS124	Bali	Schiefer mit Knickbändern	Skilarmi		35.40641	24.87147	1
LS125	PQ	Qz-Gang in Scherband	Skilarmi		35.40894	24.87057	1
LS126	PQ	"Albitgneis" Metavulkanit	Grenze zu Vasilikon		35.39756	24.97368	1
LS127	PQ	"Albitgneis" Metavulkanit	Grenze zu Vasilikon	267/25	35.39773	24.97470	1
LS128	Bali	Quarzgänge in Schwarzschiefer	E Sisses	012/40	35.39426	24.90098	2
LS129	Bali	Marmor Bali beach	Bali Strand		35.40916	24.78314	1(Dia)
LS130	O. Fodele	heller fossilreicher Marmor	W Bali New Road		35.40874	24.75491	1(Dia)
LS131	Ostkreta	Altkristallin Ostkreta	Ostkreta	358/13	35.17661	25.92808	
LS132	Bali	Schiefer	Faltenkern W Fodele	060/45	35.38284	24.93636	1
LS133	Bali	Schiefer mit cc	Faltenkern W Fodele	010/46	35.38367	24.93830	2
LS134	Bali	Quarzit mit cc	Faltenkern W Fodele		35.38367	24.93830	2
LS135	Bali	Quarzit mit Qz-Gang	Faltenkern W Fodele	038/42	35.38473	24.93968	1
LS136	U-F	Schwarzschiefer	E Sisses New Road	107/19	35.39371	24.89964	1
LS137	U-F	Schwarzschiefer	E Sisses New Road		35.39371	24.89964	
LS138	Bali/PQ	Schwarzschieferkonglomerat	Pelekida	020/26	35.40763	24.85404	1
LS139	Bali/PQ	Schwarzschieferkonglomerat	Pelekida	003/30	35.40872	24.85256	1
LS140	PQ	lagiger Quarzit	Skilarmi	359/20	35.40768	24.87100	1
LS141	Bali?	Quarzit grobkörnig, Bali?	Skilarmi	350/24	35.40720	24.87117	1
LS142	Bali?	schiefriger Metasandstein, Bali	Skilarmi	050/31	35.40542	24.87038	1
LS143	Bali?	grobklastisches Metasediment	Skilarmi	102/09	35.40542	24.87038	2
LS144	PQ	massiver Quarzit	Skilarmi		35.40679	24.87131	1
LS147	Sisses	Sandstein Sisses für Datierung	E Sisses an New Road		35.39281	24.89749	1
LS148	PQ	Metavulkanit?	NW Fodele		35.39383	24.94238	1

Name	Unit	Description	Locality	Orientation	Latitude	Longitude	Thin Sec.
LS149	PQ	Quarzit mit Streckungslinear	NW Fodele	090/40	35.39374	24.94160	
LS150	PQ	Schiefer mit Krenulationsfaltung	NW Fodele		35.39374	24.94160	1
LS151	PQ	Quarzit	NW Fodele		35.39469	24.93977	1
LS152	PQ	Schiefer mit Quarzgang	NW Fodele		35.39469	24.93977	1
LS153	PQ	Metavulkanit (?)	N Fodele		35.38939	24.95273	1
LS154	U-Fodele	Sandstein U-F zur Datierung	Pera Galinos		35.39478	24.92422	1
LS155	PQ	Qz-Linse mit grünlichem Zeug	Pera Galinos		35.39804	24.92320	
LS156	PQ	deformierter Metavulkanit (?)	Pera Galinos	022/30	35.39895	24.92273	1
LS157	PQ	grünlicher Schwarzschiefer	Pera Galinos	008/45	35.39718	24.92308	
LS158	PQ	weiß staubender Quarzit/Fsp	NW von Bali		35.41603	24.77456	1
LS159	PQ	Quarzit mit cc	NW von Bali		35.41481	24.77376	1
LS160	PQ	weiß staubender Quarzit/Fsp	NW von Bali		35.41429	24.77387	1
LS161	PQ	weiß staubender Quarzit/Fsp	NW von Bali		35.41429	24.77387	1
LS162	Bali	feinkörniges Metakonglomerat	NW von Bali		35.41429	24.77387	1
LS163	Bali	Schwarzschiefer	Westl. Almyrida		35.40467138	24.85889914	
LS164	Bali	Qz-Gängchen in Schiefer	Westl. Almyrida		35.40467138	24.85889914	
LS165	Bali	Metasandstein	Westl. Almyrida	024/45	35.40536159	24.85888188	
LS166	Bali	Chert	Westl. Almyrida		35.40563622	24.85958872	
LS167	PQ	grünlicher Schiefer	Westl. Almyrida		35.40563622	24.85958872	
LS168	Bali/PQ	Schwarzschiefer	Westl. Almyrida		35.40538665	24.86212953	
LS169	PQ	Marmor	Westl. Almyrida		35.40630464	24.8661603	1 (Dia)
LS170	PQ	Albit-Schiefer, ähnlich LS86	Bali W		35.41582962	24.78469189	
LS171	PQ	dunkler Qz-reicher Schiefer	Bali W		35.41434787	24.77393012	
LS172	Bali/PQ	gröbkörnig, evtl. wie LS162?	Bali W		35.41430395	24.77421585	
LS173	PQ	Quarzitscherband	Nördlich Fodele		35.38770431	24.95448469	
LS174	PQ	Quarzit mit Qz im boudin neck	Nördlich Fodele	074/32	35.38781038	24.9539879	2
LS175	PQ	Quarzgang, Ab-Schiefer	Nördlich Fodele		35.39388889	24.95083333	1
LS176	PQ	schwarze Quarzlage	Nördlich Fodele		35.39593186	24.95222602	
LS177	PQ	Quarzgang in Quarzit	Straße nach Achlada		35.39859932	24.95233457	
LS178	PQ	Violetter Schiefer (Chloritoid?)	Straße nach Achlada	332/24	35.40037771	24.95430557	1
LS179	PQ	Qz-Gang an Scherband	Weg NW Fodele		35.39233879	24.95784558	1
LS180	PQ	Heller Violettschiefer	Straße nach Achlada	358/34	35.40244758	24.95886491	
LS181	PQ	Dunkler Schiefer mit Quarzgang	Straße nach Achlada	356/35	35.40249707	24.95886097	1
LS182	PQ	Schiefer	Straße nach Achlada	356/20	35.40231456	24.9584174	
LS183	PQ	Marmor	Straße nach Achlada		35.40231456	24.9584174	
LS184	PQ	Heller Schiefer mit Fältelung	Straße nach Achlada	052/70	35.39821606	24.96834157	
LS185	PQ	Heller Schiefer	Straße nach Achlada		35.39672588	24.97365536	
LS186	PQ	grünlicher Schiefer	Straße nach Achlada		35.39846768	24.96817175	
LS187	PQ	Phyllit mit Quarzgang	E Almyrida		35.40585922	24.87498578	
LS188	PQ	Massiger Phyllit	E Almyrida	020/50	35.40596705	24.87533228	
LS189	Bali	Grünlichem Schiefer	Faltenkern W Fodele		35.38433793	24.94216438	1
LS190	Bali	grünlicher Schwarzschiefer	Faltenkern W Fodele	356/65	35.38416667	24.94194444	1
LS191	Bali	Schiefer	Faltenkern W Fodele		35.38384996	24.94239596	1
LS192A	PQ	Verfalteter Schiefer mit Qz-Gang	E Sisses		35.39792822	24.90125072	
LS192B	PQ	Verfalteter Schiefer	E Sisses		35.39792822	24.90125072	
LS193	PQ/Pali	Heller Schiefer	E Sisses		35.39783321	24.90126749	
LS194	Bali	Schwarzschiefer	E Sisses		35.39667303	24.90089399	
LS195	Bali	Schwarzschiefer	E Sisses		35.39524237	24.90188548	
LS196	PQ?	Phyllit mit Krenulation	E Sisses		35.39526257	24.91236504	
LS197	PQ	Schwarzschiefer mit Qz-Gang	Pera Galinos	039/65	35.39715621	24.92302515	
LS198	PQ	Quarzit mit Qz-Gängen	Pera Galinos		35.39749199	24.92300444	2
LS199	PQ	Bunter Schiefer mit Cc	Pera Galinos		35.3974357	24.9231606	
LS200	PQ	Phyllit	Pera Galinos	022/50	35.40017336	24.92428268	
LS201	PQ	Ab-Schiefer mit großen Fsp?	Pera Galinos		35.40026694	24.92448175	
LS202	PQ	Albitschiefer	Pera Galinos	359/41	35.40268416	24.92111726	1
LS203	PQ	grobklast. Metasediment, porös	Pera Galinos		35.40559339	24.92458259	
LS204	PQ	Bunter Phyllit	Pera Galinos	352/60	35.40561606	24.92472122	
LS205	PQ	Quarzlinse, konkordant	SE Fodele Vassilikon		35.37672838	24.9648112	
LS206	PQ	Albitschiefer	SE Fodele Vassilikon		35.37672838	24.9648112	1
LS207	PQ	Verfalteter Quarzgang in Phyllit	SE Fodele Vassilikon	056/37	35.37328865	24.9741012	
LS208	PQ	Heller Schiefer wie LS178	SE Fodele Vassilikon	130/24	35.37474706	24.98010884	1
LS209	PQ	Schiefer	SE Fodele Vassilikon		35.37609973	24.9819604	
LS210	PQ	Schiefer	SE Fodele Vassilikon		35.37609973	24.9819604	
LS211	PQ	"Gneis"	SE Fodele Vassilikon		35.37609973	24.9819604	

Name	Unit	Description	Locality	Orientation	Latitude	Longitude	Thin Sec.
LS212	PQ	Silbrig-grüner Phyllit	SE Fodele Vassilikon		35.37609973	24.9819604	
LS213	PQ	Schiefer	SE Fodele Vassilikon		35.37615158	24.98205428	
LS214	PQ	Silbergrüner Schiefer	SE Fodele Vassilikon		35.37615158	24.98205428	1
LS215	PQ	Hellgrauer Schiefer mit Qz-Gang	SE Fodele Vassilikon		35.37619198	24.98297059	
LS216	PQ	Grüner Schiefer mit Qz-Gang	SE Fodele Vassilikon		35.37619198	24.98297059	1
LS217	PQ	Violetter Schiefer	SE Fodele Vassilikon	299/44	35.37675252	24.98144391	1
LS218	PQ	Quarzgang aus Boudin neck	SE Fodele Vassilikon		35.37242163	24.97693746	
LS219	PQ	Gneis mit Karpholit	N Fodele, nach Achlada		35.40179731	24.95785128	
LS221	PQ	Phyllit mit Quarzgang	N Fodele		35.39879784	24.95215151	1
LS222	PQ	Phyllit mit Quarzgang	N Fodele		35.39879784	24.95215151	1
LS223	PQ (?) Bali	grobklastisches Metasediment	W Bali		35.41370837	24.77451375	
LS224	PQ (?) Bali	grobkörniger Gneis	W Bali	350/26 (zweit	35.41416116	24.77459581	1
LS225	PQ (?) Bali	Chert	W Bali		35.41428399	24.77385144	1
LS226	PQ (?) Bali	Schwarzschiefer	W Bali		35.41428399	24.77385144	1
LS227	PQ (?) Bali	Albitschiefer	W Bali	323/46	35.41435394	24.77356007	1
LS228	PQ (?) Bali	Albitschiefer	W Bali		35.41428446	24.77417487	1
LS229	PQ (?) Bali	heller Schiefer	W Bali	008/31	35.41372191	24.7746041	
LS230	UF/Bali	dunkler Metasandstein	W Bali		35.40904732	24.75460413	
LS231	UF/Bali	Schwarzer Metasandstein	W Bali		35.40904732	24.75460413	
LS232	Sisses (???	schwarzer harter Schiefer	SW Bali		35.40669112	24.76000979	
LS233	TPQ?	Quarzgang mit Fsp?	W nach Almyrida	016/46	35.40570466	24.86430975	1
LS234	TPQ	Quarzgänge in Albitschiefer	W nach Almyrida		35.40555714	24.86184463	2
LS235	TPQ	Albitschiefer (?)	NW Fodele		35.39114345	24.94189373	1
LS236	TPQ	Schwarzschiefer + Qz-Gang	NW Fodele	009/60	35.39155073	24.94251768	
LS237	TPQ	Quarzgang in Quarzit	NW Fodele		35.391339	24.93601659	1
LS238	TPQ	Albitschiefer mit Qz-Lage	NW Fodele	029/31	35.39510826	24.9377094	1
LS239	TPQ	"Gneis"	NW Fodele		35.39519987	24.93768836	1
LS240	TPQ	Quarzreicher Schiefer	NW Fodele		35.4002977	24.94285346	1
LS241	TPQ	violetter Schiefer	NW Fodele		35.40059329	24.94303585	1
LS242	TPQ	Violetter Schiefer	Schweinezucht		35.39314978	24.93018011	
LS243	TPQ	Quarzgang	Faltenkern		35.38456307	24.93968334	1
LS244	Bali	Quarzkonglomerat	Bali		35.41036311	24.77973743	1
LS245	Bali	Quarzkonglomerat	Bali		35.41036311	24.77973743	1
LS246	Bali	Quarzkonglomerat	Bali		35.41036311	24.77973743	
LS247	TPQ	Marmor N Evita	N Evita, Bali		35.41752134	24.78076723	1+1(Dia)
LS248	TPQ	Phyllit bei Marmor N von Evita	N Evita, Bali	340/35	35.41752134	24.78076723	1
LS249	Untere Fo	brekziierter Dolomitmarmor	Pera Galinos		35.3969889	24.92276925	1
LS250	TPQ/BALI	Chertboudin mit boudin neck	E Sisses	062/50	35.39522954	24.90030776	1
LS251	TPQ	Quarzgang an Scherband	E Sisses	058/44	35.39823404	24.90161316	1
LS252	TPQ	Verfalteter Albitschiefer	E Sisses		35.40111012	24.90291964	
LS253	TPQ	Quarzgang im Albitschiefer	N Almyrida	118/45	35.40930842	24.87487396	
LS254	TPQ	Quarzgänge in Quarzit	N Almyrida	044/56	35.4107848	24.87859536	2
LS255	TPQ	Albitschiefer grobkörnig	N Almyrida	070/16	35.41398133	24.88240485	1
LS256	TPQ	Qz-Gang in hellgrünem Schiefer	S Fodele	098/20	35.3574171	24.96524027	1
LS257	Bali	Schiefer Bali mit Qz-Gang	W Bali	001/56	35°24'38'' N	24°46'12'' E	1
LS258	Bali	Schiefer Bali	W Bali		35°24'38'' N	24°46'12'' E	
LS259	PQ	Schiefer PQ mit Qz-Gang	W Bali		35°24'48'' N	24°44'09'' E	1
LS260	PQ	Albitschiefer	W Bali	024/23	35°24'48'' N	24°44'09'' E	1
LS261A	Bali	Qz-Kongo Komp. Rhyolith	Bali beach		35° 24' 32" N	24°47' 00" E	1
LS261B	Bali	Qz-Kongo Komp. Diaphtorit	Bali beach		35° 24' 32" N	24°47' 00" E	1
LS261C	Bali	Qz-Kongo Komp. Metapsammit?	Bali beach		35° 24' 32" N	24°47' 00" E	1
LS261D	Bali	Qz-Kongo . Diaphtorit	Bali beach		35° 24' 32" N	24°47' 00" E	1
LS261E	Bali	Qz-Kongo Komp. Rhyolith	Bali beach		35° 24' 32" N	24°47' 00" E	1
LS261F	Bali	Qz-Kongo Komp. Glimmerschiefer	Bali beach		35° 24' 32" N	24°47' 00" E	1
LS261G	Bali	Qz-Kongo Komp. Albitit	Bali beach		35° 24' 32" N	24°47' 00" E	1
LS263	PQ (?) Bali	kleiner Quarzgang diskordant	S Fodele		35.360048	24.964258	1
LS264	PQ	Metavulkanit Panormo	Panormo		35.421681	24.696131	1
LS265	PQ	konkordanter Quarzgang	Panormo	310/60	35.422371	24.696669	
LS267	PQ	konkordanter Quarzgang	Bali W	325/46	35.410833	24.767222	
LS272	PQ	Metavulkanit blau	Bali W		35.414942	24.767427	
LS274	PQ	Marmor	Achlada	160/50	35.406411	24.986824	
LS275	Bali	Rhyolith Komponente Qz-konglo	Bali beach		35.409266	24.783171	1
LS277	Bali	verfalteter Chert	Bali W	355/30	35.413829	24.768472	
LS278	PQ	Metavulkanit grün	Bali W	340/30	35.414801	24.768353	1

Name	Unit	Description	Locality	Orientation	Latitude	Longitude	Thin Sec.
LS279	PQ	konkordanter Qz-Gang	Bali W	004/49	35.41466	24.768259	
LS281	PQ	konkordanter Qz-Gang verfaltet	Bali W		35.415749	24.76715	
LS282	PQ	gebänderter Metavulkanit	Bali W		35.415153	24.767166	1
LS283	PQ	Marmor	Bali W		35.412793	24.761191	
LS284	PQ	diskordant und konkordant	Bali W	PQ	35.412404	24.757493	
LS285	Bali	Brekzie Schwarzschiefer	Bali W		35.411064	24.762127	
LS286	Sisses	Sisses Konglomerat	New Road	068/29	35.392807	24.893244	2
LS287	Sisses	Phyllit mit Scherbandfoliation	Bali W	012/60	35.405532	24.755407	
LS288	Sisses	Metasandstein mit Quarzlagen	Bali W	012/36	35.403217	24.754075	
LS290	Sisses	Dunkler Marmor	Bali W	018/55	35.403974	24.753907	
LS291	PQ	Quarzit/Phyllit mit Qz-Lagen	Faratsi		35.33955	24.792426	
LS293	Aloides be	Gigilos Sandstein	Vosakos		35.363471	24.845004	
LS294	PQ	diskordant und konkordant	Kontakt zu Vasilikon		35.372483	24.989804	
LS295	PQ	diskordant	Kontakt zu Vasilikon		35.372483	24.989804	
LS296	PQ	diskordant	Kontakt zu Vasilikon	029/40	35.372483	24.989804	
LS297	PQ	Diskordant an Scherbandgrenze	Weg zum Vasilikon	040/59	35.380956	24.979762	
LS298	PQ	konkordant	Weg zum Vasilikon		35.384776	24.976688	
LS300	PQ	Albitschiefer mit Scherbändern	Aliki	028/64	35.412209	24.880921	
LS301	PQ	konkordant	NE Aliki	080/35	35.412209	24.880921	
LS302	PQ	konkordant	NE Aliki	348/71	35.412209	24.880921	
LS303	Bali	konkordant	Bali W Kontakt	332/40	35.413006	24.774674	
LS304	Bali	konkordant	Bali W Kontakt	003/51	35.413006	24.774674	
LS305	PQ?	konkordant	Bali W Kontakt		35.413006	24.774674	
LS307	PQ	konkordant und verfaltet	S Vasilikon	354/35	35.353699	24.988586	
LS308	PQ	konkordant	S Vasilikon	342/15	35.349261	24.990708	
LS309	PQ	Marmor	Damasta				1
LS310	PQ	Konkordant und diskordant	E Sisses	130/35	35.401637	24.899532	
LS311	PQ	Konkordant und diskordant	E Sisses	008/09	35.401875	24.898796	
LS312	PQ	Konkordant und diskordant	E Sisses	032/23	35.403748	24.896319	1
LS313	PQ	Konkordant und diskordant	E Fodele	147/37	35.376474	24.977702	
LS314	PQ	konkordant und verfaltet	E Fodele	168/50	35.376474	24.977702	
LS315	PQ	subkonkordant	E Fodele	350/25	35.381119	24.969167	
LS316	PQ	subkonkordant	E Fodele	023/40	35.379643	24.971495	
LS317	PQ	Konkordant und diskordant	E Fodele	029/44	35.378752	24.972153	1
LS318	PQ	kleine Qz-Linsen und Lagen	E Fodele	066/30	35.374281	24.975472	1
LS319	PQ	subkonkordant	E Fodele	034/30	35.374416	24.972502	
LS320	PQ	subkonkordant	E Fodele		35.371473	24.969666	
LS321	PQ	Phyllit mit Lawsonit?	Westkreta Strovles		35.340573	23.665531	
LS322	Sisses	Metabauxit	S Sisses		35.386667	24.891833	
LS323	Aloides be	Chertkonkretion	S Sisses		35.36915	24.871412	
EW1	PQ	Quarzit mit schwarzen Qz-Komp.	Pera Galinos		35°24'02.2"N	24°55'26.6"E	
MW1	Bali	Tonschiefer	E von Sisses	042/46?	35°23'37.8"N	24°54'04.1"E	
AG23	Untere Fo	unreiner foliierter Marmor	Mülldeponie	024/28	35° 23' 26'' N	24° 55' 29'' E	1
MV1	Sisses	Grüner Phyllit	Mülldeponie	017/5	35° 23' 25'' N	24° 55' 32,5'' E	
SO1	Sisses?	Dolomit mit Gang	Mülldeponie		35° 23' 18'' N	24° 55' 48'' E	1
JG11	Bali	grobklastisches Metasediment	Mülldeponie	013/17	35° 23' 12'' N	24° 55' 53'' E	2
GW1	Bali / PQ	Metasandstein	W Almyrida	024/32	35° 24' 20'' N	24° 51' 39,7'' E	1
GW2	Bali/PQ	Glimmerschiefer	W Almyrida	030/30	35° 24' 21'' N	24° 51' 41,6'' E	3
MV2	PQ	Quarzit	Nähe Pera Galinos??	334/29			
MS1	Aloides be	Calcitmarmor	S Sisses	010/35	35° 22' 10'' N	24° 52' 20'' E	
MS1	Bali	Schiefer	Eingang Mülldeponie		35.391917 N	24.921667 E	2
MS2	Sisses?	Schiefer	Mülldeponie		35.387972 N	24.930500 E	1
MS5	Bali?	Chert?	Faltenkern		35.382444 N	24.947778 E	1
CG1	PQ	verfalteter Quarzit	Almyrida	024/60	35°24'33.4"N	24°52'12.9"E	
BH1	Bali	Schwarzer Schiefer	E Sisses	350/17	35° 23' 41'' N	24° 54' 1'' E	1
BH2	Stromatoli	Stromatolithmarmor	S Sisses	290/52	35° 22' 47,6'' N	24° 53' 17,5'' E	
RH1	PQ	Glimmerschiefer	Straße westlich Bali	324/24	35° 24' 45'' N	24° 46' 24'' E	1
SL01	PQ	Phyllit	NE Fodele		35°23'05.9"N	24°57'28.9"E	
SL02	Sisses	Grüner Phyllit	NW Fodele	070/45	35°23'13.2"N	24°56'57.7"E	
SL03	Stromatoli	Fe-Mineralisation	SW Fodele		35° 22' 03'' N	24° 57' 06'' E	
PK01	Bali	boudin-neck Phyllit	Bali Nase in Hafenbucht		35° 24' 50'' N	24° 46' 60'' E	1
SZ1	PQ	Quarzgang PQ	Almyrida	006/60	35°24'33,3''	24°52'12,8''	1
SZ2	PQ	Quarzgang PQ	Almyrida		35°24'33,3''	24°52'12,8''	1

Name	Unit	Description	Locality	Orientation	Latitude	Longitude	Thin Sec.
SZ3	PQ	Quarzgang PQ	Pera Galinos		35°24'14,2''	24°55'18,6''	1
SZ4	PQ	Quarzgang PQ	Bali	025/27	35°24'44,5''	24°46'53,3''	1
SZ5	PQ	Quarzgang PQ	Pera Galinos		35°23'50,8''	24°55'22,7''	2
SZ6	PQ	Quarzgang PQ	Pera Galinos		35°23'56,6''	24°55'21,9''	1
TK1	PQ	Albitschiefer	Aliki		35°24'38''	24°52'32''	1
TK2	PQ	Albitschiefer	Aliki		35°24'36''	24°52'31''	1
TK3	PQ	Albitschiefer	Bali Evita		35°24'57''	24°47'05''	1
TK4	PQ	Albitschiefer	Bali Evita		35°24'57''	24'47'05''	
TK5	PQ	Albitschiefer	Bali Evita		35°24'57''	24'47'05''	1
PM1	PQ	Quarzgang	Bali W	338/40	35.413643	24.774527	1
PM2	PQ	Quarzgang	Bali W	184/21	35.413643	24.774527	
PM3	PQ	Quarzgang	Aliki	346/42	35.409257	24.875025	1
PM4	PQ	Quarzgang	Aliki	017/75	35.409257	24.875025	1
PM5	PQ	Quarzgang	Bali	002/34	35.413643	24.774527	1
JL1, PD1	PQ		Weg zum Vasilikon		35.38075	24.979425	
JL2	PQ		Weg zum Vasilikon		35.374829	24.980616	
	Proben älter als 2016						
AN2	PQ	Phyllit	Pera Galinos		35.394667	24.924278	1
AN4	PQ	Carbonatic phyllite	Pera Galinos		35.395972	24.922639	1
AN7	PQ	Quarzit	Pera Galinos		35.397894	24.922381	1
AN8	PQ	Phyllit, crenulation cleavage	Pera Galinos		35.397894	24.922381	1
RG1	Bali	Quarzkonglomerat					1
RG2	Bali/PQ	Chert?					1
RG3	Bali/PQ	Metasandstein					1
RG4	Bali/PQ	Schiefer					1
RG5	Bali/PQ	Quarzit					2
RG7	Bali/PQ	Marmor					1
RG9	Bali/PQ	Marmor					1
RG10	Bali/PQ	Quarz					1
RG11	PQ	Metavulkanit	W Bali				1
MB1a-c	Bali	Schiefer mit Qz-Gängchen	Pelekhida		35°24'29''N	24°50'57''E	3+
MB2	PQ	Quarzit mit Quarzgang					2
MH3	Bali	Quarzkonglomerat					1
MH4	Bali	Quarzkonglomerat					1
MH5	Bali	Quarzkonglomerat					1
P022	Sisses	Schiefer	NW Sportplatz		35°23'21''N	24°55'59''E	1
P025	Sisses	Schiefer	ESE Sportplatz		35°23'14''N	24°56'10''E	1
P050	Balil?	Schiefer mit Quarzgang	Mülldeponie		35°23'08''N	24°55'51''E	1
P101	U Fodele	Karbonat	N Mülldeponie		35°23'35''N	24°55'27''E	2
XA	Bali	Metasandstein					1
XB75	Bali	Quarzkonglomerat					1
XB125	Bali	Quarzkonglomerat					2
XB710	Bali	Quarzkonglomerat					1
XC11	Bali	Quarzkonglomerat					1
XC18	Bali	Quarzkonglomerat					1
CT62	PQ	Quarzit	Pera Galinos				1
CT75x	Bali	deformiertes Qz-Kongo	Faltenkern				1
CT83	PQ	Schiefer	Eingang Mülldeponie				2
CT756	Bali	Qz-Kongo-Metasandstein gradiert	Bali beach				1
CT757	Bali	deformiertes Qz-Kongo	Faltenkern				2
CT768		Quarzit					1
CT780		Chertkomponente in Schiefer					4
CT781	Bali	Metasandstein	Eingang Mülldeponie		35°23'31''N	24°55'18''E	1
CT782		Schiefer					3
CT783		Schiefer					2
CT784		Quarzit					2
CT785	Bali	Quarz-Konglomerat	Bali beach				13
CT811		Quarzit					1
CT812		Schiefer mit Knickfalten					1
CT814		Schiefer mit Crenulation Cleavage					2
CT817	Bali	Schiefer mit Qz-Gang	Pelekhida		35°24'29''N	24°50'57''E	2
CT818	Bali	Quarzkonglomerat					1
CT819	Bali	deformiertes Qz-Kongo	Faltenkern				1

grain	$^{207}Pb^{a}$ (cps)	$\frac{Th^{b}}{U}$	$^{206}Pbc^{c}$ (%)	$\frac{^{206}Pb^{d}}{^{238}U}$	±2σ (%)	$\frac{^{207}Pb^{d}}{^{235}U}$	±2σ (%)	$\frac{^{207}Pb^{d}}{^{206}Pb}$	±2σ (%)	rho^{e}	$\frac{^{206}Pb}{^{238}U}$	±2σ (Ma)	$\frac{^{207}Pb}{^{235}U}$	±2σ (Ma)	$\frac{^{207}Pb}{^{206}Pb}$	±2σ (Ma)	conc. (%)
LS144 PQ																	
A563	734	1.64	2.2	0.07390	3.3	0.5766	8.6	0.05659	7.9	0.39	460	15	462	32	475	175	97
A564	3319	0.76	0.8	0.07572	3.0	0.5895	4.7	0.05646	3.6	0.64	471	14	471	18	471	81	100
A544	847	1.08	0.9	0.08688	3.3	0.7	7.3	0.05844	6.5	0.45	537	17	539	31	546	143	98
A598	1164	1.62	3.5	0.08889	3.2	0.7231	9.2	0.05901	8.6	0.35	549	17	553	40	567	188	97
A574	300	1.02	0.7	0.08935	3.7	0.7296	10.0	0.05922	9.3	0.37	552	20	556	44	575	202	96
A591	1566	0.77	0.2	0.09071	3.1	0.7367	5.3	0.0589	4.3	0.58	560	16	560	23	563	95	99
A583	1115	0.57	2.5	0.09123	3.1	0.7528	8.2	0.05984	7.6	0.37	563	17	570	37	598	166	94
A566	3183	1.15	1.7	0.09128	3.1	0.7412	5.1	0.05889	4.0	0.61	563	17	563	22	563	88	100
A590	985	0.69	0.1	0.09146	3.1	0.7495	5.5	0.05944	4.5	0.57	564	17	568	24	583	98	97
A589	977	0.63	0.4	0.09188	3.0	0.75	5.1	0.0592	4.0	0.60	567	17	568	22	575	88	99
A579	3298	0.76	4.5	0.09290	3.1	0.7563	8.2	0.05904	7.5	0.39	573	17	572	36	569	164	101
A561	2797	0.99	1.2	0.09291	3.0	0.7585	4.8	0.05921	3.7	0.63	573	17	573	21	575	81	100
A554	769	0.93	0.3	0.09394	3.3	0.7688	5.7	0.05936	4.7	0.57	579	18	579	25	580	101	100
A582	1262	1.02	0.3	0.09408	3.1	0.7763	4.9	0.05984	3.8	0.63	580	17	583	22	598	82	97
A26	9845	1.07	0.5	0.09451	2.1	0.7841	2.9	0.06017	2.0	0.73	582	12	588	13	610	42	95
A558	2604	1.23	0.2	0.09463	3.0	0.7757	4.0	0.05945	2.6	0.76	583	17	583	18	584	57	100
A14	11272	0.42	2.5	0.09485	2.1	0.7887	4.2	0.06031	3.6	0.50	584	12	590	19	615	78	95
A66	6613	0.86	8.1	0.09563	2.3	0.7834	9.5	0.05941	9.2	0.24	589	13	587	43	582	201	101
A565	1539	1.20	0.3	0.09578	3.0	0.806	4.3	0.06103	3.0	0.71	590	17	600	20	640	65	92
A557	3252	0.93	5.4	0.09601	3.1	0.7859	7.8	0.05937	7.2	0.39	591	17	589	35	581	156	102
A577	3164	0.58	0.2	0.09625	3.0	0.7924	4.0	0.05971	2.6	0.76	592	17	593	18	593	56	100
A555	4787	0.72	12.9	0.09643	3.3	0.7956	10.5	0.05984	9.9	0.32	593	19	594	48	598	215	99
A09	12760	1.95	12.3	0.09694	2.5	0.8033	10.8	0.0601	10.5	0.23	596	14	599	50	607	227	98
A25	11773	0.36	0.2	0.09716	2.1	0.8096	2.4	0.06043	1.1	0.89	598	12	602	11	619	23	97
A587	561	0.76	0.4	0.09779	3.2	0.8128	6.3	0.06028	5.4	0.51	601	19	604	29	614	117	98
A593	790	0.84	6.2	0.09795	3.4	0.8061	11.6	0.05969	11.0	0.29	602	20	600	54	592	239	102
A23	1000	0.59	12.4	0.09809	3.0	0.8182	16.4	0.06049	16.1	0.19	603	18	607	78	621	348	97
A11	2509	0.78	0.4	0.09838	2.1	0.813	3.4	0.05994	2.6	0.63	605	12	604	16	601	57	101
A12	3481	0.76	0.5	0.09862	2.2	0.8081	3.1	0.05943	2.2	0.70	606	13	601	14	583	48	104
A64	7019	0.66	10.0	0.09882	2.4	0.8139	9.1	0.05973	8.8	0.26	607	14	605	42	594	191	102
A54	7042	0.61	0.2	0.10070	2.1	0.836	2.6	0.06024	1.6	0.79	618	12	617	12	612	35	101

grain	^{207}Pb[a] (cps)	Th[b] / U	^{206}Pbc[c] (%)	^{206}Pb[d] / ^{238}U	±2σ (%)	^{207}Pb[d] / ^{235}U	±2σ (%)	^{207}Pb[d] / ^{206}Pb	±2σ (%)	rho[e]	^{206}Pb / ^{238}U	±2σ (Ma)	^{207}Pb / ^{235}U	±2σ (Ma)	^{207}Pb / ^{206}Pb	±2σ (Ma)	conc. (%)
LS151 PQ																	
A459	854	1.44	0.4	0.08035	3.1	0.6428	6.7	0.05802	5.9	0.47	498	15	504	27	530	129	94
A474	3007	0.22	0.1	0.08608	3.0	0.6912	4.7	0.05824	3.6	0.64	532	15	534	20	539	79	99
A444	689	0.94	0.5	0.08693	3.1	0.7081	6.1	0.05908	5.3	0.51	537	16	544	26	570	114	94
A522	4054	0.09	0.1	0.08793	3.0	0.7148	3.7	0.05896	2.1	0.82	543	16	548	16	566	46	96
A411	1240	0.71	0.1	0.08841	3.1	0.7152	4.6	0.05867	3.3	0.68	546	16	548	20	555	73	98
A438	494	2.16	1.9	0.08848	3.4	0.7224	7.0	0.05922	6.1	0.48	547	18	552	30	575	134	95
A464	5625	0.25	0.5	0.08984	3.0	0.7257	3.8	0.05858	2.3	0.79	555	16	554	16	552	51	101
A527	951	1.97	5.4	0.09040	3.4	0.7443	10.8	0.05971	10.2	0.31	558	18	565	48	593	222	94
A516	1998	0.77	0.6	0.09290	3.0	0.7628	4.8	0.05955	3.7	0.63	573	17	576	21	587	80	98
A499	5402	0.98	0.2	0.09629	3.0	0.7904	3.7	0.05953	2.3	0.80	593	17	591	17	587	49	101
A447	2358	0.14	0.1	0.09958	3.1	0.8277	4.0	0.06029	2.5	0.77	612	18	612	18	614	54	100
A446	1876	0.21	0.1	0.10020	3.1	0.8351	4.1	0.06045	2.7	0.76	616	18	616	19	620	57	99
A437	2429	0.38	0.1	0.10030	3.0	0.8347	4.2	0.06033	2.9	0.72	616	18	616	20	615	63	100
A485	1686	0.50	1.3	0.10130	3.3	0.8506	5.6	0.06089	4.5	0.59	622	20	625	26	635	96	98
A428	1992	0.22	0.5	0.10210	3.0	0.8445	4.8	0.05997	3.8	0.63	627	18	622	23	602	81	104
A479	2676	0.34	7.0	0.10220	3.2	0.8663	8.3	0.06145	7.6	0.38	627	19	634	40	655	164	96
A417	734	0.91	0.8	0.10270	3.2	0.8654	5.5	0.06109	4.4	0.59	630	19	633	26	642	95	98
A487	2596	0.38	0.1	0.10290	3.0	0.8621	3.8	0.06078	2.3	0.80	631	18	631	18	632	50	100
A418	3667	0.86	0.2	0.10310	3.0	0.8596	3.9	0.06045	2.5	0.77	633	18	630	18	620	53	102
A429	1337	1.54	0.8	0.10340	3.1	0.8672	7.0	0.06084	6.3	0.44	634	19	634	34	634	136	100
A518	971	0.60	0.4	0.10360	3.2	0.8658	5.6	0.06061	4.6	0.58	636	20	633	27	625	99	102
A478	808	0.49	0.4	0.10470	3.2	0.8701	5.2	0.06028	4.1	0.62	642	20	636	25	614	88	105
A423	1692	0.01	0.0	0.10510	3.0	0.9028	4.5	0.06233	3.3	0.67	644	19	653	22	685	71	94
A490	1875	0.40	0.3	0.10820	3.1	0.9235	4.3	0.06187	3.0	0.72	663	20	664	21	670	64	99
A519	1842	0.46	0.2	0.10920	3.1	0.9405	4.3	0.06248	3.0	0.71	668	19	673	21	690	65	97
A482	1313	1.43	0.2	0.10970	3.1	0.9368	5.7	0.06197	4.8	0.54	671	20	671	28	673	103	100
A521	2684	0.40	0.2	0.11050	3.1	0.9467	4.2	0.06211	2.9	0.73	676	20	676	21	678	62	100
A486	378	0.38	0.5	0.11130	3.5	0.9788	6.1	0.06378	4.9	0.58	680	23	693	31	734	104	93
A520	1984	0.49	0.2	0.11210	3.1	0.9599	4.4	0.06208	3.2	0.69	685	20	683	22	677	69	101
A449	4274	0.79	0.9	0.11560	5.9	1.024	7.2	0.06423	4.0	0.83	705	40	716	37	749	84	94

grain	^{207}Pb[a] (cps)	U[b] (ppm)	Pb[b] (ppm)	Th[b] / U	^{206}Pbc[c] (%)	^{206}Pb[d] / ^{238}U	±2σ (%)	^{207}Pb[d] / ^{235}U	±2σ (%)	^{207}Pb[d] / ^{206}Pb	±2σ (%)	rho[e]	^{206}Pb / ^{238}U	±2σ (Ma)	^{207}Pb / ^{235}U	±2σ (Ma)	^{207}Pb / ^{206}Pb	±2σ (Ma)	conc. (%)
LS 162 NW Bali																			
A091	7364	590	23	0.02	0.2	0.04290	2.1	0.3099	2.6	0.05239	1.6	0.79	271	6	274	6	302	37	90
A85	5392	348	20	0.65	0.0	0.05313	2.1	0.3898	2.8	0.05321	1.8	0.76	334	7	334	8	338	41	99
A83	4873	124	8	0.64	5.1	0.05396	2.3	0.3979	6.0	0.05348	5.5	0.38	339	7	340	17	349	125	97
A121	11771	773	48	0.88	1.3	0.05524	2.0	0.4052	3.3	0.05321	2.5	0.63	347	7	345	10	338	57	103
A97	3879	233	14	0.63	0.1	0.05627	2.1	0.4159	3.3	0.0536	2.5	0.64	353	7	353	10	354	57	100
G 102	3703	204	13	0.64	0.9	0.05724	2.2	0.4229	4.0	0.05359	3.4	0.54	359	8	358	12	354	76	101
A98	4172	237	14	0.48	0.4	0.05741	2.1	0.4255	3.3	0.05375	2.6	0.63	360	7	360	10	361	58	100
A122	6640	364	25	0.75	0.4	0.06185	2.1	0.4688	2.5	0.05497	1.4	0.83	387	8	390	8	411	32	94
A128	3743	156	12	0.17	0.3	0.07689	2.1	0.6018	2.9	0.05676	2.0	0.74	478	10	478	11	482	43	99
A88	2125	90	7	0.34	0.3	0.07801	2.1	0.6102	4.0	0.05673	3.4	0.52	484	10	484	16	481	76	101
A94	7880	341	26	0.20	0.3	0.07881	2.1	0.6186	3.0	0.05692	2.2	0.69	489	10	489	12	489	48	100
A142	4522	174	14	0.14	0.3	0.08114	2.1	0.6431	2.9	0.05749	2.0	0.73	503	10	504	11	510	43	99
A115	18766	756	64	0.53	0.2	0.08154	2.1	0.6494	2.4	0.05776	1.3	0.84	505	10	508	10	521	29	97
A132	5744	193	18	0.88	0.8	0.08255	2.1	0.6582	3.4	0.05783	2.7	0.61	511	10	514	14	523	60	98
A143	2615	102	9	0.38	0.3	0.08412	2.1	0.6702	3.3	0.05778	2.5	0.64	521	11	521	14	521	56	100
A130	10063	265	22	0.14	0.9	0.08607	2.3	0.7024	3.4	0.05919	2.4	0.70	532	12	540	14	574	52	93
A109	516	17	2	0.65	0.7	0.08826	2.7	0.7138	6.1	0.05865	5.5	0.43	545	14	547	26	554	120	98
A134	4544	162	14	0.21	0.2	0.08869	2.1	0.716	3.0	0.05855	2.1	0.71	548	11	548	13	551	46	99
A114	10225	347	29	0.04	0.1	0.08949	2.1	0.72	2.7	0.05835	1.7	0.78	553	11	551	11	543	37	102
A125	6589	208	24	1.47	0.3	0.09019	2.1	0.7409	3.7	0.05958	3.1	0.57	557	11	563	16	588	67	95
A129	2947	103	10	0.66	0.6	0.09114	2.2	0.7389	3.3	0.0588	2.5	0.67	562	12	562	14	560	54	100
A79	7077	236	23	0.58	0.1	0.09181	2.1	0.7443	3.1	0.0588	2.3	0.67	566	11	565	13	560	50	101
A89	5328	177	17	0.58	0.2	0.09259	2.1	0.7512	3.2	0.05885	2.4	0.67	571	12	569	14	561	51	102
A123	5415	178	20	1.22	0.1	0.09331	2.1	0.7553	3.3	0.05871	2.6	0.64	575	12	571	15	556	56	103
A126	7738	248	22	0.16	0.1	0.09378	2.2	0.7653	2.7	0.05918	1.7	0.79	578	12	577	12	574	36	101
A127	6732	220	20	0.22	0.1	0.09487	2.1	0.7774	3.0	0.05943	2.2	0.69	584	12	584	13	583	47	100
A78	1927	63	7	1.11	0.8	0.09653	2.1	0.7979	3.4	0.05995	2.7	0.62	594	12	596	16	602	58	99
A111	2246	73	9	1.53	0.8	0.09723	2.1	0.7992	3.3	0.05961	2.6	0.63	598	12	596	15	589	56	101
A96	38942	158	31	0.67	27.9	0.09886	3.5	0.8171	10.0	0.05994	9.4	0.35	608	21	606	47	602	202	101
A99	6434	203	21	0.52	0.3	0.09979	2.1	0.8319	2.9	0.06046	2.0	0.72	613	12	615	13	620	43	99
A113	14375	327	33	0.21	2.3	0.09996	2.1	0.8374	3.8	0.06076	3.2	0.56	614	13	618	18	631	69	97
A139	3185	72	8	0.43	1.4	0.10010	2.5	0.8331	4.4	0.06039	3.6	0.57	615	15	615	20	618	78	100
A95	6162	185	22	1.09	0.4	0.10070	2.1	0.8404	3.1	0.06053	2.3	0.68	619	12	619	14	623	49	99

grain	^{207}Pb[a] (cps)	U[b] (ppm)	Pb[b] (ppm)	Th[b]/U	^{206}Pbc[c] (%)	$^{206}Pb/^{238}U$[d]	±2σ (%)	$^{207}Pb/^{235}U$[d]	±2σ (%)	$^{207}Pb/^{206}Pb$[d]	±2σ (%)	rho[e]	$^{206}Pb/^{238}U$	±2σ (Ma)	$^{207}Pb/^{235}U$	±2σ (Ma)	$^{207}Pb/^{206}Pb$	±2σ (Ma)	conc. (%)
LS 154 Lower Fodele																			
A171	705	46	3	0.69	0.8	0.05165	2.3	0.3764	5.6	0.05285	5.1	0.40	325	7	324	16	322	117	101
A184	7809	458	26	0.53	0.3	0.05196	2.2	0.3847	3.1	0.0537	2.1	0.72	327	7	330	9	359	48	91
9 150	7954	397	20	0.11	0.1	0.05291	2.0	0.3907	2.6	0.05356	1.6	0.79	332	7	335	7	352	36	94
A169	31658	1302	70	0.10	0.6	0.05764	2.5	0.4351	2.9	0.05474	1.3	0.88	361	9	367	9	402	30	90
A163	5449	206	14	0.54	3.1	0.05993	2.2	0.4465	6.2	0.05403	5.8	0.36	375	8	375	20	372	130	101
A155	8086	370	23	0.22	0.3	0.06539	2.2	0.5021	2.7	0.0557	1.5	0.83	408	9	413	9	440	33	93
A172	2768	127	8	0.34	0.1	0.06586	2.2	0.5011	3.0	0.05518	2.0	0.74	411	9	412	10	420	45	98
A154	16521	665	45	0.35	0.9	0.06622	2.4	0.5025	3.7	0.05504	2.9	0.64	413	10	413	13	414	64	100
A202	17261	817	61	0.74	0.2	0.06709	2.3	0.5117	2.7	0.05532	1.5	0.83	419	9	420	9	425	34	98
A173	3848	170	13	0.60	1.0	0.07023	2.1	0.5359	4.0	0.05535	3.4	0.53	438	9	436	14	426	76	103
A219	14395	504	39	0.15	0.2	0.08038	2.1	0.6434	2.4	0.05805	1.2	0.86	498	10	504	10	532	27	94
A214	27010	980	79	0.23	1.2	0.08172	2.2	0.6496	3.0	0.05766	2.1	0.72	506	11	508	12	517	46	98
A180	26610	641	54	0.15	0.9	0.08607	5.3	0.704	5.5	0.05932	1.5	0.96	532	27	541	23	579	34	92
A221	6593	128	14	0.70	1.7	0.08843	3.3	0.7207	7.6	0.0591	6.9	0.43	546	17	551	33	571	149	96
A193	6868	229	23	0.83	0.1	0.08859	2.1	0.719	2.8	0.05887	1.9	0.75	547	11	550	12	562	40	97
A157	16281	386	37	0.28	0.7	0.09284	2.1	0.7661	2.7	0.05985	1.7	0.78	572	12	577	12	598	37	96
A210	3023	62	7	1.13	3.1	0.09361	2.2	0.7597	7.1	0.05887	6.7	0.31	577	12	574	31	562	146	103
A187	15873	454	43	0.35	0.3	0.09458	2.5	0.7871	3.1	0.06036	1.7	0.83	583	14	590	14	617	37	94
A189	18027	565	57	0.45	0.2	0.09812	2.1	0.816	2.5	0.06032	1.2	0.87	603	12	606	11	615	26	98
A205	16355	472	46	0.22	0.2	0.09938	2.1	0.8288	2.6	0.06049	1.6	0.80	611	12	613	12	621	34	98
A213	17314	382	37	0.16	0.5	0.09958	2.1	0.8246	2.6	0.06006	1.5	0.82	612	12	611	12	606	32	101
A216	2591	77	10	1.59	0.7	0.09986	2.2	0.8332	3.4	0.06052	2.6	0.64	614	13	615	16	622	56	99
A174	6501	192	20	0.53	0.3	0.10030	2.1	0.8398	2.9	0.06075	2.0	0.71	616	12	619	14	630	44	98
A156	20681	584	60	0.34	0.3	0.10080	2.1	0.8334	2.8	0.05995	1.8	0.75	619	13	615	13	602	40	103
A161	3560	102	10	0.27	0.1	0.10360	2.1	0.8664	3.2	0.06068	2.4	0.65	635	13	634	15	628	53	101
A209	4240	115	13	0.68	0.1	0.10530	2.1	0.8899	3.2	0.0613	2.4	0.66	645	13	646	16	650	52	99
A160	15632	316	34	0.21	2.1	0.10620	2.1	0.9057	3.6	0.06184	3.0	0.57	651	13	655	18	668	64	97
A170	63782	762	84	0.20	3.1	0.10870	3.3	0.9701	4.6	0.06472	3.2	0.71	665	21	688	23	765	68	87
A204	3009	77	9	0.51	0.2	0.10910	2.1	0.9237	3.2	0.06138	2.4	0.67	668	13	664	16	653	51	102
A203	17450	391	45	0.32	0.7	0.11020	2.1	0.9441	2.8	0.06212	1.9	0.74	674	13	675	14	678	41	99
A218	4678	119	14	0.55	0.3	0.11220	2.1	0.9714	3.0	0.06277	2.1	0.71	686	14	689	15	701	44	98
A208	4287	114	13	0.41	0.4	0.11260	2.1	0.9611	3.0	0.06192	2.2	0.69	688	14	684	15	671	47	102

grain	$^{207}Pb^{a}$ (cps)	U^{b} (ppm)	Pb^{b} (ppm)	$\frac{Th^{b}}{U}$	$^{206}Pbc^{c}$ (%)	$\frac{^{206}Pb^{d}}{^{238}U}$	±2σ (%)	$\frac{^{207}Pb^{d}}{^{235}U}$	±2σ (%)	$\frac{^{207}Pb^{d}}{^{206}Pb}$	±2σ (%)	rho[e]	$\frac{^{206}Pb}{^{238}U}$	±2σ (Ma)	$\frac{^{207}Pb}{^{235}U}$	±2σ (Ma)	$\frac{^{207}Pb}{^{206}Pb}$	±2σ (Ma)	conc. (%)
LS147 Sisses																			
A263	2995	616	12	0.13	1.1	0.01842	2.1	0.1231	6.9	0.04847	6.6	0.31	118	2	118	8	122	154	96
A277	8276	590	25	0.20	2.8	0.04219	2.1	0.3005	5.1	0.05165	4.7	0.40	266	5	267	12	270	108	99
A325	8820	446	17	0.03	1.1	0.04234	3.1	0.3052	3.8	0.05228	2.2	0.81	267	8	270	9	298	50	90
A268	3496	234	11	0.47	0.2	0.04305	2.4	0.3109	3.1	0.05237	2.0	0.77	272	6	275	7	302	45	90
A250	3153	157	8	0.57	7.0	0.04699	2.4	0.3384	9.5	0.05223	9.2	0.25	296	7	296	25	295	210	100
A310	6854	305	19	0.84	0.6	0.05139	3.0	0.3764	5.0	0.05312	4.0	0.61	323	10	324	14	334	90	97
A244	13124	642	35	0.39	2.7	0.05191	2.1	0.3813	4.5	0.05328	4.0	0.46	326	7	328	13	341	91	96
A256	6999	280	16	0.21	2.0	0.05321	3.8	0.3953	4.8	0.05388	2.9	0.79	334	12	338	14	366	66	91
A232	7544	486	24	0.10	0.0	0.05349	2.1	0.3929	2.7	0.05327	1.7	0.77	336	7	336	8	340	39	99
A291	4514	215	13	0.49	0.3	0.05550	2.3	0.4148	2.8	0.05421	1.7	0.81	348	8	352	8	380	37	92
A290	8335	381	26	0.84	0.6	0.05914	2.4	0.443	3.1	0.05433	2.0	0.77	370	9	372	10	385	45	96
A333	5026	206	14	0.40	0.4	0.06457	2.2	0.4942	2.9	0.05551	1.8	0.77	403	9	408	10	433	40	93
A258	6711	315	23	0.52	0.5	0.06841	2.2	0.523	2.7	0.05546	1.4	0.84	427	9	427	9	431	32	99
A302	15425	558	36	0.07	0.9	0.06910	5.2	0.5396	5.5	0.05663	1.7	0.95	431	22	438	20	477	39	90
A327	6187	272	19	0.39	0.2	0.07092	2.1	0.5532	2.7	0.05657	1.7	0.77	442	9	447	10	475	38	93
A279	8923	242	23	0.75	1.1	0.07327	2.9	0.581	3.5	0.05751	2.0	0.82	456	13	465	13	511	44	89
A292	6232	271	23	0.94	0.5	0.07356	2.1	0.5719	2.8	0.05638	1.8	0.75	458	9	459	10	467	41	98
A273	6388	202	16	0.52	0.4	0.07514	2.6	0.5828	3.7	0.05626	2.7	0.69	467	11	466	14	462	59	101
A233	8863	267	21	0.31	0.2	0.07815	3.0	0.6176	3.5	0.05732	1.7	0.87	485	14	488	14	504	38	96
A243	4635	149	15	0.86	0.3	0.08457	2.2	0.6805	2.9	0.05836	2.0	0.74	523	11	527	12	543	43	96
A261	17561	527	45	0.27	0.6	0.08472	2.1	0.6762	2.7	0.05789	1.7	0.77	524	10	525	11	526	37	100
A324	24999	896	80	0.46	0.5	0.08681	2.1	0.6976	2.4	0.05828	1.3	0.85	537	11	537	10	540	28	99
A280	13261	433	39	0.34	0.3	0.08943	2.1	0.7283	2.5	0.05906	1.4	0.83	552	11	556	11	569	30	97
A297	8242	242	23	0.58	1.3	0.08950	2.2	0.7277	3.5	0.05897	2.8	0.62	553	12	555	15	566	60	98
A288	8051	256	23	0.33	0.1	0.09118	2.1	0.7367	2.7	0.0586	1.7	0.77	563	11	560	12	552	38	102
A252	3441	55	6	0.85	4.9	0.09180	2.5	0.7534	7.4	0.05952	6.9	0.34	566	14	570	33	586	150	97
A305	12788	308	29	0.30	0.8	0.09207	2.1	0.7616	2.6	0.05999	1.6	0.80	568	12	575	12	603	34	94
B 241	3831	62	7	0.78	2.9	0.09353	2.2	0.7798	5.7	0.06047	5.3	0.38	576	12	585	26	620	115	93
A312	8834	123	14	0.31	8.2	0.09461	2.4	0.7852	7.6	0.06019	7.2	0.31	583	13	588	35	610	157	95
P 285	7726	110	10	0.03	0.0	0.09574	2.1	0.7899	2.6	0.05984	1.6	0.79	589	12	591	12	598	35	99
A225	5415	161	19	1.38	0.4	0.09618	2.1	0.7988	3.5	0.06023	2.8	0.60	592	12	596	16	612	60	97
A230	7915	251	23	0.02	0.0	0.09785	2.0	0.8058	2.5	0.05973	1.4	0.82	602	12	600	11	594	31	101

8.3 U-Pb data: concordia diagrams

LS162

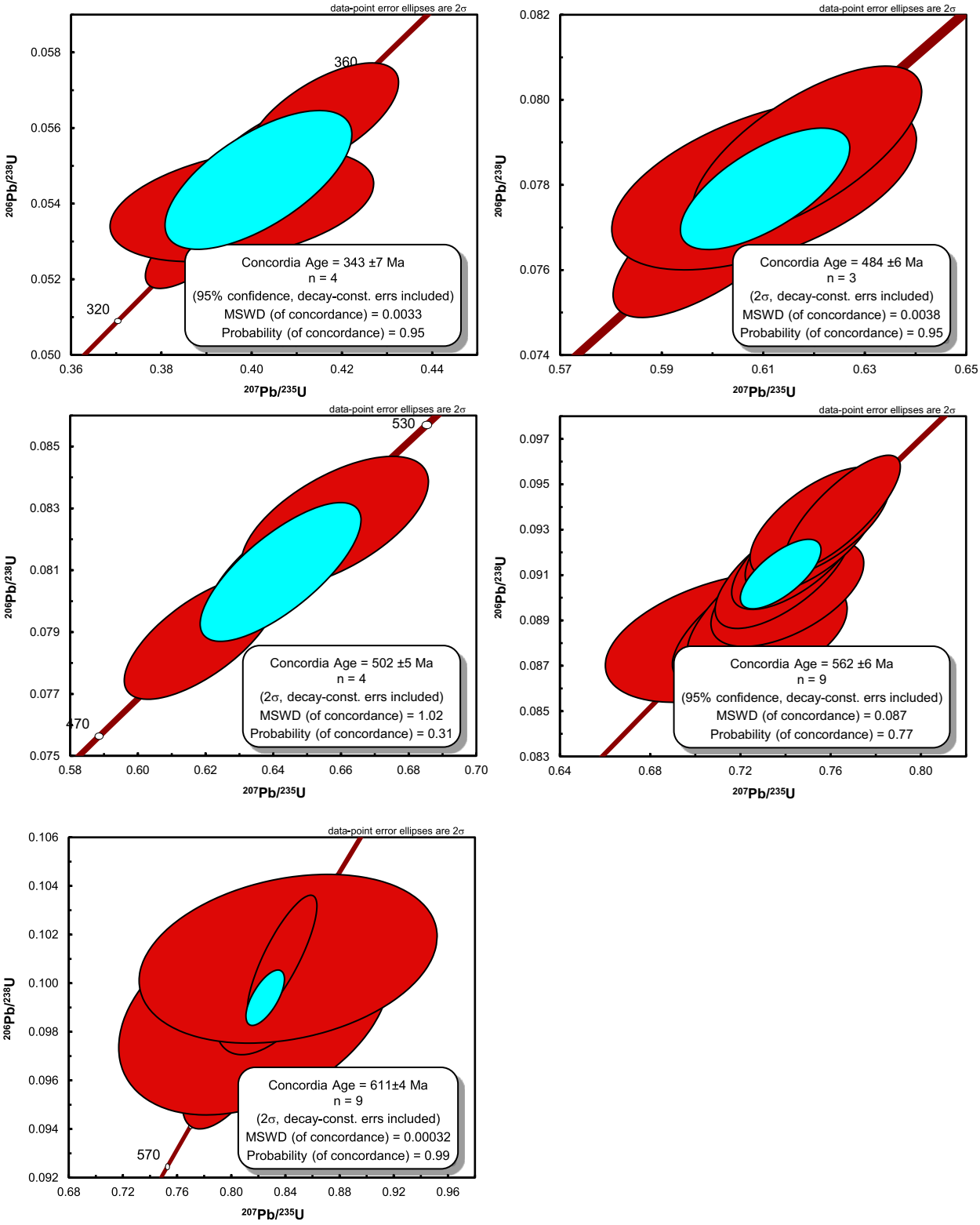

LS154

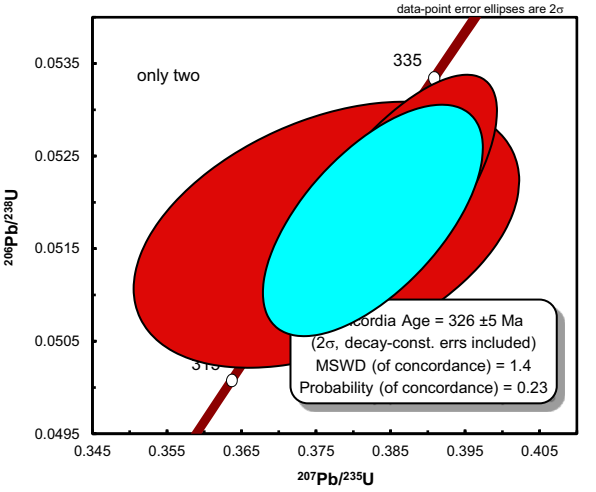
data-point error ellipses are 2σ
only two
335
Concordia Age = 326 ±5 Ma
(2σ, decay-const. errs included)
MSWD (of concordance) = 1.4
Probability (of concordance) = 0.23
206Pb/238U
207Pb/235U

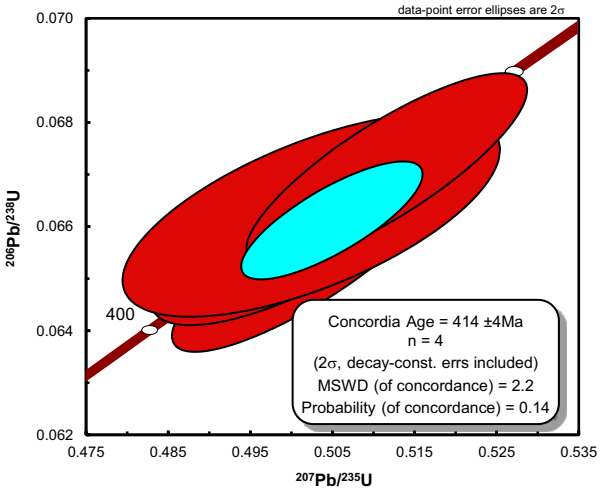
data-point error ellipses are 2σ
400
Concordia Age = 414 ±4Ma
n = 4
(2σ, decay-const. errs included)
MSWD (of concordance) = 2.2
Probability (of concordance) = 0.14
206Pb/238U
207Pb/235U

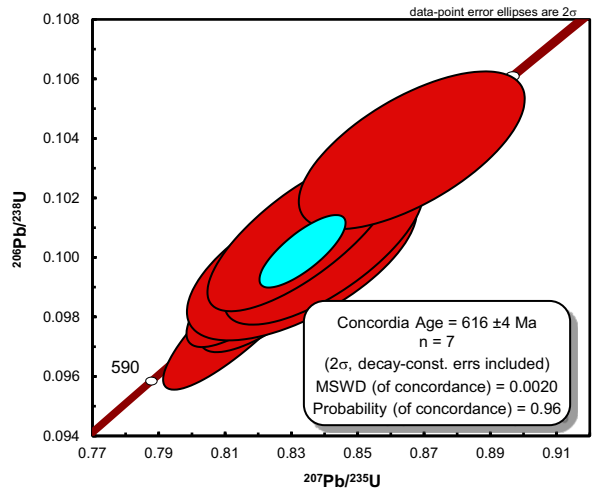
data-point error ellipses are 2σ
590
Concordia Age = 616 ±4 Ma
n = 7
(2σ, decay-const. errs included)
MSWD (of concordance) = 0.0020
Probability (of concordance) = 0.96
206Pb/238U
207Pb/235U

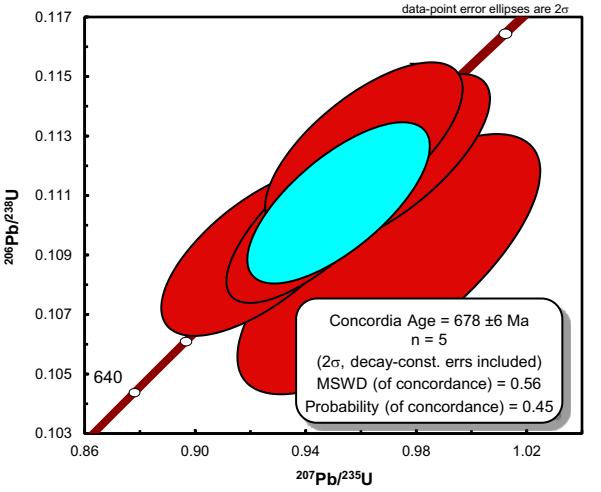
data-point error ellipses are 2σ
640
Concordia Age = 678 ±6 Ma
n = 5
(2σ, decay-const. errs included)
MSWD (of concordance) = 0.56
Probability (of concordance) = 0.45
206Pb/238U
207Pb/235U

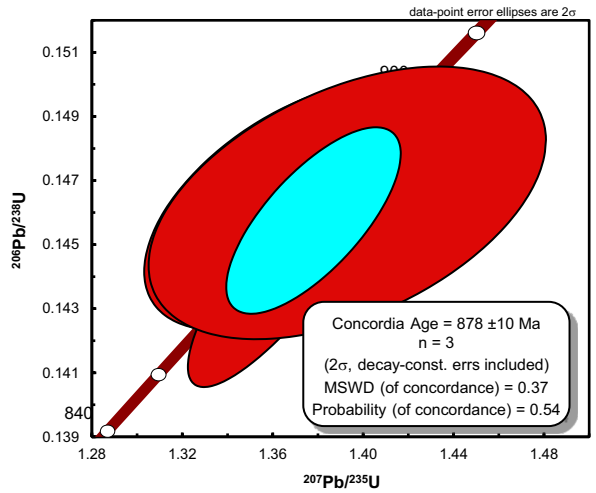
data-point error ellipses are 2σ
840
Concordia Age = 878 ±10 Ma
n = 3
(2σ, decay-const. errs included)
MSWD (of concordance) = 0.37
Probability (of concordance) = 0.54
206Pb/238U
207Pb/235U

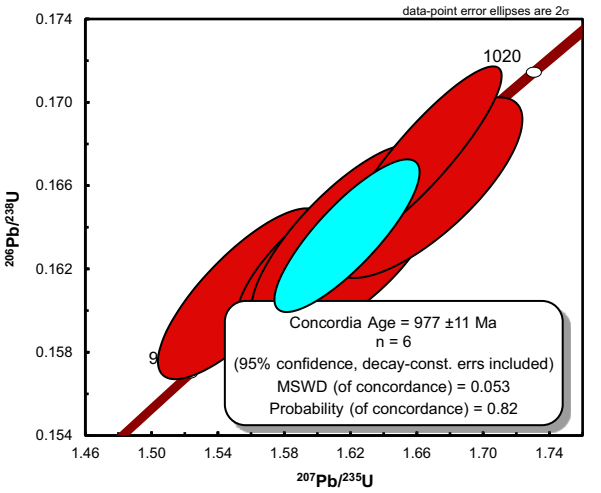
data-point error ellipses are 2σ
1020
Concordia Age = 977 ±11 Ma
n = 6
(95% confidence, decay-const. errs included)
MSWD (of concordance) = 0.053
Probability (of concordance) = 0.82
206Pb/238U
207Pb/235U

LS147

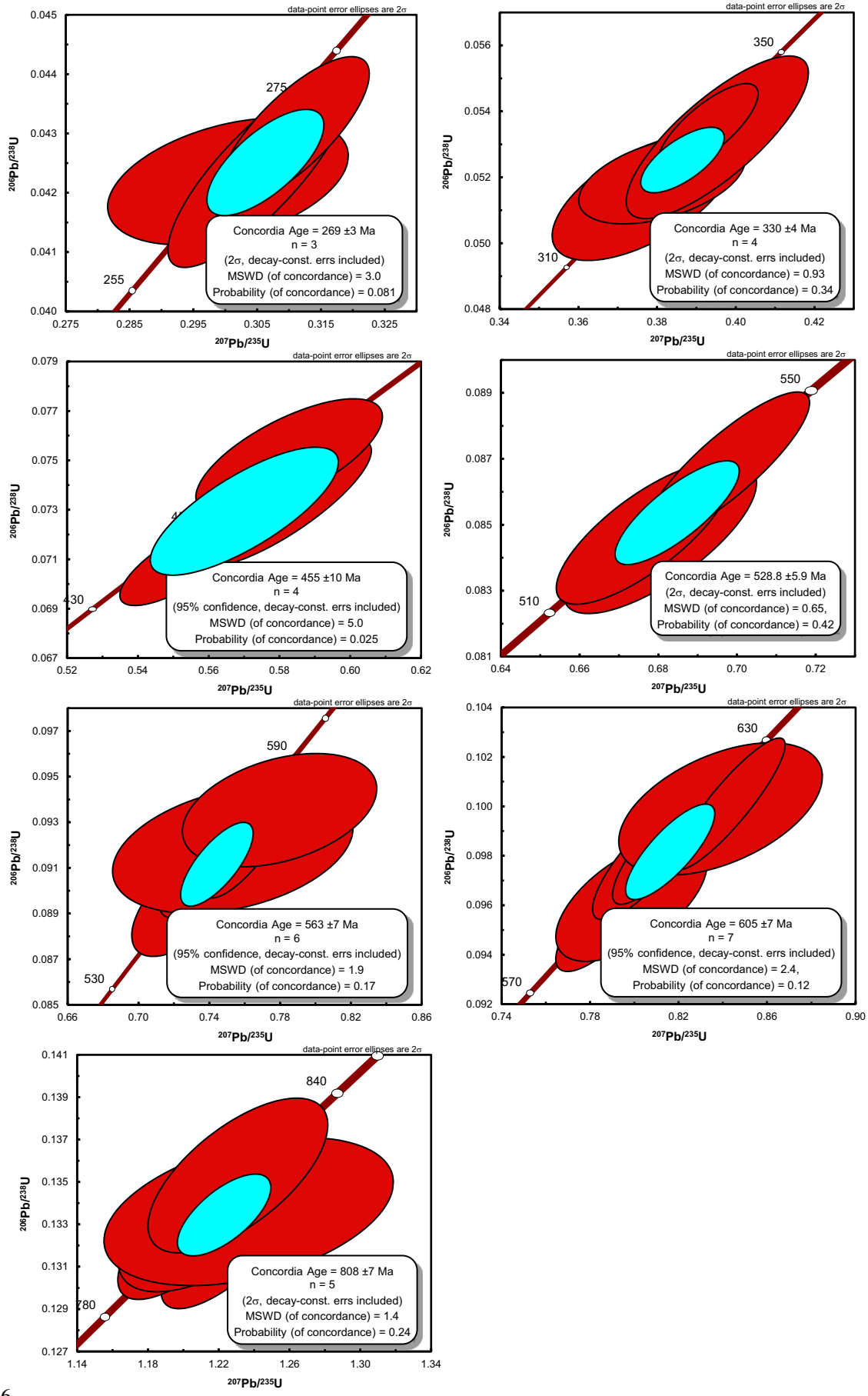
data-point error ellipses are 2σ
Concordia Age = 269 ±3 Ma
n = 3
(2σ, decay-const. errs included)
MSWD (of concordance) = 3.0
Probability (of concordance) = 0.081
Concordia Age = 330 ±4 Ma
n = 4
(2σ, decay-const. errs included)
MSWD (of concordance) = 0.93
Probability (of concordance) = 0.34
Concordia Age = 455 ±10 Ma
n = 4
(95% confidence, decay-const. errs included)
MSWD (of concordance) = 5.0
Probability (of concordance) = 0.025
Concordia Age = 528.8 ±5.9 Ma
(2σ, decay-const. errs included)
MSWD (of concordance) = 0.65,
Probability (of concordance) = 0.42
Concordia Age = 563 ±7 Ma
n = 6
(95% confidence, decay-const. errs included)
MSWD (of concordance) = 1.9
Probability (of concordance) = 0.17
Concordia Age = 605 ±7 Ma
n = 7
(95% confidence, decay-const. errs included)
MSWD (of concordance) = 2.4,
Probability (of concordance) = 0.12
Concordia Age = 808 ±7 Ma
n = 5
(2σ, decay-const. errs included)
MSWD (of concordance) = 1.4
Probability (of concordance) = 0.24
206Pb/238U
207Pb/235U

LS151

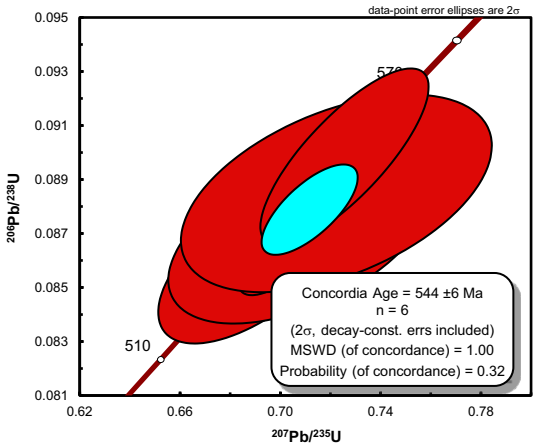
data-point error ellipses are 2σ
Concordia Age = 544 ±6 Ma
n = 6
(2σ, decay-const. errs included)
MSWD (of concordance) = 1.00
Probability (of concordance) = 0.32
510
206Pb/238U
207Pb/235U

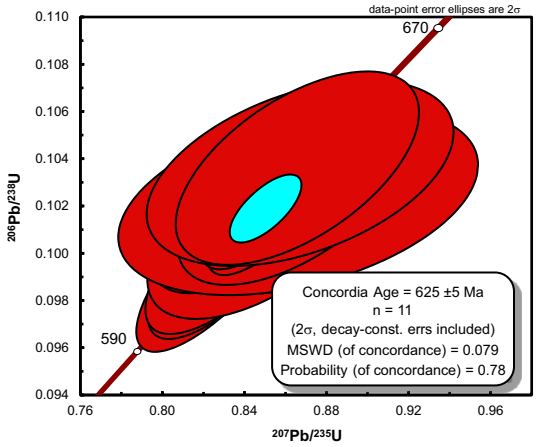
data-point error ellipses are 2σ
670
Concordia Age = 625 ±5 Ma
n = 11
(2σ, decay-const. errs included)
MSWD (of concordance) = 0.079
Probability (of concordance) = 0.78
590
206Pb/238U
207Pb/235U

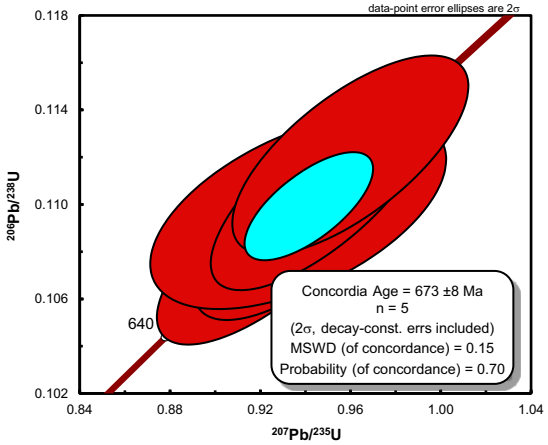
data-point error ellipses are 2σ
Concordia Age = 673 ±8 Ma
n = 5
(2σ, decay-const. errs included)
MSWD (of concordance) = 0.15
Probability (of concordance) = 0.70
640
206Pb/238U
207Pb/235U

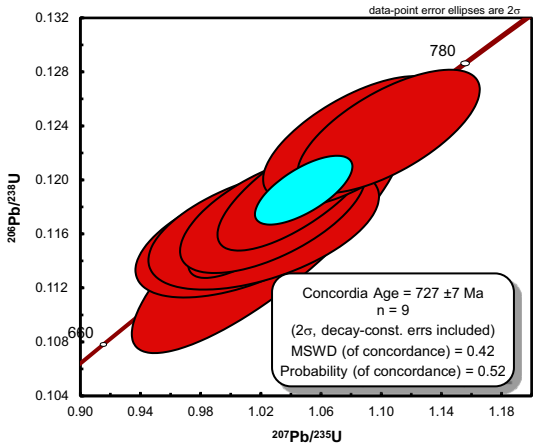
data-point error ellipses are 2σ
780
Concordia Age = 727 ±7 Ma
n = 9
(2σ, decay-const. errs included)
MSWD (of concordance) = 0.42
Probability (of concordance) = 0.52
660
206Pb/238U
207Pb/235U

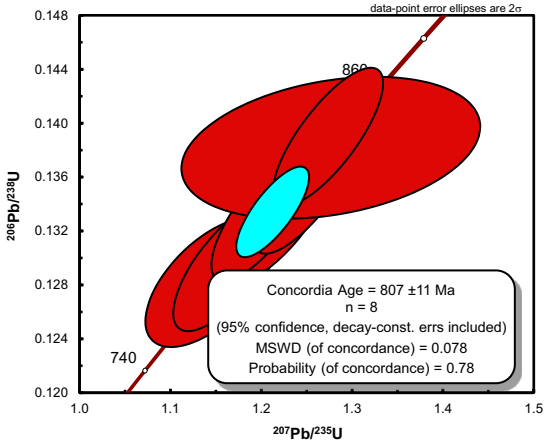
data-point error ellipses are 2σ
Concordia Age = 807 ±11 Ma
n = 8
(95% confidence, decay-const. errs included)
MSWD (of concordance) = 0.078
Probability (of concordance) = 0.78
740
206Pb/238U
207Pb/235U

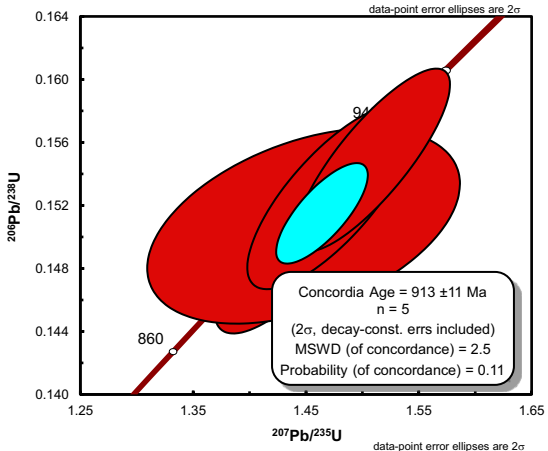
data-point error ellipses are 2σ
Concordia Age = 913 ±11 Ma
n = 5
(2σ, decay-const. errs included)
MSWD (of concordance) = 2.5
Probability (of concordance) = 0.11
860
206Pb/238U
207Pb/235U

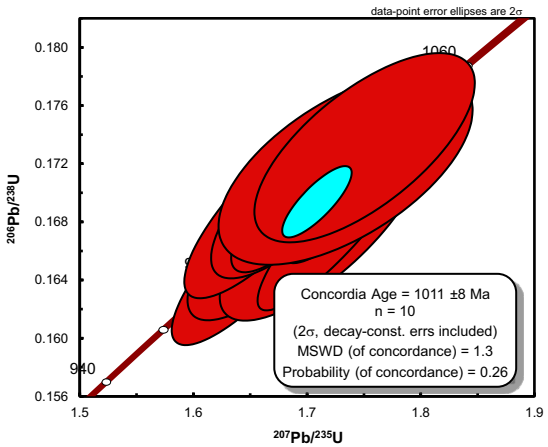
data-point error ellipses are 2σ
1060
Concordia Age = 1011 ±8 Ma
n = 10
(2σ, decay-const. errs included)
MSWD (of concordance) = 1.3
Probability (of concordance) = 0.26
940
206Pb/238U
207Pb/235U

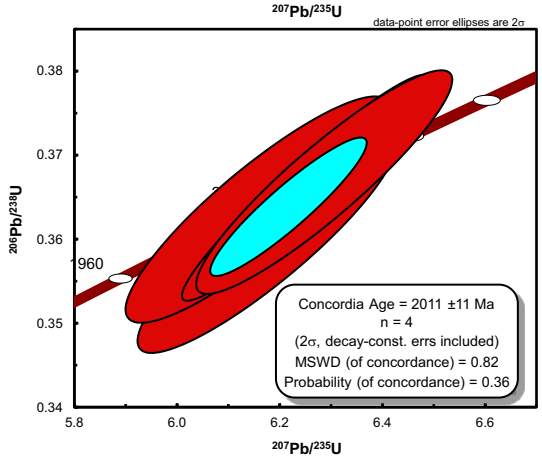
data-point error ellipses are 2σ
Concordia Age = 2011 ±11 Ma
n = 4
(2σ, decay-const. errs included)
MSWD (of concordance) = 0.82
Probability (of concordance) = 0.36
960
206Pb/238U
207Pb/235U

LS144

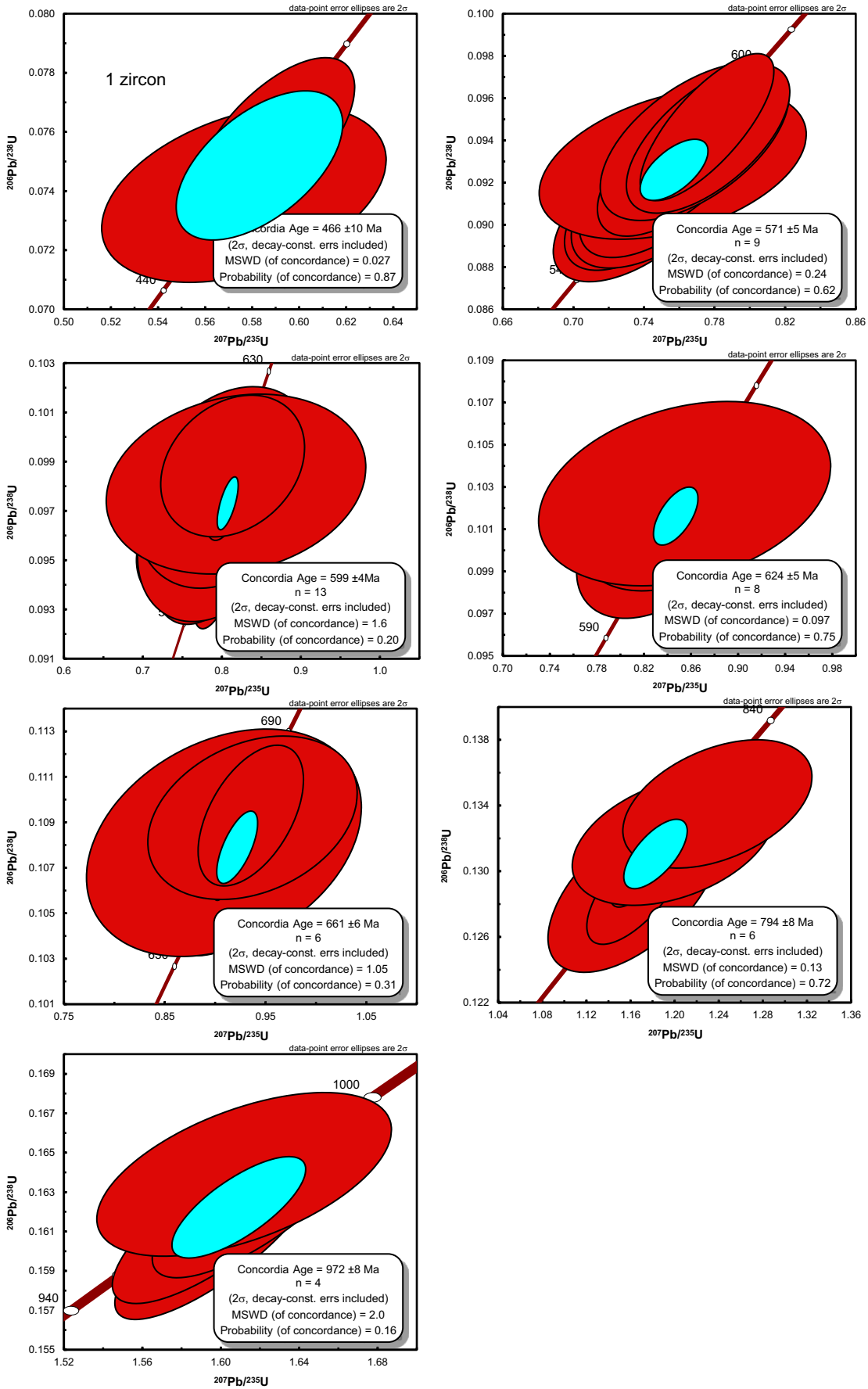
data-point error ellipses are 2σ
1 zircon
Concordia Age = 466 ±10 Ma
(2σ, decay-const. errs included)
MSWD (of concordance) = 0.027
Probability (of concordance) = 0.87
440
Concordia Age = 571 ±5 Ma
n = 9
(2σ, decay-const. errs included)
MSWD (of concordance) = 0.24
Probability (of concordance) = 0.62
600
630
Concordia Age = 599 ±4Ma
n = 13
(2σ, decay-const. errs included)
MSWD (of concordance) = 1.6
Probability (of concordance) = 0.20
Concordia Age = 624 ±5 Ma
n = 8
(2σ, decay-const. errs included)
MSWD (of concordance) = 0.097
Probability (of concordance) = 0.75
590
690
Concordia Age = 661 ±6 Ma
n = 6
(2σ, decay-const. errs included)
MSWD (of concordance) = 1.05
Probability (of concordance) = 0.31
840
Concordia Age = 794 ±8 Ma
n = 6
(2σ, decay-const. errs included)
MSWD (of concordance) = 0.13
Probability (of concordance) = 0.72
1000
940
Concordia Age = 972 ±8 Ma
n = 4
(2σ, decay-const. errs included)
MSWD (of concordance) = 2.0
Probability (of concordance) = 0.16
206Pb/238U
207Pb/235U

Raman measurements of two samples of the Bali beds (LS75 and LS104) and two samples of the PQ s.str. (LS110 and LS255)

Sample	D1					G					D2					R1	R2	T [°C] after Beyssac et al. (2002)			T [°C] after Rahl et al. (2005)		
	Amplitude	Position	FHWM	Analytic Area	Area %	Amplitude	Position	FHWM	Analytic Area	Area %	Amplitude	Position	FHWM	Analytic Area	Area %				**Mean T**	St.dev		**Mean T**	St.dev
LS75_1	329.49	1353.54	39.28	19764.53	55.72	329.49	1586.42	28.06	13682.48	38.57	90.17	1621.77	20.20	2027.25	5.71	1.00	0.56	393			383		
LS75_2	635.04	1352.41	39.28	38993.60	56.91	573.50	1586.98	28.06	25152.93	36.71	166.67	1621.21	23.57	4371.56	6.38	1.11	0.57	388			387		
LS75_3	1778.04	1351.86	34.80	93174.54	48.76	1882.48	1583.61	28.06	78654.20	41.16	685.90	1620.65	17.96	19253.13	10.08	0.94	0.49	424			448		
LS75_4	567.09	1351.85	39.28	34627.18	54.57	555.13	1585.30	29.18	25321.47	39.91	175.21	1620.65	17.96	3501.52	5.52	1.02	0.55	398			399		
LS75_5	891.88	1351.85	43.77	60682.74	57.98	717.95	1586.98	32.55	36526.98	34.90	271.37	1619.53	24.69	7456.74	7.12	1.24	0.58	383			393		
LS75_6	486.32	1352.41	39.28	28034.50	50.24	540.17	1584.74	29.18	23560.65	42.22	172.22	1621.21	15.71	4206.41	7.54	0.90	0.50	417			425		
LS75_7	673.08	1352.41	37.04	38750.08	52.36	669.23	1585.30	29.18	30526.12	41.24	223.08	1621.77	19.08	4736.66	6.40	1.01	0.52	408			420		
LS75_8	498.29	1350.73	53.87	41961.04	59.68	396.58	1586.98	39.28	24351.32	34.63	139.32	1620.65	25.81	4002.19	5.69	1.26	0.60	375			376		
LS75_9	1465.81	1351.29	51.63	118290.00	58.07	1209.40	1588.10	40.40	72765.19	35.72	482.91	1619.53	23.57	12666.31	6.22	1.21	0.58	383			388		
LS75_10	327.78	1352.41	43.77	22426.75	53.22	332.91	1585.86	33.67	16902.84	40.11	93.59	1619.53	21.33	2810.58	6.67	0.98	0.53	404	**397**	15	407	**403**	21
LS104_1	1797.01	1350.73	47.14	132410.00	63.73	1070.51	1586.98	35.91	57252.24	27.56	514.96	1617.85	29.17	18089.94	8.71	1.68	0.64	357			369		
LS104_2	1797.01	1350.73	58.36	159560.00	67.45	974.36	1590.35	40.40	61538.06	26.01	440.17	1617.85	29.17	15462.77	6.54	1.84	0.67	341			335		
LS104_3	857.26	1351.85	41.53	55646.66	59.08	630.77	1586.98	33.67	33198.16	35.25	237.61	1621.21	20.20	5341.95	0.67	1.36	0.59	378			394		
LS104_4	3363.25	1346.80	58.36	306820.00	63.98	2098.29	1585.86	42.65	139890.00	29.17	833.33	1615.60	28.06	32867.14	6.85	1.60	0.64	356			362		
LS104_5	607.69	1352.41	42.65	40512.55	58.09	481.20	1585.86	32.55	24481.77	35.10	211.11	1621.21	20.20	4746.26	6.81	1.26	0.58	382			394		
LS104_6	957.69	1351.29	43.77	63116.55	59.36	755.56	1584.74	31.43	37114.77	34.90	257.26	1619.53	20.20	6104.52	5.74	1.27	0.59	377			381		
LS104_7	1583.33	1351.29	39.28	97221.58	52.31	1583.33	1584.18	30.30	74999.51	40.36	589.74	1619.53	17.96	13620.52	7.33	1.00	0.52	408			419		
LS104_8	1371.79	1350.17	58.36	121800.00	61.75	918.80	1589.79	44.89	64477.01	32.69	311.97	1618.41	29.17	10959.05	5.56	1.49	0.62	366			378		
LS104_9	1465.81	1350.73	53.87	120140.00	58.84	1220.09	1587.54	40.40	70716.90	34.63	493.59	1619.53	22.44	13338.01	6.53	1.20	0.59	379			379		
LS104_10	1269.23	1350.73	38.16	75708.00	54.76	1166.67	1584.18	28.06	51168.03	37.01	457.26	1620.65	17.96	11383.69	8.23	1.09	0.55	397	**374**	19	407	**382**	23
LS110_1	621.37	1352.41	44.89	43604.45	57.53	470.94	1585.86	38.16	28090.98	37.06	149.57	1619.53	21.32	4102.20	5.41	1.32	0.58	385			406		
LS110_2	400.00	1351.85	46.02	28771.74	60.20	266.67	1587.54	39.28	16374.16	34.26	79.49	1619.53	21.32	2649.56	5.54	1.50	0.60	373			395		
LS110_3	614.53	1352.97	39.28	36726.54	50.95	511.97	1586.42	39.28	31409.39	43.57	139.32	1622.90	23.56	3952.88	5.48	1.20	0.51	414			463		
LS110_4	3363.25	1346.80	58.36	306820.00	64.64	2166.67	1585.30	42.65	144440.00	30.43	833.33	1615.60	26.40	23421.45	4.93	1.55	0.65	353			351		
LS110_5	579.06	1351.85	40.40	35595.51	57.64	453.42	1585.30	31.43	21658.09	35.07	196.15	1621.21	19.08	4505.48	7.30	1.28	0.58	385			401		
LS110_6	827.35	1350.73	43.77	56607.82	59.52	592.31	1585.86	35.91	33252.14	34.96	216.24	1619.53	22.80	5248.81	5.52	1.40	0.60	376			393		
LS110_7	715.38	1351.85	43.77	48947.05	59.34	480.77	1588.10	39.28	29520.72	35.79	165.38	1621.77	22.80	4014.40	4.87	1.49	0.59	377			403		
LS110_8	495.30	1351.29	43.77	33888.67	55.95	363.68	1588.10	42.65	24244.85	40.03	100.43	1621.21	22.80	2437.69	4.02	1.36	0.56	392			428		
LS110_9	835.90	1351.85	43.77	57192.61	60.18	570.94	1586.98	40.41	31660.39	33.31	211.97	1620.65	23.57	6183.34	6.51	1.46	0.60	373			392		
LS110_10	723.08	1351.29	43.77	48152.42	58.57	492.31	1586.98	38.16	29365.53	35.72	165.38	1620.65	23.56	4692.53	5.71	1.47	0.59	380	**381**	15	410	**404**	27
LS255_1	405.13	1349.05	39.28	23353.87	53.41	389.74	1583.05	33.67	19205.20	43.92	53.85	1621.21	20.40	1169.43	2.67	1.04	0.53	403			414		
LS255_2	380.77	1350.17	43.77	26052.46	56.80	361.54	1583.05	33.67	17815.35	38.84	71.15	1619.53	26.40	1999.83	4.36	1.05	0.57	388			380		
LS255_3	252.14	1351.29	41.53	15283.65	55.14	228.21	1582.49	33.67	11245.15	40.57	51.71	1617.85	21.60	1189.09	4.29	1.10	0.55	396			405		
LS255_4	1072.65	1350.17	40.40	64090.25	54.08	1038.46	1583.05	33.67	51171.74	43.18	115.38	1619.53	26.40	3242.97	2.74	1.03	0.54	400			406		
LS255_6	995.73	1349.05	40.41	56883.61	54.63	901.71	1583.05	33.67	44433.07	42.68	115.38	1619.53	22.80	2800.75	2.69	1.10	0.55	398			410		
LS255_7	458.97	1350.17	41.53	27821.43	53.86	435.90	1583.61	33.09	22655.21	43.86	51.28	1618.97	21.60	1179.26	2.28	1.05	0.54	401			411		
LS255_8	2076.92	1349.61	40.41	118650.00	54.39	2000.00	1581.93	33.67	90469.44	41.47	371.79	1617.85	22.80	9024.63	4.14	1.04	0.54	399			403		
LS255_9	564.10	1350.17	40.41	32225.91	55.66	486.32	1583.61	33.67	23964.38	41.39	70.51	1619.53	22.80	1711.57	2.96	1.16	0.56	393			407		
LS255_11	351.92	1351.85	40.41	20104.57	53.37	321.15	1583.61	34.79	16352.84	43.41	55.77	1620.65	20.40	1211.20	3.22	1.10	0.53	404			423		
LS255_12	570.09	1349.61	40.41	32567.70	49.62	669.23	1582.49	31.42	30778.85	46.90	105.13	1619.53	20.40	2283.18	3.48	0.85	0.50	420	**400**	8	423	**408**	11

8.5 Electron microprobe data of monazite

Electron microprobe measurements of monazite in albite schist from the PQ s.str. north of Bali village (sample LS86).

Measurement No.	LS86-Mnz1 6	LS86-Mnz2 7	LS86-Mnz4 9	LS86-Mnz5 10	LS86-Mnz6 11	LS86-Mnz8 13	LS86-Mnz9 14	LS86-Mnz10 15	LS86-Mnz11 16	LS86-Mnz12c 18
CaO	0.29	0.42	0.58	0.47	0.23	0.53	0.16	0.32	0.53	0.57
Y_2O_3	0.82	0.67	0.66	0.58	0.47	0.67	0.55	0.60	0.71	0.89
ThO_2	1.96	3.29	7.95	5.89	2.33	6.42	0.67	3.21	6.62	4.11
SiO_2	0.16	0.34	1.25	0.82	0.29	0.90	0.25	0.37	1.07	0.46
UO_2 Corr	0.02	0.02	0.07	0.07	0.02	0.07	0.00	0.02	0.05	0.03
P_2O_5	30.80	30.48	28.78	29.67	30.30	29.16	30.50	30.21	29.32	30.29
PbO	<d.l.	<d.l.	<d.l.	<d.l.	<d.l.	<d.l.	<d.l.	<d.l.	<d.l.	<d.l.
Dy_2O_3	0.55	0.49	0.42	0.40	0.29	0.44	0.32	0.39	0.47	0.66
Gd_2O_3	3.02	1.78	2.86	1.99	1.15	2.26	0.63	2.19	2.41	3.73
Sm_2O_3	4.36	2.02	4.53	3.18	1.38	3.71	1.22	2.76	3.96	5.72
Pr_2O_3	3.90	3.29	3.50	3.35	3.17	3.43	3.30	3.36	3.51	3.90
Nd_2O_3	17.29	12.19	16.07	14.42	11.19	15.47	11.85	13.63	15.90	18.94
Ce_2O_3	31.05	34.63	27.14	31.22	35.61	28.74	37.04	33.34	29.12	27.33
La_2O_3	7.55	12.18	7.15	10.61	14.12	8.35	16.15	10.06	8.65	5.74
As_2O_5	0.14	0.09	0.12	0.11	0.07	0.14	0.07	0.10	0.14	0.18
Total	101.93	101.89	101.09	102.77	100.62	100.29	102.69	100.55	102.44	102.54
La/Nd	0.5	1.0	0.5	0.8	1.3	0.6	1.4	0.8	0.6	0.3

Acknowledgement

First of all I thank my supervisor Prof. Claudia A. Trepmann. Her door was always open for discussions and she always provided valuable advice and motivation. Fruitful discussions in the field, but also her cheerful manner and spirit for informal discussions at dinners or coffee breaks, contributed to always having great time during collaborative field work in Crete. I'm very grateful for her constant support and advice during preparation of manuscripts and sometimes exhausting review processes.

Many thanks to Jochen Krahl, who provided constant advice and was always instantly available for questions and discussions on the fascinating geology of Crete, regardless of the medium (via mail, textmessage or in person) and regardless of the location, in Munich or in the field on Crete. I'm grateful for the possibility to profit from his vast knowledge on the Cretan geology.

I also want to thank my other Co-authors Emilie Janots, who is greatly missed in Munich since she had to leave to return to France, and Wolfgang Dörr for his straightforward cooperation during the preparation of the manuscript on zircon data.

Many thanks for fruitful discussions to Gernold Zulauf (also for showing us the geology of Eastern Crete) and to Otto Förster.

For having a great time during fieldwork in Crete I also especially want to thank Miriam Dühnforth, who is also greatly missed at the institute in Munich since she had to leave.

Namvar Jahanmehr is greatly acknowledged for preparing hundreds of thin sections. Linda Marko is acknowledged for help with isotopic analyses. For help with zircon separation I want to thank Ferdinand Kirchner, and Elisabeth von Berg for support and possibility to use the lab for my attempt to separate conodonts from marbles. I thank Rosa Susnjar for managing all the administrative work and overviewing finances of the project. I thank David Planner for providing always friendly and fast support with IT.

Many thanks also to my colleges Felix Hentschel, Alexander Reul, Dorothea Frieling, Thomas Kunzmann, and all other friends and colleges from LMU.

The Deutsche Forschungsgemeinschaft is acknowledged for funding the project (DFG Grant no. TR534/5-1).

And last but not least I want to thank my family for their support and for being there for me. I especially thank Moritz Gamperl and Tamara Seybold for discussions and support during finishing of my thesis.